

論文 / 著書情報
Article / Book Information

題目(和文)	重力波信号増幅システムにおける光熱効果及び非線形光学効果の研究
Title(English)	Photothermal and nonlinear optical effects in the signal amplification system for a gravitational wave detector
著者(和文)	小田部 荘達
Author(English)	Sotatsu Otabe
出典(和文)	学位:博士(理学), 学位授与機関:東京工業大学, 報告番号:甲第12310号, 授与年月日:2023年3月26日, 学位の種別:課程博士, 審査員:宗宮 健太郎,上妻 幹旺,佐藤 琢哉,陣内 修,相川 清隆
Citation(English)	Degree:Doctor (Science), Conferring organization: Tokyo Institute of Technology, Report number:甲第12310号, Conferred date:2023/3/26, Degree Type:Course doctor, Examiner:,,,,,
学位種別(和文)	博士論文
Type(English)	Doctoral Thesis

Ph.D. Thesis

Photothermal and Nonlinear Optical Effects
in the Signal Amplification System
for a Gravitational Wave Detector

Department of Physics
Tokyo Institute of Technology

Sotatsu Otabe

February 23, 2023



Abstract

The inception of gravitational wave astronomy has revealed astonishing astronomical insights and also underscored the importance of further improving the sensitivity of detectors. High-frequency gravitational waves emitted from binary neutron star post-merger remnants contain critical information about high-density nuclear materials that cannot be accessed by terrestrial experiments. However, high-frequency gravitational waves have yet to be observed and are unlikely to be observed because of the lack of sensitivity of modern gravitational wave detectors. Intracavity signal amplification using nonlinear optical effects is a promising technique for dramatically improving the sensitivity of gravitational wave detectors in the high-frequency band. The signal amplification effect generates a stiff optical spring that can amplify high-frequency gravitational wave signals at its resonant frequency. In this thesis, we construct an intracavity signal amplification system using two nonlinear optical effects, namely, optical parametric amplification and the optical Kerr effect, and investigate the behavior of the optical spring generated in the cavity. We found that the photothermal effect caused by thermal absorption in a nonlinear optical crystal is an essential characteristic of a signal amplification system. We developed a method to precisely estimate the photothermal parameters by measuring the susceptibility of an optomechanical oscillator. Finally, we successfully observed an optical spring enhanced by the intracavity signal amplification effect by appropriately eliminating the photothermal effect from the measurement results. This study revealed the impact of intracavity signal amplification on optomechanical systems and demonstrated a signal amplification system that improved the sensitivity of gravitational wave detectors in the high-frequency band.

Contents

Chapter 1	Introduction	1
Chapter 2	Gravitational waves and their detection	3
2.1	Detectability of gravitational waves	3
2.1.1	Gravitational waves generated by the compact binary system	3
2.1.2	Impact of gravitational waves on the optical interferometer	4
2.2	Detection of gravitational waves	6
2.2.1	Binary black hole merger	6
2.2.2	Binary neutron star merger	7
2.2.3	Neutron star-black hole coalescence and mass gap	7
2.3	Potential candidates	7
2.3.1	Supermassive black hole binaries	8
2.3.2	Supernovae	8
2.3.3	Rotating neutron stars	8
2.3.4	Binary neutron star post-merger remnants	8
2.3.5	Stochastic background	9
2.4	History and future plans of the gravitational wave detector	9
2.4.1	Resonant bar detectors	9
2.4.2	Laser interferometer and optomechanics	10
2.4.3	First-generation gravitational wave detectors	10
2.4.4	Second-generation gravitational wave detectors	10
2.4.5	Future plans	11
2.5	Fundamental noise sources of the gravitational wave detector	12
2.5.1	Seismic noise	13
2.5.2	Newtonian noise	13
2.5.3	Thermal noise	13
2.5.4	Radiation pressure noise	14
2.5.5	Shot noise	14
2.6	Summary of this chapter	14
Chapter 3	Quantum noise in gravitational wave detectors	16
3.1	Two-photon formalism	16

3.1.1	Quadrature decomposition of quantized electro-magnetic fields	17
3.1.2	Spectral density	19
3.1.3	Correspondence to classical electromagnetic field	19
3.2	Definition of operators	20
3.2.1	Transmission, reflection, and superposition	20
3.2.2	Propagation	21
3.2.3	Optical parametric amplification	22
3.2.4	Gravitational wave signal and ponderomotive squeezing	23
3.2.5	Optical Kerr effect	25
3.3	Fundamental theory of quantum noise in gravitational wave detectors	26
3.3.1	Michelson interferometer	26
3.3.2	Fabry-Perot cavity	30
3.3.3	Dual Recycling Michelson interferometer	34
3.4	Advanced techniques for sensitivity improvement	38
3.4.1	Back action evasion by the homodyne detection	39
3.4.2	Input squeezing	40
3.4.3	Detuning of the signal recycling cavity	42
3.5	Application of intracavity squeezing for the gravitational wave detector	49
3.5.1	Broadband bandwidth enhancement based on intracavity squeezing	49
3.5.2	Signal amplification system with a stiff optical spring	52
3.6	Summary of this chapter	56
Chapter 4	Signal amplification experiment based on the OPA scheme	57
4.1	Equivalency of the optical spring in the DRMI and Fabry-Perot cavity	57
4.1.1	Optical spring in the DRMI with intracavity squeezing	58
4.1.2	Optical spring in the Fabry-Perot cavity with intracavity squeezing	62
4.2	Linear signal acquisition methods	66
4.2.1	Pound-Drever-Hall method	67
4.2.2	Phase-locking loop	70
4.2.3	Control of the squeezing angle with the coherent control field	71
4.3	OPA experiment	73
4.3.1	Experimental setup	73

	4.3.2	Estimation of OPA from the transmitted light measurement	76
	4.3.3	Controlling the squeezing angle in the detuned OPO cavity	80
	4.3.4	Measurement of susceptibility of the mechanical suspension	82
	4.3.5	Measurement of susceptibility of the optomechanical oscillator	84
	4.3.6	Suppression of the OPA process	88
4.4		Summary of this chapter	89
Chapter 5		Photothermal effect on the signal amplification system	92
5.1		Overview of photothermal effects in an optical interferometer	92
5.2		Theoretical principles of the photothermal effect	94
	5.2.1	Fundamental equations of the photothermal effect	94
	5.2.2	Time response of the cavity with photothermal effect	95
	5.2.3	Frequency response of the cavity with photothermal effect	97
	5.2.4	Photothermal effect on an optical spring	98
5.3		Experiments on the photothermal effect	100
	5.3.1	Experimental setup	100
	5.3.2	Cavity spectrum with the photothermal effect	102
	5.3.3	Slow photothermal effect	103
	5.3.4	Self-locking of the cavity based on the photothermal effect	105
	5.3.5	Transfer function measurement with a PZT	106
	5.3.6	Transfer function measurement with a suspended mirror	108
	5.3.7	Comparison of methods for estimating the photothermal absorption rate	112
5.4		Summary of this chapter	114
Chapter 6		Signal amplification experiment based on Kerr scheme	116
6.1		Theory of intracavity signal amplification based on the Kerr effect	116
	6.1.1	Enhancement of the optical spring based on the Kerr effect	117
	6.1.2	Optomechanical system with photothermal and Kerr effects	119
6.2		Kerr experiments	122
	6.2.1	Experimental setup	122
	6.2.2	Confirmation of Kerr effect	123
	6.2.3	Enhancement of optical spring by Kerr effect	124

	6.2.4 Estimation of Kerr lensing effect	129
6.3	Summary of this chapter	130
Chapter 7	Conclusion	132
7.1	Theoretical overview	132
7.2	Summary of experiments	133
7.3	Prospects	133
Appendix A	Derivation of gravitational waves	135
A.1	Propagation of gravitational waves	135
A.2	Impact of gravitational waves on free masses	137
A.3	Radiation of gravitational waves	138
	A.3.1 Generation of gravitational waves	138
	A.3.2 Quadrupole formula	139
A.4	Principle of interferometric gravitational wave detectors .	140
A.5	Amplitude spectral density	141
Appendix B	Nonlinear optical effects	142
B.1	Overview of nonlinear optical effects	142
B.2	Principle of three-wave mixing	143
	B.2.1 Coupled-wave equations	144
	B.2.2 Phase matching and quasi-phase matching	145
B.3	Second harmonic generation	146
	B.3.1 SHG with low conversion efficiency	146
	B.3.2 SHG with a periodically polled crystal	147
	B.3.3 SHG with high conversion efficiency	148
	B.3.4 Cascaded nonlinear optical effect	149
B.4	Optical parametric process	150
	B.4.1 Optical parametric amplification	150
	B.4.2 Optical parametric oscillator	151
Appendix C	Quantum noise in advanced interferometers	154
C.1	Resonant sideband extraction and its applications	154
	C.1.1 Fabry-Perot Michelson interferometer	154
	C.1.2 Resonant sideband extraction interferometer . . .	156
	C.1.3 Long signal recycling cavity	159
	C.1.4 Quantum expander	161
C.2	Frequency-dependent squeezing	163
	C.2.1 Input squeezing with a filter cavity	164
Appendix D	Sideband cooling with intracavity squeezing	167
D.1	Thermal phonon number	167
D.2	Radiation pressure phonon number	168
Appendix E	Supplementary materials for the experiments	173

E.1	Feedback control	173
	E.1.1 Stability of the feedback control	173
	E.1.2 Phase compensation	174
E.2	Design of cavities	175
	E.2.1 ABCD matrix	175
	E.2.2 Gaussian beam	177
	E.2.3 Self-consistent equation	178
	E.2.4 Design of bow-tie cavities	179
E.3	Circuit used in the experiment	182
Bibliography		186

List of Figures

2.1	Schematic of a compact binary star system	4
2.2	Effect of gravitational waves on free masses	5
2.3	Impact of gravitational waves on the Michelson interferometer	5
2.4	Waveform of GW150914	6
2.5	Sensitivity of KAGRA	12
3.1	Schematic diagram of each factor configuring an optical interferometer	21
3.2	Schematic of the Michelson interferometer	27
3.3	Sensitivity of the Michelson interferometer	29
3.4	Schematic of the Fabry-Perot cavity	30
3.5	Intracavity power of the Fabry-Perot cavity	31
3.6	Schematic of the dual recycling Michelson interferometer	35
3.7	Sensitivity of the dual recycling Michelson interferometer	36
3.8	Sensitivity of the DRMI as determined by shot noise	37
3.9	Sensitivity of the DRMI to several homodyne angles	40
3.10	Schematic of input squeezing for the DRMI	41
3.11	Sensitivity of the DRMI with input squeezing	42
3.12	Sensitivity of the DRMI with the detuning of the SRC measured using the DC offset	44
3.13	Modification of the standard quantum limit based on an optical spring	46
3.14	Sensitivity of the DRMI with the detuning of the SRC measured using contrast defect	46
3.15	Schematic of the Fabry-Perot cavity as an intracavity carrier criterion	47
3.16	Sensitivity of the detuned DRMI or Fabry-Perot cavity	48
3.17	Schematic of intracavity squeezing for DRMI	50
3.18	Sensitivity of the intracavity-squeezed DRMI	51
3.19	Sensitivity of the intracavity-squeezed DRMI determined by the shot noise	52
3.20	Sensitivity of the intracavity-squeezed DRMI with detuned SRC	54
3.21	Sensitivity of the intracavity-squeezed DRMI with detuned SRC for several squeezing angles	55

4.1	Schematic of intracavity squeezing for the DRMI	58
4.2	Qualitative illustration of an optical spring	60
4.3	Optical spring constant and optical damping constant with intra- cavity squeezing ($\theta = 0$)	61
4.4	Optical spring constant and optical damping constant with intra- cavity squeezing ($\theta = -\pi/4$)	62
4.5	Schematic of intracavity squeezing for the Fabry-Perot cavity . .	62
4.6	Schematic of intracavity squeezing for the Fabry-Perot cavity as an intracavity carrier criterion	63
4.7	Comparison of intracavity light power with intracavity squeezing	65
4.8	Intracavity light power with intracavity squeezing ($\theta_{\text{inc}} = 0$) . . .	66
4.9	Intracavity light power with intracavity squeezing ($\theta_{\text{inc}} = \pi/2$) .	67
4.10	Schematic of the PDH method for the Fabry-Perot cavity	68
4.11	Error signals obtained using the PDH technique	70
4.12	Schematic of the phase-locking loop	71
4.13	Schematic of the coherent control method for the detuned OPO cavity	72
4.14	Error signal obtained using the coherent control method	73
4.15	Amplitude of the error signal obtained using the coherent control method	74
4.16	Setup of the OPA experiment	74
4.17	Transmitted light power from the OPO cavity (without OPA) . .	77
4.18	Transmitted light power from the OPO cavity (carrier 0.5 mW, $\theta_{\text{inc}} = 0$)	77
4.19	Transmitted light power from the OPO cavity (carrier 0.5 mW, $\theta_{\text{inc}} = \pi/4$)	78
4.20	Transmitted light power from the OPO cavity (carrier 50 mW, $\theta_{\text{inc}} = 0$)	79
4.21	Measurement of the input light power and maximum power am- plification rate	79
4.22	Error signal generated using the coherent control method (de- modulation phase 0 deg)	80
4.23	Error signal generated using the coherent control method (de- modulation phase 90 degrees)	81
4.24	Picture and drawing of the suspension	82
4.25	Phase measurement results of the susceptibility of mechanical suspensions	83
4.26	Phase measurement results of the susceptibility of the optome- chanical oscillator (carrier 4 mW)	85
4.27	Estimation of the impact of OPA ($\sigma = 0.76$)	86
4.28	Estimation of the impact of OPA ($\sigma = 0.39$)	86
4.29	Phase measurement results of the susceptibility of the optome- chanical oscillator (carrier 50 mW)	87
4.30	Measured transmitted power of the carrier light	88

4.31	Estimation of the impact of OPA ($\sigma = 0.99$)	90
5.1	Schematic of the optical cavity containing an absorptive crystal .	93
5.2	Simulation results of the spectrum with the photothermal effect .	96
5.3	Experimental setup using a PZT	100
5.4	Experimental setup using a suspended mirror	101
5.5	Transmission power obtained from the cavity scan	102
5.6	Measurement results of slow thermal relaxation	104
5.7	Measurement results of slow photothermal absorption	104
5.8	Temperature and transmitted power during the self-locking of the cavity	105
5.9	Phase measurement results of the frequency response of the cav- ity using a PPLN crystal	106
5.10	Estimation of the photothermal relaxation rate for a PPKTP crystal	107
5.11	Measurements of the ring down of the mirror using the shadow sensing method	108
5.12	Estimation results of the Q factor of the mechanical suspension .	109
5.13	Measurement results of the transfer function	110
5.14	Estimation results of the optical spring constant	111
5.15	Estimation results of the photothermal absorption rate	112
5.16	Estimated maximum value of the optical spring constant and photothermal absorption rate	113
5.17	Estimation of the photothermal absorption rate using a fixed mirror	114
6.1	Schematic of Fabry-Perot cavity containing a Kerr medium . . .	117
6.2	Normalized intracavity power as a function of mirror displacement	118
6.3	Optical spring constant and optical damping constant with intra- cavity Kerr squeezing	119
6.4	Crystal temperature and transmitted light power at resonance . .	123
6.5	Transmitted light power from the cavity under the first phase- mismatched condition	124
6.6	Measured transfer function of the optical system with a suspended mirror	125
6.7	Measured transfer function of the optical system with a PZT (strong Kerr effect)	126
6.8	Measured transfer function of the optical system with a PZT (moderate Kerr effect)	126
6.9	Measured transfer function of the optical system with a PZT (weak Kerr effect)	127
6.10	Enhancement of the optical spring based on the Kerr effect . . .	128
6.11	Comparison of the optical spring constants for different gains of the Kerr effect	129
B.1	Schematic of periodic poling	146
B.2	Relationship between phase mismatch and SHG efficiency	147

B.3	Relationship between quasi-phase mismatch and SHG efficiency	148
B.4	Relationship between the intensity of the pump light and conversion efficiency of OPO	153
C.1	Schematic of the Fabry-Perot Michelson interferometer	155
C.2	Schematic of the dual-recycling Fabry-Perot Michelson interferometer	156
C.3	Sensitivity of DRFPMI with BSR	158
C.4	Sensitivity of DRFPMI with BRSE	159
C.5	Sensitivity of DRFPMI determined by shot noise	160
C.6	Sensitivity of the RSE interferometer with a long SRC	161
C.7	Schematic of intracavity squeezing for the RSE interferometer .	162
C.8	Sensitivity of the RSE interferometer with intracavity squeezing .	164
C.9	Schematic of frequency-dependent input squeezing with filter cavity	165
C.10	Sensitivity with frequency-dependent input squeezing by the filter cavity	166
D.1	Schematic of sideband cooling with intracavity squeezing	169
D.2	Modification of the radiation pressure phonon number by the intracavity squeezing	172
E.1	Block diagram of the optical system	173
E.2	Schematic of an optical element modifies the trajectory of the ray	175
E.3	Ray tracing by the ABCD matrix	176
E.4	Schematic of a bow-tie cavity	179
E.5	Waist sizes of the SHG cavity	180
E.6	Waist sizes of the OPO cavity	181
E.7	Waist sizes of the OPO cavity with Kerr lens	182
E.8	Circuit of the mixier	183

List of Tables

4.1	Mirrors that constitute the SHG cavity	75
4.2	Mirrors that constitute the OPO cavity	76
4.3	Estimated parameters of mechanical suspensions	83
5.1	Mirrors that constitute the cavity for the photothermal experiment	101

Glossary

ϵ_0	dielectric constant of vacuum
μ_0	permeability of vacuum magnetic constant
c	speed of light
\hbar	reduced Planck constant
k_B	Boltzmann constant
G	Newtonian constant of gravitation
λ_0	wavelength of carrier light
ω_0	angular frequency of carrier light
k_0	wavenumber of carrier light
m	mass of the mirror
L	arm length, half cycle length of the cavity
ϕ	phase change in the free space
α	phase delay in the free space
κ	optomechanical coupling constant in the free space
ξ	homodyne angle
S_h	power spectral density of signal-to-noise ratio
\hbar_{SQL}	standard quantum limit
\mathcal{F}	finesse of the cavity
β	phase delay by the cavity
\mathcal{K}	optomechanical coupling constant by the cavity
γ	cavity decay rate
Δ	cavity detuning
Σ	squeezing decay rate
ω_{th}	photothermal absorption rate
γ_{th}	photothermal relaxation rate

SQL	Standard Quantum Limit
FSR	Free Spectrum Range
FWHM	Full Width at Half Maximum
HWHM	Half Width at Half Maximum
PRC	Power Recycling Cavity
SRC	Signal Recycling Cavity
PRM	Power Recycling Mirror
SRM	Signal Recycling Mirror
ITM	Input Test Mass
ETM	End Test Mass
SRMI	Signal Recycling Michelson Interferometer
DRMI	Dual Recycling Michelson Interferometer
FPMI	Fabry-Perot Michelson Interferometer
DRFPMI	Dual Recycling Fabry-Perot Michelson Interferometer
RSE	Resonant Sideband Extraction
BSR	Broadband Signal Recycling
DSR	Detuned Signal Recycling
BRSE	Broadband Resonant Sideband Extraction
SHG	Second Harmonic Generation
OPA	Optical Parametric Amplification
OPO	Optical Parametric Oscillator
RF	Radio Frequency
DC	Direct Current
AC	Alternate Current
PDH	Pound-Drever-Hall
PLL	Phase Locking Loop
EOM	Electro-Optical Modulator
AOM	Acousto-Optic Modulator
HWP	Half-Wave Plate
QWP	Quarter-Wave Plate
BS	Beam Splitter
PD	Photodetector
AOI	Angle of Incidence
ROC	Radius of Curvature
PZT	lead zirconate titanate, $\text{Pb}(\text{Zr}_x, \text{Ti}_{1-x})\text{O}_3$
NLC	Nonlinear Optical Crystal
PPLN	Periodically Poled LiNbO_3
PPKTP	Periodically Poled KTiOPO_4
RMSE	Root Mean Square Error
TT	Transverse-Traceless
OLTF	Open Loop Transfer Function
OLG	Open Loop Gain
CLTF	Closed Loop Transfer Function
UGF	Unity Gain Frequency
LO	Local Oscillator

Chapter 1

Introduction

Gravitational waves are ripples propagating in space-time at the speed of light, which is derived from the framework of general relativity [1, 2]. Gravitational wave detection was first achieved in 2015 [3]; since then, more than 90 gravitational wave events have been observed [4]. Notably, the gravitational wave generated from a binary neutron star merger was observed in 2017 [5], and follow-up observations using electromagnetic telescopes identified an electromagnetic counterpart [6]. Multimessenger observations with gravitational and electromagnetic waves provided several insights, such as the origin of short gamma-ray bursts [7], the synthesis of very heavy elements via the r-process [8], and new independent measurements of the Hubble constant [9].

Current gravitational wave detectors [10–12] are designed with the best sensitivity in the bandwidth of ~ 100 Hz to observe the inspiral phase of binary neutron star coalescence. However, high-frequency gravitational waves of a few kilohertz (kHz) are predicted to be emitted from supernovae [13], certain rotating neutron stars [14], and binary neutron star post-merger remnants [15, 16]. In particular, the gravitational waves emitted after binary neutron star coalescence are expected to provide essential information for determining the equation of state for the neutron star [17]. However, the sensitivity of the current gravitational wave detectors in the high-frequency band is limited by noise arising from the quantum nature of laser light [18], and high-frequency gravitational waves are unlikely to be observed. High-frequency gravitational waves are of considerable interest, and a new gravitational wave detector designed specifically to observe such events has been proposed [19]. Further research and development are essential for improving the sensitivity of gravitational wave detectors.

Signal amplification using an optical spring is a technique that improves the sensitivity of gravitational wave detectors within a specific bandwidth [20]. An optical spring is generated when the radiation pressure force is proportional to the displacement of the mirror, and the gravitational wave signal can be amplified at its resonant frequency. However, it is difficult to generate an optical spring with a high resonant frequency because its spring constant is proportional to the laser light power. There are limits to the intensity of usable, stable laser sources, and intense laser light causes thermal lensing and other harmful effects. In addition,

increasing the finesse of the cavity reduces the bandwidth of the detector, and high-frequency gravitational waves cannot be detected.

A signal amplification system using nonlinear optical effects is proposed to generate a stiff optical spring [21]. The response rate of the cavity to the signal can be increased by inducing nonlinear optical effects inside the cavity. In other words, the radiation pressure force responds more sensitively to the displacement of the mirror, so that the resonant frequency of the optical spring can be increased without changing the intracavity laser light power. If an optical spring with a resonant frequency of a few kHz is generated using this technique, high-frequency gravitational waves with a high signal-to-noise ratio can be observed.

A verification-of-principle experiment for the signal amplification method must be conducted before its implementation in an actual gravitational wave detector. The essence of a signal amplification system is the enhancement of the optical spring by the nonlinear optical effect. Observing the change in the resonant frequency of the optical spring due to intracavity signal amplification is essential for demonstrating the practicality of this method. Furthermore, intracavity nonlinear interactions may allow macroscopic oscillators to cool down to the quantum ground state [22–24]. By investigating the impact of nonlinear optical effects on optomechanical coupling, we can demonstrate the potential of developing optomechanical systems that cannot be achieved using conventional techniques.

This thesis attempts to configure a signal amplification system using two nonlinear optical effects, optical parametric amplification and the optical Kerr effect, and observe an optical spring enhanced by the intracavity signal amplification effect. Because we conducted the experiment using the Fabry-Perot cavity, which is a more straightforward optical system than the basic configuration of the gravitational wave detector, the correspondence between the configured optical system and the actual gravitational wave detector is carefully discussed. In addition, the intense laser light incident on the nonlinear optical crystal may generate photothermal effects that can influence the radiation pressure force and optical spring constant. To distinguish between the impacts of the photothermal and nonlinear optical effects on the optical spring, methods for modeling and parameter estimation of the photothermal effect are discussed in detail.

This thesis is organized as follows. Chapter 2 briefly reviews the sources of gravitational waves and their detection methods. Chapter 3 discusses quantum noise in laser interferometric gravitational wave detectors and outlines a method to improve the sensitivity by intracavity signal amplification. Chapter 4 introduces signal amplification experiments using optical parametric amplification and discusses problems with experiments that use the Fabry-Perot cavity. Chapter 5 discusses the photothermal effect, a problem that affects experiments with strong intracavity powers, and describes a method for estimating photothermal parameters in the signal amplification system. Chapter 6 introduces the signal amplification experiment using the Kerr effect and presents the experimental results obtained. Chapter 7 provides a summary and future perspectives.

Chapter 2

Gravitational waves and their detection

Gravitational waves are ripples that propagate at the speed of light through space-time and are generated from the asymmetric acceleration motion of a massive object. This chapter briefly reviews the characteristics and sources of gravitational waves and gravitational wave detectors.

2.1 Detectability of gravitational waves

This section provides a rough estimate of the parameters of gravitational waves and briefly discusses the techniques to detect them.

2.1.1 Gravitational waves generated by the compact binary system

Einstein predicted the existence of gravitational waves in 1916 [1, 2]. However, the existence of gravitational waves or astronomical phenomena that emit detectable gravitational waves has been discussed for a long time. In 1974, Hulse and Taylor discovered the neutron star binary system PSR B1913+16, and reported that its orbital period was decreasing [25]. As discussed in App. A.3.2, this phenomenon is considered because of the energy being extracted from the binary system owing to gravitational waves. The observed values agree with the theoretical predictions based on general relativity with high accuracy [26]. This discovery is crucial for indirectly confirming the existence of gravitational waves and indicating the possibility of an astronomical phenomenon of binary compact object mergers.

Let us consider a binary system comprising compact objects as a gravitational wave source, as shown in Fig. 2.1. This system is expected to emit gravitational waves as its semi-major axis decreases and eventually merges. Let the mass of the compact objects be the solar mass $\sim 2 \times 10^{30}$ kg, and the semi-major axis be the solar radius $\sim 7 \times 10^8$ m. Using Eq. (A.31), the power of the gravitational

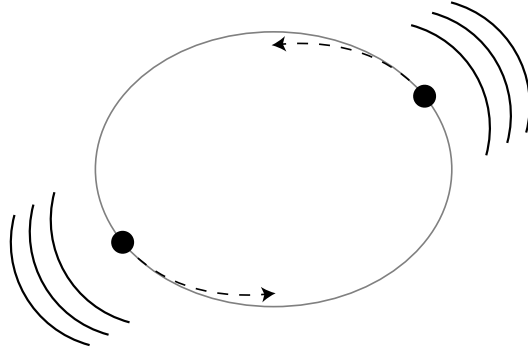


Fig. 2.1: Schematic of a compact binary star system.

wave emitted from the binary system is approximately $\sim 2 \times 10^{24}$ W, which is comparable to the solar radiation flux of $\sim 3 \times 10^{26}$ W. Using Eq. (A.32), the time variation of the semi-major axis can be estimated as $\sim 3 \times 10^{-9}$ m/s, where the semi-major axis decreases and the angular velocity increases very slowly. Using Eq. (A.33), binary star coalescence occurs in $\sim 2 \times 10^{17}$ s, which is comparable to the age of the universe $\sim 4 \times 10^{17}$ s. If binary star systems similar to these parameters have been potentially configured in the universe, it is not surprising for a coalescence event to occur.

Let us roughly estimate the frequency and amplitude of the gravitational waves that can be observed. Assuming a binary merger is imminent, let the semi-major axis be 100 km, which is ten times the radius of a typical neutron star. The frequency of the emitted gravitational wave is twice the Kepler frequency and is obtained as ~ 200 Hz from Eq. (A.30). The velocity of the compact object becomes $\sim 5 \times 10^7$ m/s, approximately 0.2 times the speed of light. As binary neutron star mergers rarely occur unless, from a location with many galaxies, we assume that gravitational waves are emitted from the Virgo cluster, which is about ~ 20 Mpc away. From Eq. (A.27), the strain of the gravitational wave, in this case, is $\sim 6 \times 10^{-23}$, which is equivalent to a ratio of about 1/10 of the radius of a hydrogen atom and the distance between the earth to the sun.

2.1.2 Impact of gravitational waves on the optical interferometer

Gravitational waves are transverse waves propagating at the speed of light and possess two polarizations, $+$ and \times modes. The effect of gravitational waves appears in the distance between two or more free masses, as expressed in Eqs. (A.19) and (A.20). The effect of gravitational waves on free masses is shown in Fig. 2.2. The differential displacement of space must be measured with high precision to detect gravitational waves.

Currently, laser interferometric gravitational wave detectors based on the Michelson interferometer (Fig. 2.3(a)) are widely used. The interference condi-

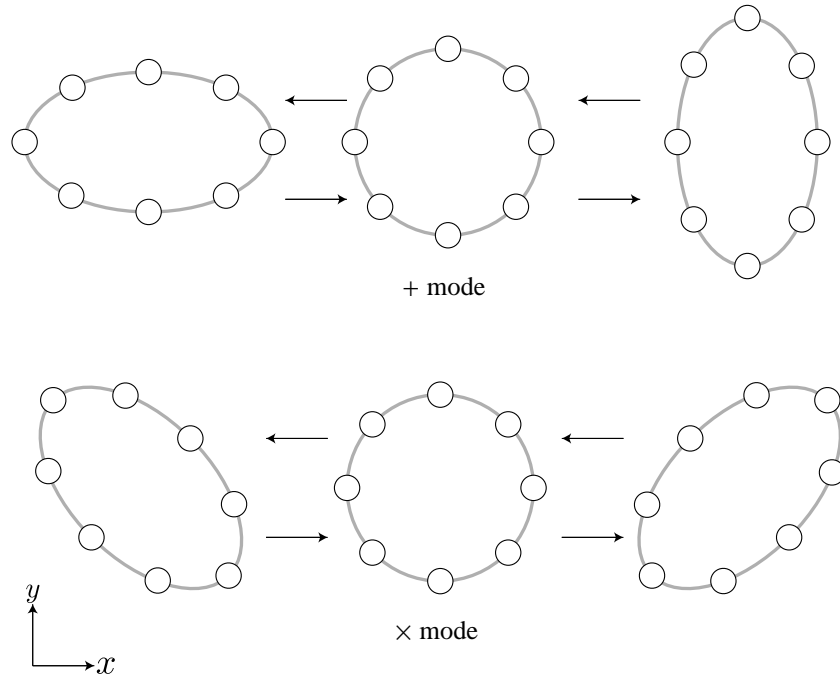


Fig. 2.2: Displacement of the free masses when gravitational waves are incident. Suppose that gravitational waves of + and \times modes are incident from the direction perpendicular to the paper, respectively.

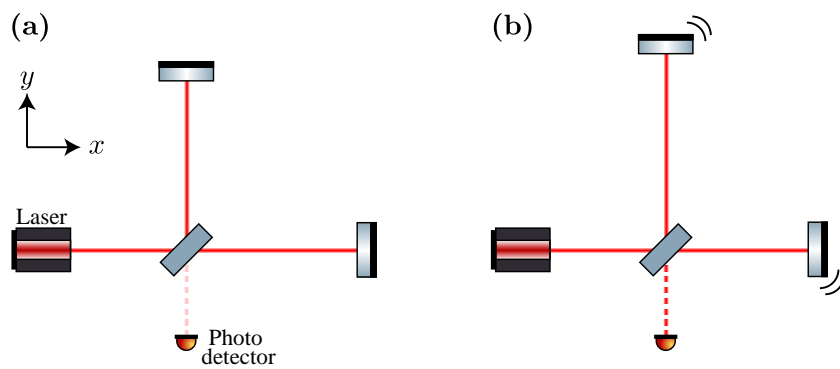


Fig. 2.3: Impact of gravitational waves on the Michelson interferometer. **(a)** Condition without gravitational waves. **(b)** + mode gravitational waves are incident from the direction perpendicular to the paper.

tion should be such that no light comes to the output port where the photodetector is placed. When a gravitational wave arrives, the arm length between the beamsplitter and end mirror varies (Fig. 2.3(b)). The gravitational wave produces a differential displacement with regard to the mirrors, which changes the interference condition. In other words, the gravitational wave signal is converted into a light signal, and the waveform of the gravitational wave can be observed.

2.2 Detection of gravitational waves

Gravitational waves were first detected in 2015 [3] by Advanced LIGO [10]. Since then, approximately 90 binary compact object mergers have been observed [4]. This section briefly introduces the gravitational wave events that have been observed.

2.2.1 Binary black hole merger

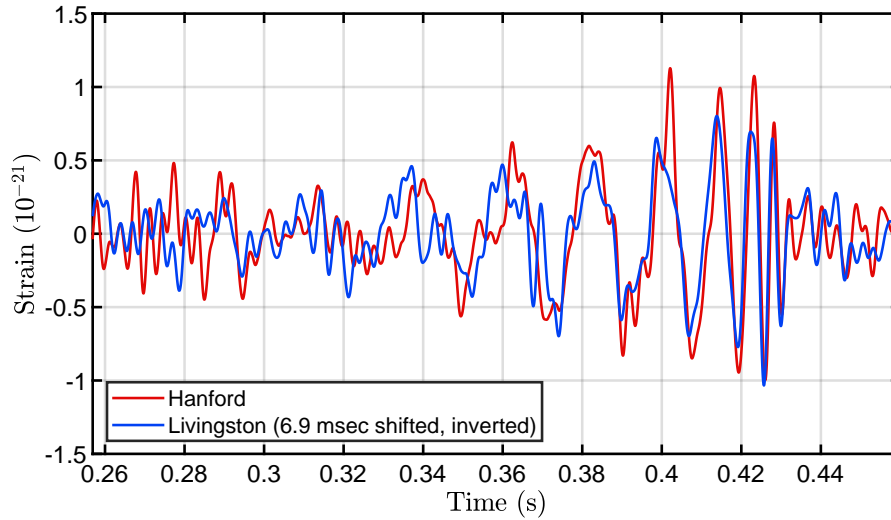


Fig. 2.4: Waveform of GW150914 [3]. Two detectors observed them in Hanford and Livingston in the USA.

GW150914 [3] was the first-ever gravitational wave detected. Fig. 2.4 shows the waveform of GW150914. This gravitational wave is analyzed to be emitted from the merger of two black holes with a mass of approximately 30 solar masses. Almost all the gravitational waves detected to date have been associated with binary black hole mergers, and black holes with similar masses have also been observed. However, stellar black holes formed from a typical core-collapse supernova are known to have a mass of approximately 15 solar masses or less [27]. The origin of these black holes has been theorized as the formation of a binary system from massive stars of population III [28] or the observation of primordial black

holes [29].

2.2.2 Binary neutron star merger

GW170817 [5] is the gravitational wave from the binary neutron star merger, detected by the two LIGO detectors and Advanced VIRGO [11]. The observations have imposed new limits on the parameters for the tidal deformation of neutron stars, and three gravitational wave detectors have provided precise estimates of sky localization. Based on this information, follow-up observations were performed using electromagnetic wave telescopes, and an electromagnetic counterpart was discovered with NGC4993 as the host galaxy [6]. A short gamma-ray burst GRB170817A was observed approximately 1.7 seconds after the merger [7], confirming that the binary neutron star merger is associated with a short gamma-ray burst. The difference in the arrival time between the gravitational wave and gamma-ray burst indicates that there is almost no difference between the speed of gravity and light. In addition, the transient optical and near-infrared sources of kilonova have been observed for long durations [8], indicating that the synthesis of very heavy elements via the r-process is associated with binary neutron star mergers. Furthermore, the multi-messenger observations provided a new method of measuring the Hubble constant without using the cosmic distance ladder [9] because gravitational wave observations can directly determine the absolute distance to the source.

2.2.3 Neutron star-black hole coalescence and mass gap

GW200105 and GW200115 [30] are the gravitational waves from the neutron star and black hole coalescence. A pulsar in a neutron star-black hole binary is yet to be discovered, and this event confirms the direct evidence of the existence of this type of binary system, which is a key objective for radio observations [31]. In addition, GW190814 [32] is a gravitational wave event in which one of the compact objects constituting the binary system is not identified. This gravitational wave is analyzed as being associated with the merger of a black hole and a 2.6 solar mass compact object, which is either the lightest black hole or the heaviest neutron star ever discovered in a binary compact object system. It is also worth noting that the mass ratio of compact objects is approximately 9. Considering the inferred merger rate, there is no reasonable explanation for this event in all the current models of the formation and mass distribution of compact-object binaries.

No electromagnetic counterparts have been identified in these events.

2.3 Potential candidates

As current gravitational wave detectors are sensitive to the ~ 100 Hz band, gravitational wave events detected so far are associated with the binary mergers of stellar mass compact objects. This section briefly describes candidates and their

theoretically predicted frequencies that are yet to be detected [33–35].

2.3.1 Supermassive black hole binaries

Nearby galaxies possess a supermassive black hole with $10^6 \sim 10^9$ solar mass at their center, and its merging is related to the merging of the host galaxy [36]. Several scenarios exist for the formation process of supermassive black hole binaries, and the chirp mass distribution is currently uncertain. They emit gravitational waves in the mHz band or lower.

2.3.2 Supernovae

Core-collapse supernovae may involve aspherical motions at core bounce, which can produce gravitational waves [13]. The gravitational core collapse should dynamically proceed for the emission of the gravitational waves, and the inverse of the dynamical timescale corresponds to the typical frequency of the gravitational waves. This process is a promising candidate for a gravitational wave source and is predicted to emit gravitational waves at approximately 1 kHz. The gravitational waves have information deep inside the supernova core, and the simultaneous observation of it and neutrinos will help significantly progress in the understanding of the explosion mechanism.

2.3.3 Rotating neutron stars

Pulsars are interpreted as highly magnetized rotating neutron stars whose axial asymmetry is a source of gravitational wave emission [14]. The amplitude of the gravitational waves depends on the deformation of the neutron star; however, it is currently undetermined because of the lack of information on the equation of state for neutron stars. The frequency of the emitted gravitational waves is twice the rotation frequency of the neutron star, and known pulsars usually have precisely determined frequency evolutions. There are more than 200 known pulsars in the $10 \sim 1000$ Hz range, many of which have been imposed upper limits on ellipticity based on gravitational wave observations [37].

2.3.4 Binary neutron star post-merger remnants

GW170817 and GW190425 [5, 38] have detected the inspiral phase of binary neutron star mergers. Theoretically, gravitational waves are expected to be emitted from the remnants that form after the merger. The fate of remnants depends on the mass of the binary star. It may immediately collapse as a black hole, form a rapidly rotating and oscillating hypermassive or supramassive neutron star that eventually collapses, or form an infinitely stable neutron star [15, 16]. The emitted gravitational waves have been simulated [39–55] using various candidate equations of state for neutron stars [17], and the predicted frequency is approximately

2 ~ 4 kHz. The gravitational waves emitted from the remnant provide information about the radius and maximum mass of the neutron star. The observation of such gravitational wave signals would play an essential role in determining the equation of state for neutron stars and contribute to high-density matter physics in a manner that cannot be possible with terrestrial experiments. Moreover, understanding post-merger evolution provides new insights into short gamma-ray bursts and kilonovae.

2.3.5 Stochastic background

Stochastic gravitational wave background can be generated from the superposition of many independent sources [56]. Stochastic gravitational waves have been potentially generated in all frequency bands, and various candidates have been discussed. In addition to well-known astronomical phenomena such as binary black holes, binary neutron stars, supernovae, or pulsars, several models suggest that they are generated from cosmic strings or first-order phase transitions in the early universe. There was also a possibility that the background gravitational waves were generated during inflation [57]. Although the amplitude of the predicted gravitational waves is small, the energy density per logarithmic frequency is constant in the band above 10^{-17} Hz.

2.4 History and future plans of the gravitational wave detector

Since the existence of gravitational waves was predicted in 1915, they had not been directly detected for 100 years. The amplitude of gravitational waves is minimal, and developing a probe with low noise enough to detect them is challenging. This section briefly describes the history and future plans of gravitational wave detectors.

2.4.1 Resonant bar detectors

In 1969, Weber reported that gravitational waves were detected using a resonant bar detector made of aluminum [58]. These gravitational waves were analyzed as coming from the center of the Milky Way galaxy. However, the energy of the astronomical event estimated from its amplitude was far too significant, and today this event is considered a false positive. Follow-up experiments have been conducted worldwide using resonant bar detectors; however, the results have been negative about detection [59].

A resonant bar detector is sensitive in a very narrow band around the resonant frequency of a block of metal; thus, it cannot observe the waveform of a gravitational wave. In addition, the performance of the detector is limited by the size of the block of metal that can be produced. In the 1970s, the laser interferometric

gravitational wave detector was proposed that did not suffer from the aforementioned drawbacks [60].

2.4.2 Laser interferometer and optomechanics

While thermal noise limits the sensitivity of resonant bar detectors, the principle sensitivity of laser interferometric gravitational wave detectors is limited by the quantum nature of the light. Quantum noise includes not only the effect of quantum fluctuations in detected photon numbers but also the effect of the mirrors that constitute the detector being fluctuated by force caused by changes in the momentum of the light. The field of physics that deals with the interaction between the mechanical motion of a massive object and radiation pressure force generated by light is known as optomechanics [61], which has been the focus of various studies. In the 1980s, ponderomotive quantum noise generated by optomechanical coupling was recognized as a factor determining the principle sensitivity of laser interferometric gravitational wave detectors [18], indicating the possibility of gravitational wave detection using large-scale laser interferometers.

2.4.3 First-generation gravitational wave detectors

In the 1980s-1990s, prototypes with arm lengths of several m \sim 10 m were constructed in several countries [62]. Moreover, a large-scale laser interferometer was designed based on the insights obtained from the prototype because the response to gravitational waves is better with a longer arm length, as discussed in App. A.4. In the 2000s, gravitational wave detectors with arm-lengths of several hundred to a few thousand meters were operational such as LIGO at Hanford in Washington and Livingston in Louisiana in the USA [63], VIRGO at Pisa in Italy [64], TAMA300 at Tokyo in Japan [65], and GEO600 at Hanover in Germany [66]. These were known as first-generation gravitational wave detectors, whose primary aim was to verify the principle of large-scale gravitational wave detectors. GEO600 is still operating with upgrades [67] and plays an essential role as a demonstration detector for advanced technologies [68].

2.4.4 Second-generation gravitational wave detectors

Based on the success of first-generation detectors, second-generation gravitational wave detectors were constructed in the 2010s to directly detect gravitational waves. They are designed to detect a few events per year of binary neutron star mergers, whose detection rate can be theoretically predicted [69]; thus, they possess the best sensitivity of $\sim 3 \times 10^{-24} \text{ Hz}^{-1/2}$ in the band of $\sim 100 \text{ Hz}$.

Advanced LIGO [10] was constructed on the infrastructure of the initial version of the LIGO detector. The arm length was 4 km. The first gravitational wave event, GW150914 [3], was observed by two detectors during the first observing run in 2015. The sky-averaged sensitivities to binary neutron star coalescences during

the third observing run in 2019 were 111 Mpc for LIGO Hanford and 134 Mpc for LIGO Livingston [70]. Moreover, there are plans to construct the third LIGO detector in India [71].

Advanced VIRGO [11] was constructed on the infrastructure of the initial version of the VIRGO detector. The arm length was 3 km. VIRGO was part of the second observing run in 2017, detecting GW170817 [5] and others. As the VIRGO detector is located far from the LIGO detectors, their simultaneous observations can significantly improve the estimation accuracy of sky localization. For example, the sky localization of GW170817 is 190 deg^2 for Hanford-Livingston; however, it is 31 deg^2 for Hanford-Livingston-VIRGO. VIRGO detector contributed to the identification of the electromagnetic counterpart.

KAGRA [12] was constructed at Gifu in Japan. The arm length was 3 km. KAGRA was part of the last stage of the third observing run in 2020 [72]. Sky localization was expected to be significantly improved by the continuous participation of KAGRA [73]. KAGRA incorporates several advanced technologies, e.g., underground construction, cooling of the mirror to cryogenic temperatures, and signal amplification via optomechanical coupling [74]. These are the critical technologies for the third-generation gravitational wave detectors that will be constructed in the future. KAGRA would also play a key role as a technological demonstrator.

2.4.5 Future plans

Following the direct detection of gravitational waves in 2015, plans for third-generation gravitational wave detectors are taking shape. The Einstein Telescope [75] possesses an arm length of 10 km and constitutes interferometers specialized for low-frequency and high-frequency bands, respectively. Cosmic Explorer [76] possesses an arm length of 40 km and will be upgraded to low-temperature operation from room-temperature operation [77]. The third-generation gravitational wave detectors can observe high-redshift astronomical phenomena in the early universe and are expected to be able to explore the dark ages of the universe.

While it would take decades to construct a third-generation gravitational wave detector, a detector specialized for a particular frequency can be built at a lower cost in a short period. NEMO [19] is a gravitational wave detector specialized to detect neutron star post-merger remnants. Its sensitivity in the kHz band is comparable to that of third-generation gravitational wave detectors, although it possesses an arm length of 4 km. Several advanced technologies will be used to achieve this sensitivity^{*1}.

The aforementioned detectors are ground-based; however, there are plans to configure laser interferometers in outer space. In outer space, it is possible to de-

^{*1} One of the techniques is the reduction of quantum noise based on the long-signal recycling cavity (refer to App.C.1.3).

tect low-frequency gravitational waves below 1 Hz because they are not affected by seismic noise, which is discussed later. In addition, arm lengths that are difficult to achieve with ground-based detectors can be considered. Plans for space detectors are LISA [78], which targets $0.1 \sim 100$ mHz with an arm length of $\sim 10^9$ m, and DECIGO [79], which targets $0.1 \sim 10$ Hz with an arm length of $\sim 10^6$ m, and others.

2.5 Fundamental noise sources of the gravitational wave detector

The performance of a gravitational wave detector at a given frequency is determined by the ratio of the signal response to the amplitude spectral density^{*2} of the noise at that frequency, which is known as the sensitivity of the gravitational wave detector. Fig. 2.5 shows the sensitivity curve of KAGRA. The following subsec-

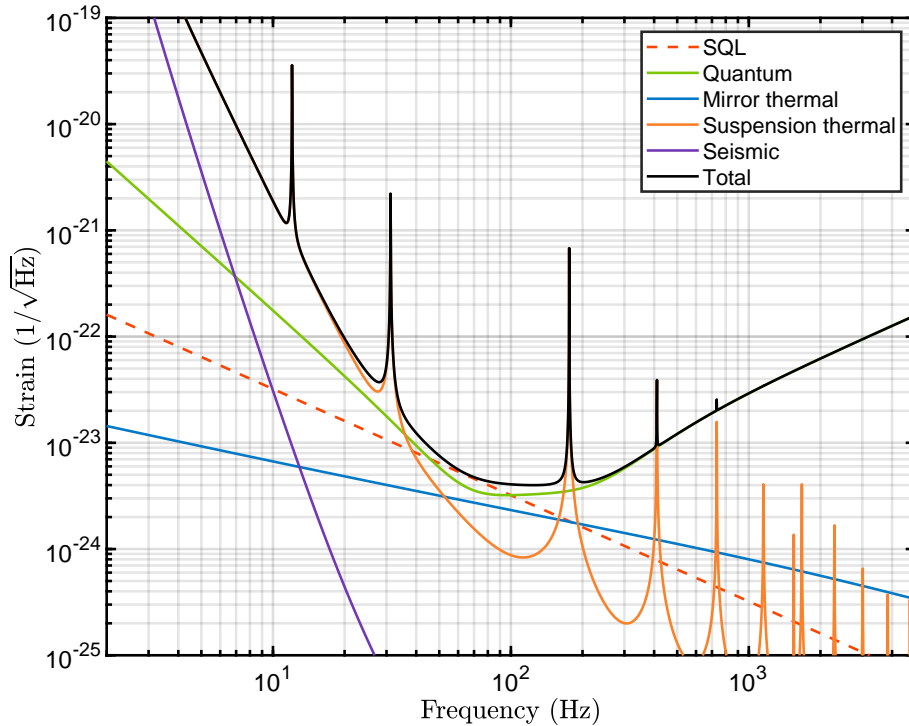


Fig. 2.5: Sensitivity of KAGRA [12].

tions describe noise sources that determine the design sensitivity of a gravitational wave detector, from a low-frequency band to a high-frequency band.

^{*2} See App. A.5.

2.5.1 Seismic noise

Mirrors that constitute the gravitational wave detector must be free mass in the observation band because they are subject to the force of gravitational waves. Thus, a suspension with a sufficiently low resonant frequency should be used. Seismic noise is caused by ground vibrations transmitted from the suspension system and vibrating the mirrors. The amplitude spectral density of the ground vibration is experientially known to inversely decrease as the frequency square, limiting sensitivity in the low-frequency band below ~ 10 Hz. Seismic noise can be reduced by isolating vibrations using the suspension system. However, the size of the pendulum is limited with regard to its construction, and it is not easy to reduce the resonance frequency below ~ 0.1 Hz. In actual gravitational wave detectors, multi-stage pendulums are used to improve the vibration isolation effect. In addition, seismic noise can be further reduced by two orders of magnitude by constructing underground, as KAGRA [80].

2.5.2 Newtonian noise

Newtonian noise is caused by fluctuations in the gravitational field of materials around the mirror, such as the earth's crust and atmosphere [81]. This effect is minimal and is considered negligible for second-generation gravitational wave detectors. However, in third-generation gravitational wave detectors with dramatically improved sensitivity, the Newtonian noise limits the sensitivity around ~ 10 Hz. In addition, fluctuations in the gravity gradient caused by groundwater might limit the design sensitivity of KAGRA [82].

2.5.3 Thermal noise

Thermal noise is caused by the random exchange of energy with the heat bath, which excites vibrations in the suspension and mirror. Based on the fluctuation-dissipation theorem [83], the power spectral density of thermal noise is proportional to temperature and mechanical loss. Mechanical loss is the reciprocal of the general Q factor of the material, and materials and conditions with low energy loss must be considered to reduce thermal noise.

Herein, we briefly outline the thermal noise of the mirror. Various factors contribute to the thermal noise of the mirror. The primary mirror thermal noises can be classified into thermoelastic and Brownian noises. Thermoelastic noise is caused by the temperature dependence of the value of the thermal expansion coefficient [84]. When a temperature gradient exists on the mirror, the mirror is distorted non-uniformly, resulting in thermoelastic noise. The source of this mechanical loss is defined as thermoelastic damping. Brownian noise is caused by Brownian motion [85] and is an empirically known thermal noise apart from thermoelastic noise. The source of this mechanical loss has been identified as

non-viscous damping and is known as structural damping.

The mirror is coated with dielectric multilayers to achieve high reflectivity. Thermoelastic noise can be categorized into substrate thermoelastic noise, which is caused by the temperature dependence of the thermal expansion coefficient of the substrate, and thermo-optic noise, which is caused by the difference in the thermal expansion coefficient and refractive index between the substrate and coating [86]. Moreover, Brownian noise can be categorized into substrate Brownian noise, which is caused by the structural damping of the substrate, and coating Brownian noise, which is caused by the structural damping of the coating. In addition to these types of noises, other types of mirror thermal noise have been considered, e.g., thermal noise caused by the temperature dependence of the refractive index of the substrate, which can fluctuate the phase of the light transmitted through the mirror, referred to as thermo-refractive noise [87].

Thermal noise limits sensitivity in the bandwidth of approximately $10 \sim 100$ Hz.

2.5.4 Radiation pressure noise

When a mirror reflects light, the mirror receives a force from the light because the photons undergo a momentum change in the mirror. This force is known as the radiation pressure force. If the number of photons is constant, the radiation pressure force becomes constant. However, when the photon number fluctuates according to the quantum nature of light, the radiation pressure force fluctuates, and radiation pressure noise is induced. Radiation pressure noise is the principal noise in the band below ~ 100 Hz; however, it has never been observed in gravitational wave detectors because the reduction of thermal noise in this band is difficult. In one experiment with a macroscopic test mass, radiation pressure noise was observed at ~ 10 kHz with a mirror of ~ 50 ng [88].

2.5.5 Shot noise

Quantum fluctuations in the number of photons at the detection cause shot noise and the fluctuations are statistical; therefore, the shot noise is frequency-independent and considered white noise. The sensitivity is limited by shot noise in the high-frequency band above ~ 100 Hz.

2.6 Summary of this chapter

As gravitational waves cause differential strain in interferometers, they can be detected using optical interferometers. Gravitational waves generated from the binary black hole merger and the inspiral phase of the binary neutron star merger have been observed and significantly contributed to astronomy and cosmology. However, gravitational waves emitted from supernovae or binary neutron star post-merger remnants are yet to be detected and can be detected with a ground-based

gravitational wave detector. Such sources are expected to emit high-frequency gravitational waves of a few kHz, and the predicted frequency range is relatively narrow. In other words, there is a possibility to detect these gravitational waves by constructing a gravitational wave detector with a narrow but sensitive bandwidth in the high-frequency band.

The principle sensitivity of the gravitational wave detector is determined by radiation pressure noise and shot noise resulting from the quantum nature of light, which are referred to as quantum noise. The sensitivity of current gravitational wave detectors in the kHz band becomes limited owing to quantum noise. It is essential to understand quantum noise for designing detectors that can detect high-frequency gravitational waves. Intuitively, the higher the light power, the less fluctuation in the number of photons at the detection and the greater the fluctuation in the radiation pressure force. Radiation pressure noise and shot noise possess a trade-off relationship for light power, and the limit of sensitivity determined from them is known as the standard quantum limit [89]. The next chapter discusses quantum noise in detail.

Chapter 3

Quantum noise in gravitational wave detectors

Current gravitational wave detectors are based on laser interferometry, whose principle sensitivity is determined by the quantum fluctuations of the vacuum state. This chapter discusses quantum noise in gravitational wave detectors and a method for improving sensitivity within the high-frequency band using intracavity squeezing.

3.1 Two-photon formalism

Let us consider interfering laser light with a single angular frequency of ω_0 . This light is known as carrier light because it carries the gravitational wave signal. The change in the arm length caused by the gravitational wave of angular frequency Ω corresponds to the frequency modulation of the carrier light. When the plane wave $E(t) = E_0 \cos \omega_0 t$ is modulated with the modulation index $\beta_0 \ll 1$, the light field can be written as

$$\begin{aligned} E_{\text{mod}}(t) &= E_0 \cos(\omega_0 t - \beta_0 \sin \Omega t) \\ &\simeq E_0 \cos \omega_0 t + E_0 \beta_0 \sin \omega_0 t \sin \Omega t \\ &= E_0 \cos \omega_0 t - \frac{1}{2} E_0 \beta_0 \cos(\omega_0 + \Omega)t + \frac{1}{2} E_0 \beta_0 \cos(\omega_0 - \Omega)t. \end{aligned} \tag{3.1}$$

The first term denotes the carrier light itself, and the second and third terms imply that the gravitational wave produces light with frequency Ω higher and lower than the carrier light; these light fields are known as upper and lower sidebands, respectively. The gravitational wave detector identifies sidebands generated by gravitational waves while significantly reducing the noise of the angular frequency Ω . However, when the classical noise at Ω is negligible, the sensitivity of the gravitational wave detector is limited by the quantum fluctuations of the light field at frequencies $\omega_0 + \Omega$ and $\omega_0 - \Omega$. The two-photon formalism [90, 91] is a notation

for calculating the electric field and its fluctuations by focusing on photons of the aforementioned frequencies. In this section, we derive the notation necessary to calculate the quantum noise in the gravitational wave detector.

3.1.1 Quadrature decomposition of quantized electromagnetic fields

Electromagnetic waves are derived from Maxwell's equations. Considering the real and imaginary components of the vector potential as the generalized coordinate and momentum, the energy of the electromagnetic field in a cube with a volume of $V = l^3$ can be formulated similarly to the Hamiltonian of the harmonic oscillator. In other words, the electromagnetic field can be quantized by imposing the appropriate commutation relation. The quantized electric field $\hat{\mathbf{E}}$ can be defined as

$$\hat{\mathbf{E}}(\mathbf{r}, t) = \sum_{\mu, \mathbf{k}} i \sqrt{\frac{\hbar \omega_{\mathbf{k}}}{2 \varepsilon_0 V}} \left(\hat{a}_{\mathbf{k}}^{\mu} e^{-i(\omega_{\mathbf{k}} t - \mathbf{k} \cdot \mathbf{r})} - (\hat{a}_{\mathbf{k}}^{\mu})^{\dagger} e^{i(\omega_{\mathbf{k}} t - \mathbf{k} \cdot \mathbf{r})} \right) \mathbf{e}_{\mu}(\mathbf{k}), \quad (3.2)$$

where \mathbf{r} denotes the displacement vector, \mathbf{k} denotes the wavenumber vector, $\omega_{\mathbf{k}}$ denotes the angular frequency, and $\mathbf{e}_{\mu}(\mathbf{k})$ ($\mu = 1, 2$) denotes the unit vector of polarization of the electromagnetic field, both of which are orthogonal to the traveling direction of the electromagnetic field. The commutation relation between the creation operator $(\hat{a}_{\mathbf{k}'}^{\nu})^{\dagger}$ and annihilation operator $\hat{a}_{\mathbf{k}}^{\mu}$ is

$$[\hat{a}_{\mathbf{k}}^{\mu}, (\hat{a}_{\mathbf{k}'}^{\nu})^{\dagger}] = \delta_{\mathbf{k}\mathbf{k}'} \delta_{\mu\nu}. \quad (3.3)$$

To denote the electric field using the frequency domain creation and annihilation operators, the addition of the quantized electric field for the wavenumber is redefined as an integral over the frequency. The magnitude of the electric field in free space ($l \rightarrow \infty$) propagating along the z-axis can be written as

$$\hat{E}(t) = \int_0^{\infty} \sqrt{\frac{\hbar \omega}{4 \pi \varepsilon_0 c \mathcal{A}}} (\hat{a}_{\omega} e^{-i\omega t} + \hat{a}_{\omega}^{\dagger} e^{i\omega t}) d\omega, \quad (3.4)$$

where $V/l \rightarrow \mathcal{A}$ denotes the effective beam cross-section. Here, we converted $\sum_{\mathbf{k}} \rightarrow 1/(2\pi c/l) \int d\omega$ and $i\sqrt{2\pi c/l} \hat{a}_{\mathbf{k}} \exp(i\omega z/c) \rightarrow \hat{a}_{\omega}$. The commutation relation

$$[\hat{a}_{\omega}, \hat{a}_{\omega'}^{\dagger}] = 2\pi \delta(\omega - \omega') \quad (3.5)$$

is nonzero, and the others are 0 from the conversion of $\delta_{\mathbf{k}\mathbf{k}'} \rightarrow 2\pi c/l \times 2\pi \delta(\omega - \omega')$.

Only the electric field fluctuations, comprising the creation and annihilation operators of frequencies corresponding to the upper and lower sidebands, contribute to the signal-to-noise ratio. Therefore, the quantized electric field for the vacuum

state can be defined as an integral over the angular frequency Ω :

$$\hat{E}(t) = \sqrt{\frac{\hbar\omega_0}{4\pi\epsilon_0 c\mathcal{A}}} \int_0^\infty \left[e^{-i\omega_0 t} (\hat{a}_+ e^{-i\Omega t} + \hat{a}_- e^{i\Omega t}) + e^{i\omega_0 t} (\hat{a}_+^\dagger e^{i\Omega t} + \hat{a}_-^\dagger e^{-i\Omega t}) \right] d\Omega, \quad (3.6)$$

where $\hat{a}_+ = \hat{a}_{\omega_0+\Omega}$ and $\hat{a}_- = \hat{a}_{\omega_0-\Omega}$ denote the annihilation operators for the upper and lower sidebands, respectively. Here, we assume $\Omega \ll \omega_0$. The commutation relations

$$[\hat{a}_+, \hat{a}_+^\dagger] = 2\pi\delta(\Omega - \Omega'), \quad [\hat{a}_-, \hat{a}_-^\dagger] = 2\pi\delta(\Omega - \Omega') \quad (3.7)$$

are nonzero, and the others are 0. Furthermore, we define

$$\hat{a}_1(\Omega) = \frac{\hat{a}_+ + \hat{a}_-^\dagger}{\sqrt{2}}, \quad (3.8)$$

$$\hat{a}_2(\Omega) = \frac{\hat{a}_+ - \hat{a}_-^\dagger}{\sqrt{2}i}. \quad (3.9)$$

The electric field can be denoted by these two quadratures:

$$\hat{E}(t) = \sqrt{\frac{4\pi\hbar\omega_0}{\epsilon_0 c\mathcal{A}}} [\hat{a}_1(t) \cos(\omega_0 t) + \hat{a}_2(t) \sin(\omega_0 t)], \quad (3.10)$$

where

$$\hat{a}_j(t) = \int_0^\infty (\hat{a}_j(\Omega) e^{-i\Omega t} + \hat{a}_j(\Omega)^\dagger e^{i\Omega t}) \frac{d\Omega}{2\pi} \quad (j = 1, 2) \quad (3.11)$$

is the amplitude and phase quadratures, respectively. They are so-called because of their correspondence to the classical electric field, as discussed later. From $\hat{a}_j(-\Omega) = \hat{a}_j^\dagger(\Omega)$, the Fourier transform of each quadrature can be defined as

$$a_j(\Omega) = \int_{-\infty}^{+\infty} a_j(t) e^{-i\Omega t} dt \quad (j = 1, 2). \quad (3.12)$$

The commutation relations

$$[\hat{a}_1(\Omega), \hat{a}_2^\dagger(\Omega')] = -[\hat{a}_2(\Omega), \hat{a}_1^\dagger(\Omega')] = i2\pi\delta(\Omega - \Omega') \quad (3.13)$$

are nonzero, and the others are 0.

If we consider a signal with frequency Ω , we need to calculate two quadratures, i.e., $a_1(\Omega)$ and $a_2(\Omega)$. Then, the transformation of the light field via interference, propagation, and other factors is calculated using an operator denoted by a matrix. Unless otherwise noted, we denote quadratures in the frequency domain as a vector:

$$\mathbf{a} = \begin{pmatrix} a_1 \\ a_2 \end{pmatrix}. \quad (3.14)$$

3.1.2 Spectral density

Suppose that the state $|\text{in}\rangle$ is incident on the interferometer, and the sum of the gravitational wave signal and noise resulting from the incident fluctuations is obtained. The operator of the signal-to-noise ratio is obtained as $\hat{h}_n(\Omega)$. The one-sided spectral density of sensitivity $S_h(f)$ is defined by the ensemble average:

$$\frac{1}{2} \langle \text{in} | (\hat{h}_n(\Omega) \hat{h}_n^\dagger(\Omega') + \hat{h}_n^\dagger(\Omega') \hat{h}_n(\Omega)) | \text{in} \rangle = \frac{1}{2} 2\pi \delta(\Omega - \Omega') S_h(f). \quad (3.15)$$

We consider the situation where a coherent state, which becomes 0 by acting with annihilation operators for an arbitrary frequency, is incident to the interferometer. We denote the vacuum state as $|0\rangle$. From the commutation relations (3.7) and (3.13), we obtain

$$\frac{1}{2} \langle 0 | (\hat{a}_j \hat{a}_{k'}^\dagger + \hat{a}_{k'}^\dagger \hat{a}_j) | 0 \rangle = \frac{1}{2} 2\pi \delta(\Omega - \Omega') \delta_{jk}. \quad (3.16)$$

Therefore, if the sensitivity operator can be defined as $\hat{h}_n(\Omega) = \eta_1 \hat{a}_1 + \eta_2 \hat{a}_2$, the sensitivity determined by the quantum noise can be calculated as

$$S_h(f) = |\eta_1|^2 + |\eta_2|^2. \quad (3.17)$$

3.1.3 Correspondence to classical electromagnetic field

Herein, we have considered quantum fluctuations at sideband frequencies. Moreover, we can consider quantum states corresponding to carrier light. The carrier light corresponds to an electromagnetic field of angular frequency ω_0 with specific linear polarization taking $n (\neq 0)$ photon states $|n\rangle$. The quantized electromagnetic field can be written as

$$\hat{E}(\mathbf{r}, t) = i \sqrt{\frac{\hbar \omega_0}{2 \epsilon_0 V}} \left(\hat{a} e^{-i(\omega_0 t - \mathbf{k}_0 \cdot \mathbf{r})} - \hat{a}^\dagger e^{i(\omega_0 t - \mathbf{k}_0 \cdot \mathbf{r})} \right), \quad (3.18)$$

and we can calculate the expectation of light power P_E :

$$P_E = 2 \int \frac{\epsilon_0}{2} \langle n | \hat{E}^\dagger \hat{E} | n \rangle d\mathbf{r} = n \hbar \omega_0. \quad (3.19)$$

The intensity of the classical plane wave $E(t) = E_0 \cos \omega_0 t$ can be calculated as $P_E = E_0^2 \hbar \omega_0 / 2$ considering the time average of $\cos^2 \omega_0 t$. The square of the dimensionless electric field amplitude E_0^2 corresponds to twice the photon number.

To calculate the transformation caused by the interferometer for the carrier light, let us denote the carrier light in a vector similar to light field fluctuation. In other words, when the sum of the light field fluctuations and carrier light is defined as

$$E(t) = (E_1 + e_1(t)) \cos \omega_0 t + (E_2 + e_2(t)) \sin \omega_0 t, \quad (3.20)$$

the vector corresponding to the carrier light is as follows:

$$\mathbf{E} = \begin{pmatrix} E_1 \\ E_2 \end{pmatrix}, \quad (3.21)$$

where E_1 and E_2 denote the dimensionless amplitudes of the carrier light for each quadrature, and the light field fluctuations are denoted by the corresponding lowercase e_1 and e_2 . The light power, including the fluctuation, can be observed by measuring the sum of the carrier light and light field fluctuation:

$$P_E^{\text{tot}} \simeq \frac{\hbar\omega_0}{2}(E_1^2 + E_2^2 + 2(E_1e_1 + E_2e_2)) = P_E + \delta P_E. \quad (3.22)$$

Note that this equation is different from the standard definition of the inner product because the time average of the product between different quadratures is 0. The light field fluctuations can be measured via carrier light as $\delta P_E = \hbar\omega_0(E_1e_1 + E_2e_2)$. The carrier light used for measurement is known as the local oscillator, and the relative angle to the incident light field $\xi_E = \arctan(E_2/E_1)$ is known as the homodyne angle.

Let us consider the physical meaning of each quadrature. The incident light field $A(t)$ is generally defined with an initial phase of 0. In other words, as $A_1 = A_0, A_2 = 0$, we can define $A(t) = A_0 \cos \omega_0 t$. When the amplitude and phase of the carrier light fluctuate by $\delta A_0(t)$ and $\delta \phi_0(t)$, respectively, the sum of the carrier light and light field fluctuations $A'(t)$ can be written as

$$\begin{aligned} A'(t) &= (A_0 + \delta A_0) \cos(\omega_0 t - \delta \phi_0) \\ &\simeq (A_0 + \delta A_0) \cos \omega_0 t + A_0 \delta \phi_0 \sin \omega_0 t. \end{aligned} \quad (3.23)$$

This equation indicates that a_1 and a_2 correspond to the amplitude and phase fluctuations. For this reason, a_1 is referred to as amplitude quadrature and a_2 as phase quadrature. In addition to quantum light field fluctuations, classical intensity and frequency noise can be calculated as amplitude and phase quadratures. As expressed in Eq. (3.1), the gravitational wave signal appears in the phase quadrature.

3.2 Definition of operators

In the previous section, we discussed the notations for the carrier light and light field fluctuation in a 2×1 vector. The two-photon formalism calculates the relationship between the input and output light fields by denoting the transformations that the light field undergoes in the interferometer as a 2×2 matrix. This section derives the transformation caused by each factor configuring the interferometer, as shown in Fig. 3.1.

3.2.1 Transmission, reflection, and superposition

Let us consider the interference of the light field with a symmetric mirror, as shown in Fig. 3.1(1), which possesses no optical loss and whose power reflectivity

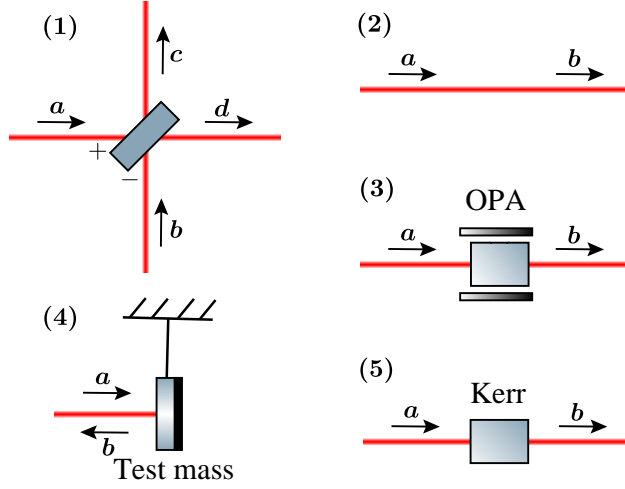


Fig. 3.1: Schematic diagram of each factor configuring an optical interferometer. (1): superposition, (2): propagation, (3): optical parametric amplification, (4): ponderomotive squeezing, and (5): optical Kerr effect.

and transmissivity are r^2 and t^2 , respectively. The phase difference between the transmitted light and reflected light is $\pi/2$, and $r^2 + t^2 = 1$ because of the energy conservation law. The absolute phase change that occurs during transmission and reflection is not essential for an optical interferometer because it is indistinguishable from propagation. This mirror can be considered equivalent to an asymmetric mirror with a phase change of 0 in transmission to both sides, reflection from one side, and π in reflection from the other side. When the light fields interfere on this mirror, the carrier light and light field fluctuations are written as the same formula:

$$C = rA + tB, \quad (3.24)$$

$$D = tA - rB, \quad (3.25)$$

$$c(\Omega) = ra(\Omega) + tb(\Omega), \quad (3.26)$$

$$d(\Omega) = ta(\Omega) - rb(\Omega). \quad (3.27)$$

3.2.2 Propagation

Let us consider the case where the light field propagates in free space with distance L , as shown in Fig. 3.1(2). It is equivalent to time being delayed by $\tau = L/c$; thus, the light field after propagation can be written as

$$B(t) = (A_1 + a_1(t - \tau)) \cos \omega_0(t - \tau) + (A_2 + a_2(t - \tau)) \sin \omega_0(t - \tau). \quad (3.28)$$

Therefore, we obtain

$$B = R(\phi)A, \quad (3.29)$$

$$b(t) = R(\phi)a(t - \tau), \quad (3.30)$$

where $\phi \equiv \omega_0 \tau \pmod{2\pi}$ denotes the phase change caused by propagation and $R(\phi)$ denotes the rotation matrix:

$$R(\phi) = \begin{pmatrix} \cos \phi & -\sin \phi \\ \sin \phi & \cos \phi \end{pmatrix}. \quad (3.31)$$

Based on the Fourier transform of light field fluctuations, we obtain

$$\mathbf{b}(\Omega) = \mathbf{e}^{i\alpha} R(\phi) \mathbf{a}(\Omega), \quad (3.32)$$

where $\alpha = -\Omega \tau$ denotes the phase delay of the light field.

3.2.3 Optical parametric amplification

Optical parametric amplification (OPA), one of the nonlinear optical effects, is a phenomenon in which the second harmonic of the carrier light (pump light) is down-converted into two lights, i.e., the signal light and idler light. The degenerated OPA, in which the signal and idler frequencies are equal to the carrier frequency, provides a correlation between quantum fluctuations corresponding to the upper and lower sidebands. The factor that provides such effects is known as a squeezer, which converts the quantum fluctuations of the coherent state into those of the squeezed state. OPA is a valuable way to generate a squeezed state over a wide frequency bandwidth [92–94].

Let us consider the degenerated OPA for the carrier light, as shown in Fig. 3.1(3). From Eq. (B.39), we obtain

$$\begin{aligned} B(t) = & [A_1 \cos \omega_0 t + A_2 \sin \omega_0 t] \cosh u \\ & + [A_1 \cos(\omega_0 t - 2\theta) - A_2 \sin(\omega_0 t - 2\theta)] \sinh u, \end{aligned} \quad (3.33)$$

where $s = e^u$ and θ denote the squeezing factor and squeezing angle, respectively. Thus, we obtain

$$\mathbf{B} = S(u, \theta) \mathbf{A}, \quad (3.34)$$

where $S(u, \theta)$ denotes the squeezing matrix defined as

$$\begin{aligned} S(u, \theta) = & \begin{pmatrix} \cosh u + \sinh u \cos 2\theta & \sinh u \sin 2\theta \\ \sinh u \sin 2\theta & \cosh u - \sinh u \cos 2\theta \end{pmatrix} \\ = & R(\theta) \begin{pmatrix} s & 0 \\ 0 & 1/s \end{pmatrix} R(-\theta). \end{aligned} \quad (3.35)$$

Now let us consider the correlation between the upper and lower sidebands. Based on Eqs. (B.39) and (B.40), the relationship between the upper and lower sidebands of the output light field b_+ and b_- can be written as

$$b_+ = a_+ \cosh u + e^{2i\theta} a_-^\dagger \sinh u, \quad (3.36)$$

$$b_-^\dagger = e^{-2i\theta} a_+ \sinh u + a_-^\dagger \cosh u. \quad (3.37)$$

The amplitude quadrature of the output light field fluctuation can be calculated using Eq. (3.8):

$$\begin{aligned} b_1 &= \frac{1}{\sqrt{2}} \left(a_+ \cosh u + e^{2i\theta} a_-^\dagger \sinh u + e^{-2i\theta} a_+ \sinh u + a_-^\dagger \cosh u \right) \\ &= \frac{1}{2} \left[(a_1 + ia_2) (\cosh u + e^{-2i\theta} \sinh u) + (a_1 - ia_2) (\cosh u + e^{2i\theta} \sinh u) \right] \\ &= (\cosh u + \cos 2\theta \sinh u) a_1 + (\sin 2\theta \sinh u) a_2. \end{aligned} \quad (3.38)$$

The phase quadrature of the output light field fluctuation can be calculated using Eq. (3.9):

$$b_2 = (\sin 2\theta \sinh u) a_1 + (\cosh u - \cos 2\theta \sinh u) a_2. \quad (3.39)$$

Therefore, the input-output relation of light field fluctuations can be denoted using a squeezing matrix:

$$\mathbf{b}(\Omega) = S(u, \theta) \mathbf{a}(\Omega). \quad (3.40)$$

3.2.4 Gravitational wave signal and ponderomotive squeezing

Interferometric gravitational wave detectors consist of mirrors that are free masses for gravitational waves to detect the displacement of the gravitational wave. When the test mass reflects the light field, a signal proportional to the slight displacement of the mirror is added to the light field fluctuation. Furthermore, the quadratures of the light field fluctuations are transformed into each other via the radiation pressure force. This transformation is known as ponderomotive squeezing [95] because the mirror acts as a squeezer for quantum fluctuations.

Let us consider the situation where the carrier light is reflected by the test mass and the mirror moves by a small displacement $\delta x(t)$, as shown in Fig. 3.1(4). Considering the phase change on reflection, the reflected light field can be calculated as

$$B(t) \simeq (A_1 + a_1(t) - 2A_2 k_0 \delta x(t)) \cos \omega_0 t + (A_2 + a_2(t) + 2A_1 k_0 \delta x(t)) \sin \omega_0 t. \quad (3.41)$$

Thus, we obtain

$$\mathbf{B} = \mathbf{A}, \quad (3.42)$$

$$\mathbf{b}(t) = \mathbf{a}(t) + 2k_0 \begin{pmatrix} -A_2 \\ A_1 \end{pmatrix} \delta x(t). \quad (3.43)$$

To investigate the frequency response to the light field fluctuations, we formulate the equation of motion with regard to the displacement of the mirror. The mirror is affected by force caused by the gravitational wave, mechanical restoring

force of the suspension, and radiation pressure force F_{rpf} . Based on the impulse-momentum relationship, we consider the first-order approximation of the fluctuating part of the radiation pressure force:

$$F_{\text{rpf}}^{\text{tot}}(t) = 2\hbar k_0 \times \frac{1}{2}((A_1 + a_1(t))^2 + (A_2 + a_2(t))^2) \simeq F_{\text{rpf}} + \delta F_{\text{rpf}}(t). \quad (3.44)$$

The constant radiation pressure force $F_{\text{rpf}} = \hbar k_0(A_1^2 + A_2^2)$ is balanced with the mechanical restoring force. The equation of motion for the displacement fluctuation of the mirror can be written as

$$m \frac{d^2(\delta x(t))}{dt^2} = \delta F_{\text{rpf}} + \frac{1}{2}mL \frac{d^2 h(t)}{dt^2}, \quad (3.45)$$

where L denotes the arm length of the interferometer, $\delta F_{\text{rpf}}(t) = 2\hbar k_0(A_1 a_1(t) + A_2 a_2(t))$ denotes the radiation pressure fluctuation, and the second term on the right side denotes the force caused by the gravitational wave. As the gravitational wave impacts the distance between the two free masses, the displacement resulting from the gravitational wave is nondimensionalized by L and denoted as $h(t)$. The Fourier transform of Eq. (3.45) obtains

$$\delta x(\Omega) = -\frac{2\hbar k_0}{m\Omega^2}(A_1 a_1(\Omega) + A_2 a_2(\Omega)) + \frac{1}{2}Lh(\Omega). \quad (3.46)$$

Thus, we can calculate the Fourier transform of Eq. (3.43) as follows:

$$\mathbf{b}(\Omega) = P(\kappa, \xi_A)\mathbf{a}(\Omega) + \frac{\sqrt{2\kappa}}{h_{\text{SQL}}}\mathbf{n}_{A\perp}h(\Omega), \quad (3.47)$$

where

$$P(\kappa, \xi_A) = R(\xi_A) \begin{pmatrix} 1 & 0 \\ -\kappa & 1 \end{pmatrix} R(-\xi_A) \quad (3.48)$$

denotes the ponderomotive squeezing matrix, and

$$\mathbf{n}_{A\perp} = \begin{pmatrix} -\sin \xi_A \\ \cos \xi_A \end{pmatrix} \quad (3.49)$$

denotes the unit vector perpendicular to the carrier \mathbf{A} . Here, $\xi_A = \arctan(A_2/A_1)$ denotes the relative angle of the carrier light,

$$\kappa = \frac{8P_A\omega_0}{mc^2\Omega^2} \quad (3.50)$$

denotes the optomechanical coupling constant in the free space, and

$$h_{\text{SQL}} = \sqrt{\frac{8\hbar}{mL^2\Omega^2}} \quad (3.51)$$

denotes the standard quantum limit (SQL) [89] of a laser interferometric gravitational wave detector comprising free masses.

The first term of Eq. (3.47) represents the transformation of light field fluctuations caused by reflection on the mirror. $P(\kappa, \xi_A)$ can be resolved as follows:

$$P(\kappa, \xi_A) = R(\xi_A)S(-u_P, \theta_P)R(-\phi_P)R(-\xi_A), \quad (3.52)$$

where $u_P = \text{arcsinh}(\kappa/2)$, $2\theta_P = \text{arccot}(\kappa/2)$, and $\phi_P = \arctan(\kappa/2)$ are defined, indicating that the mirror acts as a frequency-dependent squeezer.

The second term of Eq. (3.47) indicates that fluctuations with the same frequency as the gravitational wave are generated as a signal in the direction perpendicular to the carrier. Assuming for simplicity that the incident carrier A is in the amplitude quadrature ($A_1 = A_0$, $A_2 = 0$), the time domain signal $b'(t)$ with frequency Ω can be written as

$$b'(t) = b'_0 \begin{pmatrix} 0 \\ \sin \Omega t \end{pmatrix}, \quad (3.53)$$

where b'_0 denotes the amplitude of the signal. As expressed in Eq. (3.1), in the formula before applying the quadrature decomposition, it can be denoted as the sum of the upper sideband $b'_\uparrow(t)$ and lower sideband $b'_\downarrow(t)$:

$$b'_\uparrow(t) = -\frac{b'_0}{2} \cos((\omega_0 + \Omega)t), \quad (3.54)$$

$$b'_\downarrow(t) = \frac{b'_0}{2} \cos((\omega_0 - \Omega)t). \quad (3.55)$$

3.2.5 Optical Kerr effect

The optical Kerr effect is a method of generating the squeezing state from intense carrier light. The ordinary light Kerr effect is one of the third-order nonlinear optical effects, a phenomenon in which the refractive index changes in proportion to the light power. Although third-order nonlinear optical effects require extremely high intensity, the chain of second-order nonlinear optical effects can induce a refractive index change proportional to the light power. This phenomenon is known as the cascaded nonlinear optical effect and can be used as a Kerr squeezer [96,97]. Note that the Kerr effect in this study is produced by second-order cascaded nonlinear optical effects instead of third-order nonlinear optical effects.

Let us consider Kerr squeezing caused by cascaded nonlinear optical effects, as shown in Fig. 3.1(5). The carrier light is proportionally phase shifted to the input

power, as in Eq. (B.33). The output light field can be denoted as follows^{*1} [98]:

$$\begin{aligned} B(t) &= (A_0 + a_1(t)) \cos(\omega_0 t - \Phi_A - \delta\Phi_A(t)) + a_2(t) \sin(\omega_0 t - \Phi_A - \delta\Phi_A(t)) \\ &\simeq [(A_0 + a_1(t)) (\cos \Phi_A - \delta\Phi_A(t) \sin \Phi_A) - a_2(t) \sin \Phi_A] \cos \omega_0 t \\ &\quad + [(A_0 + a_1(t)) (\sin \Phi_A + \delta\Phi_A(t) \cos \Phi_A) + a_2(t) \cos \Phi_A] \sin \omega_0 t, \end{aligned} \quad (3.56)$$

where $\Phi_A = d_K P_A = \hbar \omega_0 d_K A_0^2 / 2$ denotes the phase change caused by the Kerr effect, $\delta\Phi_A(t) = \hbar \omega_0 d_K A_0 a_1(t)$ denotes the phase change fluctuations caused by intensity fluctuations, and d_K denotes the constant value representing the gain of the Kerr effect. The light power and its fluctuations were obtained from Eq. (3.22). The phase of the carrier light changes owing to the Kerr effect:

$$B = R(\Phi_A)A. \quad (3.57)$$

Moreover, light field fluctuations are squeezed by the phase change fluctuation caused by the Kerr effect:

$$b = R(\Phi_A)P(-2\Phi_A, 0)a. \quad (3.58)$$

Kerr squeezing can be denoted by the same matrix as ponderomotive squeezing. However, the Kerr effect provides frequency-independent squeezing and can generate a squeezed state over a wide frequency band. In addition, the squeezing factor and squeezing angle are uniquely determined based on the input light power and cannot be separately adjusted.

3.3 Fundamental theory of quantum noise in gravitational wave detectors

The current gravitational wave detectors are compound optical interferometers based on the Michelson interferometer. This section describes the characteristics of the Michelson interferometer and its problems and discusses the fundamental properties of the optical cavity and sensitivity of the dual recycling Michelson interferometer. The parameters used in the plots in this section are $L = 3$ km for the arm length and $m = 23$ kg for the mass of the mirror unless otherwise noted.

3.3.1 Michelson interferometer

First, we derive the quantum noise of the Michelson interferometer, which is the most straightforward configuration for a laser interferometric gravitational wave detector. The light field and its fluctuations are defined as shown in Fig. 3.2. The carrier light G ($G_1 = G_0$, $G_2 = 0$) and its fluctuation g are injected from the

^{*1} The derivation in this section is also based on personal communication with Wataru Usukura.

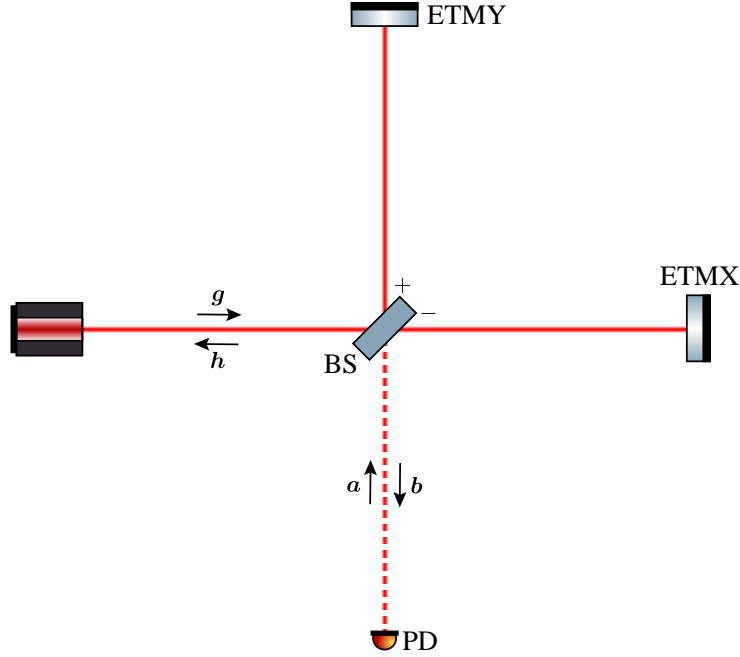


Fig. 3.2: Schematic of the Michelson interferometer. After the laser light is separated using a beam splitter and reflected by the test masses, the interference light is measured using a photodetector. The end mirrors are supposed to work as a test mass.

input port, and the light field fluctuation \mathbf{a} is injected from the output port. We can measure $\mathbf{H} + \mathbf{h}$ and $\mathbf{B} + \mathbf{b}$ at the input and output ports, respectively. The beam splitter (BS) is isotropic and has an identical power reflectivity and transmissivity of 0.5. The end mirrors of the x and y arms are known as the end test mass X (ETMX) and end test mass Y (ETMY), respectively. Let L_x be the x arm length corresponding to the distance between BS and ETMX and L_y be the y arm length corresponding to the distance between BS and ETMY. The phase change during arm propagation is $\phi_x \equiv L_x \omega_0 / c \pmod{2\pi}$ and $\phi_y \equiv L_y \omega_0 / c \pmod{2\pi}$, respectively. The lengths of both arms are approximately equal ($L_x \simeq L_y \simeq L$); thus, the phase delay of the light field fluctuation is $\alpha = -L\Omega/c$ for both arms.

The input-output relation of the carrier light can be calculated as

$$\mathbf{B}' = R(-2\phi_x)\mathbf{B} = \frac{1}{2}[-I + R(2\phi_-)]\mathbf{G}, \quad (3.59)$$

$$\mathbf{H}' = R(-2\phi_x)\mathbf{H} = \frac{1}{2}[I + R(2\phi_-)]\mathbf{G}, \quad (3.60)$$

where we defined the relative phase as $\phi_- = \phi_y - \phi_x$. Note that the measurement position does not affect the intensity measurement; therefore, $P_{B'}^{\text{tot}} = P_B^{\text{tot}}$ and $P_{L'}^{\text{tot}} = P_L^{\text{tot}}$. The output carrier light depends only on the relative phase between the x and y arms. When we set $\phi_- = 0$, the carrier light does not transmit to the output port of the Michelson interferometer, and this condition is known as the

dark fringe. Conversely, when we set $\phi_- = \pi/2$, all carrier light incident on the interferometer comes to the output port, and this condition is known as the bright fringe. Other conditions (such as $\phi_- = \pi/4$) are known as mid-fringes because the carrier light transmits to the input and output ports.

Now let us calculate the input-output relation of the light field fluctuations. Note that gravitational waves cause differential displacement of the interferometer arms. Calculating $\mathbf{b}' = R(-2\phi_x)\mathbf{b}$ and $\mathbf{h}' = R(-2\phi_x)\mathbf{h}$ similarly to the carrier light, we obtain

$$\begin{aligned} \mathbf{b}' = & \frac{1}{2}e^{2i\alpha} [-I + R(2\phi_-)] P(\kappa, 0)\mathbf{g} + \frac{1}{2}e^{2i\alpha} [I + R(2\phi_-)] P(\kappa, 0)\mathbf{a} \\ & + e^{i\alpha} \frac{\sqrt{2\kappa}}{h_{\text{SQL}}} \frac{1}{2} \begin{pmatrix} -\sin(2\phi_-) \\ 1 + \cos(2\phi_-) \end{pmatrix} h(\Omega), \end{aligned} \quad (3.61)$$

$$\begin{aligned} \mathbf{h}' = & \frac{1}{2}e^{2i\alpha} [I + R(2\phi_-)] P(\kappa, 0)\mathbf{g} + \frac{1}{2}e^{2i\alpha} [-I + R(2\phi_-)] P(\kappa, 0)\mathbf{a} \\ & + e^{i\alpha} \frac{\sqrt{2\kappa}}{h_{\text{SQL}}} \frac{1}{2} \begin{pmatrix} -\sin(2\phi_-) \\ -1 + \cos(2\phi_-) \end{pmatrix} h(\Omega), \end{aligned} \quad (3.62)$$

where SQL is denoted as $h_{\text{SQL}} = \sqrt{4\hbar/(mL^2\Omega^2)}$ and the coupling constant can be denoted as $\kappa = 4P_G\omega_0/(mc^2\Omega^2)$ because the carrier light power at test masses is $P_G/2$. All the signals transmit to the output port when the interferometer operates in the dark fringe, as seen from the gravitational wave signal term. Therefore, the Michelson interferometer should be operated at the dark fringe when used as a gravitational wave detector.

Considering $\phi_- = 0$ in Eq. (3.62), we obtain

$$\mathbf{b}' = e^{2i\alpha} \begin{pmatrix} 1 & 0 \\ -\kappa & 1 \end{pmatrix} \mathbf{a} + e^{i\alpha} \frac{\sqrt{2\kappa}}{h_{\text{SQL}}} \begin{pmatrix} 0 \\ 1 \end{pmatrix} h(\Omega). \quad (3.63)$$

The first term corresponds to noise resulting from light field fluctuations, and the second term corresponds to the gravitational wave signal. Although \mathbf{a} is $\mathbf{0}$ in the classical theory, it can no longer be assumed to be $\mathbf{0}$ owing to the quantum fluctuations of the vacuum state while considering quantum noise. By operating at the dark fringe, the light field fluctuations of the incident field are canceled; however, the vacuum field \mathbf{a} works as noise. As all the signals are observed in the phase quadrature, we measure with the homodyne angle of $\pi/2$ ^{*2}. The operator of

^{*2} For perfect dark fringe, the output carrier light is $\mathbf{B}' = 0$; thus, the intensity measurement cannot be performed. The carrier light in the phase quadrature can be obtained by slightly shifting the operating point, as can be derived from Eq. (3.59). Moreover, the carrier light in the amplitude quadrature is obtained from the reflectance and curvature errors of ETMs and other components. The former carrier light is known as the DC offset, and the latter carrier light is known as the contrast defect. The ratio of the DC offset and contrast defect determines the homodyne angle.

the signal-to-noise ratio $h_n(\Omega)$ can be defined as

$$h_n(\Omega) = \frac{h_{\text{SQL}}}{\sqrt{2\kappa}} (-\kappa k_1 + k_2) e^{i\alpha}, \quad (3.64)$$

and the one-sided power spectral density of the signal-to-noise ratio $S_h(\omega)$ is obtained from Eq. (3.17):

$$S_h(\Omega) = \frac{h_{\text{SQL}}^2}{2} \left(\kappa + \frac{1}{\kappa} \right). \quad (3.65)$$

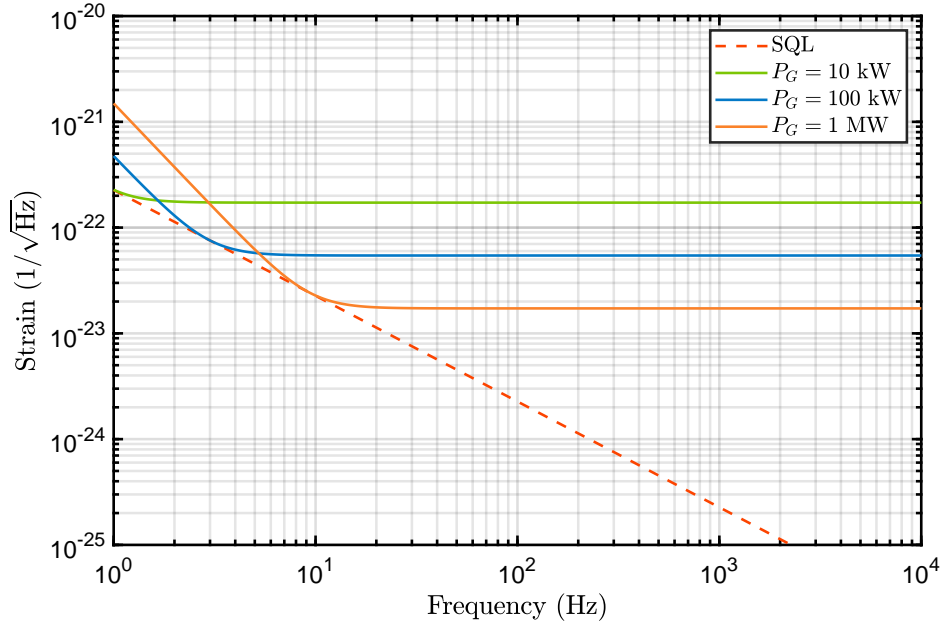


Fig. 3.3: Sensitivity of the Michelson interferometer as determined by quantum noise.

The amplitude spectral density $\sqrt{S_h(\Omega)}$ corresponds to the sensitivity of the Michelson interferometer. Fig. 3.3 shows the sensitivity curve of the Michelson interferometer determined by quantum noise. A lower strain indicates lower noise and better performance as a gravitational wave detector. The low-frequency band of Fig. 3.3 is proportional to f^{-2} and corresponds to the first term of Eq. (3.65). This term represents the radiation pressure noise, in which the amplitude quadrature of the vacuum field acts as radiation pressure fluctuations and is converted into the noise of the phase quadrature via mirror fluctuations. In contrast, the high-frequency band shown in Fig. 3.3 is proportional to f^0 and corresponds to the second term of Eq. (3.65). This term represents the shot noise, in which the phase quadrature of the vacuum field directly acts as the noise. The radiation pressure and shot noise have a trade-off relationship for laser power, and when they are comparable ($\kappa = 1$), the amplitude spectral density equals h_{SQL} .

The sensitivity of the Michelson interferometer is limited by shot noise at $f \sim 100$ Hz. Shot noise refers to sensing noise, which can be reduced by increasing the laser light power or enhancing the signal response. However, stable laser sources are available up to approximately 100 W, and the Michelson interferometer does not improve the signal response. Optical cavities are used within the main interferometer in actual gravitational wave detectors to solve this problem.

3.3.2 Fabry-Perot cavity

Optical cavity is a system in which the light travels between the mirrors multiple times and constructively interferes. Here we discuss the characteristics of the simple cavity, which is a Fabry-Perot cavity.



Fig. 3.4: Schematic of the Fabry-Perot cavity. The end mirror is supposed to work as a test mass.

The Fabry-Perot cavity consists of two mirrors, as shown in Fig. 3.4. Let r_I^2 and r_E^2 be the power reflectivities of the input and end mirrors, $t_I^2 = 1 - r_I^2$ and $t_E^2 = 1 - r_E^2$ be the intensity transmissivities of the input and end mirrors, L be the distance between the input and end mirrors, and $\phi \equiv L\omega_0/c \pmod{2\pi}$ be the phase change per half cycle. The input-output relation of the carrier light can be written as

$$\begin{aligned} B &= -r_I A + t_I D, \quad C = t_I A + r_I D, \\ D &= R(\phi) F, \quad E = R(\phi) C, \quad F = r_E E, \quad G = t_E E. \end{aligned} \quad (3.66)$$

By solving for reflected light B and transmitted light G , we obtain

$$\begin{aligned} B &= [-r_I I + t_I^2 r_E [I - r_I r_E R(2\phi)]^{-1} R(2\phi)] A \\ &= -r_I A_0 \begin{pmatrix} 1 \\ 0 \end{pmatrix} + \frac{t_I^2 r_E A_0}{1 + r_I^2 r_E^2 - 2r_I r_E \cos 2\phi} \begin{pmatrix} \cos 2\phi - r_I r_E \\ \sin 2\phi \end{pmatrix}, \end{aligned} \quad (3.67)$$

$$\begin{aligned} G &= t_I t_E [I - r_I r_E R(2\phi)]^{-1} R(\phi) A \\ &= \frac{t_I t_E A_0}{1 + r_I^2 r_E^2 - 2r_I r_E \cos 2\phi} \begin{pmatrix} (1 - r_I r_E) \cos 2\phi \\ (1 + r_I r_E) \sin 2\phi \end{pmatrix}. \end{aligned} \quad (3.68)$$

Therefore, the reflected light power P_B and transmitted power P_G can be written

as

$$P_B = \frac{r_I^2 + r_E^2 - 2r_I r_E \cos 2\phi}{1 + r_I^2 r_E^2 - 2r_I r_E \cos 2\phi} P_A, \quad (3.69)$$

$$P_G = \frac{t_I^2 t_E^2}{1 + r_I^2 r_E^2 - 2r_I r_E \cos 2\phi} P_A. \quad (3.70)$$

We obtain $P_B + P_G = P_A$ according to the energy conservation law.

The intracavity power P_E can be written as

$$P_E = \frac{t_I^2}{1 + r_I^2 r_E^2 - 2r_I r_E \cos 2\phi} P_A, \quad (3.71)$$

which is a periodic function for ϕ . Fig. 3.5 shows the intracavity power as a function of ϕ . The intracavity power reaches its maximum with $2\phi \equiv 0 \pmod{2\pi}$,

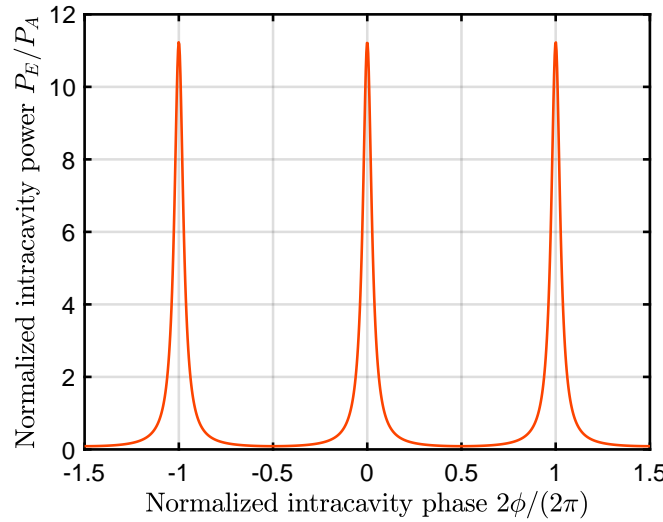


Fig. 3.5: Intracavity power of the Fabry-Perot cavity. The parameters are set to $r_I = \sqrt{0.7}$ and $r_E = 1$. Here, we define ϕ so that the intracavity power becomes a periodic function.

which corresponds to the resonance state. The free spectrum range (FSR) refers to the interval at which the resonance state is observed. The interval of the cavity length and frequency of the laser corresponding to the FSR are

$$L_{\text{FSR}} = \frac{\lambda_0}{2}, \quad (3.72)$$

$$f_{\text{FSR}} = \frac{c}{2L}, \quad (3.73)$$

respectively. We often refer to f_{FSR} as FSR. If the reflectivity of the mirror is sufficiently high and the resonance is sufficiently sharp, the frequency corresponding

to the full width at half maximum (FWHM) of the resonance spectrum can be calculated as

$$f_{\text{FWHM}} = \frac{1 - r_I r_E}{\pi \sqrt{r_I r_E}} f_{\text{FSR}}, \quad (3.74)$$

and the ratio of FSR to FWHM is referred to as the cavity finesse \mathcal{F} :

$$\mathcal{F} = \frac{f_{\text{FSR}}}{f_{\text{FWHM}}} = \frac{\pi \sqrt{r_I r_E}}{1 - r_I r_E}. \quad (3.75)$$

Assume that T_I , T_E , and ϕ are much smaller than unity. By approximating Eqs. (3.75) and (3.71), we obtain

$$\mathcal{F} \simeq \frac{2\pi}{T_I + T_E} = \pi \frac{f_{\text{FSR}}}{\gamma_I + \gamma_E}, \quad (3.76)$$

$$P_E \simeq \frac{T_I}{\frac{1}{4}(T_I + T_E)^2 + 4\phi^2} P_A = \frac{2\mathcal{F}}{\pi} \frac{\gamma_I(\gamma_I + \gamma_E)}{(\gamma_I + \gamma_E)^2 + \Delta^2} P_A, \quad (3.77)$$

where we defined $T_I = t_I^2$ and $T_E = t_E^2$, and $\gamma_I = T_I c / (4L)$ is the decay rate for the input mirror, $\gamma_E = T_E c / (4L)$ is the decay rate for the end mirror, and $\Delta = \phi c / L$ is the cavity detuning. The following relationships between reflectivity and transmissivity were used:

$$r \simeq 1 - \frac{1}{2}T - \frac{1}{8}T^2, \quad (3.78)$$

$$\frac{1}{r} \simeq 1 + \frac{1}{2}T + \frac{3}{8}T^2. \quad (3.79)$$

The intracavity power is denoted by the Lorentzian curve. The Fabry-Perot cavity can be divided into three states according to the relationship between the optical losses of the input coupler (input mirror) and others (in this case, the end mirror). In the case where $T_I > T_E$ refers to over-coupling, $T_I = T_E$ refers to critical coupling, and $T_I < T_E$ refers to under-coupling. The intracavity power at the resonance state ($\phi = 0$) for each case can be written as

$$P_E \simeq \frac{2\mathcal{F}}{\pi} P_A \quad (T_I \gg T_E), \quad (3.80)$$

$$P_E \simeq \frac{\mathcal{F}}{\pi} P_A \quad (T_I = T_E), \quad (3.81)$$

$$P_E \simeq 0 \quad (T_I \ll T_E). \quad (3.82)$$

In the case of perfect over-coupling, robust light intensity is stored in the cavity, and all the incident light field is reflected ($P_B \simeq P_A$). In the case of critical coupling, all the incident light field is transmitted ($P_G \simeq P_A$). In the case of under-coupling, light cannot be stored in the cavity; thus, the cavity must be configured to avoid under-coupling.

Now let us calculate the input-output relation of the light field fluctuations in the case of perfect over-coupling ($r_I = r$, $t_I = t$, $r_E^2 = 1$). Here, only the end mirror is supposed to work as a test mass; thus, we obtain

$$\begin{aligned} \mathbf{b} &= -r\mathbf{a} + t\mathbf{d}, \quad \mathbf{c} = t\mathbf{a} + r\mathbf{d}, \quad \mathbf{d} = e^{i\alpha} R(\phi) \mathbf{f}, \\ \mathbf{e} &= e^{i\alpha} R(\phi) \mathbf{c}, \quad \mathbf{f} = P(\kappa, \xi_E) \mathbf{e} + \frac{\sqrt{2\kappa}}{h_{\text{SQL}}} \mathbf{n}_{E\perp} h(\Omega), \end{aligned} \quad (3.83)$$

where $\alpha = -L\Omega/c$ denotes the phase delay per half cycle. If we consider the case of a resonance state ($\phi = 0$), we obtain $\kappa = 8P_E\omega_0/(mc^2\Omega^2) \simeq 16\mathcal{F}P_A\omega_0/(\pi mc^2\Omega^2)$ and $h_{\text{SQL}} = \sqrt{8\hbar/(mL^2\Omega^2)}$. The reflected light field fluctuation \mathbf{b} can be written as

$$\begin{aligned} \mathbf{b} &= \left[-rI + \frac{t^2 e^{2i\alpha}}{(1 - re^{2i\alpha})^2} \begin{pmatrix} 1 - re^{2i\alpha} & 0 \\ -\kappa & 1 - re^{2i\alpha} \end{pmatrix} \right] \mathbf{a} \\ &\quad + \frac{te^{i\alpha}}{(1 - re^{2i\alpha})^2} \frac{\sqrt{2\kappa}}{h_{\text{SQL}}} \begin{pmatrix} 0 \\ 1 - re^{2i\alpha} \end{pmatrix} h(\Omega). \end{aligned} \quad (3.84)$$

By approximating that $T = t^2$ and α are much smaller than unity, we obtain

$$\mathbf{b} \simeq \frac{\gamma - i\Omega}{\gamma + i\Omega} \begin{pmatrix} 1 & 0 \\ -\frac{\gamma\iota}{\Omega^2(\gamma^2 + \Omega^2)} & 1 \end{pmatrix} \mathbf{a} + \frac{\gamma - i\Omega}{\sqrt{\gamma^2 + \Omega^2}} \frac{\sqrt{\frac{2\gamma\iota}{\Omega^2(\gamma^2 + \Omega^2)}}}{h_{\text{SQL}}} \begin{pmatrix} 0 \\ 1 \end{pmatrix} h(\Omega), \quad (3.85)$$

where we defined

$$\gamma = \frac{Tc}{4L}, \quad (3.86)$$

$$\iota = \frac{8P_E\omega_0}{mLc}. \quad (3.87)$$

Furthermore, to correspond with the response of the Michelson interferometer (3.63), we define

$$\mathcal{K} = \frac{\gamma\iota}{\Omega^2(\gamma^2 + \Omega^2)}, \quad (3.88)$$

$$\beta = \arctan(-\Omega/\gamma), \quad (3.89)$$

and finally, we obtain

$$\mathbf{b} = e^{2i\beta} \begin{pmatrix} 1 & 0 \\ -\mathcal{K} & 1 \end{pmatrix} \mathbf{a} + e^{i\beta} \frac{\sqrt{2\mathcal{K}}}{h_{\text{SQL}}} \begin{pmatrix} 0 \\ 1 \end{pmatrix} h(\Omega). \quad (3.90)$$

The signal response of Eq. (3.85) shows that the Fabry-Perot cavity behaves as a first-order low-pass filter with the cavity decay rate γ as a pole:

$$\frac{b_2(\Omega)}{h(\Omega)} \sim \frac{1}{1 + i\Omega/\gamma}. \quad (3.91)$$

Here input light field fluctuation α is ignored. Therefore, γ is also referred to as the cavity pole. The frequency corresponding to the cavity pole is equal to the frequency corresponding to half width at half maximum (HWHM) $f_{\text{HWHM}} = f_{\text{FWHM}}/2$:

$$\frac{\gamma}{2\pi} = f_{\text{HWHM}}. \quad (3.92)$$

In a frequency band sufficiently lower than the cavity decay rate ($\Omega \ll \gamma$), optomechanical coupling constant by the cavity \mathcal{K} can be written as

$$\mathcal{K} \simeq \frac{8P_A\omega_0}{mc^2\Omega^2} \left(\frac{2\mathcal{F}}{\pi} \right)^2, \quad (3.93)$$

which is $(2\mathcal{F}/\pi)^2$ times the coupling constant in the free mass. In addition to the enhancement of the laser light power by a factor of $2\mathcal{F}/\pi$, as in Eq. (3.77), the response of the signal is also enhanced by a factor of $2\mathcal{F}/\pi$. In other words, the Fabry-Perot cavity is a cavity that amplifies the light power and the response to the signal simultaneously. However, the standard quantum limit h_{SQL} remains unchanged because the same factor amplifies the incident vacuum field. In the frequency band $\Omega \ll \gamma$, the phase delay resulting from the reflection by the Fabry-Perot cavity β can be written as

$$\beta \simeq \frac{2\mathcal{F}}{\pi} \alpha. \quad (3.94)$$

The time delay in the cavity is enhanced by a factor of $2\mathcal{F}/\pi$ compared to free space, indicating the effective propagation length increases.

3.3.3 Dual Recycling Michelson interferometer

The cavity significantly reduces shot noise, a problem with the Michelson interferometer. The actual gravitational wave detector improves the sensitivity by implementing optical cavities within the Michelson interferometer. In particular, the current gravitational wave detectors have two recycling cavities. Cavities consisting of a mirror at the input and output ports of the Michelson interferometer are known as the power recycling cavity (PRC) and signal recycling cavity (SRC), respectively. The dual recycling Michelson interferometer (DRMI) includes these two recycling cavities.

Let us consider the DRMI as shown in Fig. 3.6. Let r_p^2 and t_p^2 be the power reflectivity and transmissivity of the input port mirror (power recycling mirror: PRM) and r_s^2 and t_s^2 be those of the output port mirror (signal recycling mirror: SRM), L be the arm length of the Michelson interferometer, and l be the distance from BS to SRM. When the Michelson interferometer part operates at the dark fringe, all the carrier light transmits to the input port, and all the signal transmits to the output port. Thus the functions of the PRC and SRC can be separated. When the PRC is in resonance, the input-output relation of the carrier light can be written

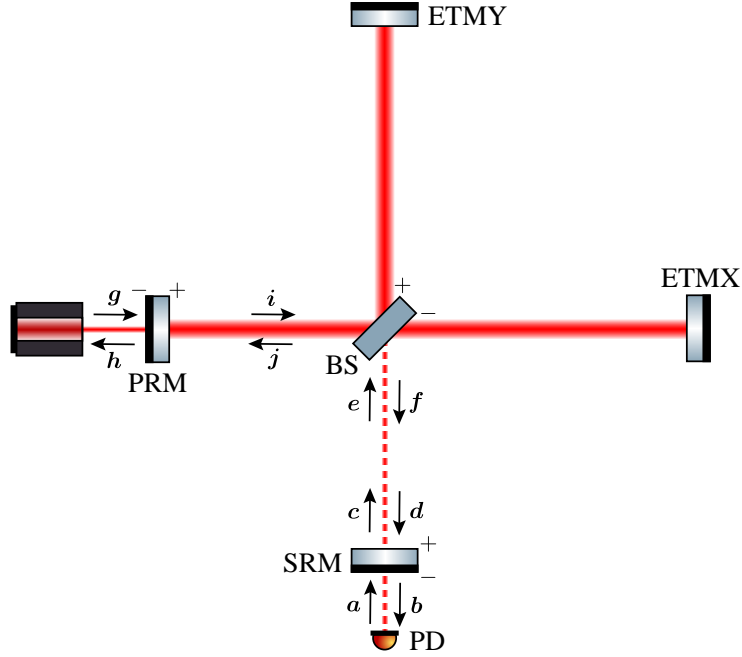


Fig. 3.6: Schematic of the dual recycling Michelson interferometer. The end mirrors are supposed to work as a test mass, and the two recycling mirrors do not receive force from gravitational waves.

as

$$\mathbf{H} = -r_P \mathbf{G} + t_P \mathbf{J}, \quad \mathbf{I} = t_P \mathbf{G} + r_P \mathbf{J}, \quad \mathbf{J} = \mathbf{I}, \quad (3.95)$$

and solving for \mathbf{I} , we obtain

$$\mathbf{I} = \frac{t_P}{1 - r_P} \mathbf{G} \simeq \frac{2}{t_P} \mathbf{G}, \quad (3.96)$$

indicating that the effective incident laser light power into the BS is amplified by a factor of $4/t_P^2 = 2\mathcal{F}_P/\pi$, where $\mathcal{F}_P = 2\pi/t_P^2$ is the finesse of the PRC. The power recycling increases the input laser power because the fluctuations of the input carrier light incident from the input port are reflected to the input port and do not affect the measurement at the output port.

Let $\alpha_{\text{arm}} = -L\Omega/c$ be the phase delay in the arm and $\phi \equiv l\omega_0/c \pmod{2\pi}$ and $\alpha_S = -l\Omega/c$ be the phase change and delay between the BS and SRM, respectively. The input-output relation of the light field fluctuation can be written as

$$\begin{aligned} \mathbf{b} &= -r_S \mathbf{a} + t_S \mathbf{d}, \quad \mathbf{c} = t_S \mathbf{a} + r_S \mathbf{d}, \quad \mathbf{d} = e^{i\alpha_S} R(\phi) \mathbf{f}, \\ \mathbf{e} &= e^{i\alpha_S} R(\phi) \mathbf{c}, \quad \mathbf{f} = e^{2i\alpha_{\text{arm}}} P(\kappa, 0) \mathbf{e} + e^{i\alpha_{\text{arm}}} \frac{\sqrt{2\kappa}}{h_{\text{SQL}}} \begin{pmatrix} 0 \\ 1 \end{pmatrix} h(\Omega), \end{aligned} \quad (3.97)$$

where we defined $\kappa = 4P_I\omega_0/(mc^2\Omega^2) \simeq 8P_G\mathcal{F}_P\omega_0/(\pi mc^2\Omega^2)$ and $h_{\text{SQL}} =$

$\sqrt{4\hbar/mL^2\Omega^2}$. When the SRC is in resonance ($\phi = 0$), Eq. (3.97) can be solved similarly to the Fabry-Perot cavity with the phase delay $\alpha = \alpha_{\text{arm}} + \alpha_S$:

$$\mathbf{b} = e^{2i\beta} \begin{pmatrix} 1 & 0 \\ -\mathcal{K} & 1 \end{pmatrix} \mathbf{a} + e^{i\beta} \frac{\sqrt{2\mathcal{K}}}{h_{\text{SQL}}} \begin{pmatrix} 0 \\ 1 \end{pmatrix} h(\Omega), \quad (3.98)$$

where we defined $T_S = t_S^2$, $\gamma = T_S c / (4(L + l))$, $\iota = 4P_I \omega_0 / (m(L + l)c)$, $\mathcal{K} = \gamma \iota / (\Omega^2(\gamma^2 + \Omega^2))$, and $\beta = \arctan(-\Omega/\gamma)$. Whereas the Fabry-Perot cavity enhances the laser light power and signal response by a factor of $2\mathcal{F}/\pi$, the power recycling cavity enhances the laser light power by $2\mathcal{F}_P/\pi$, and the signal recycling cavity enhances the signal response by $2\mathcal{F}_S/\pi$ ($\mathcal{F}_S = 2\pi/T_S$). Dual recycling identically impacts the interferometer as a Fabry-Perot cavity.

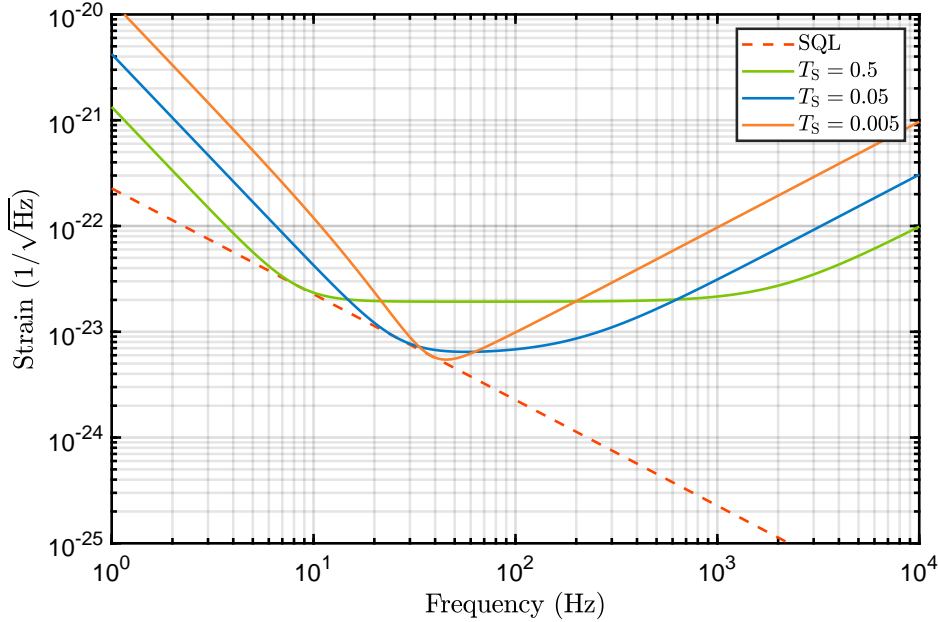


Fig. 3.7: Sensitivity of the dual recycling Michelson interferometer as determined by quantum noise. The light power on the beam splitter is set to $P_I = 100$ kW, and the SRC length is neglected ($l \ll L$).

The sensitivity of the DRMI can be calculated as in the Michelson interferometer:

$$S_h(\Omega) = \frac{h_{\text{SQL}}^2}{2} \left(\mathcal{K} + \frac{1}{\mathcal{K}} \right). \quad (3.99)$$

Fig. 3.7 shows the sensitivity of the DRMI. Peak sensitivity improves with the higher finesse of the SRC, indicating that the SRC enhances signal response and reduces shot noise. In contrast, the sensitivity worsens in proportion to f^1 at the high-frequency band because the low-pass characteristics of the cavity attenuate signals with a frequency higher than the cavity decay rate. For example, we can

calculate $\gamma \sim 2\pi \times 2 \times 10^2$ Hz for $T = 0.05$, indicating that the cavity decay rate corresponds to the frequency at which the sensitivity begins to deteriorate.

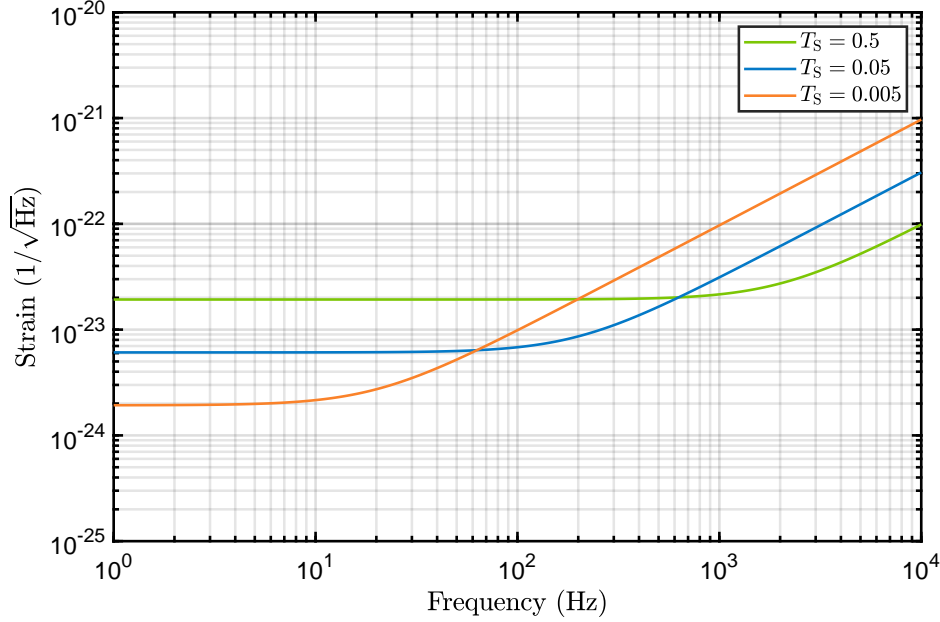


Fig. 3.8: Sensitivity of the dual recycling Michelson interferometer as determined by shot noise. The parameters are set to the same as in Fig. 3.7.

To examine the relationship between the peak sensitivity and bandwidth, only the shot noise, which is the second term of Eq. (3.99), is shown in Fig. 3.8. The sensitivity deteriorates in the high-frequency band because of signal attenuation. In contrast, the shot noise is a constant independent of frequency and inversely proportional to the laser light power in the arm. By decreasing T_S , the finesse of the SRC can be improved, and shot noise can be reduced; however, the cavity decay rate also decreases, and the bandwidth of the interferometer is narrowed. This trade-off relationship is known as the Mizuno limit [99] and is a consequence of the quantum Cramer-Rao bound [100]. For the DRMI, the product of peak sensitivity and bandwidth is a constant value independent of finesse:

$$\lim_{\Omega \rightarrow 0} \frac{2\mathcal{K}}{h_{\text{SQL}}^2} \times \gamma = \frac{mL^2\iota}{2\hbar}. \quad (3.100)$$

Another possible configuration in which the cavity is implemented in a Michelson interferometer is the Fabry-Perot Michelson interferometer (FPMI), which implements Fabry-Perot cavities in both arms^{*3}. As the Fabry-Perot cavity simultaneously amplifies the intracavity power and signals, the sensitivity of the FPMI matches that of the DRMI except for a factor.

^{*3} See App. C.1.1.

One advantage of the DRMI is that it can reduce the frequency noise of the laser light. Owing to slight contrast errors in actual Michelson interferometers, the frequency fluctuations of the laser light can leak out to the output port and cause frequency noise. Using power recycling, the frequency noise of the laser light can be reduced owing to the low-pass feature of the PRC. In contrast, the FPMI cannot reduce frequency noise because common-mode noises, such as laser frequency noise, and differential signals, such as gravitational wave signals, are simultaneously amplified in the arm. Note that the frequency noise also depends on the readout method; thus, the aforementioned explanation may not apply in some cases. One disadvantage of the DRMI is that the light power in the BS increases as the light power in the arms increases, and thermal lensing effects in the BS can prevent the proper operation of the DRMI [101].

The second-generation gravitational wave detectors are based on an interferometer configuration with both the arm cavities and two recycling cavities. This interferometer configuration is known as a resonant sideband extraction (RSE) interferometer [102] because the SRC is used to reduce the arm cavity decay rate^{*4}.

3.4 Advanced techniques for sensitivity improvement

The quantum noise of the gravitational wave detector discussed in the last section has a limit for the spectral density, known as SQL. We can beat the SQL by correlating the amplitude and phase quadratures of the vacuum field at incidence, within the interferometer, or at the measurement. Measurements using such techniques are sometimes referred to as quantum non-demolition measurements [103]. This section briefly discusses homodyne detection, input squeezing, and optical spring as techniques that may allow us to beat the SQL.

We discuss the DRMI considered in Sec. 3.3.3 as the basic configuration to compare each technique. The sensitivity of the DRMI deteriorates above the cavity decay rate of the SRC γ . We can calculate the angular frequency at which the spectral density matches SQL (where the coupling constant takes $\mathcal{K} = 1$) as follows:

$$\Omega_{\text{SQL}} = \gamma \sqrt{\frac{1}{2} \left(-1 + \sqrt{1 + \frac{4\iota}{\gamma^3}} \right)}. \quad (3.101)$$

An actual gravitational wave detector should be set to around $\Omega_{\text{SQL}} \simeq \gamma$ to maintain bandwidth while improving peak sensitivity. In the plots presented in this section, unless otherwise noted, the parameters are set to $\gamma = 2\pi \times 100 \text{ Hz}$ and $\iota = 2\gamma^3$, and we denote $r_S = r$ and $t_S = t$.

^{*4} See App. C.1.2.

3.4.1 Back action evasion by the homodyne detection

We have been assuming that the homodyne angle is set to $\pi/2$ to maximize the magnitude of the signal. Here, we examine the sensitivity when the amplitude quadrature of the local oscillator is not 0. This situation corresponds to the case where the DC offset, the local oscillator of the phase quadrature, is reduced, and the influence of the contrast defect, the local oscillator of the amplitude quadrature, cannot be neglected.

Suppose that a vacuum field \mathbf{a} is incident on the interferometer and the output light field fluctuation \mathbf{b} can be written as follows:

$$\mathbf{b} = \mathbb{A}\mathbf{a} + \mathcal{H}h(\Omega) = \begin{pmatrix} A_{11} & A_{12} \\ A_{21} & A_{22} \end{pmatrix} \mathbf{a} + \begin{pmatrix} \mathcal{H}_1 \\ \mathcal{H}_2 \end{pmatrix} h(\Omega). \quad (3.102)$$

By measuring this with the carrier \mathbf{B} , the power fluctuation δP_B can be written as

$$\begin{aligned} \delta P_B &= \hbar\omega_0(b_1 B_1 + b_2 B_2) \\ &= \hbar\omega_0 [(A_{11}B_1 + A_{21}B_2)a_1 + (A_{21}B_1 + A_{22}B_2)a_2 + (\mathcal{H}_1 B_1 + \mathcal{H}_2 B_2)]. \end{aligned} \quad (3.103)$$

Thus, the sensitivity can be formulated as

$$\begin{aligned} S_h(\Omega) &= \frac{|A_{11} \cos \xi_B + A_{21} \sin \xi_B|^2 + |A_{12} \cos \xi_B + A_{22} \sin \xi_B|^2}{|\mathcal{H}_1 \cos \xi_B + \mathcal{H}_2 \sin \xi_B|^2} \\ &= \frac{\mathbf{w}_B \mathbb{A} \mathbb{A}^\dagger \mathbf{w}_B^T}{\mathbf{w}_B \mathcal{H} \mathcal{H}^\dagger \mathbf{w}_B^T}, \end{aligned} \quad (3.104)$$

where $\xi_B = \arctan(B_2/B_1)$ denotes the homodyne angle and $\mathbf{w}_B = (\cos \xi_B \ \sin \xi_B)$ denotes the unit vector perpendicular to the carrier light. As shown in Eq.(3.103), the term $A_{11} \cos \xi_B + A_{21} \sin \xi_B$ is the noise derived from the amplitude quadrature of the vacuum field, and the term $A_{21} \cos \xi_B + A_{22} \sin \xi_B$ is derived from the phase quadrature. From Eq. (3.98), the sensitivity of DRMI can be calculated as follows:

$$S_h(\Omega) = \frac{h_{\text{SQL}}^2}{2\mathcal{K}} [(\cot \xi_B - \mathcal{K})^2 + 1]. \quad (3.105)$$

We note that the first term becomes 0 at frequencies where $\xi_B = \text{arccot} \mathcal{K}$, which can be explained as follows. The output power fluctuations have two terms derived from the amplitude quadrature of the vacuum field a_1 . $\cos \xi_B a_1$ denotes the term that appears in the amplitude quadrature of the output light via direct reflection, and $-\mathcal{K} \sin \xi_B a_1$ denotes the term that appears in the phase quadrature of the output light via fluctuations of the mirror. They are quantum correlated, and radiation

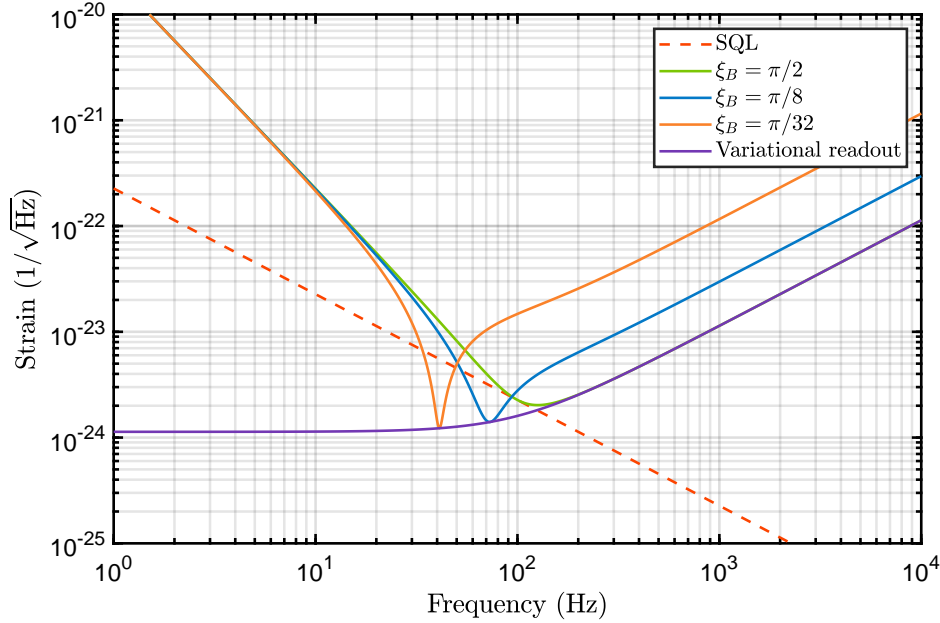


Fig. 3.9: Sensitivity of the DRMI to several homodyne angles.

pressure noise can be evaded at the frequency where they are canceled. A technique that avoids radiation pressure noise, e.g., homodyne detection, is known as back action evasion.

The sensitivity of DRMI with homodyne detection is shown in Fig. 3.9. As the homodyne angle approaches 0, it becomes possible to significantly beat SQL. However, the shot noise in the high-frequency band degrades as the magnitude of the readable signal reduces. The variational readout corresponds to the measurement with a frequency-dependent homodyne angle that optimizes sensitivity [104]. Current gravitational wave detectors measure the output light at a fixed homodyne angle, providing the best observation rate of gravitational wave events.

3.4.2 Input squeezing

We have assumed that a coherent vacuum field is injected into the interferometer. By performing OPA for the incident vacuum field, it is possible to inject the squeezed vacuum field into the interferometer [105]. This technique is known as input squeezing or external squeezing.

Let us consider injecting a squeezed vacuum field into the interferometer, as shown in Fig. 3.10. The Faraday isolator is a group of optical elements that transmits light incident from the front direction and reflects light incident from the opposite direction. In this figure, the light propagating downward is transmitted. Let $s = e^u$ be the squeezing factor of the squeezer and θ be the squeezing angle. The light field fluctuation incident on the interferometer is modified as

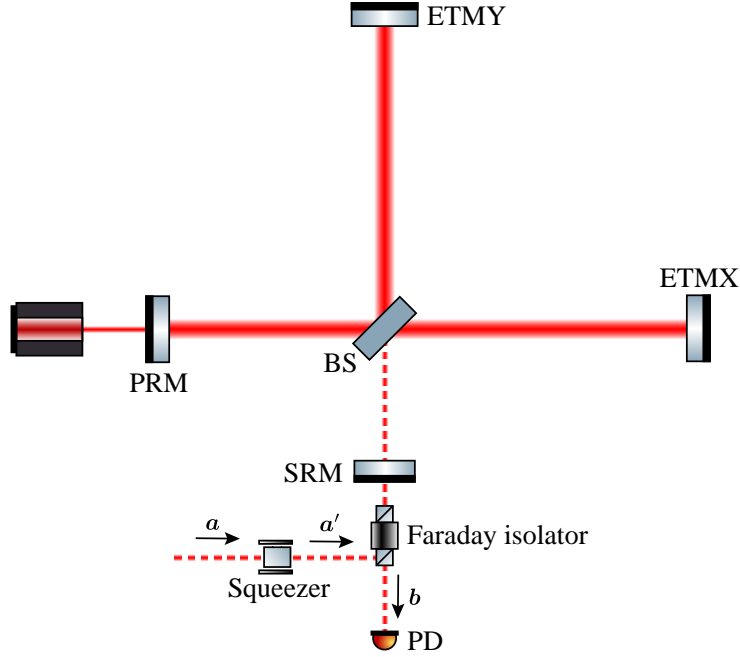


Fig. 3.10: Schematic of input squeezing for the DRMI. The vacuum field is squeezed, passes through the Faraday isolator, and is incident on the main interferometer.

$a \rightarrow a' = S(u, \theta)a$. Therefore, Eq. (3.98) can be rewritten as

$$b = e^{2i\beta} \begin{pmatrix} 1 & 0 \\ -\mathcal{K} & 1 \end{pmatrix} S(u, \theta)a + e^{i\beta} \frac{\sqrt{2\mathcal{K}}}{h_{\text{SQL}}} \begin{pmatrix} 0 \\ 1 \end{pmatrix} h(\Omega), \quad (3.106)$$

and the sensitivity can be written as

$$S_h(\Omega) = \frac{h_{\text{SQL}}^2}{2\mathcal{K}} [(\sinh u \sin 2\theta - \mathcal{K}(\cosh u + \sinh u \cos 2\theta))^2 + ((\cosh u - \sinh u \cos 2\theta) - \mathcal{K} \sinh u \sin 2\theta)^2]. \quad (3.107)$$

Sensitivity curves are shown in Fig. 3.11. Compared to the case without input squeezing ($s = 0$), the shot noise is reduced when $\theta = 0$, and the radiation pressure noise is reduced when $\theta = \pi/2$, i.e., $\theta = 0$ and $\theta = \pi/2$ exhibit the same effect when the incident light power increases and decreases, respectively, as can be obtained from the following:

$$S_h(\Omega)|_{\theta=0} = \frac{h_{\text{SQL}}^2}{2} \left(s^2 \mathcal{K} + \frac{1}{s^2 \mathcal{K}} \right). \quad (3.108)$$

When $\theta = \pi/4$, a correlated vacuum field between amplitude and phase quadratures is injected, which can beat the SQL, as can be obtained from the following:

$$S_h(\Omega)|_{\theta=\pi/4} = \frac{h_{\text{SQL}}^2}{2} \left[\left(\mathcal{K} + \frac{1}{\mathcal{K}} \right) \cosh 2u - 2 \sinh 2u \right]. \quad (3.109)$$

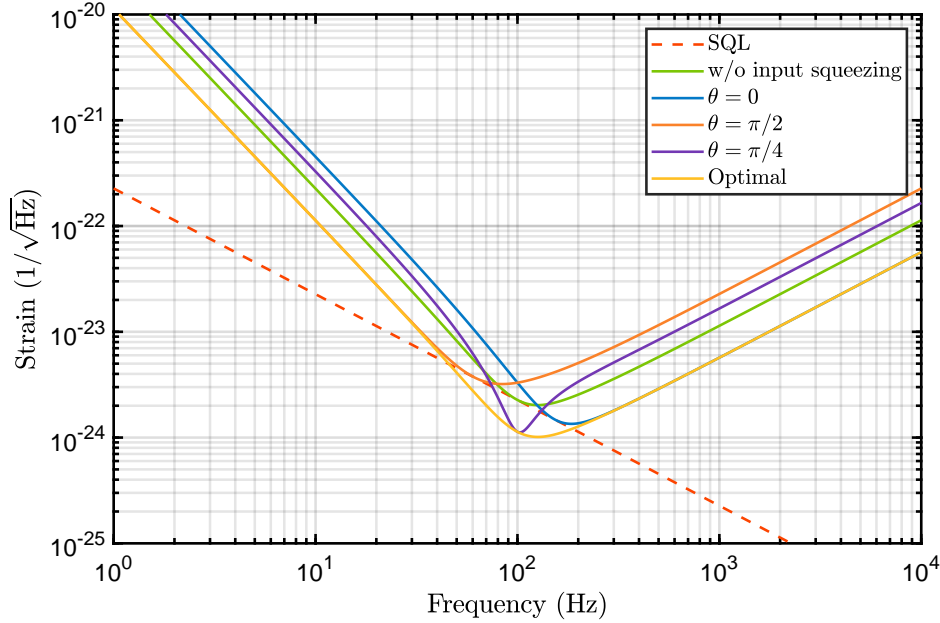


Fig. 3.11: Sensitivity of the DRMI with input squeezing. The parameter is set to $s = 2$. Optimal sensitivity can be achieved when $\theta = \arctan \mathcal{K}$.

In addition, considering a frequency-dependent squeezing angle that minimizes Eq. (3.107), when $\theta = \arctan \mathcal{K}$, we obtain

$$S_h(\Omega)|_{\theta=\arctan \mathcal{K}} = \frac{h_{\text{SQL}}^2}{2s^2} \left(\mathcal{K} + \frac{1}{\mathcal{K}} \right). \quad (3.110)$$

Thus, if we achieve the ideal frequency-dependent squeezing angle, sensitivity can be improved in all frequency bands. Frequency-dependent squeezing can be achieved using a detuned high-finesse cavity, known as a filter cavity^{*5} [95]. The principle of frequency-dependent squeezing using a filter cavity was verified in the MHz band [106], audio band [107], and detection band of an actual gravitational wave detector [108, 109]. Based on the results of proof-of-principle experiments, it has been adopted to upgrade advanced detectors [110]. For example, the filter cavity for advanced LIGO was constructed in 2022 [111].

3.4.3 Detuning of the signal recycling cavity

We have been assuming that the cavities are in resonance. When the cavity is detuned from the resonance state, an optical spring is generated, and the gravitational wave signal can be amplified at its resonance frequency [20]. The optical spring is generated by detuning the SRC in gravitational wave detectors because

^{*5} See also App. C.2.1.

the detuning of the arm cavity reduces the intracavity power. Signal amplification based on an optical spring is adequate for detectors where the influence of thermal noise is negligible and quantum noise is dominant in the observation bandwidth. For example, the SRC of KAGRA will be detuned, thereby improving the observation range of the inspiral phase of the binary neutron star merger [12, 74, 112].

Let us consider the detuning of the SRC in the DRMI^{*6}. Solving Eq. (3.97) with $\phi \neq 0$, we obtain

$$\begin{aligned} \mathbf{b} &= \left[-rI + t^2 e^{2i\alpha} [I - r e^{2i\alpha} R(\phi) P(\kappa, 0) R(\phi)]^{-1} R(\phi) P(\kappa, 0) R(\phi) \right] \mathbf{a} \\ &\quad + t e^{i\alpha} \frac{\sqrt{2\kappa}}{h_{\text{SQL}}} [I - r e^{2i\alpha} R(\phi) P(\kappa, 0) R(\phi)]^{-1} R(\phi) \begin{pmatrix} 0 \\ 1 \end{pmatrix} h(\Omega) \\ &= \frac{1}{C} [\mathbb{A} \mathbf{a} + \mathcal{H} h(\Omega)], \end{aligned} \quad (3.111)$$

with

$$C = r e^{2i\alpha} + \frac{1}{r} e^{-2i\alpha} - 2(\cos 2\phi + \frac{\kappa}{2} \sin 2\phi), \quad (3.112)$$

$$A_{11} = A_{22} = \left(r + \frac{1}{r} \right) \left(\cos 2\phi + \frac{1}{2} \kappa \sin 2\phi \right) - 2 \cos 2\alpha, \quad (3.113)$$

$$A_{12} = - \left(\frac{1}{r} - r \right) \left(\sin 2\phi + \frac{1}{2} \kappa (1 - \cos 2\phi) \right), \quad (3.114)$$

$$A_{21} = \left(\frac{1}{r} - r \right) \left(\sin 2\phi - \frac{1}{2} \kappa (1 + \cos 2\phi) \right), \quad (3.115)$$

$$\mathcal{H} = t \frac{\sqrt{2\kappa}}{h_{\text{SQL}}} \begin{pmatrix} -(\frac{1}{r} e^{-i\alpha} + e^{i\alpha}) \sin \phi \\ (\frac{1}{r} e^{-i\alpha} - e^{i\alpha}) \cos \phi \end{pmatrix}. \quad (3.116)$$

By approximating that T , α , ϕ , and κ are much smaller than unity^{*7}, we obtain

$$\mathbf{b} = \frac{1}{C} [\mathbb{M} \mathbf{a} + \mathcal{D} h(\Omega)], \quad (3.117)$$

with

$$\mathcal{C} = \Omega^2 [(\gamma + i\Omega)^2 + \Delta^2] - \Delta\iota/2, \quad (3.118)$$

$$\mathbb{M} = \begin{pmatrix} \Omega^2(\Omega^2 + \gamma^2 - \Delta^2) + \Delta\iota/2 & -2\gamma\Delta\Omega^2 \\ 2\gamma\Delta\Omega^2 - \gamma\iota & \Omega^2(\Omega^2 + \gamma^2 - \Delta^2) + \Delta\iota/2 \end{pmatrix}, \quad (3.119)$$

$$\mathcal{D} = \frac{\sqrt{2\gamma\iota}}{h_{\text{SQL}}} \begin{pmatrix} -\Delta\Omega \\ (\gamma + i\Omega)\Omega \end{pmatrix}, \quad (3.120)$$

^{*6} The calculations for the RSE interferometer are detailed in [113].

^{*7} The magnitude of κ depends on the frequency; however, in the frequency band under consideration ($\Omega \sim \gamma$), it has a similar magnitude as T .

where $\Delta = \phi c/L$ denotes the cavity detuning of the SRC. The sensitivity can be calculated as

$$S_h(\Omega) = \frac{|M_{11} \cos \xi_B + M_{21} \sin \xi_B|^2 + |M_{12} \cos \xi_B + M_{22} \sin \xi_B|^2}{|\mathcal{D}_1 \cos \xi_B + \mathcal{D}_2 \sin \xi_B|^2}. \quad (3.121)$$

At a frequency that results in $\mathcal{C} = 0$, apparently, the signal and noise are simultaneously amplified regardless of the homodyne angle. The optical system is sensitive to mirror fluctuations at the aforementioned frequency, implying that an optical spring is generated. By approximating $\Omega \ll \gamma$, the resonant frequency of the optical spring ω_{OS} can be obtained^{*8}:

$$\omega_{OS} = \sqrt{\frac{\Delta \iota}{2(\gamma^2 + \Delta^2)}}. \quad (3.122)$$

Let us discuss a measurement using the DC offset of the Michelson interferometer. The homodyne angle corresponds to the angle of the DC signal: $\xi_B = \arctan(\mathcal{D}_2/\mathcal{D}_1)|_{\Omega \rightarrow 0} = \arctan(-\gamma/\Delta)$. The sensitivity curve is shown in

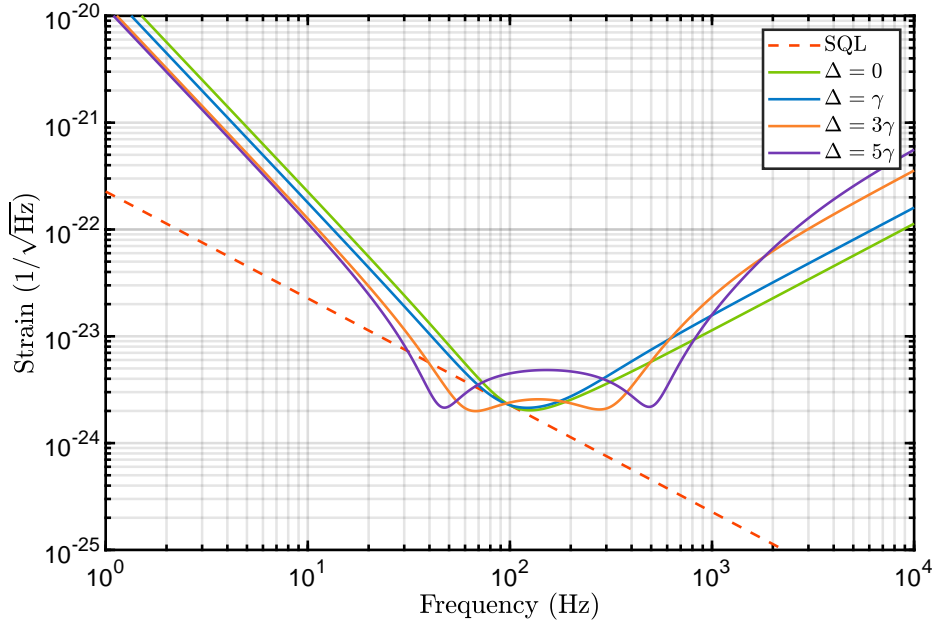


Fig. 3.12: Sensitivity of the DRMI with the detuning of the SRC. Output light field fluctuation is measured using the DC offset.

Fig. 3.12. Two dips are formed in the sensitivity curve when the cavity detuning is sufficiently larger than the cavity decay rate. The frequencies of the dips

^{*8} For the parameters considered, this approximate formula is valid for $\Delta \gg \gamma$.

are obtained from the frequency at which a term derived from the amplitude quadrature is 0, i.e.,

$$\omega_{\text{DC-OS}} = \sqrt{\frac{(\Delta^2 + 2\gamma^2)\iota}{2\Delta(\gamma^2 + \Delta^2)}}, \quad (3.123)$$

$$\omega_{\text{DC-OR}} = \sqrt{\gamma^2 + \Delta^2}. \quad (3.124)$$

$\omega_{\text{DC-OS}}$ corresponds to the dip frequency on the lower frequency side. When cavity detuning is sufficiently large ($\Delta \gg \gamma$), $\omega_{\text{DC-OS}}$ coincides with ω_{OS} , and it is possible to beat the SQL in a narrow band around this frequency. The sensitivity in this band corresponds to the ratio of the signal amplified by the optical spring to the noise whose amplification based on the optical spring is suppressed by the back action evasion [114]. In contrast, $\omega_{\text{DC-OR}}$ corresponds to the dip frequency on the higher frequency side. When $\Delta \gg \gamma$, we obtain $\omega_{\text{DC-OR}} \simeq \Delta := \omega_{\text{OR}}$, corresponding to the resonance condition for one sideband. The resonance of the signal forms a dip on the higher frequency side, and this phenomenon is known as optical resonance.

Moreover, we can regard the SQL itself as being modified by the optical spring [103]. We have assumed that the test mass behaves as a free mass, as in Eq. (3.45). However, when the test mass is bounded by the optical spring, the equations of motion are modified and the SQL is changed as follows:

$$h_{\text{SQL}}^{\text{OS}} = \sqrt{\frac{|\Omega^2 - \omega_{\text{opt}}^2|}{\Omega^2}} h_{\text{SQL}}. \quad (3.125)$$

Fig. 3.13 shows the sensitivity for $\Delta = 5\gamma$ by dividing the terms derived from amplitude and phase quadrature of Eq. (3.121), which are

$$S_h^{\text{amp}}(\Omega) = \frac{|M_{11} \cos \xi_B + M_{21} \sin \xi_B|^2}{|\mathcal{D}_1 \cos \xi_B + \mathcal{D}_2 \sin \xi_B|^2}, \quad (3.126)$$

$$S_h^{\text{phase}}(\Omega) = \frac{|M_{12} \cos \xi_B + M_{22} \sin \xi_B|^2}{|\mathcal{D}_1 \cos \xi_B + \mathcal{D}_2 \sin \xi_B|^2}, \quad (3.127)$$

respectively, as discussed in Sec. 3.4.1. The sum of the two terms does not beat the SQL modified by the optical spring. The sensitivity near the resonant frequency of the optical spring has improved because the optical spring reduces SQL itself. The depth of the dips is determined based on the terms derived from the phase quadrature. If $\Delta \gg \gamma$, $\sqrt[3]{\iota}$, the depths of the two dips become equal and can be calculated as follows:

$$S_h(\omega_{\text{DC-OS}})|_{\xi_B=\arctan(-\gamma/\Delta)} \approx S_h(\omega_{\text{DC-OR}})|_{\xi_B=\arctan(-\gamma/\Delta)} \approx \frac{8\hbar\gamma}{mL^2\iota}. \quad (3.128)$$

Next, let us discuss a measurement using the contrast defect of the Michelson interferometer. The homodyne angle corresponds to the orthogonal angle of the

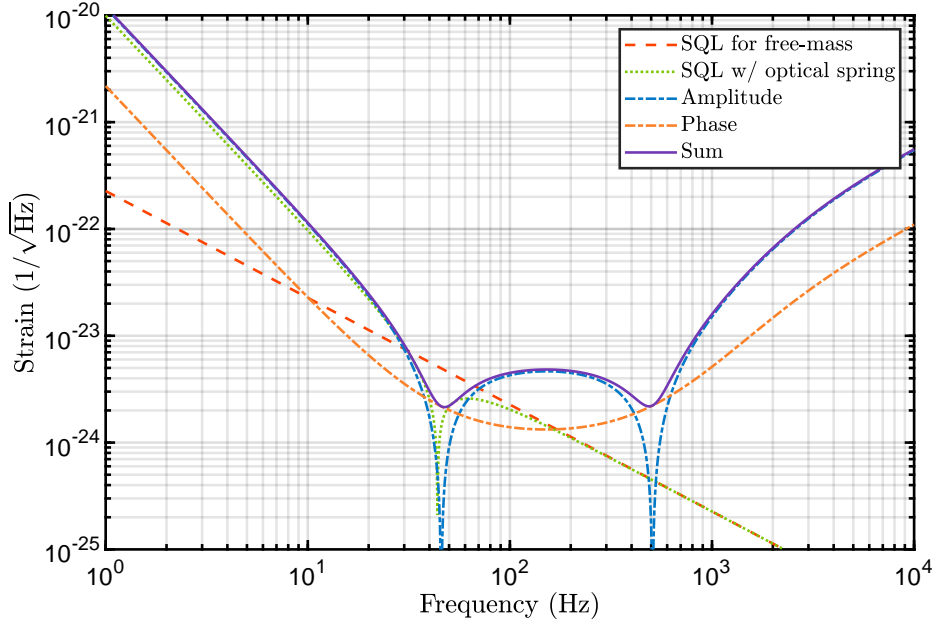


Fig. 3.13: Sensitivity of the DRMI with the detuning of the SRC. Output light field fluctuation is measured with the DC offset, and we set $\Delta = 5\gamma$.

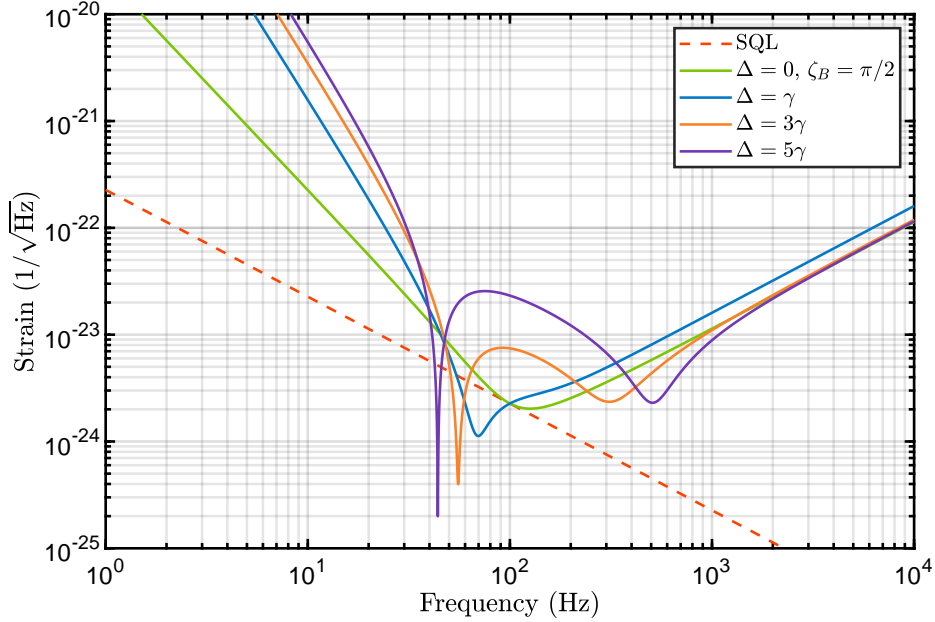


Fig. 3.14: Sensitivity of the DRMI with the detuning of the SRC. Output light field fluctuation is measured using the contrast defect. The signal does not appear in amplitude quadrature for $\Delta = 0$; thus, the homodyne angle is set to $\pi/2$.

DC signal: $\xi_B = \arctan(\Delta/\gamma)$. The sensitivity curve is shown in Fig. 3.14. When the cavity detuning is sufficiently large, a dip on the lower frequency side appears at frequencies where the terms derived from the amplitude and phase quadratures are 0. This frequency can be calculated as

$$\omega_{\text{CD-OS}} = \sqrt{\frac{\Delta_\epsilon}{2(\gamma^2 + \Delta^2)}}, \quad (3.129)$$

which coincides with the resonance frequency of the optical spring ω_{OS} . A dip on the higher frequency side appears at the frequency where the term derived from the phase quadrature is 0. This frequency can be calculated as

$$\omega_{\text{CD-OR}} = \sqrt{\gamma^2 + \Delta^2}, \quad (3.130)$$

which coincides with the frequency of optical resonance ω_{OR} when $\Delta \gg \gamma$.

Let us consider the significance of the measurement using the contrast defect in terms of its correspondence with the Fabry-Perot cavity. In the DRMI, the PRC amplifies the intra-arm power, the SRC amplifies the signal, and the PRC is resonant, generating signals in the phase quadrature. In contrast, the Fabry-Perot cavity simultaneously amplifies the intracavity power and signal. Its characteristics can be considered equivalent to the DRMI except for the factor, as denoted in Eqs. (3.90) and (3.98). However, when the incident carrier is in the amplitude quadrature (Fig. 3.4), the detuned cavity does not generate the signal in the phase quadrature; therefore, there is no direct correspondence with the DRMI. Then, as shown in Fig. 3.15, we consider that the incident carrier is rotated by $\varphi = -\arctan(\Delta/\gamma)$ so that the intracavity carrier becomes in the amplitude quadrature. Here,

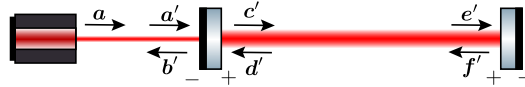


Fig. 3.15: Schematic of the Fabry-Perot cavity as intracavity carrier criteria. The initial phase of the incident carrier is $\varphi = -\arctan(\Delta/\gamma)$.

$$\mathbf{a}' = R(\varphi)\mathbf{a}. \quad (3.131)$$

In this case, the intracavity carrier \mathbf{E}' is in the amplitude quadrature, and the signal appears in the phase quadrature of the reflected light field fluctuation \mathbf{f}' . Although the intracavity power varies with cavity detuning, we can consider this Fabry-Perot cavity to be equivalent to the DRMI by normalizing the parameters affected by the intracavity power.

The contrast defect vector of the Michelson interferometer is in the same direction as the carrier vector reflected by the end mirror. In other words, the measurement using the contrast defect corresponds to the measurement of a detuned Fabry-Perot cavity with reflected light. When considering light field fluctuations within a Fabry-Perot cavity, we need to transform the noise matrix as $\mathbb{M}' = \mathbb{M}R(\varphi)$. In this case, the term $M'_{11} \cos \xi_B + M'_{21} \sin \xi_B$ is the noise derived from the fluctuation in the amplitude quadrature, and the term $M'_{21} \cos \xi_B + M'_{22} \sin \xi_B$ is the noise derived from the phase quadrature.

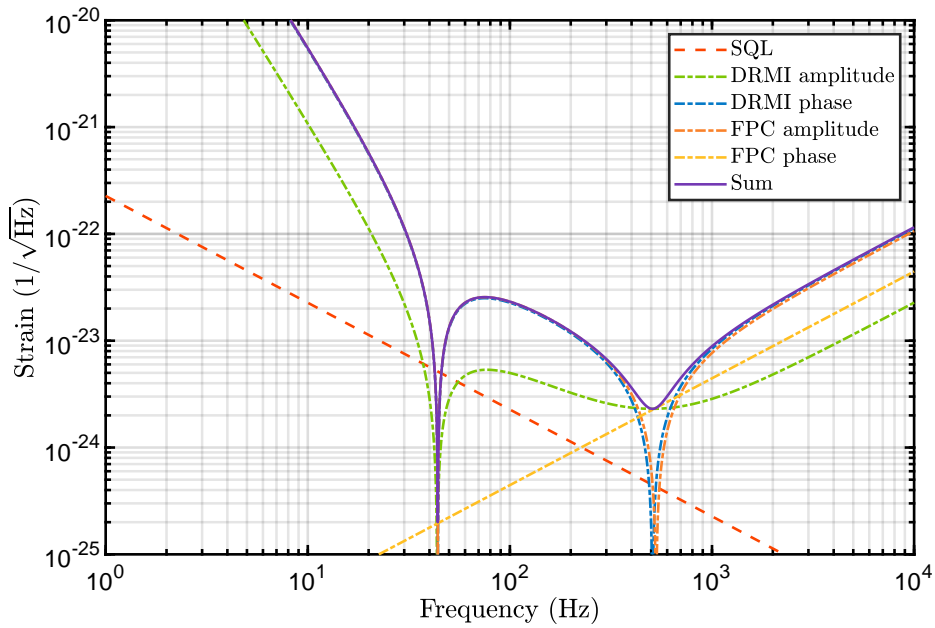


Fig. 3.16: Sensitivity of the DRMI with the detuning of the SRC or the sensitivity of the detuned Fabry-Perot cavity. Output light field fluctuation is measured with the contrast defect, and the parameter is set to $\Delta = 5\gamma$.

Fig. 3.16 shows the sensitivity for $\Delta = 5\gamma$ by dividing the terms derived from the amplitude and phase quadratures. We calculated the DRMI with the detuned SRC and detuned Fabry-Perot cavity, respectively. The transformation $\mathbb{M} \rightarrow \mathbb{M}'$ does not affect sensitivity, and the sum spectral density of the term derived from the amplitude and phase quadratures is identical for each case. For the Fabry-Perot cavity, both dips are formed at frequencies where the term derived from the amplitude quadrature is 0. In addition, phase fluctuations, such as the frequency noise of the incident laser on the Fabry-Perot cavity, become the noise proportional to f^1 [115].

Although it is challenging to demonstrate the case of beating the (free-mass) SQL based on an optical spring, we can observe the reduction in the classical noise when the classical light field fluctuations entering the interferometer can be regarded as white noise [116]. This study demonstrated classical back-action eva-

sion via optical spring by injecting classical amplitude noise into a Fabry-Perot cavity. As discussed, the DRMI can be considered to be equivalent to the Fabry-Perot cavity by formulating the appropriate analogy, implying that noise reduction using an optical spring can be implemented in the interferometer configuration of an actual gravitational wave detector. Moreover, we demonstrate that the intracavity loss causes a difference in the resonant frequency of the optical spring and frequency of the lower side dip in the spectrum.

3.5 Application of intracavity squeezing for the gravitational wave detector

Intracavity squeezing, or internal squeezing, is a technique of squeezing inside a cavity where signals are generated, amplified, or extracted. Intracavity squeezing causes vacuum field squeezing or anti-squeezing and signal amplification or attenuation simultaneously; thus, sensitivity improves when vacuum field squeezing is greater than signal attenuation. Intracavity squeezing without cavity detuning can increase the effective bandwidth over a wide bandwidth. Considering detuning, the optical spring generated in the interferometer can be enhanced by the signal amplification effect of intracavity squeezing. In this section, we derive the sensitivity of the DRMI with intracavity squeezing and discuss its advantages compared to other techniques, e.g., input squeezing.

3.5.1 Broadband bandwidth enhancement based on intracavity squeezing

When OPA occurs in a cavity where carriers are inside, in addition to the squeezing effect on light field fluctuations, intracavity power increases or decreases. Furthermore, when the cavity is detuned, the quadratures of the intracavity carriers are converted to each other. The basic configuration of gravitational wave detectors with intracavity squeezing is a system in which the squeezer is inserted into the SRC with no carriers, as shown in Fig. 3.17. When the squeezing angle is set to $\theta = 0$, \mathbf{d} in Eq. (3.97) is modified to $\mathbf{d} = e^{i\alpha s} R(\phi) S(s) \mathbf{f}$ with $S(s) = \text{diag}(s, 1/s)$, the output light field fluctuation can be written as

$$\mathbf{b} = \left[-rI + t^2 e^{2i\alpha} [I - r e^{2i\alpha} R(\phi) S(s) P(\kappa, 0) R(\phi)]^{-1} R(\phi) S(s) P(\kappa, 0) R(\phi) \right] \mathbf{a} \\ + t e^{i\alpha} \frac{\sqrt{2\kappa}}{h_{\text{SQL}}} [I - r e^{2i\alpha} R(\phi) S(s) P(\kappa, 0) R(\phi)]^{-1} R(\phi) S(s) \begin{pmatrix} 0 \\ 1 \end{pmatrix} h(\Omega). \quad (3.132)$$

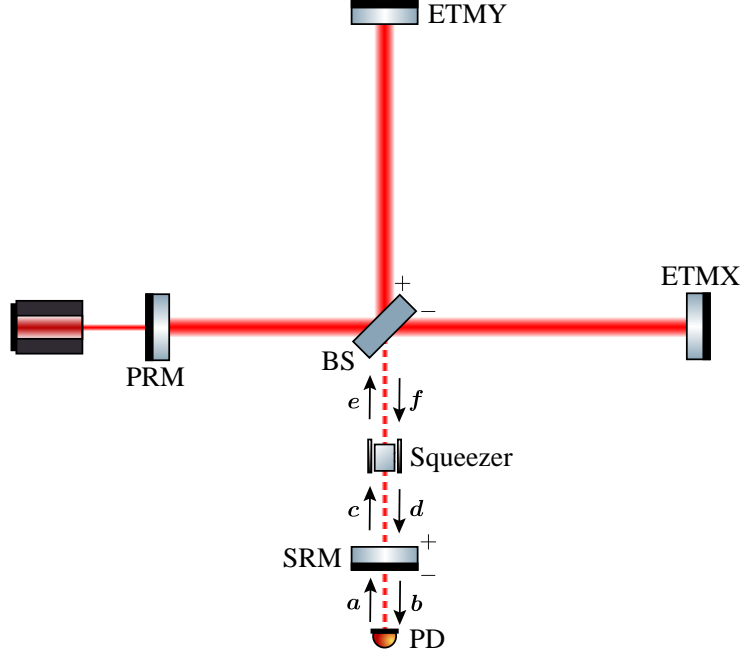


Fig. 3.17: Schematic of intracavity squeezing for the DRMI. The pump light is injected from the BS to the SRM, and the light field is not squeezed in the path from the SRM to the BS.

By assuming that the SRC is in resonance ($\phi = 0$), we obtain

$$\mathbf{b} = \left[-rI + \frac{t^2 e^{2i\alpha}}{(1 - rse^{2i\alpha})(1 - rs^{-1}e^{2i\alpha})} \begin{pmatrix} s - re^{2i\alpha} & 0 \\ -s^{-1}\kappa & s^{-1} - re^{2i\alpha} \end{pmatrix} \right] \mathbf{a} + \frac{te^{i\alpha}}{(1 - rse^{2i\alpha})(1 - rs^{-1}e^{2i\alpha})} \frac{\sqrt{2\kappa}}{h_{\text{SQL}}} \begin{pmatrix} 0 \\ s^{-1} - re^{2i\alpha} \end{pmatrix} h(\Omega). \quad (3.133)$$

By approximating that $T = t^2$, α and $u = \log s$ are much smaller than unity, we obtain

$$\mathbf{b} \simeq e^{2i\beta_{\text{IS}}} \begin{pmatrix} \frac{\gamma + \Sigma + i\Omega}{\gamma - \Sigma + i\Omega} & 0 \\ -\frac{\gamma + \Sigma + i\Omega}{\gamma - \Sigma + i\Omega} \mathcal{K}_{\text{IS}} & \frac{\gamma - \Sigma - i\Omega}{\gamma + \Sigma - i\Omega} \end{pmatrix} \mathbf{a} + e^{i\beta_{\text{IS}}} \frac{\sqrt{2\mathcal{K}_{\text{IS}}}}{h_{\text{SQL}}} \begin{pmatrix} 0 \\ 1 \end{pmatrix} h(\Omega), \quad (3.134)$$

where $\gamma = Tc/(4(L + l))$ denotes the cavity decay rate and $\Sigma = uc/(2(L + l))$ denotes the squeezing decay rate. We defined effective phase delay $\beta_{\text{IS}} = \arctan(-\Omega/(\gamma + \Sigma))$ and effective coupling constant $\mathcal{K}_{\text{IS}} = \gamma\iota/(\Omega^2((\gamma + \Sigma)^2 + \Omega^2))$. Intracavity squeezing changes the effective cavity decay rate to $\gamma + \Sigma$ and increases the DC signal by a factor of $\gamma/(\gamma + \Sigma)$. Moreover, frequency-dependent squeezing is performed for the vacuum field. The sensitivity can be calculated as

$$S_h = \frac{h_{\text{SQL}}^2}{2} \left(s_{\text{IS}}^2 \mathcal{K}_{\text{IS}} + \frac{1}{s_{\text{IS}}^2 \mathcal{K}_{\text{IS}}} \right), \quad (3.135)$$

where $s_{\text{IS}}^2 = ((\gamma + \Sigma)^2 + \Omega^2)/((\gamma - \Sigma)^2 + \Omega^2)$ denotes the effective squeezing factor.

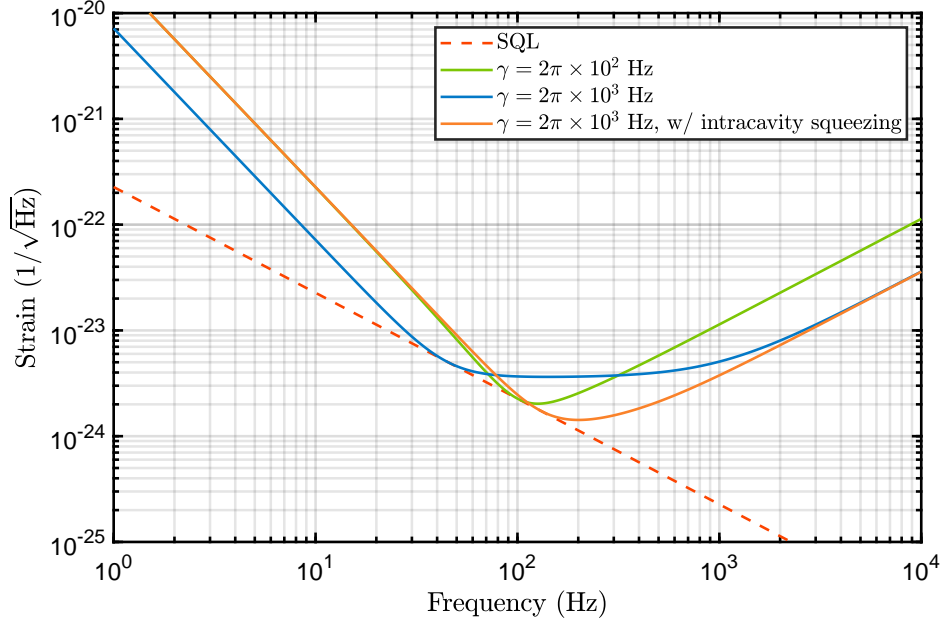


Fig. 3.18: Sensitivity of the intracavity-squeezed DRMI. The parameter is set to $\iota = 2 \times (2\pi \times 10^2)^3 \text{ Hz}^3$ for all the cases.

Intracavity squeezing without cavity detuning can enhance the effective bandwidth of the interferometer by combining with low-finesse SRC. Sensitivity curves are shown in Fig. 3.18. The green, blue, and orange lines present the cases of high-finesse SRC, low-finesse SRC, and low-finesse SRC with intracavity squeezing. We set the squeezing decay rate as $\Sigma = a(1 - \sqrt{1/a})\gamma$, where a denotes the multiplying factor for the cavity decay rate, to ensure that the sensitivity of the low-frequency band with intracavity squeezing is consistent with the high finesse case. As observed from the comparison of radiation pressure noise, intracavity squeezing increases the effective finesse. However, the sensitivity of the high-frequency band does not deteriorate, indicating that the effective bandwidth increases.

A comparison of the shot noise is shown in Fig. 3.19. As denoted in Eq. (3.100), there is a trade-off relationship between the shot noise level and bandwidth with respect to the finesse of the SRC. Intracavity squeezing can modify this relationship. The peak sensitivity and bandwidth product can be written as

$$\lim_{\Omega \rightarrow 0} \frac{2s_{\text{IS}}^2 \mathcal{K}_{\text{IS}}}{h_{\text{SQL}}^2} \times \gamma = \frac{mL^2 \iota}{2\hbar} \times \frac{1}{(1 - \sigma)^2}, \quad (3.136)$$

where $\sigma = \Sigma/\gamma$ denotes the normalized squeezing decay rate. If we set $\sigma = 1 - \sqrt{1/a}$, the sensitivity-bandwidth limit is improved by the factor of a .

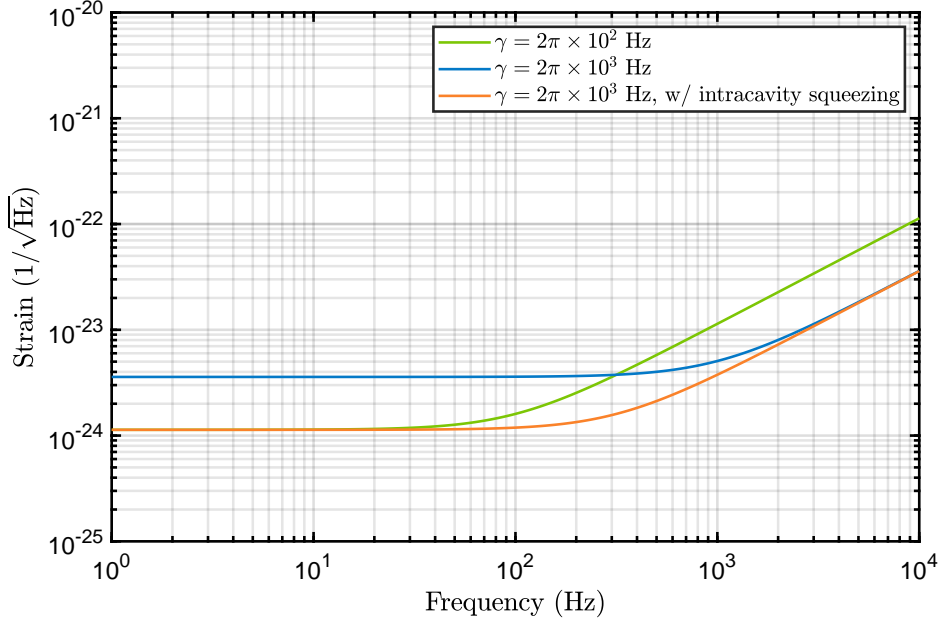


Fig. 3.19: Sensitivity of the intracavity-squeezed DRMI determined by the shot noise. The parameters are set to the same values as in Fig. 3.18.

Intracavity squeezing can increase the effective bandwidth but cannot beat the SQL. Practically, it is necessary to consider the optical losses caused by the installation of the nonlinear optical crystal in the cavity, which may limit the optical design of the main interferometer. It has been experimentally confirmed that the product of peak sensitivity and bandwidth can be improved by intracavity squeezing [117].

3.5.2 Signal amplification system with a stiff optical spring

In the last subsection, we discussed the intracavity-squeezed DRMI without cavity detuning. Intracavity squeezing produces not only frequency-dependent squeezing but also changes the properties of the cavity, including the optomechanical coupling constant. Thus, we consider detuning the SRC to generate an optical spring. The intracavity squeezing enhances the optical spring generated in this system, which makes it possible to generate a stiff optical spring with a high resonance frequency without increasing the intra-arm power [21].

By solving Eq. (3.132) as $S(s) \rightarrow S(u, \theta)$ and $\phi \neq 0$, the input-output relation can be calculated as

$$\mathbf{b} = \frac{1}{C'} [\mathbb{A}' \mathbf{a} + \mathcal{H}' h(\Omega)], \quad (3.137)$$

with

$$C' = re^{2i\alpha} + \frac{1}{r}e^{-2i\alpha} - \frac{1}{2} \left[(s + \frac{1}{s})(2 \cos 2\phi + \kappa \sin 2\phi) - (s - \frac{1}{s})\kappa \sin 2(\phi + \theta) \right], \quad (3.138)$$

$$A'_{11} = -2 \cos 2\alpha - \frac{1}{4} (s - \frac{1}{s})\kappa (\frac{1}{r} - r + (r + \frac{1}{r}) \cos 2\phi) \sin 2\theta + \frac{1}{4} (r + \frac{1}{r})(s + \frac{1}{s})(2 \cos 2\phi + \kappa \sin 2\phi) - \frac{1}{4} (s - \frac{1}{s})(2(r - \frac{1}{r}) + (r + \frac{1}{r})\kappa \sin 2\phi) \cos 2\theta, \quad (3.139)$$

$$A'_{12} = \frac{1}{4} (r - \frac{1}{r}) \left[2(s + \frac{1}{s}) \sin 2\phi + \kappa (s + \frac{1}{s} - (s - \frac{1}{s}) \cos 2\theta)(1 - \cos 2\phi) - (s - \frac{1}{s}) \sin 2\theta(2 + \kappa \sin 2\phi) \right], \quad (3.140)$$

$$A'_{21} = \frac{1}{4} (\frac{1}{r} - r) \left[(s - \frac{1}{s})\kappa \cos 2\theta - (s + \frac{1}{s})\kappa(1 + \cos 2\phi) + (s - \frac{1}{s})(\kappa \cos 2(\theta + \phi) + 2 \sin 2\theta) + 2(s + \frac{1}{s}) \sin 2\phi \right], \quad (3.141)$$

$$A'_{22} = -2 \cos 2\alpha - \frac{1}{4} (s - \frac{1}{s})\kappa (r - \frac{1}{r} + (r + \frac{1}{r}) \cos 2\phi) \sin 2\theta + \frac{1}{4} (r + \frac{1}{r})(s + \frac{1}{s})(2 \cos 2\phi + \kappa \sin 2\phi) - \frac{1}{4} (s - \frac{1}{s})(2(\frac{1}{r} - r) + (r + \frac{1}{r})\kappa \sin 2\phi) \cos 2\theta, \quad (3.142)$$

$$\mathcal{H}' = t \frac{\sqrt{2\kappa}}{h_{\text{SQL}}} \begin{pmatrix} -e^{i\alpha} \sin \phi + \frac{1}{2r} e^{-i\alpha} [-(s + \frac{1}{s}) \sin \phi + (s - \frac{1}{s}) \sin(2\theta + \phi)] \\ -e^{i\alpha} \cos \phi + \frac{1}{2r} e^{-i\alpha} [(s + \frac{1}{s}) \cos \phi - (s - \frac{1}{s}) \cos(2\theta + \phi)] \end{pmatrix}. \quad (3.143)$$

Furthermore, a similar approximation in Eq. (3.134) yields

$$\mathbf{b} = \frac{1}{C'} [\mathbb{M}' \mathbf{a} + \mathcal{D}' h(\Omega)], \quad (3.144)$$

with

$$C' = \Omega^2 [(\gamma + i\Omega)^2 + \Delta^2 - \Sigma^2] + (-\Delta + \Sigma \sin 2\theta)\iota/2, \quad (3.145)$$

$$M'_{11} = \Omega^2 [\gamma^2 + \Omega^2 - \Delta^2 + \Sigma^2 + 2\Sigma\gamma \cos 2\theta] + (\Delta - \Sigma \sin 2\theta)\iota/2, \quad (3.146)$$

$$M'_{12} = 2\gamma [-\Delta + \Sigma \sin 2\theta] \Omega^2, \quad (3.147)$$

$$M'_{21} = 2\gamma [\Delta + \Sigma \sin 2\theta] \Omega^2 - \gamma\iota, \quad (3.148)$$

$$M'_{22} = \Omega^2 [\gamma^2 + \Omega^2 - \Delta^2 + \Sigma^2 - 2\Sigma\gamma \cos 2\theta] + (\Delta - \Sigma \sin 2\theta)\iota/2, \quad (3.149)$$

$$\mathcal{D}' = \frac{\sqrt{2\iota\gamma}}{h_{\text{SQL}}} \begin{pmatrix} (-\Delta + \Sigma \sin 2\theta)\Omega \\ (\gamma + i\Omega - \Sigma \cos 2\theta)\Omega \end{pmatrix}. \quad (3.150)$$

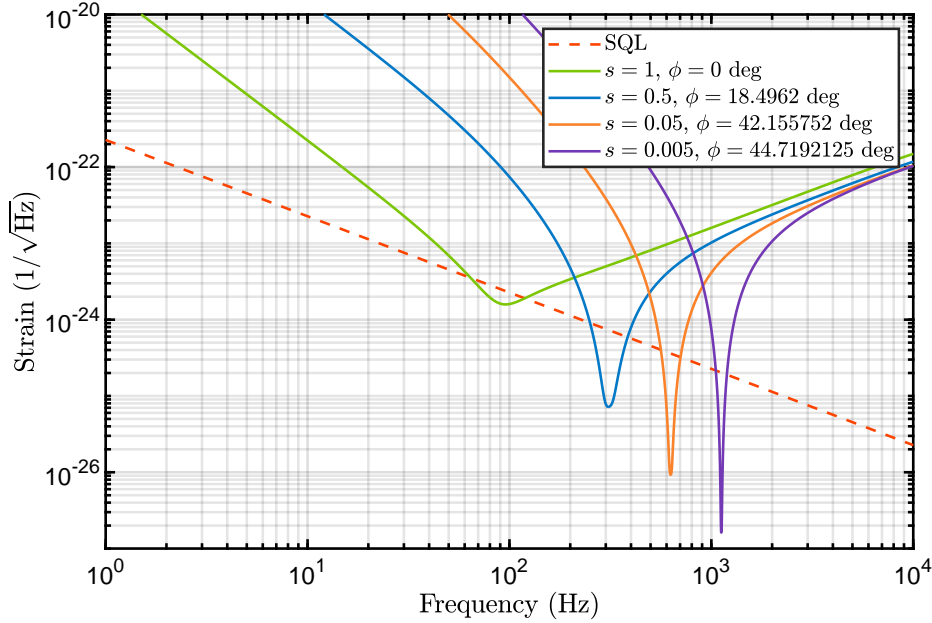


Fig. 3.20: Sensitivity of the intracavity-squeezed DRMI with detuned SRC. The parameters are set to $\theta = 0$, $r = \sqrt{1 - 4L\gamma/c}$ and $\xi_B = \pi/4$. The lower limit of the vertical axis is changed to 10^{-27} .

The sensitivity curve with $\theta = 0$ is shown in Fig. 3.20. Strong squeezing shifts the dip to the high-frequency band. ϕ is adjusted to match the frequencies of the optical spring and optical resonance, which is $\pi/4$ in the limit of $s \rightarrow 0$. Eq. (3.138) is used for the plots as it requires significant detuning. The homodyne angle is set to $\pi/4$ because the relative angle of the signal becomes $\pi/4$ with $s \rightarrow 0$.

The resonance frequency of the optical spring is shifted to a higher frequency band without changing the input power, resulting from intracavity squeezing that modifies the optomechanical properties of the cavity. In other words, the dip is formed by an optical spring enhanced by the intracavity signal amplification. The enhanced optical spring can achieve narrow but extremely good sensitivity at a certain frequency compared to input squeezing and other techniques. The dip frequency can be shifted by changing the cavity detuning and squeezing factor; thus, if the frequency of the dip matches the theoretically predicted high-frequency gravitational wave signals, such as those emitted from supernovae or binary neutron star post-merger remnants, we can detect these events with good sensitivity.

The depth and linewidth of the dip can be adjusted by tuning the squeezing angle θ . We calculate the case where the transfer matrices from BS to SRM and from SRM to BS are equivalent with $U = R(\phi/2)S(u, \theta)R(\phi/2)$. In other words,

the input-output relation is modified as

$$\mathbf{b} = \left[-rI + t^2 e^{2i\alpha} [I - r e^{2i\alpha} U P U]^{-1} U P U \right] \mathbf{a} + t e^{i\alpha} \frac{\sqrt{2\mathcal{K}}}{h_{\text{SQL}}} [I - r e^{2i\alpha} U P U]^{-1} U \begin{pmatrix} 0 \\ 1 \end{pmatrix} h(\Omega). \quad (3.151)$$

The sensitivity curves are shown in Fig. 3.21. By appropriately selecting θ , a

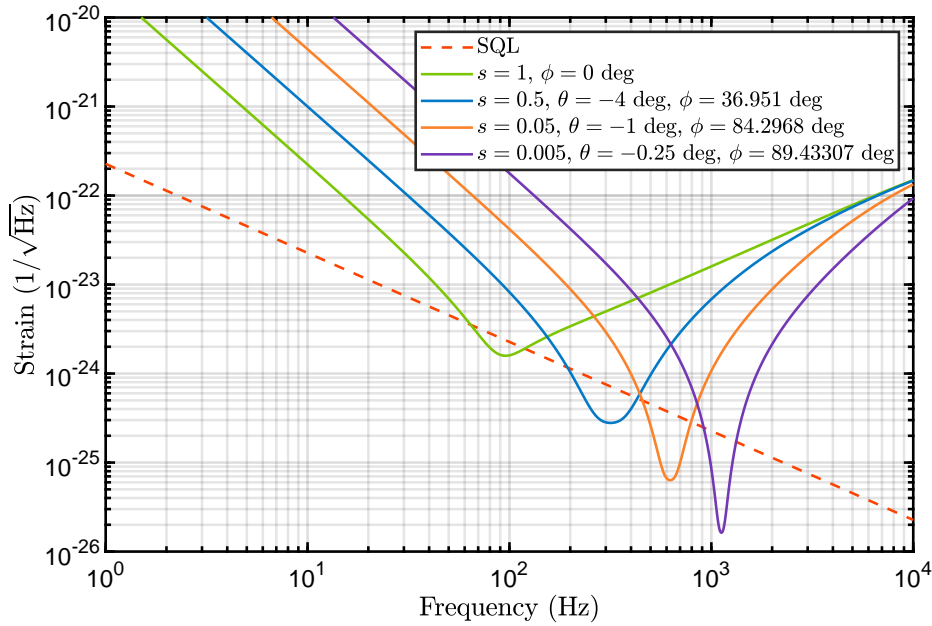


Fig. 3.21: Sensitivity of the intracavity-squeezed DRMI with detuned SRC. The parameters are set to $r = \sqrt{1 - 4L\gamma/c}$ and $\xi_B = \pi/4$. The lower limit of the vertical axis is changed to 10^{-26} .

broadband dip can be formed in the high-frequency band while minimizing sensitivity deterioration in the low-frequency band.

Although performing frequency-dependent cavity detuning is challenging, it is possible to provide the frequency-dependent squeezing angle using a filter cavity. In particular, the resonant frequency of the optical spring changes as the squeezing angle varies. Further sensitivity improvement may be possible with intracavity squeezing by achieving an ideal frequency-dependent squeezing angle [118].

In this section, we discussed the enhancement of the optical spring based on intracavity squeezing, and this technique can also be applied to various optomechanical systems. As intracavity squeezing changes the properties of the cavity, it is possible to realize optomechanical systems that cannot be achieved with conventional techniques. In particular, intracavity squeezing can cool optomechanical

oscillators in the unresolved sideband regime to the ground state^{*9} [22–24]. There are many theoretical studies related to the impact of intracavity squeezing on optomechanical systems [119–132], and experimental verification is expected to be realized.

3.6 Summary of this chapter

In this chapter, we calculated the sensitivity of the gravitational wave detectors, which is determined by the quantum noise. The Michelson interferometer is the most elementary configuration of an interferometric gravitational wave detector. However, it is essential to enhance the laser light power and signal response with cavities because shot noise limits the sensitivity of the Michelson interferometer. In addition, the optical spring, which can be generated by detuning the signal recycling cavity, can beat the free-mass SQL. This phenomenon is produced by the reduction in the SQL owing to the optical spring generated in the arm. In addition, the optical spring can be enhanced by intracavity squeezing to amplify high-frequency gravitational waves.

Theoretical results indicate that intracavity squeezing can significantly improve sensitivity. Nevertheless, it is essential to conduct a verification-of-principle experiment before implementing intracavity squeezing in an actual large-scale gravitational wave detector. Then, is it reasonable to conduct a verification experiment with the DRMI? To operate the DRMI, it is necessary to control the three degrees of freedom of the Michelson interferometer, PRC, and SRC. Moreover, as discussed in the next chapter, the OPA requires the control of at least three degrees of freedom. In other words, the system shown in Fig. 3.17 is a complex system that requires at least six degrees of freedom of control. Although the PRC can be removed in principle because it only increases the input light power, it becomes challenging to generate an observable optical spring with a weak radiation pressure force acting on the test mass. In addition, actual Michelson interferometers have non-negligible contrast errors, making it difficult to construct an SRC with high finesse.

Therefore, we focus on the equivalence of the DRMI and Fabry-Perot cavity. As shown in Fig. 3.16, the two interferometers are equivalent in terms of quantum noise. We can predict that the enhancement of the optical spring based on intracavity squeezing can be demonstrated in a Fabry-Perot cavity. However, we must consider the requirements to assume that it is equivalent to the optical spring generated in the DRMI.

^{*9} See App.D.

Chapter 4

Signal amplification experiment based on the OPA scheme

The signal amplification system discussed in Sec. 3.5.2 is a promising scheme to improve the sensitivity of gravitational wave detectors in the high-frequency band. The essence of this system is the enhancement of the optical spring based on intracavity squeezing. The experimental goal of this thesis is to observe an optical spring enhanced by the signal amplification effect. We should measure the impact of nonlinear optical effects on the optical spring. Hence, we considered experimenting with the Fabry-Perot cavity, which is an experimentally tractable interferometer compared with the actual interferometer configuration of the gravitational wave detector, e.g., dual recycling Michelson interferometer (DRMI). This chapter discusses an experimental method for performing proof-of-principle experiments on the signal amplification system using a Fabry-Perot cavity and the results of experiments with the optical parametric amplification (OPA) scheme.

4.1 Equivalency of the optical spring in the DRMI and Fabry-Perot cavity

As light possesses momentum, the test mass receives a radiation pressure force F_{rad} when it reflects the laser light. If the radiation pressure force is proportional to the displacement of the test mass, a spring comprising light is generated. Suppose that the displacement of a test mass fluctuates by $\delta x(\Omega)$ when a mirror reflects the light field and its fluctuation $\mathbf{A} + \mathbf{a}(\Omega)$. From Eq. (3.44), the radiation pressure fluctuation can be divided into terms proportional to $\delta x(\Omega)$ and other terms as

$$\delta F_{\text{rpf}}(\Omega) = 2\hbar k_0 (A_1 a_1(\Omega) + A_2 a_2(\Omega)) = -K_{\text{opt}}(\Omega) \delta x(\Omega) + \delta F_{\text{qrp}}(\Omega), \quad (4.1)$$

where $K_{\text{opt}}(\Omega)$ denotes the complex optical spring constant and $\delta F_{\text{qp}}(\Omega)$ denotes the quantum radiation pressure fluctuation^{*1}. Here, we need to consider the radiation pressure fluctuation response to the slight displacement of the mirror rather than the ponderomotive squeezing resulting from the mirror reflection. When the light field fluctuation $\mathbf{a}(\Omega)$ is reflected by the test mass, the reflected electric field fluctuation $\mathbf{b}(\Omega)$ is obtained as

$$\mathbf{b}(\Omega) = \mathbf{a}(\Omega) + 2k_0 A_0 \mathbf{n}_{A\perp} \delta x(\Omega) \quad (4.2)$$

from the Fourier transform of Eq. (3.43). Here, $\mathbf{n}_{A\perp}$ denotes the unit vector perpendicular to the carrier light.

4.1.1 Optical spring in the DRMI with intracavity squeezing

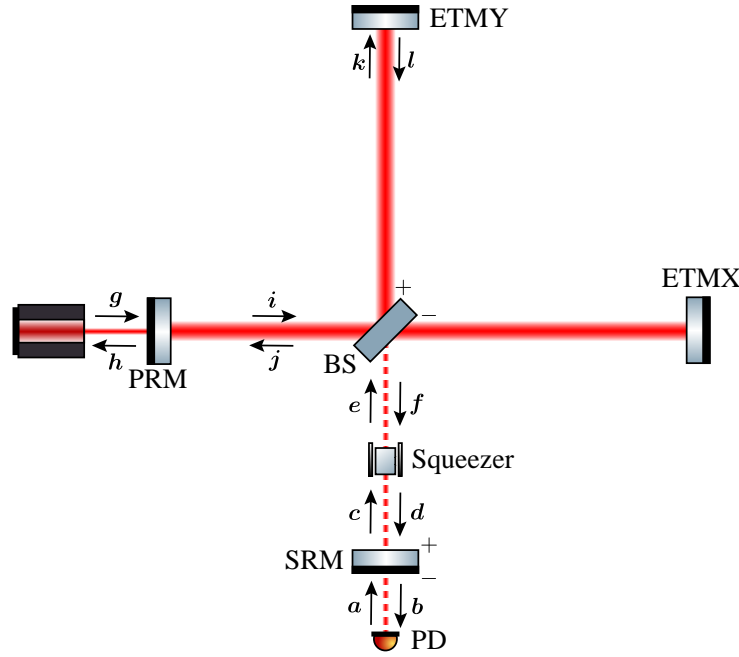


Fig. 4.1: Schematic of intracavity squeezing for the DRMI. Only the end mirror of the y-arm is supposed to work as a test mass. The pump light is injected from the beam splitter to the signal recycling mirror, and the light field is not squeezed in the path from the SRM to the BS.

Let us consider an optical spring generated in the DRMI with intracavity squeezing as considered in Sec. 3.5.2. The schematic of DRMI is shown in Fig. 4.1. We calculate the radiation pressure fluctuation that is acting on the end mirror of the y arm. The light field is squeezed in the path from the beam splitter (BS) to the signal recycling mirror (SRM) in the signal recycling cavity (SRC). We set the

^{*1} See App. D.

squeezing angle θ as 0 when the light field is squeezed. In other words, the phase of the light field does not change in the path from the SRM to the BS and from the BS to the nonlinear optical crystal (NLC); however, the phase changes by 2ϕ in the path from the NLC to the SRM. Suppose that the SRC length is sufficiently shorter than the arm length and the phase delay in the SRC is negligible. Let L be the arm length, $\alpha = -L\Omega/c$ be the phase delay during propagation in the arm, r^2 and $t^2 = T$ be the power reflectivity and transmissivity of the SRM, and $s = e^u$ be the squeezing factor. The input-output relation can be written as

$$\begin{aligned} b &= -ra + td, \quad c = ta + rd, \quad d = R(2\phi)S(u, \theta)f, \quad e = c, \\ f &= e^{2i\alpha}e + e^{i\alpha}k_0I_0 \begin{pmatrix} 0 \\ 1 \end{pmatrix} \delta x(\Omega), \quad k = \frac{1}{\sqrt{2}}e^{i\alpha}(e + i). \end{aligned} \quad (4.3)$$

Assume that the fluctuation of input power and radiation pressure fluctuation caused by the vacuum field can be neglected ($a = 0, g = 0$). From Eq. (4.1), the complex optical spring constant $K_{\text{opt}}(\Omega)$ can be written as

$$K_{\text{opt}}(\Omega)\delta x(\Omega) = -2\hbar k_0 K_1 k_1 = -e^{i\alpha}\hbar k_0 I_0 e_1, \quad (4.4)$$

and e can be calculated as

$$\begin{aligned} e &= k_0 I_0 r e^{i\alpha} [I - r e^{2i\alpha} R(2\phi)S(u, \theta)]^{-1} R(2\phi)S(u, \theta) \begin{pmatrix} 0 \\ 1 \end{pmatrix} \delta x(\Omega) \\ &= \frac{k_0 I_0}{r e^{2i\alpha} + r^{-1} e^{-2i\alpha} - 2 \cos 2\phi \cosh u} \\ &\quad \times \begin{pmatrix} -\sin 2\phi \cosh u + \sin(2\phi + 2\theta) \sinh u \\ -r e^{2i\alpha} + \cos 2\phi \cosh u + \cos(2\phi + 2\theta) \sinh u \end{pmatrix} \delta x(\Omega). \end{aligned} \quad (4.5)$$

Therefore, by approximating that α , ϕ , and u are much smaller than unity, we obtain

$$\begin{aligned} K_{\text{opt}}(\Omega) &\simeq \frac{k_0 P_I}{L} \frac{\Delta - \Sigma \sin 2\theta}{(\gamma + i\Omega)^2 + \Delta^2 - \Sigma^2} \\ &= \frac{k_0 P_I}{L\gamma} \frac{\delta - \sigma \sin 2\theta}{(1 + i\Omega/\gamma)^2 + \delta^2 - \sigma^2}, \end{aligned} \quad (4.6)$$

where $P_I = \hbar\omega_0 I_0^2/2$ denotes the light power at the BS, $\gamma = Tc/(4L)$ denotes the decay rate of the SRC, $\Delta = \phi c/L$ denotes the detuning of the SRC, $\delta = \Delta/\gamma$ denotes the normalized cavity detuning, $\Sigma = uc/(2L)$ denotes the squeezing decay rate, and $\sigma = \Sigma/\gamma$ denotes the normalized squeezing decay rate. If the frequency band under consideration is sufficiently lower than the cavity decay rate ($\Omega \ll \gamma$), we obtain the approximation formula:

$$\begin{aligned} K_{\text{opt}}(\Omega) &\simeq \frac{k_0 P_I}{L\gamma} \frac{\delta - \sigma \sin 2\theta}{1 + \delta^2 - \sigma^2} \left[1 - i \frac{2}{\gamma(1 + \delta^2 - \sigma^2)} \Omega \right] \\ &:= k_{\text{opt}} + i\Gamma_{\text{opt}}\Omega, \end{aligned} \quad (4.7)$$

where k_{opt} denotes the optical spring constant, and Γ_{opt} denotes the optical damping constant.

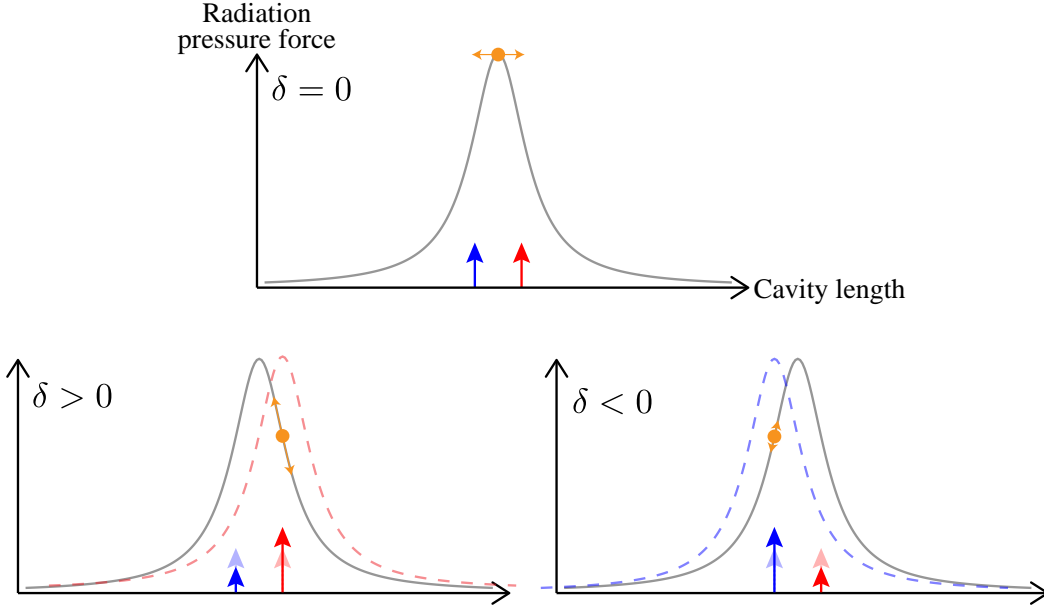


Fig. 4.2: Qualitative illustration of an optical spring. The orange dots represent the operating point, red and blue dotted curves represent the response of the cavity at the operating point, and the value of normalized cavity detuning δ determines whether the vibration, represented by the orange arrow, is amplified or damped. The blue and red arrows represent the upper and lower sidebands, respectively.

The qualitative behavior of the optical spring without intracavity squeezing ($\sigma = 0$) is illustrated in Fig. 4.2. The optical spring constant corresponds to the slope of the radiation pressure force for the cavity length. When $\delta = 0$, the radiation pressure force does not change for slight changes in the cavity length; thus, $k_{\text{opt}} = 0$. When $\delta > 0$, the radiation pressure force decreases for slight positive changes in cavity length, and light produces a restoring force, resulting in a positive optical spring ($k_{\text{opt}} > 0$). When $\delta < 0$, an optical anti-spring ($k_{\text{opt}} < 0$) is produced. In contrast, the optical damping constant corresponds to the amount of energy flow caused by the radiation pressure force. When the mirror fluctuates at an angular frequency of Ω , upper and lower sidebands of angular frequency $\omega_0 + \Omega$ and $\omega_0 - \Omega$, respectively, are generated. When $\delta = 0$, the cavity equally amplifies the sidebands; thus, $\Gamma_{\text{opt}} = 0$. When $\delta > 0$, the lower sideband is more amplified than the upper sideband, and the oscillation of the mirror deprives the energy of light. In this case, the mirror receives positive work from the light, and the oscillation of the mirror is amplified, resulting in optical anti-damping ($\Gamma_{\text{opt}} < 0$). When $\delta < 0$, the mirror receives negative work from the light, resulting in optical damping ($\Gamma_{\text{opt}} > 0$). The real and imaginary components of the complex optical spring constant have opposite signs for any cavity detuning, implying that the optical spring generated with a single carrier is always unstable. In particular, when a me-

chanical oscillator with a high mechanical Q factor is bound by an optical spring, the entire system can become unstable owing to optical anti-damping [133–135].

There are several ways to avoid this instability. A stable optical spring can be generated using multiple carrier lights [136] as the optical spring and damping constant exhibit different functional dependencies on cavity detuning. Moreover, an optical spring can be generated without using an optical cavity as long as the radiation pressure force is proportional to the displacement of the mirror [137]. In this case, the optical system does not produce optical damping because the amplification factors of the upper and lower sidebands are not different. Another method is to use the photothermal effect [138, 139]. The real and imaginary components of the optical spring can be converted to each other using the photothermal effect, which is detailed in the next chapter.

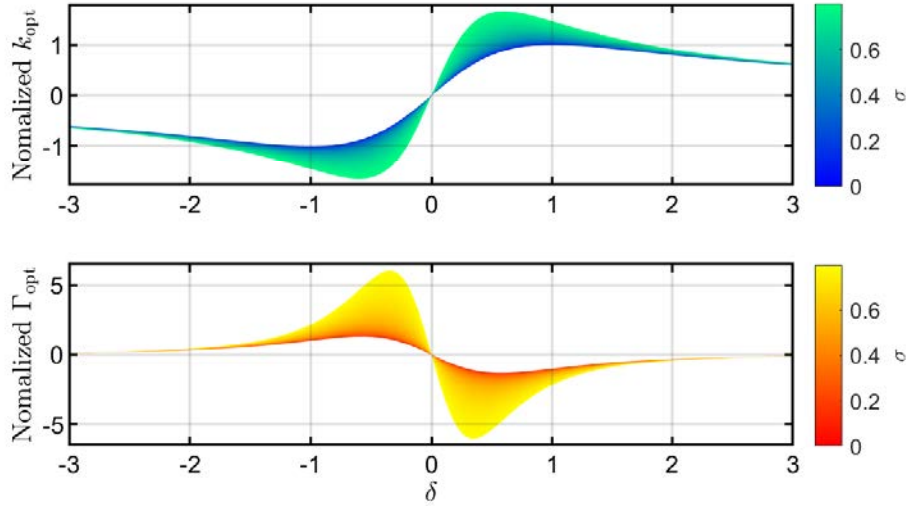


Fig. 4.3: Optical spring constant k_{opt} and optical damping constant Γ_{opt} with intracavity squeezing. We set the squeezing angle as $\theta = 0$. Each vertical axis is normalized to be 1 and -1 when $\delta = 1$ and $\sigma = 0$, respectively.

Figures 4.3 and 4.4 show the optical spring and damping constant for $\sigma > 0$. Fig. 4.3 shows the case where the squeezing angle is $\theta = 0$. The optical spring constant increases with an increase in σ , reflecting signal amplification based on intracavity squeezing. Moreover, k_{opt} and Γ_{opt} are odd functions for δ . Fig. 4.4 shows the case where the squeezing angle is $\theta = -\pi/4$. k_{opt} and Γ_{opt} are not symmetric for δ ; therefore, an optical spring is generated even when $\delta = 0$. We also note that k_{opt} and Γ_{opt} always exhibit opposite signs for any parameter.

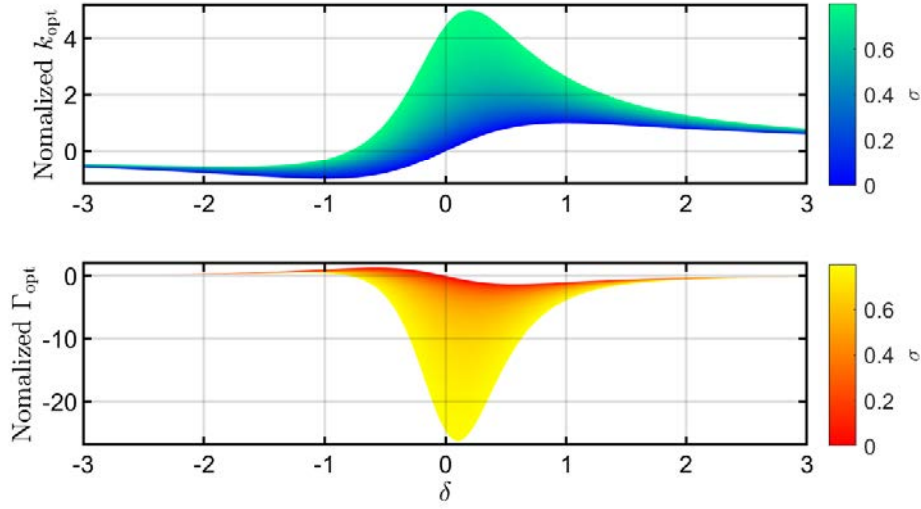


Fig. 4.4: Optical spring constant k_{opt} and optical damping constant Γ_{opt} with intracavity squeezing. We set the squeezing angle as $\theta = -\pi/4$. The vertical axis is normalized in the same manner as in Fig. 4.3.

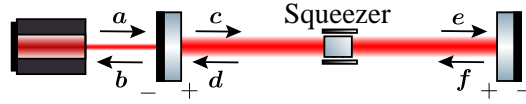


Fig. 4.5: Schematic of intracavity squeezing for the Fabry-Perot cavity. Only the end mirror is supposed to work as a test mass.

4.1.2 Optical spring in the Fabry-Perot cavity with intracavity squeezing

Let us consider the optical spring generated in the Fabry-Perot cavity with intracavity squeezing, as shown in Fig. 4.5. The carrier light with phase quadrature of 0 ($A_1 = A_0$, $A_2 = 0$) is incident on the cavity. The squeezing angle is set by supposing that the phase of the light field changes by 2ϕ on the path from the NLC to the input mirror, as for DRMI. However, as described below, the squeezing angle does not correspond to it in the DRMI. The squeezing angle, in this case, is denoted as θ_{inc} . Let L be the one-way length of the cavity, $\alpha = -L\Omega/c$ be the phase delay, r^2 and $t^2 = T$ be the power reflectivity and transmissivity of the input mirror, respectively, and $s = e^u$ be the squeezing factor. The input-output

relation of the carrier light can be written as

$$\begin{aligned} B &= -rA + tD, \quad C = ta + rd, \\ D &= R(2\phi)S(u, \theta_{\text{inc}})F, \quad E = C, \quad F = E. \end{aligned} \quad (4.8)$$

The intracavity amplitude E can be calculated as

$$\begin{aligned} E &= t[I - rR(2\phi)S(u, \theta_{\text{inc}})]^{-1}A \\ &= \frac{2}{t} \frac{1}{1 + \delta^2 - \sigma^2} \begin{pmatrix} 1 + \sigma \cos 2\theta_{\text{inc}} & -\delta + \sigma \sin 2\theta_{\text{inc}} \\ \delta + \sigma \sin 2\theta_{\text{inc}} & 1 - \sigma \cos 2\theta_{\text{inc}} \end{pmatrix} A, \end{aligned} \quad (4.9)$$

where $\gamma = Tc/(4L)$ denotes the cavity decay rate, $\Delta = \phi c/L$ denotes cavity detuning, $\delta = \Delta/\gamma$ denotes the normalized cavity detuning, $\Sigma = uc/(2L)$ denotes the squeezing decay rate, and $\sigma = \Sigma/\gamma$ denotes the normalized squeezing decay rate. The intracavity power P_E is

$$P_E = \frac{4}{T} \frac{(1 + \sigma \cos 2\theta_{\text{inc}})^2 + (\delta + \sigma \sin 2\theta_{\text{inc}})^2}{(1 + \delta^2 - \sigma^2)^2} P_A. \quad (4.10)$$

However, the signal vector generated by the fluctuations of the test mass is not directed in the phase quadrature because the intracavity carrier vector is not in the amplitude quadrature. In other words, there is no correspondence with the DRMI for the Fabry-Perot cavity defined so that the incident carrier is in the amplitude quadrature.

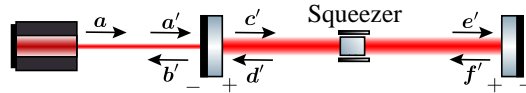


Fig. 4.6: Schematic of intracavity squeezing for the Fabry-Perot cavity as an intracavity carrier criterion. The initial phase of the incident carrier is $\varphi = -\arctan((\delta + \sigma \sin 2\theta)/(1 - \sigma \cos 2\theta))$.

Then, as shown in Fig. 4.6, we consider that the carrier with initial phase φ is incident to the cavity so that the intracavity carrier vector is directed in the amplitude quadrature ($E'_1 = E'_0$, $E'_2 = 0$). The squeezing angle, in this case, is denoted as θ . The initial phase can be calculated as $\varphi = -\arctan((\delta + \sigma \sin 2\theta)/(1 - \sigma \cos 2\theta))$. The incident carrier is converted to $A \rightarrow A' = R(\varphi)A$, where the rotation matrix can be written as

$$\begin{aligned} R(\varphi) &= \frac{1}{\sqrt{(1 - \sigma \cos 2\theta)^2 + (\delta + \sigma \sin 2\theta)^2}} \\ &\times \begin{pmatrix} 1 - \sigma \cos 2\theta & \delta + \sigma \sin 2\theta \\ -\delta - \sigma \sin 2\theta & 1 - \sigma \cos 2\theta \end{pmatrix}. \end{aligned} \quad (4.11)$$

The intracavity carrier can be written as

$$\mathbf{E}' = \frac{2}{t} \frac{1}{\sqrt{(1 - \sigma \cos 2\theta)^2 + (\delta + \sigma \sin 2\theta)^2}} \begin{pmatrix} 1 \\ 0 \end{pmatrix} A_0 = \begin{pmatrix} E'_0 \\ 0 \end{pmatrix}, \quad (4.12)$$

and we obtain intracavity power as

$$P_{E'} = \frac{4}{T} \frac{1}{(1 - \sigma \cos 2\theta)^2 + (\delta + \sigma \sin 2\theta)^2} P_A. \quad (4.13)$$

The input-output relation of the light field fluctuation can be written as

$$\begin{aligned} \mathbf{a}' &= R(\varphi)\mathbf{a}, \quad \mathbf{b}' = -r\mathbf{a}' + t\mathbf{d}', \quad \mathbf{c}' = t\mathbf{a}' + r\mathbf{d}', \\ \mathbf{d}' &= e^{i\alpha} R(2\phi)S(u, \theta)\mathbf{f}', \quad \mathbf{e}' = e^{i\alpha}\mathbf{c}', \quad \mathbf{f}' = \mathbf{e}' + 2k_0 E'_0 \begin{pmatrix} 0 \\ 1 \end{pmatrix} \delta x(\Omega). \end{aligned} \quad (4.14)$$

We neglect the input field \mathbf{a} and solve these equations for \mathbf{e}' , obtaining

$$\mathbf{e}' = 2k_0 E'_0 r e^{2i\alpha} [I - r e^{2i\alpha} R(2\phi)S(u, \theta)]^{-1} R(2\phi)S(u, \theta) \begin{pmatrix} 0 \\ 1 \end{pmatrix} \delta x(\Omega). \quad (4.15)$$

This equation is consistent with Eq. (4.5) except for the intracavity light amplitude. The complex optical spring constant $K_{\text{opt}}(\Omega)$ can be calculated in the same manner described in the previous subsection:

$$K_{\text{opt}}(\Omega) \simeq \frac{4k_0 P_{E'}}{L\gamma} \frac{\delta - \sigma \sin 2\theta}{(1 + i\Omega/\gamma)^2 + \delta^2 - \sigma^2}. \quad (4.16)$$

Therefore, the optical spring generated in the Fabry-Perot cavity is equivalent to it in the DRMI by defining the intracavity carrier as the amplitude quadrature. In other words, using the Fabry-Perot cavity, it is possible to conduct a proof-of-principle experiment of the signal amplification system discussed in Sec. 3.5.2.

Let us discuss the meaning of defining the intracavity carrier in the amplitude quadrature. In terms of sensitivity, intracavity carrier transformation associates measurements by contrast defects in the DRMI with the reflected light in the Fabry-Perot cavity, as discussed in Sec. 3.4.3. Without intracavity squeezing, the optical spring generated in the DRMI is equivalent to it in the Fabry-Perot cavity by normalizing the intracavity power, regardless of the definition of carrier quadrature. With intracavity squeezing, the phase of the incident light is relevant to the definition of the squeezing angle. When the incident carrier is defined as the amplitude quadrature, the squeezing angle θ_{inc} is independent of the quadrature of the generated signal. In contrast, when the intracavity carrier is defined as the amplitude quadrature, the squeezing angle θ is zero for squeezing the generated signal. In other words, the intracavity carrier transformation allows us to define the squeezing angle similar to that of the DRMI.

In the experiment, when we vary the cavity detuning and squeezing angle, the intracavity power follows Eq. (4.10) instead of Eq. (4.13). The theoretical squeezing angle is the phase difference between the pump light and incident light. However, experimentally, the phase of the pump light is considered to be the squeezing angle. In other words, the phase change of the pump light does not correspond linearly to the squeezing angle for the intracavity carrier criterion. The correspon-

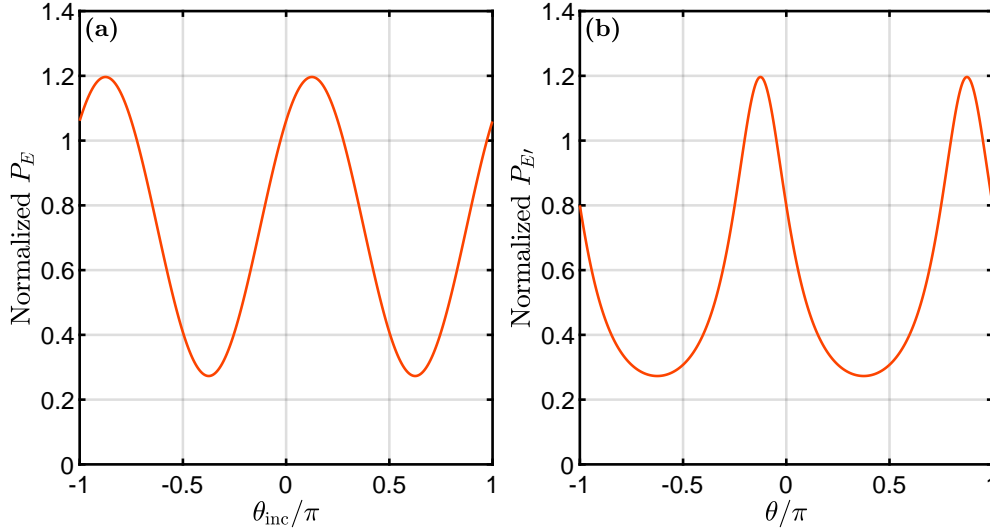


Fig. 4.7: Intracavity light power with intracavity squeezing. The parameters are set to $\delta = 1$ and $\sigma = 0.5$. The vertical axis is normalized to be 1 when $\delta = 0$ and $\sigma = 0$. The horizontal axes in (a) and (b) have different definitions, as denoted in Eqs. (4.10) and (4.13).

dence of squeezing angles is shown in Figs. 4.7(a) and (b), which show the plots of Eqs. (4.10) and (4.13), respectively. The phase of the pump light corresponds to θ_{inc} , and we can observe the sine wave by varying it, as shown in Fig. 4.7(a). However, the squeezing angle calculated from Eq. (4.10) has no correspondence to that in the DRMI. By calculating the squeezing angle from Eq. (4.13), it is possible to define the squeezing angle to correspond with it in the DRMI. The intracavity power, in this case, is obtained by nonlinearly varying the phase of the pump light, as shown in Fig. 4.7(b).

In summary, to consider the optical spring generated in the Fabry-Perot cavity equivalent to it generated in the DRMI, we need to normalize the optical spring constant by the intracavity power and define the squeezing angle with intracavity carrier transformation. The experimental procedure is as follows. First, the squeezing factor is calculated based on the maximum value of the transmitted light for varying the cavity detuning and squeezing angle. Next, we control the cavity detuning to a constant value. Finally, the squeezing angle is controlled to maintain the intracavity power. The correspondence between transmitted light power and squeezing angle is calculated using Eq. (4.13). Thus, the obtained squeezing angle

nonlinearly corresponds to the phase of the pump light.

Strong intracavity power and high signal amplification factor are required to experimentally observe an optical spring. It should be noted that a squeezing angle that yields a high signal amplification factor does not necessarily produce strong intracavity power. For example, as shown in Fig. 4.4, when $\theta = -\pi/4$ and $\sigma \sim 0.8$, a strong signal amplification factor can be obtained by setting $\delta \sim 0.2$. However, the intracavity power with these parameters, calculated from Eq. (4.13), is approximately 0.7 times that with $\delta = 0$ and $\sigma = 0$. Strong intracavity power is essential to observe the optical spring; however, a strong input power suppresses the OPA process, resulting in a lower squeezing decay rate. Therefore, the primary experimental strategy is to achieve strong intracavity power as $\theta \sim 0$ and measure the signal amplification rate at approximately $\delta \sim 1$.

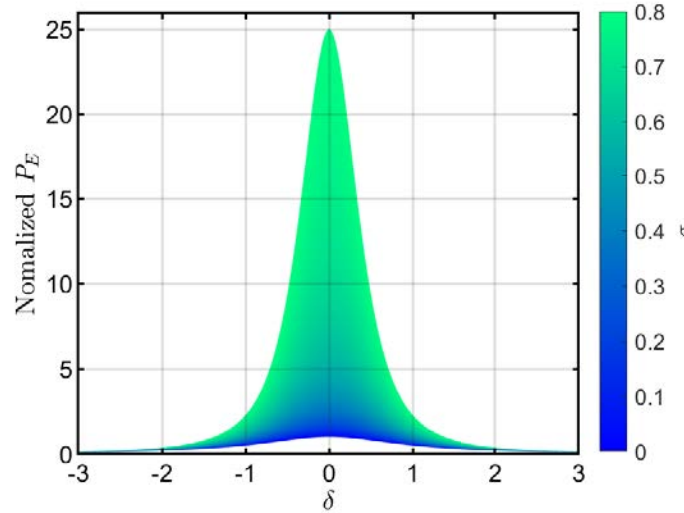


Fig. 4.8: Intracavity light power with intracavity squeezing with $\theta_{\text{inc}} = 0$ in Eq. (4.10). The vertical axis is normalized to be 1 when $\delta = 0$ and $\sigma = 0$.

Figures 4.8 and 4.9 show the intracavity power that can be measured when the phase of the pump light is kept constant. The intracavity power reaches its maximum when $\theta_{\text{inc}} = 0$ and $\delta = 0$, and it attenuates when $\theta_{\text{inc}} = \pi/2$.

4.2 Linear signal acquisition methods

To generate an optical spring in the optical interferometer, parameters such as cavity detuning and squeezing angle must be controlled to maintain values. To pull into the operating point and achieve stable operation, our experiments use feedback control^{*2}. The feedback control of an optical system requires that the

^{*2} See App. E.1.

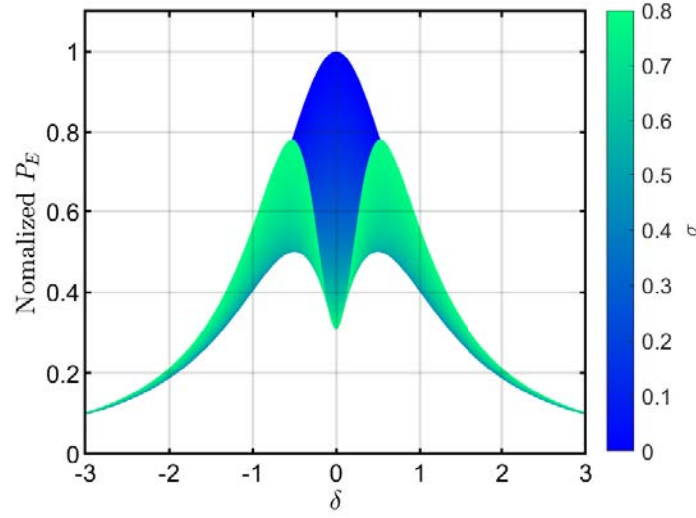


Fig. 4.9: Intracavity light power with intracavity squeezing with $\theta_{\text{inc}} = \pi/2$ in Eq. (4.10). The vertical axis is normalized in the same manner as in Fig. 4.8.

optical system responds linearly around the operating point. However, when cavity detuning is controlled to the resonance point of the Fabry-Perot cavity or when the squeezing angle is controlled to maximize the intracavity light power, the transmitted light power from the cavity does not respond linearly. In such cases, the solution is to use radio frequency (RF) sidebands or a subcarrier, whose frequency response to the optical system differs from that of the carrier, as a reference light. This section considers methods for obtaining a linear control signal (error signal) for an optical system.

4.2.1 Pound-Drever-Hall method

The Pound-Drever-Hall (PDH) technique [140] is a well-known linear signal acquisition method for the resonance point of the cavity. This technique uses RF sidebands as a reference light to obtain a linear signal around the resonance point. Fig. 4.10 shows the PDH method for the Fabry-Perot cavity. First, we obtain a formula for the RF sidebands. RF sidebands can be generated by transmitting carrier light through the electro-optic modulator (EOM) and applying phase modulation. With the incident electric field as $A(t) = A_0 \cos \omega_0 t$, the light field amplitude transmitted from the EOM $A'(t)$ can be written as

$$A'(t) = A_0 \cos(\omega_0 t + \beta \sin \omega_M t) \simeq A_0 (\cos \omega_0 t - \beta \sin \omega_0 t \sin \omega_M t). \quad (4.17)$$

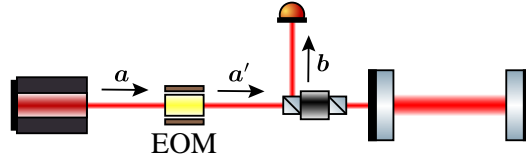


Fig. 4.10: Schematic of the PDH method for the Fabry-Perot cavity. RF sidebands are generated from phase modulation using an electro-optic modulator, and the demodulation of the reflected light obtains the error signal.

Herein, the fluctuations of the incident light field are neglected. The DC and AC components of the light field can be written as

$$\mathbf{A}' = \mathbf{A}, \quad (4.18)$$

$$\mathbf{a}'(t) = -A_0\beta \begin{pmatrix} 0 \\ \sin \omega_M t \end{pmatrix}, \quad (4.19)$$

where $\beta \ll 1$ denotes the modulation index, which is determined by the voltage applied to the EOM crystal and the conversion efficiency, and ω_M denotes the angular frequency of the AC voltage applied to the crystal. $\mathbf{a}'(t)$ represents the RF sideband and is the equivalent formula for the signal of angular frequency ω_M .

If the modulation frequency is sufficiently high, optomechanical coupling can be negligible. Let r^2 and t^2 be power reflectivity and transmissivity of the input mirror, and ϕ and α be phase change and delay during a half cycle in the cavity. The light field fluctuations reflected by the cavity can be calculated as

$$\begin{aligned} \mathbf{b}(\Omega) &= \left[-rI + t^2 [I - re^{2i\alpha} R(2\phi)]^{-1} R(2\phi) \right] \mathbf{a}' \\ &\simeq \frac{1}{(\gamma + i\Omega)^2 + \Delta^2} \begin{pmatrix} \gamma^2 - \Delta^2 + \Omega^2 & -2\gamma\Delta \\ 2\gamma\Delta & \gamma^2 - \Delta^2 + \Omega^2 \end{pmatrix} \mathbf{a}' \\ &= \frac{-A_0\beta\mathcal{F}[\sin \omega_M t]}{(\gamma + i\Omega)^2 + \Delta^2} \begin{pmatrix} -2\gamma\Delta \\ \gamma^2 - \Delta^2 + \Omega^2 \end{pmatrix}, \end{aligned} \quad (4.20)$$

where γ denotes the cavity decay rate and Δ denotes the cavity detuning. $\mathcal{F}[f(t)]$ denotes the Fourier transform. Using Dirac's delta function $\delta(\Omega)$, the signal in the frequency domain can be written as

$$\mathcal{F}[\sin \omega_M t] = i\pi(\delta(\Omega + \omega_M) - \delta(\Omega - \omega_M)). \quad (4.21)$$

When the modulation frequency is sufficiently larger than the cavity decay rate and cavity detuning, we can approximate $\mathbf{b}(\Omega)$ as follows:

$$\mathbf{b}(\Omega) \simeq A_0\beta\mathcal{F}[\sin \omega_M t] \begin{pmatrix} 0 \\ 1 \end{pmatrix}. \quad (4.22)$$

Moreover, the carrier light can be calculated as

$$B = \frac{A_0}{\gamma^2 + \Delta^2} \begin{pmatrix} \gamma^2 - \Delta^2 \\ 2\gamma\Delta \end{pmatrix}. \quad (4.23)$$

In the PDH method, we demodulate by multiplying the measured light power P_B by a signal whose phase is the same as the modulation signal ($\sim \sin \omega_M t$) or a signal whose phase is shifted by $\pi/2$ ($\sim \cos \omega_M t$). We refer to each demodulation phase as in-phase (I-phase) and quadrature-phase (Q-phase). The obtained PDH signal is passed through a low-pass filter to remove high-frequency signals and is used as the linear signal. Therefore, we need to consider the terms that are multiplied by $\sin \omega_M t$ and $\cos \omega_M t$:

$$\begin{aligned} P_B^{\omega_M} &= \frac{\hbar\omega_0}{2} 2B_2 \mathcal{F}^{-1}[b_2(\Omega)] \\ &\simeq 2 \frac{2\gamma\Delta}{\gamma^2 + \Delta^2} \beta P_A \sin \omega_M t, \end{aligned} \quad (4.24)$$

where $\mathcal{F}^{-1}[f(\Omega)]$ denotes the inverse Fourier transform. The PDH signal is obtained by demodulating with I-phase and removing the AC component, which is a linear signal around $\Delta = 0$:

$$P_B^{\text{demod-I}} \simeq \frac{2\gamma\Delta}{\gamma^2 + \Delta^2} \beta P_A. \quad (4.25)$$

Without approximation, the error signals when demodulated in I-phase and Q-phase are as follows:

$$P_B^{\text{demod-I}} = -\frac{2\gamma\Delta\omega_M^2(\gamma^2 + \Delta^2 - \omega_M^2)}{(\gamma^2 + \Delta^2)^3 + 2(\gamma^4 - \Delta^4)\omega_M^2 + (\gamma^2 + \Delta^2)\omega_M^4} \beta P_A, \quad (4.26)$$

$$P_B^{\text{demod-Q}} = -\frac{4\gamma^2\Delta\omega_M^3}{(\gamma^2 + \Delta^2)^3 + 2(\gamma^4 - \Delta^4)\omega_M^2 + (\gamma^2 + \Delta^2)\omega_M^4} \beta P_A. \quad (4.27)$$

The theoretical curve of the error signal with $\omega_M = 10\gamma$ is shown in Fig. 4.11. The I-phase signal is linear around the resonance state. However, a linear signal also appears around $\Delta = \omega_M$ because the carrier light becomes the reference light in cavity detuning where the sidebands resonate. The slope of the error signal around the sideband resonance has the opposite sign to that of the error signal around the carrier light resonance. The error signal must be fed back with the correct polarity to control the cavity to the carrier light resonance. When Q-phase signals are used, the slope of the error signal is tiny, making it difficult to pull the cavity into a resonance state. It is essential to correctly set the demodulation phase for modulation and demodulation methods, e.g., the PDH technique.

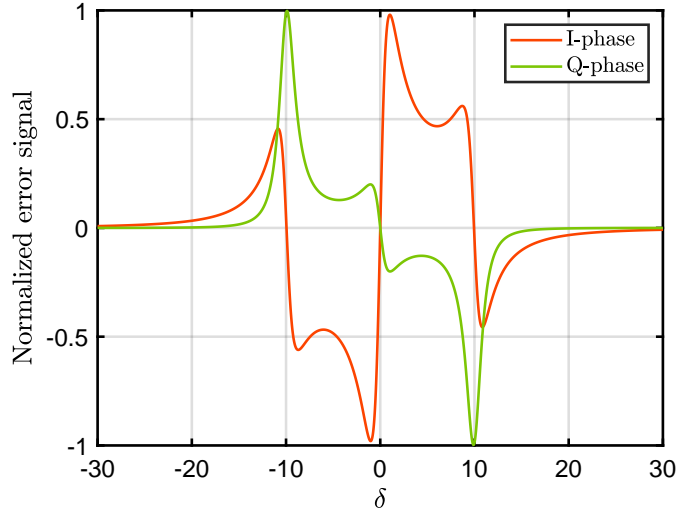


Fig. 4.11: Error signals obtained using the PDH technique. The parameter is set to $\omega_M = 10\gamma$, and the horizontal axis indicates normalized cavity detuning $\delta = \Delta/\gamma$. The vertical axis is appropriately normalized.

4.2.2 Phase-locking loop

The control method for squeezing angle uses a light whose frequency is shifted from the carrier light. This light is called a subcarrier. Let ω_M be the frequency difference from the carrier and a_0 be the amplitude; the formula of the subcarrier is

$$a(t) = a_0 \cos(\omega_0 + \omega_M)t = a_0(\cos \omega_0 t \cos \omega_M t - \sin \omega_0 t \sin \omega_M t), \quad (4.28)$$

so \mathbf{a} can be written as

$$\mathbf{a}(t) = a_0 \begin{pmatrix} \cos \omega_M t \\ -\sin \omega_M t \end{pmatrix}. \quad (4.29)$$

The carrier \mathbf{B} of phase ϕ_B interferes with the subcarrier \mathbf{a} of phase ϕ_a , as shown in Fig. 4.12. Let r^2 and t^2 be the power reflectivity and transmissivity of the mirror. The component with frequency ω_M of the light power measured by the photodetector is

$$P_C^{\omega_M} = 2rt\sqrt{P_B P_a} [\sin(\phi_B - \phi_a) \sin \omega_M t - \cos(\phi_B + \phi_a) \cos \omega_M t]. \quad (4.30)$$

By demodulating with $\sin \omega_M t$, we can obtain a linear signal around $\phi_B - \phi_a = 0$. In our experiment, we synchronize the phases of two lasers by the feedback of the error signal to the frequency tuning channel of the second laser. This control loop is known as a phase-locking loop (PLL).

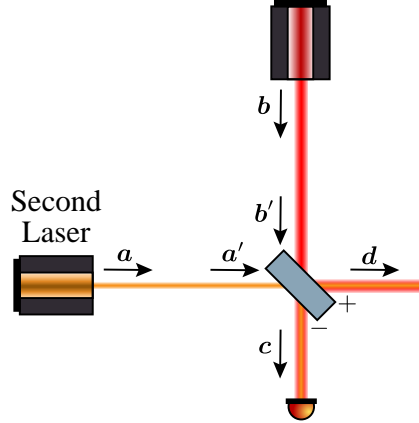


Fig. 4.12: Schematic of the phase-locking loop.

In the squeezing experiment, the OPA occurs in the optical parametric oscillator (OPO) cavity. As carrier light incident on the OPO cavity is a noise source for the squeezed vacuum field, the PLL in a typical squeezing experiment is conducted separately from the incident path to the cavity. In our experiment, the carrier light and subcarrier light must be injected into the cavity aligning the phases, so that $D + d$ becomes the incident light to the cavity.

4.2.3 Control of the squeezing angle with the coherent control field

The error signal of the squeezing angle has been studied to obtain it even when squeezing a vacuum field where no carrier light. The coherent control method [141, 142] obtains a series of error signals for OPA and homodyne detection using the subcarriers as reference light^{*3}. When performing degenerate OPA for the carrier light of frequency ω_0 , the subcarrier light of frequency $\omega_0 + \omega_M$ is converted to another subcarrier light of frequency $\omega_0 - \omega_M$ according to the energy conservation law. Both subcarrier lights are affected by OPA; however, they differently depend on the squeezing angle. Therefore, the error signal of the squeezing angle can be obtained by demodulating with a frequency difference of subcarriers, i.e., $2\omega_M$. In addition, this error signal is not affected by the carrier light because the frequency differences between the two subcarriers and carrier light are ω_M . Using the coherent control method, we can control the squeezing angle with or without the carrier light.

In our experimental system, the OPO cavity is detuned. It needs to be evident whether the coherent control method can be applied to this case. Let us consider the error signal obtained by injecting the subcarrier light into a detuned OPO cav-

^{*3} This method can be applied in various ways, e.g., the filter cavity can be controlled by coherent control fields [143, 144].



Fig. 4.13: Schematic of the coherent control method for the detuned OPO cavity.

ity and demodulating the transmitted light at frequency $2\omega_M$, as shown in Fig. 4.13. When the error signal is fed back to the phase of the pump light, it corresponds to using the squeezing angle for the incident carrier light; thus, the squeezing angle and phase change are defined as in Fig. 4.5. As the transmitted light power is proportional to the intracavity power, we need to calculate the intracavity amplitude e :

$$e = t[I - re^{i\alpha}R(2\phi)S(u, \theta_{\text{inc}})]a$$

$$\simeq \frac{2}{t} \frac{\gamma}{(\gamma + i\Omega)^2 + \Delta^2 - \Sigma^2} \begin{pmatrix} \gamma + i\Omega + \Sigma \cos 2\theta_{\text{inc}} & -\Delta + \Sigma \sin 2\theta_{\text{inc}} \\ \Delta + \Sigma \sin 2\theta_{\text{inc}} & \gamma + i\Omega - \Sigma \cos 2\theta_{\text{inc}} \end{pmatrix} a, \quad (4.31)$$

where the incident light field of subcarrier $a(\Omega)$ can be written as

$$a(\Omega) = a_0 \begin{pmatrix} \mathcal{F}[\cos \omega_M t] \\ \mathcal{F}[-\sin \omega_M t] \end{pmatrix}. \quad (4.32)$$

The intracavity subcarrier power $P_e = \hbar\omega_0/2(e_1(t)^2 + e_2(t)^2)$ is complicated. By demodulating it with the respective phase, the following error signal is obtained:

$$P_e^{\text{demod-I}} = \Lambda_0(\Lambda_1 \cos 2\theta_{\text{inc}} - \Lambda_2 \sin 2\theta_{\text{inc}}) \frac{4}{T} P_a, \quad (4.33)$$

$$P_e^{\text{demod-Q}} = \Lambda_0(\Lambda_2 \cos 2\theta_{\text{inc}} + \Lambda_1 \sin 2\theta_{\text{inc}}) \frac{4}{T} P_a, \quad (4.34)$$

with

$$\Lambda_0 = \frac{\gamma^2 \Sigma}{[\gamma^4 + 2\gamma^2(\Delta^2 - \Sigma^2 + \omega_M^2) + (-\Delta^2 + \Sigma^2 + \omega_M^2)^2]^2}, \quad (4.35)$$

$$\Lambda_1 = \gamma^4(\Delta - 3\omega_M) + (\Delta + \omega_M)(-\Delta^2 + \Sigma^2 + \omega_M^2)^2 + 2\gamma^2[\Delta^3 - \Delta^2\omega_M + \omega_M(\Sigma^2 - \omega_M^2) - \Delta(\Sigma^2 + 3\omega_M^2)], \quad (4.36)$$

$$\Lambda_2 = \gamma[\gamma^4 + 2\gamma^2(\Delta^2 - \Sigma^2 + 2\Delta\omega_M - \omega_M^2) + (\Delta^2 - \Sigma^2 - \omega_M^2)(-\Sigma^2 + (\Delta + \omega_M)(\Delta + 3\omega_M))]. \quad (4.37)$$

Fig. 4.14 shows the error signal obtained using the coherent control method. The signals demodulated by I-phase and Q-phase are orthogonal, indicating that a

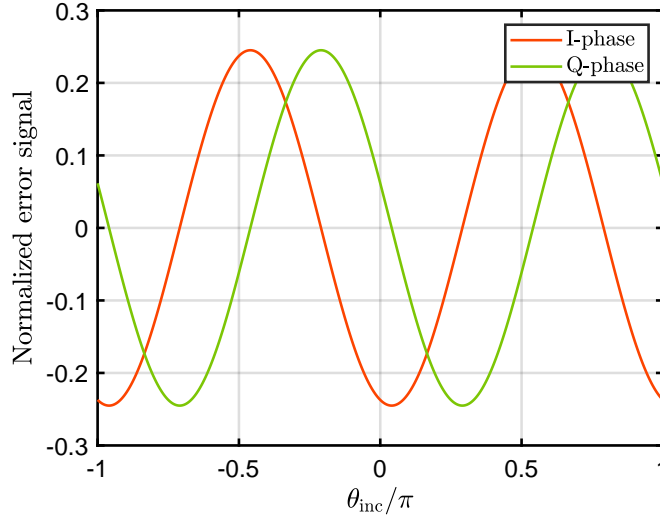


Fig. 4.14: Error signal obtained using the coherent control method. The parameters are set to $\omega_M = \gamma$, $\Delta = \gamma$, and $\Sigma = 0.5\gamma$. The horizontal axis corresponds to the relative phase of the pump light, and the vertical axis is appropriately normalized.

linear signal for any squeezing angle can be obtained by choosing the appropriate demodulation phase. The amplitude of the error signal can be calculated as

$$\sqrt{(\Lambda_0\Lambda_1)^2 + (\Lambda_0\Lambda_2)^2} = \frac{\gamma^2\Sigma\sqrt{\gamma^2 + (\Delta + \omega_M)^2}}{\gamma^4 + 2\gamma^2(\Delta^2 - \Sigma^2 + \omega_M^2) + (-\Delta^2 + \Sigma^2 + \omega_M^2)^2}. \quad (4.38)$$

Fig. 4.15 shows the error signal amplitudes for several cases of cavity detuning. When the cavity is not detuned, the error signal amplitude increases as ω_M is smaller because the two subcarriers are equally amplified. When the cavity is detuned, the intracavity power of the subcarrier with a frequency of $\omega_0 + \omega_M$ reaches its maximum when $\omega_M = \Delta$, and the intracavity power of the subcarrier with a frequency of $\omega_0 - \omega_M$ becomes maximum when $\omega_M \rightarrow 0$. The amplitude of the error signal becomes maximum when ω_M is set as the intermediate between these values.

4.3 OPA experiment

4.3.1 Experimental setup

This experiment aims to observe an optical spring enhanced by intracavity OPA. The experimental setup is shown in Fig. 4.16. The SHG cavity generated the second harmonic, which is the pump light of OPA. The OPO cavity induced the intracavity OPA. One of the mirrors that comprised the cavity is a lightweight mirror, which allowed us to observe the optical spring. In addition to the control of the

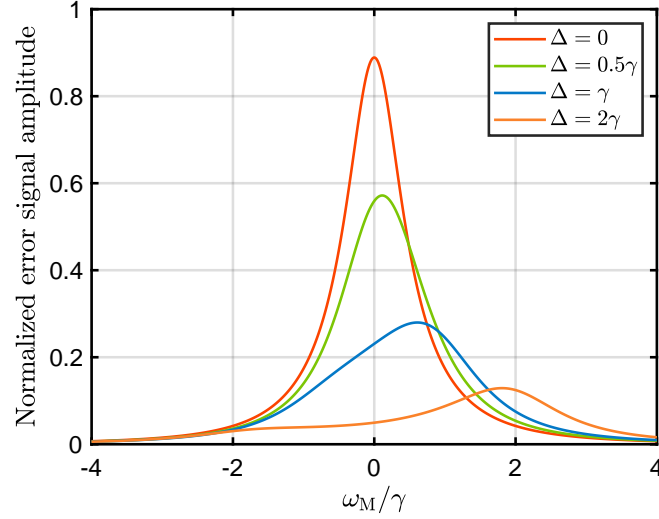


Fig. 4.15: Amplitude of the error signal obtained using the coherent control method. The parameter is set to $\Sigma = 0.5\gamma$, and the vertical axis is appropriately normalized.

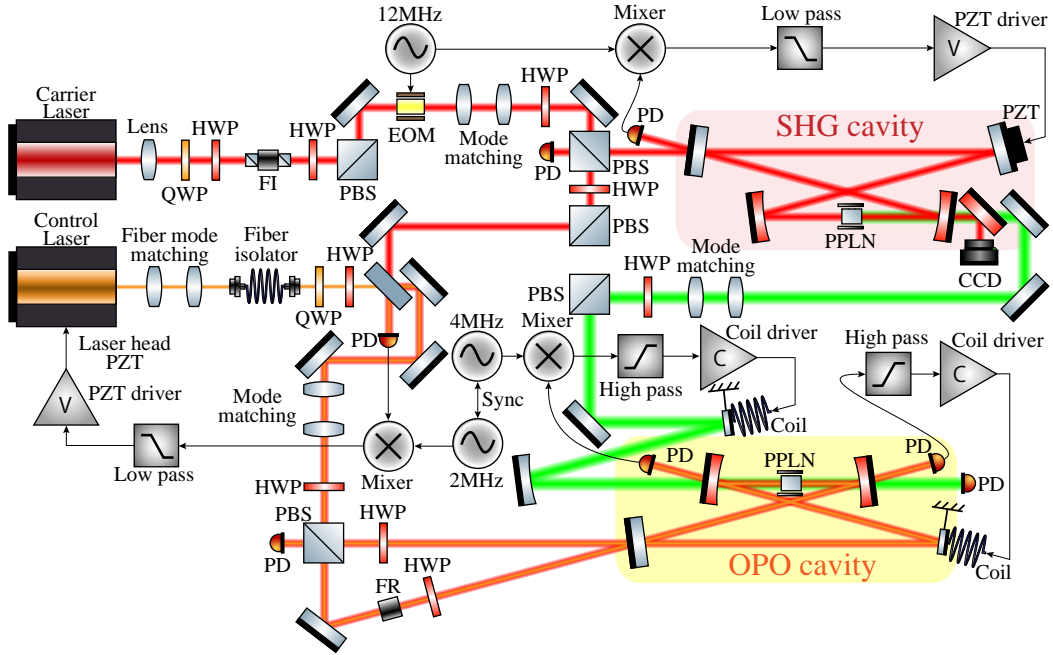


Fig. 4.16: Setup of the OPA experiment. Abbreviations are defined as follows: photodetector (PD), half-waveplate (HWP), quarter-wave plate (QWP), polarization beam splitter (PBS), electro-optic modulator (EOM), piezoelectric element (PZT), periodically poled LiNbO₃ (PPLN), Faraday isolator (FI), Faraday rotator (FR), second harmonic generation (SHG) and optical parametric oscillator (OPO).

cavity length of the two cavities, we were required to control the frequency of the coherent control field and squeezing angle. The PLL of the control laser was controlled by measuring the interference light with the carrier laser and feeding it to the frequency port of the control laser. The squeezing angle was controlled by demodulating the transmitted light of the OPO cavity at twice the PLL frequency and feeding it to the phase of the pump light. The relative phase of the pump light was controlled using a coil magnet actuator that can increase the unity gain frequency because fluctuations in the OPO cavity length are amplified by OPA, causing large fluctuations in the squeezing angle. In the loop controlled by the coil magnet actuator, a high-pass filter was used to provide a phase margin at unity gain frequency. In the loop controlled by the PZT, a low-pass filter was used to decrease the resonance peak of the PZT^{*4}.

As the single-pass SHG possesses negligible conversion efficiency, it is necessary to use a cavity to generate a high-intensity second harmonic field. We used a PPLN crystal with a crystal length of 1.0 cm as an NLC. The radius of the beam waist was designed to be approximately $40\text{ }\mu\text{m}$ to set the Rayleigh length of the beam to approximately 0.5 cm. The distance between the curved mirrors was designed to be 0.16 m, the round cavity length was 1.36 m, and the angle of incidence was 8 degrees. The cavity length was controlled to the resonance state using the PDH method. Tab. 4.1 lists the mirrors that constitute the SHG cavity. The power

Table 4.1: Mirrors that constitute the SHG cavity.

Name	Manufacturer	Number	Reflectance	AOI	ROC
Input coupler	Layertec	104373	= 94%@1064&532	6 degrees	flat
Curved mirror	Layertec	102247	> 99.9%@1064, < 5%@532	0 degrees	150 mm
Actuate mirror	Layertec	104265	> 99.9%	0 degrees	flat

reflectivity of the input coupler was set to 94% to achieve approximately critical coupling owing to the intracavity loss caused by the SHG effect. We measured the input power of the fundamental wave incident to the SHG cavity and the outgoing light power of the second harmonic wave. An outgoing light with a power of 620 mW was obtained for an input power of 610 mW. The measurement error of the power meter was 7%, and the actual conversion efficiency could be estimated to be approximately 95%. An SHG cavity with excellent conversion efficiency was constructed.

An optical spring was generated in the OPO cavity. We used a PPLN crystal as an NLC; however, it is replaced with a periodically poled KTiOPO_4 (PPKTP) crystal for some measurements. Both crystals have a crystal length of 1.0 cm; thus, the beam waist radius was designed to be approximately $40\text{ }\mu\text{m}$. The distance between the curved mirrors was designed to be 0.078 m, the round cavity length was 0.428 m, and the angle of incidence was 17 degrees. The cavity length was controlled to a detuned state based on the feedback of the transmitted power.

^{*4} See App. E.1.2.

Tab. 4.2 lists the mirrors that constitute the OPO cavity. The finesse is designed to

Table 4.2: Mirrors that constitute the OPO cavity.

Name	Manufacturer	Number	Reflectance	AOI	ROC
Input coupler	Layertec	104373	= 94%@1064	6 degrees	flat
Curved mirror	Newport&LMA	SPC025	= 99.95%@1064, < 0.25%@532	15 degrees	68.5 mm
Small mirror	Edmund	#38-901	> 99.8%@1064	0 ~ 45 degrees	flat

be approximately 100 to generate an observable optical spring while minimizing the influence of intracavity losses. The coating of the curved mirror was provided by Laboratoire des Matériaux Avancés (LMA). It possesses a remarkably high transmissivity for 532 nm light.

When OPA generates a carrier light more than the optical loss during one round of the OPO cavity, the carrier light is emitted from the cavity even if the carrier light is not incident. This oscillation state is a phenomenon referred to as the OPO. The incident second harmonic power corresponding to the oscillation threshold was approximately 150 mW. We can incident approximately 530 mW of the second harmonic, which is approximately 3.5 times the threshold. In this case, the fundamental wave emitted approximately 470 mW, and the conversion efficiency of the OPO was approximately 90%. The OPO cavity also possesses excellent conversion efficiency, and a nearly ideal intracavity OPA should be achievable.

We incident carrier light and counterpropagating light to the OPO cavity. Carrier light is amplified by the pump light; however, the counterpropagating light is not amplified because it propagates in the opposite direction to the pump light. The transmitted power of the carrier light is used to control the squeezing angle, and the transmitted power of the counterpropagating light is used to control the cavity length. By comparing the transmitted light power, we can estimate the impact of OPA. The input power of the counterpropagating light must be weak to avoid SHG effects but sufficiently strong to neglect coupling with the carrier light. Hence, in this experiment, a counterpropagating light of 10 ~ 20 mW was incident to the OPO cavity.

4.3.2 Estimation of OPA from the transmitted light measurement

First, the impact of the OPA was estimated by measuring the transmitted light power. The coil magnet actuator in the incident path of the pump light was replaced by a PZT, and the relative phase was slowly changed. In contrast, the OPO cavity length was rapidly changed. The transmitted light power that can be measured corresponds to the spectrum when the squeezing angle θ_{inc} is kept constant.

Fig. 4.17 shows the spectrum without the pump light. In this case, the carrier light is also not amplified; thus, the ordinary spectrum of the resonance is measured. The resonance spectra of the carrier light and counterpropagating light are in excellent agreement, indicating that counterpropagating light can be used as an indicator for cavity detuning.

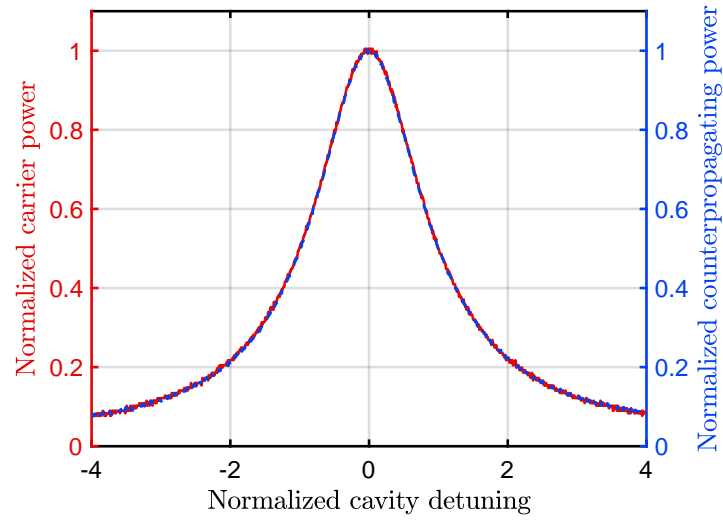


Fig. 4.17: Transmitted light power from the OPO cavity. The input power of the carrier light is 50 mW, and the pump light is not incident.

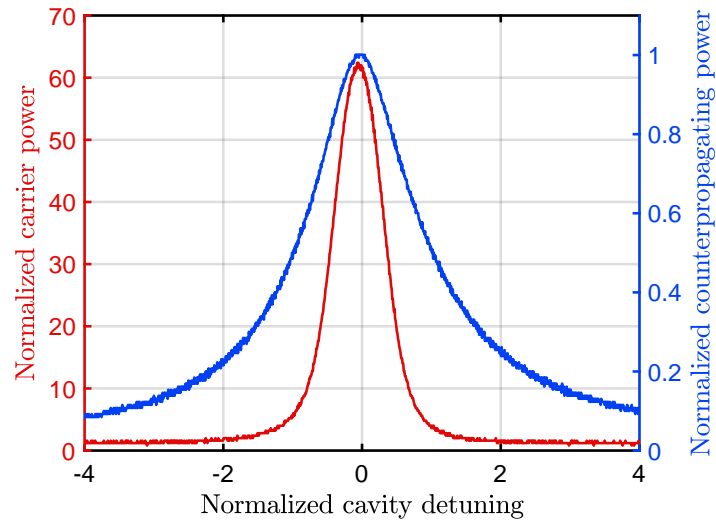


Fig. 4.18: Transmitted light power from the OPO cavity. The input power of the carrier light is 0.5 mW, and the input pump light power is approximately equal to the oscillation threshold. This spectrum corresponds to the state where the squeezing angle is $\theta_{\text{inc}} = 0$.

The spectrum with an input carrier light of 0.5 mW is shown in Fig. 4.18. The amplification rate of the carrier light varies with the squeezing angle. Herein, the spectrum is observed when power amplification is nearly maximum. The carrier light in the resonance state is amplified approximately 62 times, and from Eq. (4.10), the normalized squeezing decay rate can be calculated as $\sigma \sim 1 - 1/\sqrt{62} \sim 0.87$. When we set $\theta = 0$ and $\delta = 1$, from Eq. (4.16), the optical spring constant is enhanced by approximately 1.62 times owing to the signal amplification effect. The line width of the spectrum is narrower than that without OPA, which is qualitatively consistent with the behavior shown in Fig. 4.8.

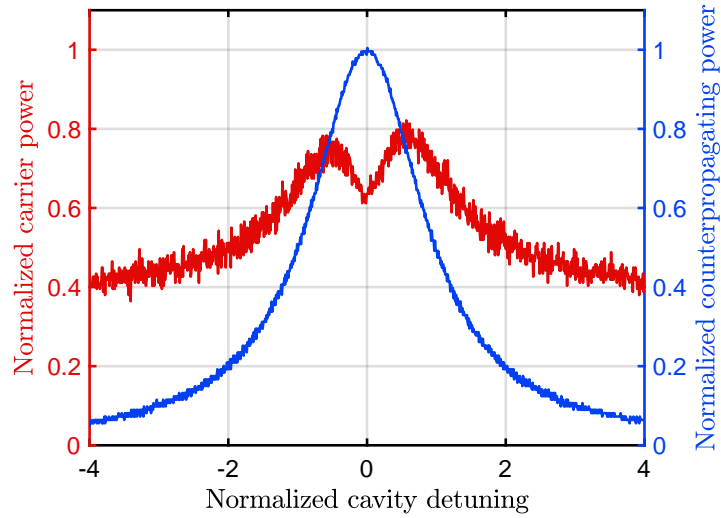


Fig. 4.19: Transmitted light power from the OPO cavity. The input power of the carrier light is 0.5 mW, and the input pump light power is approximately equal to the oscillation threshold. This spectrum corresponds to the state where the squeezing angle is $\theta_{\text{inc}} = \pi/4$.

Fig. 4.19 shows the spectrum with a squeezing angle that results in power attenuation. A response is observed in which the center of the spectrum is concave, which is qualitatively consistent with the behavior shown in Fig. 4.9. The offset of the spectrum may be because the slight pump light incident on the PD is not entirely separated.

The spectrum with an input carrier light of 50 mW is shown in Fig. 4.20. Although the spectrum is observed when power amplification is maximum, the power amplification gain is reduced to roughly 2.7 times. We conclude that the intracavity power of the carrier light is comparable to the pump light, and the OPA process may be suppressed. The squeezing decay rate can be calculated as $\sigma \sim 0.39$. When $\theta = 0$ and $\delta = 1$, the optical spring would be enhanced by only 1.08 times. However, when $\theta = -\pi/4$ and $\delta = 1$, the optical spring would be enhanced by a factor of about 1.50, although the intracavity power is not amplified much. In other words, an enhanced optical spring might be observed by choosing an appropriate

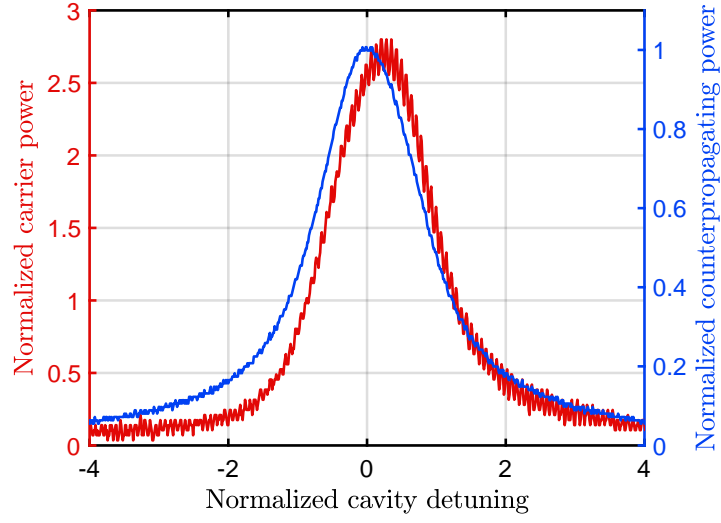


Fig. 4.20: Transmitted light power from the OPO cavity. The input power of the carrier light is 50 mW, and the input pump light power is approximately equal to the oscillation threshold. This spectrum corresponds to the state where the squeezing angle is $\theta_{\text{inc}} = 0$.

squeezing angle, even with a slight OPA gain.

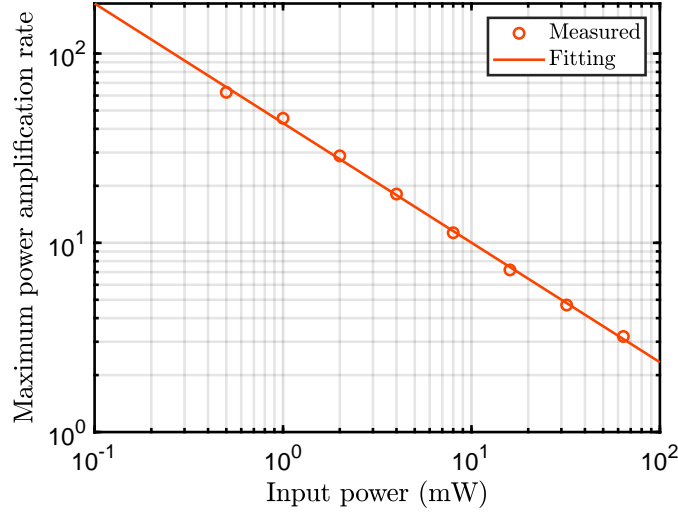


Fig. 4.21: Measurement of the input light power and maximum power amplification rate.

The maximum power amplification rate is measured for various input power values, as shown in Fig. 4.21. There is a clear proportionality on the double logarithmic graph. Let P_A (mW) be the input light power and A be the maximum power amplification rate, and assuming that $\log A = a \log P_A + b$; the parameters

can be estimated as $a = -0.63 \pm 0.01$ and $b = 3.76 \pm 0.02$. This relationship cannot be analytically obtained^{*5}.

4.3.3 Controlling the squeezing angle in the detuned OPO cavity

The most important technical issue in this experiment is controlling the squeezing angle of the detuned OPO cavity using the coherent control method. As the cavity decay rate is approximately $\gamma/2\pi \sim 3.3 \times 10^6$ Hz, the subcarrier frequency was set to 2 MHz, and the transmitted power of the carrier light was demodulated at 4 MHz. The input power was approximately 4 mW, and the subcarrier light power was approximately 1/10 of the carrier light. With cavity detuning controlled to $\delta \sim 1/\sqrt{3}$, the phase of the pump light was varied using the PZT, and we measured the error signal generated using the coherent control method.

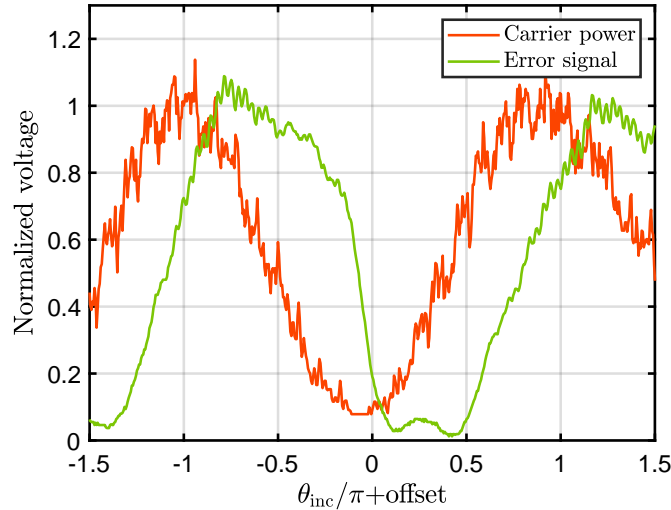


Fig. 4.22: Error signal generated using the coherent control method. The demodulation phase was set to 0 degrees. The vertical axis shows the measured voltage, which is appropriately normalized. The transmission power of the carrier light and error signal were passed through a second-order low-pass filter with cutoff frequencies of 10 kHz and 30 Hz, respectively.

Fig. 4.22 shows the error signal with the demodulation phase set to 0 degrees. We obtained an error signal whose phase differs from that of the carrier light; however, some of the difference is phase delay owing to the low-pass filter. The frequency of the error signal in this measurement is approximately 5 Hz, and the phase delay caused by the low-pass filter is estimated to be approximately 20 degrees. In contrast, the measured error signal is delayed by approximately

^{*5} See App. B.4.1.

45 ~ 90 degrees compared to the transmitted power. Therefore, we can conclude that a linear signal for the squeezing angle was obtained to maximize the amplification of the carrier light.

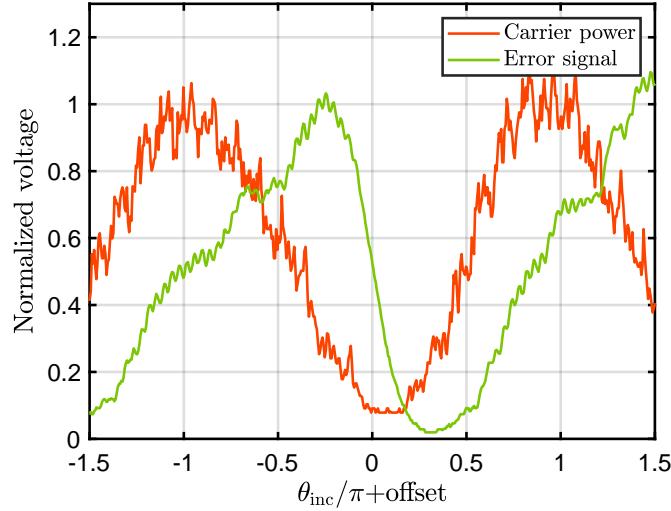


Fig. 4.23: Error signal generated using the coherent control method. The demodulation phase was set to 90 degrees, and the other settings were the same as in Fig. 4.22.

Fig. 4.23 shows the error signal with the demodulation phase set to 90 degrees. There is a difference in the phase of the error signal compared with the case with a demodulation phase of 0 degrees. However, it is not so large as the theoretical prediction of $\pi/2$. The harmonic noise is slightly generated related to the control of the PLL, and the beat between the noise and carrier light may have modified the error signal. The coherent control method cannot obtain the linear signal for some squeezing angles. However, this is the range where the transmitted power of the carrier light responds linearly. In other words, when the amplification or attenuation of the carrier light needs to be maximized, the error signal generated using the coherent control method should be used; otherwise, the transmission power of the carrier light should be directly fed back.

Moreover, the transmitted power of the carrier light comprised a large amount of noise. This amount of noise was severe in the high amplification range, indicating that the slight fluctuation in cavity detuning was amplified. The frequency corresponding to the higher order modes of mechanical suspension was dominant. This noise was not suppressed using the PZT, which possesses a low unity gain frequency. For this reason, while measuring the transfer function, we controlled the relative phase of the pump light using the same type of mechanical suspension used in the OPO cavity. The characteristics of the mechanical suspension are estimated in the next section.

4.3.4 Measurement of susceptibility of the mechanical suspension

Optical spring can be measured as a change in the resonant frequency. The equation of motion for the test mass, without an optical spring, can be written as

$$\frac{d^2 x_{\text{act}}}{dt^2} = -\Omega_m^2 x_{\text{act}} - \gamma_m \frac{dx_{\text{act}}}{dt} + F_{\text{ext}}/m, \quad (4.39)$$

where x_{act} denotes the displacement of the test mass, Ω_m denotes the resonance angular frequency of the mechanical suspension, $\Gamma_m = m\gamma_m$ denotes the damping constant of the mechanical suspension, m denotes the mass of mirror, and F_{ext} denotes the external force applied to the test mass. The susceptibility of mechanical suspension $\chi_m(\Omega)$ can be obtained from the Fourier transform of the equation of motion:

$$\chi_m(\Omega) = \frac{x_{\text{act}}(\Omega)}{F_{\text{ext}}(\Omega)} = \frac{1}{m} \frac{1}{-\Omega^2 + i\gamma_m\Omega + \Omega_m^2}. \quad (4.40)$$

If an optical spring is generated in the cavity, the mechanical suspension and optical spring are connected in parallel to the test mass. The effective resonance angular frequency becomes $\sqrt{\Omega_m^2 + \Omega_{\text{opt}}^2}$, where Ω_{opt} denotes the resonance angular frequency of the optical spring. By measuring the resonance frequency change, it is possible to estimate the effect of the optical spring [134, 135, 145].

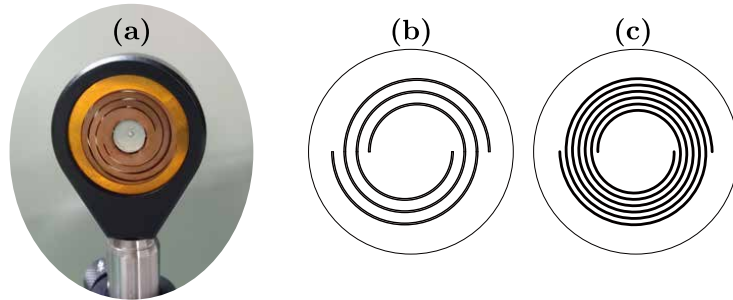


Fig. 4.24: (a) Picture of a suspended mirror. (b)(c) Drawing of the double spiral spring. The numbers of winding are 1.5 and 3.0, respectively.

We need to estimate the characteristics of the suspension before measuring the optical spring. Experimentally, we use the double spiral spring, as shown in Fig. 4.24(a). It was designed to exhibit a stiffened pitch and yaw by sandwiching the mirror between two beryllium copper plates. Moreover, we glued neodymium magnets, whose diameter and thickness are 1 mm and 0.5 mm, respectively, to the back of the mirror. It can be used as a coil magnet actuator by placing a coil behind the mirror. We further sandwiched the suspension between the brass rings to suppress higher order mechanical resonances. Two types of BeCu plates were

produced, as shown in Fig. 4.24(b)(c): one with the number of windings N of 1.5 and the other with N of 3.0. In addition, two thickness values of BeCu plate t were used: 0.10 and 0.05 mm.

To estimate the characteristics of the suspension, we configured a Michelson interferometer with one of the end mirrors as a suspended mirror. We controlled the arm length to a mid-fringe. The open-loop gain of this control system was measured to determine the susceptibility of the suspension. The phase measure-

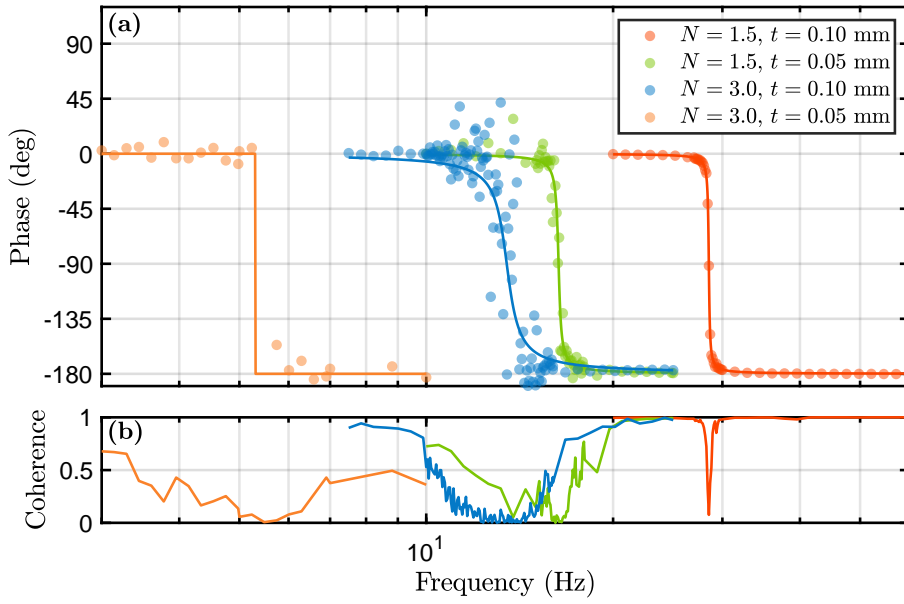


Fig. 4.25: (a) Phase measurement results of the susceptibility of mechanical suspensions. The circles indicate the measurement results, and the corresponding colored solid lines indicate the fitting results. Note that the fitting program does not work for the suspension with $N = 3.0$ and $t = 0.05$ mm. (b) Coherence between the input and measured signals. The average numbers are 200 for all the measurements.

ment results are shown in Fig. 4.25(a). The resonance frequency was decreased by increasing the number of windings and thickness. The parameters obtained from

Table 4.3: Estimated parameters of mechanical suspensions. Note that the fitting program does not work for the suspension with $N = 3.0$ and $t = 0.05$ mm.

N	t (mm)	$\Omega_m/2\pi$ (Hz)	$\gamma_m/2\pi$ (Hz)
1.5	0.10	28.529 ± 0.002	0.1785 ± 0.004
1.5	0.05	16.34 ± 0.02	0.25 ± 0.03
3.0	0.10	13.5 ± 0.1	0.9 ± 0.2
3.0	0.05	$5.3 \pm 2 \times 10^4$	$2 \times 10^{-7} \pm 0.04$

the fitting are listed in Tab. 4.3. The suspension with $N = 1.5$ and $t = 0.10$ mm provides precise measurements; however, other suspensions exhibit low coherence near the resonance frequency and poor accuracy in estimating γ_m , as shown in Fig. 4.25(b). In particular, the fitting program does not work well for suspensions with $N = 3.0$ and $t = 0.05$ mm because the frequencies at which the phase reverses cannot be measured. The resonance frequency of this suspension can be estimated and is roughly $1/5$ of the suspension with $N = 1.5$ and $t = 0.10$ mm. A mechanical suspension with a low resonant frequency can measure the optical spring with a low resonant frequency. However, significant noise and poor measurement accuracy prevent the accurate estimation of the resonant frequency. Moreover, the suspension with $N = 3.0$ exhibited poor alignment persistence; thus, in later experiments, we used a suspension with $N = 1.5$ and $t = 0.05$ mm whose resonance frequency of approximately 16 Hz. The mechanical damping constant was relatively large, and optical damping was negligible.

4.3.5 Measurement of susceptibility of the optomechanical oscillator

We measured the susceptibility of the optomechanical oscillator with OPA and attempted to observe the optical spring enhanced by OPA. First, the input power of the carrier light was set to approximately 4 mW. The phase measurement results are shown in Fig. 4.26(a). The red circles correspond to the measurements in which the incident carrier light was blocked, and cavity detuning was controlled to $\delta \sim 1/\sqrt{3}$ by the counterpropagating light. The oscillator was almost unaffected by the optical spring; thus, the resonant frequency was approximately 16 Hz. However, the transfer function was not accurately measured because of the noise near the mechanical resonance frequency, as shown in Fig. 4.26(b). The green circles correspond to the measurements with the incident carrier light, and the resonant frequency was approximately 16 Hz because carrier light power was also sufficiently weak. The blue circles corresponded to the measurement when the squeezing angle was controlled to maximize the intracavity carrier power, and the resonance frequency was at least 21 Hz or lower.

Let us estimate the resonant frequency of an optical spring. When the carrier light was injected at approximately 600 mW without OPA, we were able to measure an optical spring with a resonance frequency of approximately 50 Hz or higher. Thus, when the input power of the carrier light is 4 mW, the resonant frequency of the optical spring should be approximately 4 Hz. The estimation of the impact of OPA is shown in Fig. 4.27. As the carrier light was amplified by a factor of 16.7 at resonance, the squeezing decay rate can be estimated to be approximately $\sigma = 0.76$. Fig. 4.27(b) shows that when the squeezing angle is controlled to maximize the intracavity power P_E , the optical spring constant k_{opt} would be enhanced by approximately 2.5 times, owing to the signal amplification effect. Therefore, the optical spring constant would be enhanced by a factor of approximately $6 \times 2.5 = 15$, and the resonant frequency of the optical spring can be

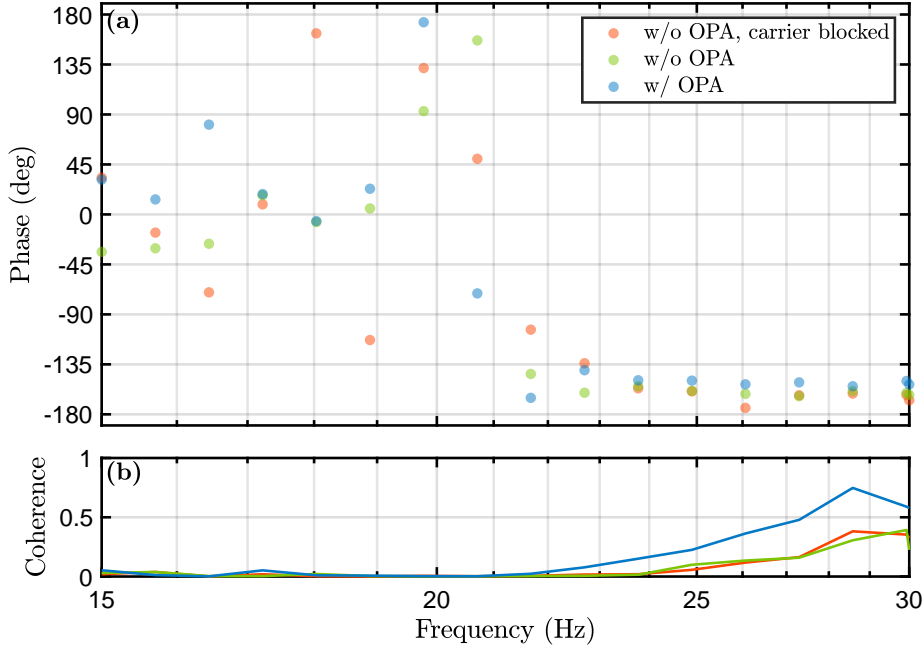


Fig. 4.26: (a) Phase measurement results of the susceptibility of the optomechanical oscillator. The input power of the carrier light was approximately 4 mW, and the carrier was amplified by a factor of up to 16.7. Normalized cavity detuning was controlled to $\delta \sim 1/\sqrt{3}$. (b) Coherence between the input and measured signals. The average numbers are 200 for all the measurements.

estimated to be approximately $4 \times \sqrt{15} \sim 15$ Hz. The resonant frequency of the compound spring was approximately $\sqrt{16^2 + 15^2} \sim 22$ Hz, and we had not been able to measure the optical spring as theoretically predicted.

It is difficult to confirm the effect of signal amplification with weak input power because strong light power amplification must be provided to observe an optical spring. Therefore, we considered injecting relatively strong input power and performing the OPA without changing the intracavity power. Only the signal amplification effect may be confirmed by comparing the optical spring constants. The input light power was set to 50 mW. In this case, the power amplification gain was decreased, and the squeezing decay rate was estimated to be approximately $\sigma = 0.39$. The estimation of the impact of OPA is shown in Fig. 4.28. The normalized intracavity power $P_{E'}$ without OPA is 0.5, and the same intracavity power is obtained with the OPA of the squeezing angle, i.e., $\theta/\pi \sim -0.35$ or $\theta/\pi \sim 0.10$. When $\theta/\pi \sim -0.35$, the optical spring constant would be enhanced by a factor of 1.4 owing to the signal amplification effect, and when $\theta/\pi \sim 0.10$, the optical spring constant would be attenuated by a factor of 0.8. Experimentally, the squeezing angle should be controlled so that the intracavity power is not changed from that without OPA. Signal amplification and signal attenuation can be switched by

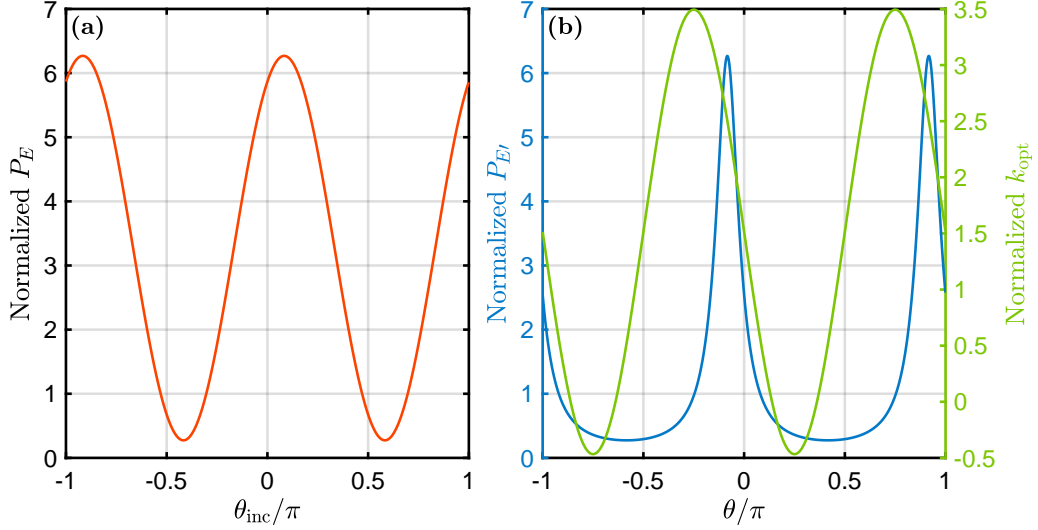


Fig. 4.27: Estimation of the impact of OPA. The parameters are set to $\sigma = 0.76$ and $\delta = 1/\sqrt{3}$. P_E and $P_{E'}$ are the intracavity power defined by Eqs. (4.10) and (4.13), respectively, and the optical spring constant k_{opt} for squeezing angle θ is shown. The left-hand vertical axes in (a) and (b) are normalized to be 1 when $\delta = 0$ and $\sigma = 0$. The right-hand vertical axis in (b) is normalized to be 1 when $\delta = 1$ and $\sigma = 0$.

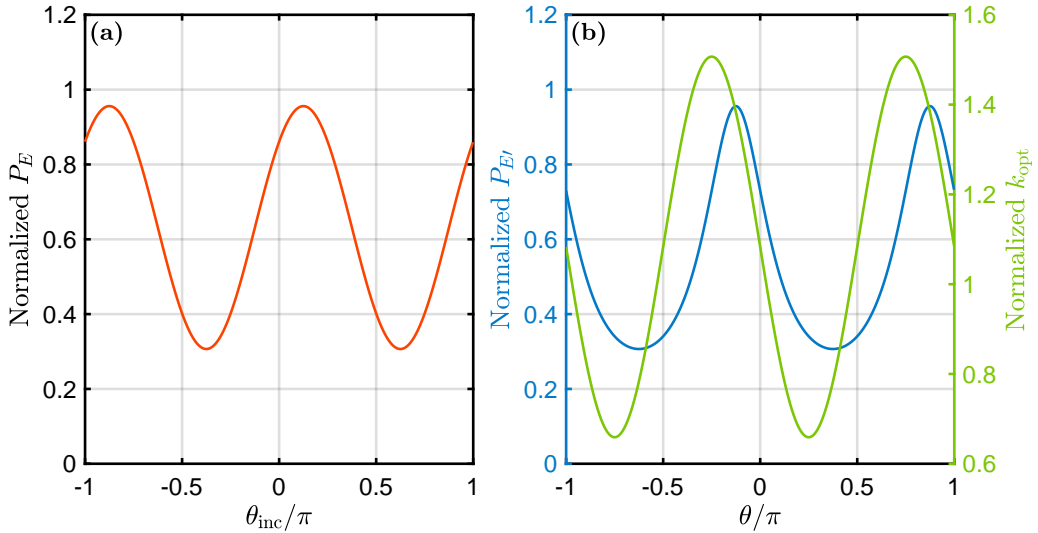


Fig. 4.28: Estimation of the impact of OPA. The parameters are set to $\sigma = 0.39$ and $\delta = 1$. The vertical axis is normalized in the same manner as in Fig. 4.27.

changing the polarity of the error signal.

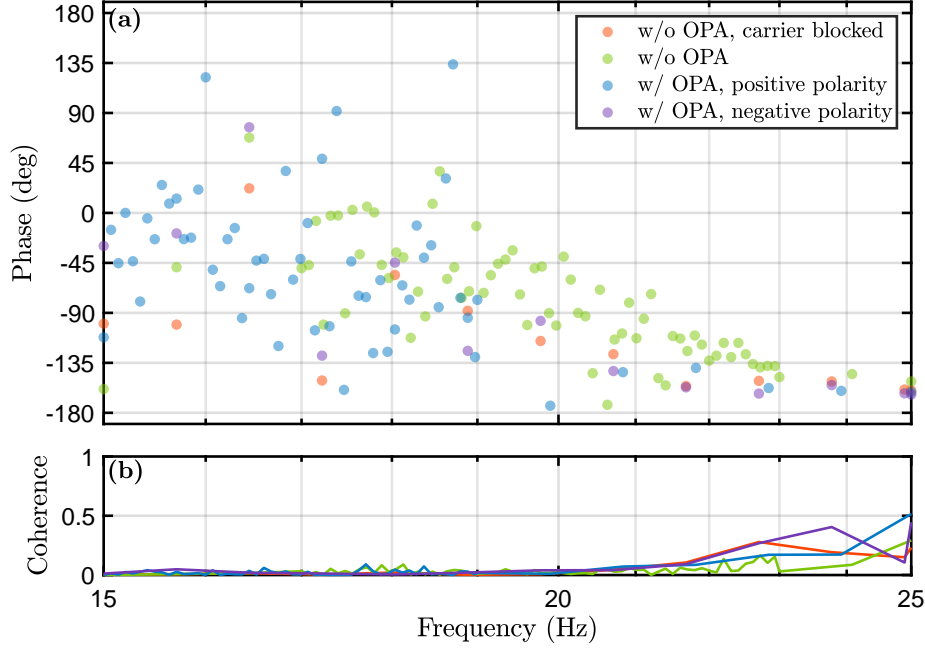


Fig. 4.29: (a) Phase measurement results of the susceptibility of the optomechanical oscillator. The input power of the carrier light was approximately 50 mW, and the carrier was amplified by a factor of up to 2.7. Normalized cavity detuning was controlled to $\delta \sim 1$. (b) Coherence between the input and measured signals. The average numbers are 200 for all the measurements.

The phase measurement results are shown in Fig. 4.29(a). The red circles correspond to the measurements in which the incident carrier light is blocked, and cavity detuning is controlled to $\delta \sim 1$ by the counterpropagating light. The oscillator was almost unaffected by the optical spring. The green circles correspond to the measurement with incident carrier light, and the impact of the optical spring appears because the incident carrier light is sufficiently strong. Although the resonance frequency is not accurately estimated in this measurement, we have generated a 50 Hz optical spring with a 600-mW carrier light; thus, in this case, we can estimate that the resonance frequency of the optical spring is approximately 14 Hz or higher. The blue and purple circles correspond to measurements with OPA, where the polarities of the feedback control signals for the squeezing angle are positive and negative, respectively. We have not identified which one corresponds to signal amplification. However, both possess resonant frequencies below 21 Hz. The resonant frequency of the optical spring enhanced by the signal amplification effect can be estimated at approximately $14 \times \sqrt{1.4} \sim 17$ Hz. The resonance frequency of the composite spring would become approximately $\sqrt{16^2 + 17^2} \sim 23$ Hz or higher. Even in this setting, we cannot measure the optical spring as theoretically

predicted.

4.3.6 Suppression of the OPA process

Despite achieving a condition in which an optical spring enhanced by the signal amplification effect can be observed with theoretical predictions, we could not confirm the enhancement of the optical spring in the transfer function measurements. In other words, the OPA process may not work as theoretically predicted. Fig. 4.30 shows the transmitted power of the carrier light with different OPA gains.

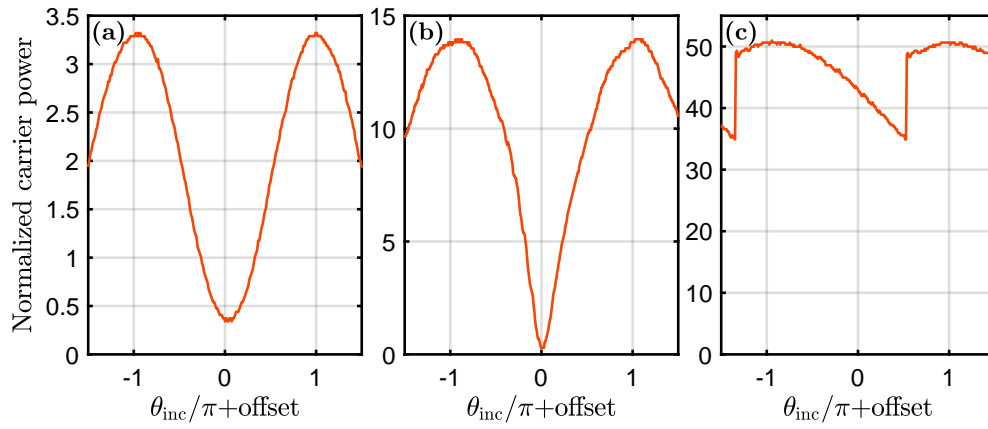


Fig. 4.30: Measured transmitted power of the carrier light. The input carrier light power is 4 mW, and normalized detuning is controlled to $\delta \sim 1/\sqrt{3}$. (a) corresponds to the low gain OPA, (b) corresponds to the high gain OPA, and (c) corresponds to the oscillation state.

Fig. 4.30(a) corresponds to the measurement with the OPA where the gain is sufficiently lower than the OPO threshold. As shown in Fig. 4.7(a), the theoretical transmitted power, in this case, depicts a sine wave; thus, the measurement results are consistent with the theory. Fig. 4.30(b) corresponds to the measurement with OPA close to the threshold. As the intracavity power increases, the sine wave gets distorted, indicating that the theoretical OPA cannot be achieved. As the measurement of the susceptibility of the optomechanical oscillator shown in the previous section was conducted with OPA close to the threshold, there is a possibility that, in this case, the OPA is not consistent with the theory. Fig. 4.30(c) corresponds to the measurement with OPA, where the gain is significantly higher than the threshold. In this case, a significant offset is added to the transmitted power because of the oscillation state. Moreover, we have found that sharp shifts in transmitted power are observed at certain squeezing angles.

OPA is an approximate solution when the attenuation of the pump light is negligible, as discussed in App. B.4.1. The distortion in the transmitted power is caused by amplification in the region where the attenuation of the pump light is non-negligible. In other words, the OPA process may not have been maintained, and

the signal amplification effect may have been suppressed. Furthermore, the signal amplification effect is not confirmed for amplification processes that do not modify the intracavity power. In this case, based on the energy conservation law, the light power of the pump light does not change. However, there is a significant amount of optical loss owing to the SHG effect caused by the robust intracavity power of the carrier light. The SHG loss would have been compensated by power amplification. In this case, the OPA process may not be maintained.

4.4 Summary of this chapter

This chapter investigated the conditions for conducting a proof-of-principle experiment of a signal amplification system in a Fabry-Perot cavity. The experiment was conducted using the OPA scheme. When we use a Fabry-Perot cavity, the optical spring constant should be normalized by the intracavity power because the intracavity power varies with cavity detuning and intracavity OPA. In addition, the squeezing angle in the Fabry-Perot cavity possesses a nonlinear relation with the squeezing angle in the DRMI. We need to estimate the correct squeezing angle with regard to the DRMI from the measurement of the intracavity power.

In the experiment, the optical spring enhanced by the signal amplification effect of the OPA was not observed. The intracavity carrier light power required to observe the optical spring was considerably strong that the attenuation of the pump light could not be neglected. Note that photothermal effects, which are discussed in the next chapter, might also have negligible impact. The threshold of the OPO limited the pump light power that can be incident to the cavity. To increase the relative light power of the pump light, the efficiency of the nonlinear optical effect must be reduced, and the threshold for oscillation must be increased. The intensity of the carrier light can be decreased by replacing the mirrors comprising the OPO cavity with a larger curvature and increasing the beam diameter. Moreover, the conversion efficiency can be decreased by reducing the finesse. However, in this case, the resonant frequency of the optical spring is significantly reduced with the finesse.

The attenuation of the pump light may be negligible by constructing a cavity for the pump light (green cavity). As discussed in App. B.4.2, OPO is a phenomenon based on the intracavity saturation of the carrier light. Similarly, if the pump light is saturated in the cavity, the attenuation in the OPO cavity may be neglected. The curved mirror that constitutes the OPO cavity of our experiment has remarkably high transmissivity for 532 nm; thus, the green cavity can be constructed to contain curved mirrors and a nonlinear optical crystal. However, the efficiency of the nonlinear optical effect must be significantly decreased because the pump light amplifies in the green cavity.

This experiment generated a measurable optical spring by increasing the intracavity power. In contrast, we can achieve a high signal amplification effect using OPA by decreasing the intracavity power. In other words, the resonant frequency of the optical spring may be increased by compensating for the weakened

intracavity power with a signal amplification effect. The estimation of the impact

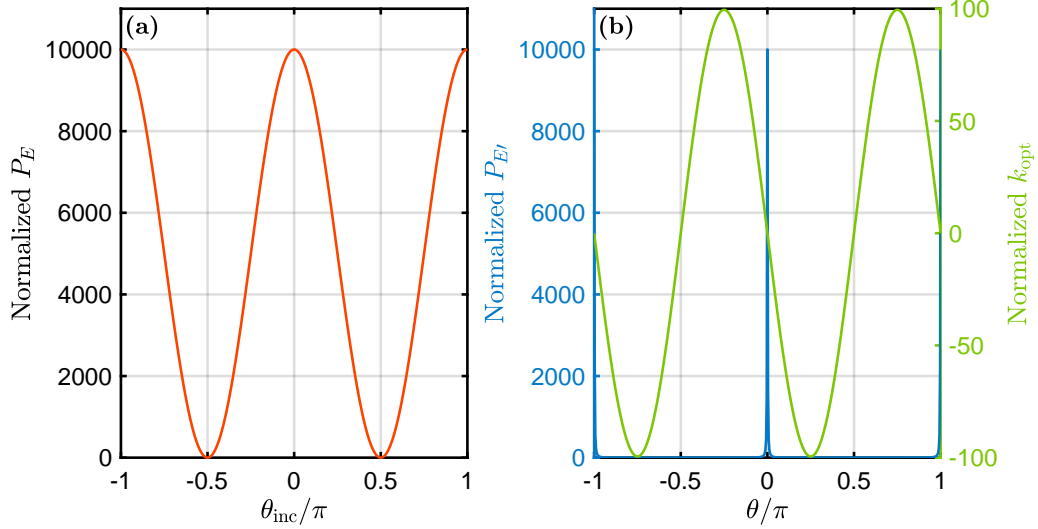


Fig. 4.31: Estimation of the impact of OPA. The parameters are set to $\sigma = 0.99$ and $\delta = 0$. The vertical axis is normalized in the same manner as in Fig. 4.27.

of OPA with $\sigma = 0.99$ is shown in Fig. 4.31, as an example that is extremely close to the oscillation state. The signal amplification factor is maximized when $\delta \simeq 0$. The normalized signal amplification factor possesses a maximum value of $2/(1 - \sigma^2)$, and the normalized power amplification factor possesses a maximum value of $1/(1 - \sigma)^2$. In other words, the maximum signal amplification factor is roughly the square root of the power amplification factor. In addition, strong power amplification and signal amplification cannot be achieved simultaneously.

When the signal amplification factor is maximized, the normalized power amplification factor becomes approximately 0.5, and the product of the input power and signal amplification factor is roughly proportional to the resonant frequency of the optical spring. As shown in Fig. 4.21, the maximum value of the power amplification factor is proportional to the -0.63 power of the input power; thus, the maximum value of the signal amplification factor can be estimated to be proportional to the -0.31 power of the input power. In other words, it is impossible to compensate for the power amplification factor based on the signal amplification effect, and the optical spring constant must decrease as the input power decreases.

Let the relationship between the input light power P_A and power amplification factor A be written as $A \sim (P_A)^a$. If there exists a regime where $a < -2$, the enhancement of the optical spring owing to the signal amplification effect becomes predominant. However, with strong signal amplification, the squeezing angle θ_{inc} must be controlled in a narrow range. For example, in the case shown in Fig. 4.31, the squeezing angle must be controlled in the range of $\theta_{\text{inc}} - \pi/2 = 0.005 \pm 0.002$ to maintain the signal amplification factor above 90. As it becomes difficult to control such a narrow range using the error signal obtained from the coherent

control method, we need to develop a new technique to obtain error signals with a very narrow linear range.

When the attenuation of the pump light is non-negligible, it is necessary to consider the general solution of coupled-wave equations for three-wave mixing. The analytical solution for a single pass was formulated by Jacobi's elliptic function [146]. Although the situation is somewhat different from our experiment, OPA caused by four-wave mixing in fiber has been simulated [147–149]. In the highly incident light intensity regime, the power amplification factor is proportional to the input power, similar to Fig. 4.21. Although additional complex simulations are required for three-wave mixing that occurs in the cavity, it may be possible to estimate the requirements to maintain the OPA process. If the OPA process is not maintained, the significance of the simulation no longer exists because there is no correspondence with intracavity squeezing in the gravitational wave detector.

We considered several ideas for improving the OPA experiment; however, a trade-off relationship with the magnitude of the optical spring constant existed. In other words, the OPA scheme cannot simultaneously achieve strong intracavity power and strong signal amplification effect. Implementing intracavity squeezing is related to not only OPA but also other nonlinear optical effects. We devised an experiment using the Kerr effect. As the Kerr effect increases with an increase in the intracavity power, a measurable optical spring can be generated and enhanced with a signal amplification effect. The next chapter discusses the photothermal effect, an essential characteristic of the signal amplification system based on the Kerr scheme.

Chapter 5

Photothermal effect on the signal amplification system

In the previous chapter, we conducted experiments based on the optical parametric amplification scheme; however, we were not able to measure the optical spring enhanced by the signal amplification effect. In addition, we found that it is necessary to develop a scheme that can simultaneously increase the intracavity power and signal amplification factor. Therefore, we planned to use the Kerr effect induced by the cascaded nonlinear optical effect. However, we found a problem associated with the photothermal effect because the Kerr scheme requires high intracavity power [150].

The photothermal effect is generally recognized as a harmful phenomenon that parasitizes the optical system. However, it is possible to design an optical interferometer with unusual properties by precisely modeling photothermal effects. In other words, the photothermal effect is not just a technical problem but an interesting phenomenon that can determine the fundamental concept of the optical system. This chapter discusses the impact of photothermal effects on the signal amplification system. We mainly discuss methods to eliminate the influence of photothermal effects; however, we investigate techniques to effectively utilize them as well.

5.1 Overview of photothermal effects in an optical interferometer

Let us consider an optical cavity that contains a medium that causes thermal absorption. The photothermal effect occurs when the absorbed laser light changes the crystal temperature, causing thermal expansion and thermo-optic effects. The impact of photothermal effects on an optical interferometer can be divided into two types: force and displacement. The photothermal force represents the force exerted on a mirror by thermal expansion, also known as the bolometric force [151–154]. The bolometric force acting on the test mass can modify the

optomechanical coupling [155–158]. The photothermal displacement represents the change in optical path length owing to thermal expansion and thermo-optic effect. A feedback mechanism can cancel the stationary photothermal displacement. However, as it takes a certain amount of time for the photothermal effect to reach an equilibrium state, the frequency response of the cavity can change owing to photothermal displacement [159].

Bolometric forces can be applied to optomechanical cooling. When the intracavity power changes owing to fluctuations in the test mass, the bolometric force fluctuates with a change in thermal absorption. This force involves a time delay that corresponds to the thermal relaxation rate. The self-cooling of the optomechanical oscillator via the photothermal effect can be achieved by enabling the bolometric force to counteract the fluctuation of the test mass. The cooling effect owing to the photothermal effect is significant in the unresolved sideband regime. In the early experiment of optomechanical cooling, the bolometric force contributed more to cooling than optical damping [156]. The heating process owing to the photothermal effect determines the cooling limit of such systems, which can be calculated based on the semiclassical theory of photon absorption shot noise [152].

In contrast, it has recently been revealed that even a change in the cavity length resulting from photothermal effects can cause remarkable phenomena. Photothermally induced transparency [160, 161] is a phenomenon that is analogous to electromagnetically induced transparency [162, 163] or optomechanically induced transparency [164–166], in which photothermal displacement results in an extremely narrow transmission window. In addition, when thermal absorption occurs faster than thermal relaxation, the photothermal effect modifies the frequency response of the cavity [159]. This phenomenon is caused by the displacement stored by the photothermal effect released during thermal relaxation, and the absorptive crystal behaves similarly to a capacitor in an electric circuit.

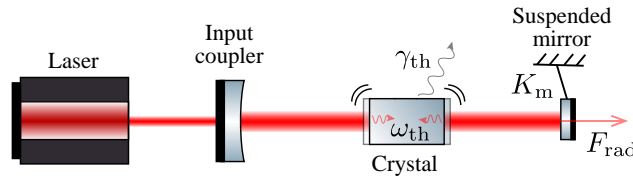


Fig. 5.1: Schematic of the optical cavity containing an absorptive crystal. The test mass is suspended by a mechanical spring with a complex spring constant K_m and receives radiation pressure force F_{rad} from the intracavity field. ω_{th} and γ_{th} are the characteristic frequencies of photothermal absorption and relaxation, respectively, which determine the impact of the photothermal effect.

The optical system under consideration is shown in Fig. 5.1. It is an optomechanical system that contains a crystal that causes thermal absorption. The photothermal displacement affects the optical cavity properties. Herein, the photothermal effect also modifies the optical spring constant because the effective cavity

length does not match the displacement of the test mass. More specifically, the real and imaginary components of the complex optical spring constant are converted into each other via the photothermal effect, which changes the susceptibility of the optomechanical oscillator. We found that the photothermal effect significantly deformed the transfer function of our experimental system. To accurately estimate the impact of intracavity squeezing on the optical spring, it is essential to estimate the photothermal effect.

5.2 Theoretical principles of the photothermal effect

5.2.1 Fundamental equations of the photothermal effect

Let us model the photothermal effect using the well-known fundamental equations for thermal absorption, thermal expansion, and thermal relaxation.

Let x_{act} denote the displacement of the test mass and x_{th} denote the photothermal displacement. The effective cavity length x in the optical system shown in Fig. 5.1 can be written as the sum of them:

$$x = x_{\text{act}} + x_{\text{th}}. \quad (5.1)$$

x_{th} is attributed to thermal expansion and thermo-optic effect. The effective thermal expansion coefficient for the sum of the two effects is defined as x_{th} differentiated by the temperature of the crystal T :

$$\frac{\partial x_{\text{th}}}{\partial T} = \alpha L', \quad (5.2)$$

that is,

$$\frac{\partial x_{\text{th}}}{\partial t} = \alpha L' \frac{\partial T}{\partial t}, \quad (5.3)$$

where L' denotes the crystal length, and α denotes the coefficient of linear thermal expansion. Therefore, x_{th} is proportional to the difference between the temperature T and surrounding temperature T_0 of the crystal:

$$x_{\text{th}} = \alpha L' (T - T_0). \quad (5.4)$$

Herein, we refer to the region that contributes to the photothermal effect as a crystal.

The crystal temperature depends on the heat inflow into and out of the crystal. The absorption of laser light causes heat inflow. The time rate of the heat flowing into the crystal w is proportional to the intracavity power P :

$$w = \alpha' L' P, \quad (5.5)$$

where α' denotes the thermal absorption coefficient. Heat outflow can be caused by various factors, which can be divided into two categories, i.e., thermal radiation and others. As thermal radiation can be negligible when the difference between T and T_0 is small, only heat outflow caused by heat conduction, heat transfer, and other related phenomena should be considered. These are proportional to $T - T_0$. The time rate of heat flow out of the crystal q can be written as

$$q = \frac{T - T_0}{k}, \quad (5.6)$$

where k denotes thermal resistance. The time derivative of the temperature T is proportional to the net heat obtained by the crystal:

$$\frac{\partial T}{\partial t} = \frac{1}{C}(w - q), \quad (5.7)$$

where C denotes the heat capacity.

Although the photothermal effect changes the effective cavity length, intracavity power P can be formulated similarly described in previous chapters by defining cavity detuning to include the photothermal displacement. In other words, with the finesse \mathcal{F} and input power P_0 , it can be written as

$$P = \frac{2\mathcal{F}}{\pi} \frac{1}{1 + \delta^2} P_0, \quad (5.8)$$

where δ denotes normalized cavity detuning:

$$\delta = \frac{2\mathcal{F}\omega_0}{\pi c} x. \quad (5.9)$$

Note that δ is not proportional to x_{act} , indicating that the photothermal effect modifies the time and frequency responses of the cavity.

5.2.2 Time response of the cavity with photothermal effect

When sufficiently large photothermal effects are induced, the time response of the cavity, such as the spectrum that can be obtained by the cavity scan, is modified. Based on the equations with regard to the photothermal effect defined in the previous subsection, the differential equation for the photothermal effect can be derived. Herein, we formulate the differential equations for x_{act} and δ to derive the change in the effective cavity length for the mirror displacement. Based on the time differentiation of Eq. (5.9), we obtain

$$\begin{aligned} \frac{\partial \delta}{\partial t} &= \frac{2\mathcal{F}\omega_0}{\pi c} \left(\frac{\partial x_{\text{th}}}{\partial t} + \frac{\partial x_{\text{act}}}{\partial t} \right) \\ &= \frac{2\mathcal{F}\omega_0}{\pi c} \left[\frac{\alpha L'}{C}(w - q) + \frac{\partial x_{\text{act}}}{\partial t} \right]. \end{aligned} \quad (5.10)$$

Here, q can be written as

$$\begin{aligned} q &= \frac{1}{k\alpha L'} x_{\text{th}} \\ &= \frac{1}{k\alpha L'} \left(\frac{\pi c}{2\mathcal{F}\omega_0} \delta - x_{\text{act}} \right), \end{aligned} \quad (5.11)$$

yielding the following equation:

$$\frac{\partial \delta}{\partial t} = -\frac{1}{kC} \delta + \frac{4\mathcal{F}^2 \omega_0 \alpha \alpha' L'^2 P_0}{\pi^2 c C} \frac{1}{1 + \delta^2} + \frac{2\mathcal{F}\omega_0}{\pi c} \left(\frac{1}{kC} x_{\text{act}} + \frac{\partial x_{\text{act}}}{\partial t} \right). \quad (5.12)$$

Further differentiating this equation with time, we obtain the second-order differential equation for δ when the test mass is moved at a constant velocity of $v = \partial x_{\text{act}}/\partial t$:

$$\frac{\partial^2 \delta}{\partial t^2} = \left(\frac{8\mathcal{F}^2 \omega_0 \alpha \alpha' L'^2 P_0}{\pi^2 c C} \frac{\delta}{(1 + \delta^2)^2} - \frac{1}{kC} \right) \frac{\partial \delta}{\partial t} + \frac{2\mathcal{F}\omega_0 v}{\pi c k C}. \quad (5.13)$$

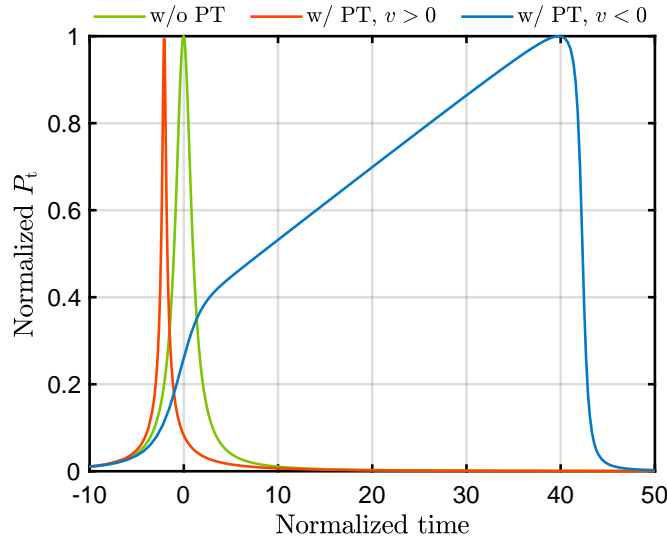


Fig. 5.2: Simulation results of the spectrum with the photothermal (PT) effect. The vertical axis denotes transmitted power, which is normalized to be 1 in the resonant state. The horizontal axis is normalized so that the half-width at half maximum of the spectrum without the photothermal effect equals 1. We used $8\mathcal{F}^2 \omega_0 \alpha \alpha' L'^2 P_0 / (\pi^2 c C) = 8$, $1/(kC) = 0.07$ and $2\mathcal{F}\omega_0 |v| / (\pi c k C) = 0.1$ as dimensionless parameters. The red and blue lines denote the cases with photothermal effects, and these cases use the same velocity magnitude $|v|$.

The simulation results of the intracavity power obtained from Eq. (5.13) are illustrated in Fig. 5.2. The qualitative explanation when $\alpha > 0$ is as follows. When the test mass is moved at a constant velocity without the photothermal effect,

a Lorentzian spectrum is obtained regardless of the direction of the movement. When the photothermal effect is included, significantly different spectra are obtained depending on the direction of the movement of the test mass. The cavity reaches the resonant state quickly for $v > 0$ because of increased thermal absorption while approaching the resonant state. Thus, a spectrum with a narrower linewidth is obtained than the case without the photothermal effect. In contrast, for $v < 0$, the photothermal effect cancels out the change in the test mass, resulting in a spectrum with an extremely broad linewidth than without the photothermal effect [139, 159, 160, 167–170]. Note that the spectrum distortion depends on not only the magnitude of the photothermal effect but also the velocity of the test mass because it takes a certain amount of time for photothermal absorption and relaxation. If the test mass is moved faster than the occurrence of the photothermal effect, the time response of the cavity results in the same response as in the case of the absence of the photothermal effect.

5.2.3 Frequency response of the cavity with photothermal effect

As discussed in the last subsection, in a band sufficiently lower than the time rate at which the photothermal effect occurs, the time response of the cavity is modified as the cavity length changes owing to thermal expansion. It implies that the photothermal effect can modify the frequency response of the cavity in a frequency band that is sufficiently lower than the characteristic frequency of the photothermal effect. Here, we derive the characteristic frequencies of the photothermal effect and investigate the frequency response of the cavity with the photothermal effect.

The relationship between cavity detuning and the displacement of the test mass is expressed in Eq. (5.12); however, the second term on the right-hand side of this equation is nonlinear for δ . We assume that δ is feedback controlled to a constant value and consider the linear response to the first-order small fluctuating term. We can approximate it with $\delta(t) = \delta_0 + d\delta(t)$ as follows:

$$\frac{1}{1 + \delta(t)^2} \simeq \frac{1}{1 + \delta_0^2} - \frac{2\delta_0}{(1 + \delta_0^2)^2} d\delta(t). \quad (5.14)$$

The same is applied for the displacement of the test mass and photothermal displacement: $x_{\text{act}}(t) = \bar{x}_{\text{act}} + dx_{\text{act}}(t)$ and $x_{\text{th}}(t) = \bar{x}_{\text{th}} + dx_{\text{th}}(t)$. The effective cavity length can be denoted as $x(t) = \bar{x} + dx(t)$ with $\bar{x} = \bar{x}_{\text{act}} + \bar{x}_{\text{th}}$ and $dx = dx_{\text{act}} + dx_{\text{th}}$. From Eq. (5.12), we obtain the differential equation for the first-order small fluctuating term. The Fourier transform of this equation can be

written as

$$i\Omega dx(\Omega) = - \left(\frac{1}{kC} + \frac{8\mathcal{F}^2\omega_0\alpha\alpha' L'^2 P_0}{\pi^2 cC} \frac{\delta_0}{(1+\delta_0)^2} \right) dx(\Omega) + \left(\frac{1}{kC} + i\Omega \right) dx_{\text{act}}(\Omega). \quad (5.15)$$

Here, we consider that $d\delta(\Omega)$ is proportional to $dx(\Omega)$ obtained from Eq. (5.9). We obtain the frequency response of the cavity, which is the response from the displacement of the test mass $dx_{\text{act}}(\Omega)$ for the effective cavity length $dx(\Omega)$:

$$H_{\text{th}}(\Omega) = \frac{dx(\Omega)}{dx_{\text{act}}(\Omega)} = \frac{\gamma_{\text{th}} + i\Omega}{(\omega_{\text{th}} + \gamma_{\text{th}}) + i\Omega}, \quad (5.16)$$

where

$$\omega_{\text{th}} = \frac{8\mathcal{F}^2\omega_0\alpha\alpha' L'^2 P_0}{\pi^2 cC} \frac{\delta_0}{(1+\delta_0)^2}, \quad \gamma_{\text{th}} = \frac{1}{kC} \quad (5.17)$$

denote the characteristic frequencies of photothermal absorption and relaxation, respectively. We refer to ω_{th} as the photothermal absorption rate and γ_{th} as the photothermal relaxation rate.

Eq. (5.16) is the same function as phase lead compensation, which possesses one pole and one zero. When the photothermal absorption rate is sufficiently large ($|\omega_{\text{th}}| \gtrsim \gamma_{\text{th}}$), the photothermal effect cannot be negligible. The qualitative explanation with $\alpha > 0$ and $\delta_0 > 0$ based on the analogy with an electric circuit are as follows. When the mirror is moved at a frequency sufficiently larger than ω_{th} , the photothermal effect is not apparent because the phase of the signal reverses before the cavity length changes owing to thermal expansion. When the mirror is moved at a frequency comparable to ω_{th} , the phase of the frequency response function leads because the cavity length stored owing to thermal expansion is released as changes in the signal. When the mirror is moved at a frequency sufficiently smaller than γ_{th} , the phase does not change because the photothermal effect reaches thermal equilibrium. However, the gain is reduced because the photothermal effect cancels the displacement of the mirror.

It should also be noted that the sign of the poles of the frequency response function can be inverted depending on the values of α and δ_0 . If a positive optical spring is generated ($\delta_0 > 0$) and the negative thermo-optic effect exceeds the thermal expansion ($\alpha < 0$), the photothermal effect can induce instability in the optical system or control system. As a result, non-stationary photothermal effects significantly influence the response of the entire system [169, 171].

5.2.4 Photothermal effect on an optical spring

Let us discuss the impact of the photothermal effect on an optical spring. In the system illustrated in Fig. 5.1, the bolometric force is not acting on the test mass; thus, the radiation pressure force should be considered. The radiation pressure

force acting on the test mass is proportional to the intracavity power. As obtained from Eqs. (5.8) and (5.14), the intracavity power is proportional to a fluctuation in the cavity length $d\delta(\Omega)$. We denote the radiation pressure force fluctuation by $dF_{\text{rad}}(\Omega)$. There is a proportionality relation between them, and the proportionality coefficient $K_{\text{opt}}(\Omega)$ denotes the complex optical spring constant:

$$dF_{\text{rad}}(\Omega) = -K_{\text{opt}}(\Omega)dx(\Omega). \quad (5.18)$$

This relationship holds with or without the photothermal effect. However, it should be noted that the effective cavity length does not correspond to the displacement of the test mass. We obtain $dx = H_{\text{th}}dx_{\text{act}}$ from Eq. (5.16); thus, the optical spring constant for the test mass can be written as $K_{\text{opt-th}} = H_{\text{th}}K_{\text{opt}}$.

If the frequency band is sufficiently lower than the cavity decay rate, the complex optical spring constant can be written as $K_{\text{opt}} = k_{\text{opt}} + i\Gamma_{\text{opt}}\Omega$, where k_{opt} denotes the optical spring constant and Γ_{opt} denotes the optical damping constant. As the influence of Γ_{opt} on the susceptibility of the optomechanical oscillator can be negligible in our experimental system, we obtain the following equation:

$$K_{\text{opt-th}} \simeq \frac{(\omega_{\text{th}} + \gamma_{\text{th}})\gamma_{\text{th}} + \Omega^2 + i\omega_{\text{th}}\Omega}{(\omega_{\text{th}} + \gamma_{\text{th}})^2 + \Omega^2} k_{\text{opt}}. \quad (5.19)$$

This equation indicates that the photothermal effect converts the real component of the optical spring constant into an imaginary component [138, 139, 170]. In particular, if ω_{th} is positive and sufficiently large, the real and imaginary components of the optical spring can be positive. In other words, a single carrier can generate a stable optical spring using the photothermal effect.

Even a slight photothermal effect can generate non-negligible optical damping when the mechanical oscillator possesses a high Q factor. It significantly modifies the susceptibility of the optomechanical oscillator $\chi_{\text{eff}}(\Omega)$, which can be written as follows:

$$\chi_{\text{eff}}(\Omega) = \frac{dx_{\text{act}}(\Omega)}{dF_{\text{ext}}(\Omega)} = \frac{1}{-m\Omega^2 + K_{\text{m}} + K_{\text{opt-th}}}, \quad (5.20)$$

where $dF_{\text{ext}}(\Omega)$ denotes the small external force applied to the oscillator, m denotes the effective mass of the oscillator, and K_{m} denotes the complex mechanical spring constant, which can be written as $K_{\text{m}} = k_{\text{m}} + i\Omega\Gamma_{\text{m}}$ with the mechanical spring constant k_{m} and the mechanical damping constant Γ_{m} . For simplicity, we consider the case where the frequency band is sufficiently lower than the characteristic frequencies of the photothermal effect ($\Omega \ll |\omega_{\text{th}}|, \gamma_{\text{th}}$). When the photothermal absorption and relaxation rates are equal ($\omega_{\text{th}} = \gamma_{\text{th}}$), optical damping produced by the photothermal effect becomes maximum. In this case, the Q factor of the optical spring can be calculated as

$$\left. \frac{\Im(K_{\text{opt-th}}/\Omega)}{\sqrt{m\Re(K_{\text{opt-th}})}} \right|_{\Omega \rightarrow 0} \simeq \frac{1}{2\sqrt{2}} \frac{\Omega_{\text{opt}}}{\gamma_{\text{th}}}, \quad (5.21)$$

where $\Omega_{\text{opt}} = \sqrt{k_{\text{opt}}/m}$ denotes the resonant frequency of the optical spring. In some cases, photothermal effects can produce significant optical damping, resulting in an overdamped system.

We can appropriately model the photothermal effect by estimating the photothermal absorption rate ω_{th} and photothermal relaxation rate γ_{th} . There are two possible methods for estimating these parameters: one is to measure H_{th} , and the other is to measure χ_{eff} . H_{th} can be obtained by measuring the transfer function from the displacement of the mirror to the transmitted light using an actuator with a sufficiently higher mechanical resonance frequency than the optical spring, e.g., a PZT. However, the phase lead caused by the photothermal effect can be measured only when thermal absorption is sufficiently faster than the thermal relaxation ($\omega_{\text{th}} > \gamma_{\text{th}}$). In contrast, χ_{eff} can be measured using a suspended mirror. In the case of $\omega_{\text{th}} \lesssim \gamma_{\text{th}}$, photothermal effects can significantly modify χ_{eff} . Even a minor photothermal effect, which cannot be estimated by measuring the frequency response of the cavity, could potentially be estimated via a measurement of the susceptibility of the optomechanical oscillator.

5.3 Experiments on the photothermal effect

The experiment of this section aims to investigate the influence of photothermal effects on the intracavity signal amplification system. Based on the discussion in the previous section, we found that it is sufficient to estimate the photothermal absorption and relaxation rates to model the photothermal effect. We report the measurement results of various phenomena caused by the photothermal effect, intending to estimate these parameters.

5.3.1 Experimental setup

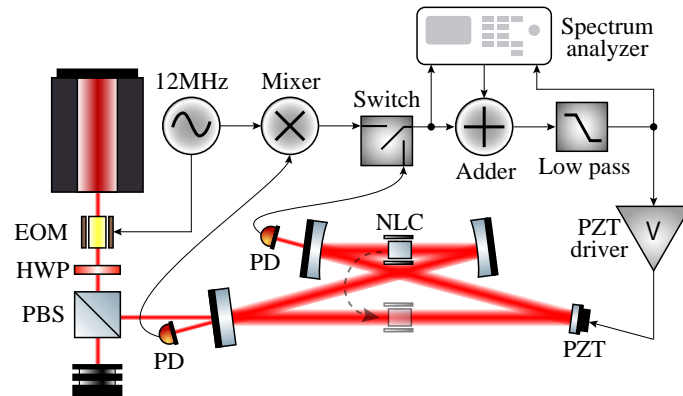


Fig. 5.3: Experimental setup using a PZT. Abbreviations are defined as follows: photodetector (PD), half-wave plate (HWP), polarization beam splitter (PBS), electro-optic modulator (EOM), and nonlinear optical crystal (NLC).

We can directly measure H_{th} using an actuator with a resonant frequency sufficiently higher than that of the optical spring, e.g., a PZT. The experimental setup using a PZT is shown in Fig. 5.3. We use the OPO cavity configured in the previous chapter for the optical system. The characteristics of the mirrors that compose the cavity are listed in Tab. 5.1. The phase of the incident light was modulated us-

Table 5.1: Mirrors that constitute the cavity for the photothermal experiment.

Name	Manufacturer	Number	Reflectance	AOI	ROC
Input coupler	Layertec	104373	= 94%@1064	6 degrees	flat
Curved mirror	Newport&LMA	SPC025	= 99.95%@1064	15 degrees	68.5 mm
Small mirror	Edmund	#38-901	> 99.8%@1064	0 ~ 45 degrees	flat

ing EOM, and we adjusted the input power using the HWP and PBS. We measured the transmitted light and reflected light for the error signal; the former was used for operating points with large cavity detuning, and the latter was used for operating points with small cavity detuning via the Pound-Drever-Hall method [140]. The beam waist exists in two points, i.e., between the curved mirrors and the flat mirrors, with a radius of approximately $40 \mu\text{m}$ and $300 \mu\text{m}$. Unless otherwise noted, NLC was installed in the former waist; however, when the mode mismatch caused by the thermal lensing effect became severe, NLC was re-installed in the latter waist. We measured the transfer function by taking the ratio of the input to the adder to the output of the filter circuit.

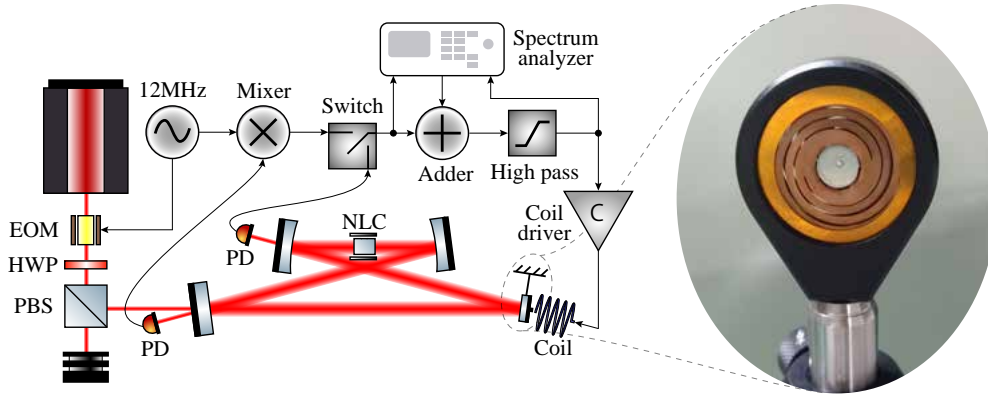


Fig. 5.4: Experimental setup using a suspended mirror.

We can measure χ_{eff} using an actuator whose resonance frequency is sufficiently lower than the optical spring. The experimental setup with a suspended mirror is shown in Fig. 5.4. A high-pass filter (phase lead compensation filter) is used to control the suspended mirror with a coil magnet actuator. The suspended mirror is the same model that is used as the mirror glued to the PZT shown in Fig. 5.3.

We used either periodically poled LiNbO_3 (PPLN) or periodically poled KTiOPO_4 (PPKTP) as the NLC. The lengths of both crystals are $L' = 10 \text{ mm}$. In this chapter, we measured transfer functions with extreme phase mismatch

conditions to reduce the influence of nonlinear optical effects as much as possible. For example, PPKTP used in our experiments is phase-matched at approximately 35°C . Nevertheless, in the transfer function measurement described in Sec. 5.3.6, we heated the crystal to 120°C to break the phase-matching condition and minimize the loss caused by the second harmonic generation. The finesse was estimated to be $\mathcal{F} = 100 \pm 10$ for both crystals by measuring with weak incident light of approximately 5 mW.

5.3.2 Cavity spectrum with the photothermal effect

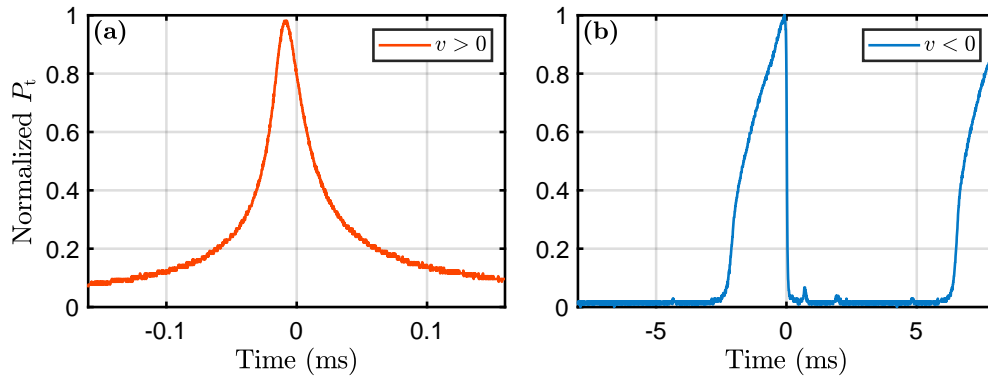


Fig. 5.5: Transmission power obtained from the cavity scan. The magnitude of the velocity of the mirror movement v is adjusted to be approximately the same for each measurement. Note that the horizontal axis denotes time; however, the scale differs by about two orders of magnitude in each plot.

First, we measured the transmitted power obtained from the cavity scan using the setup illustrated in Fig. 5.3. We used a PPLN crystal as the NLC. The measurement results are shown in Fig. 5.5. Fig. 5.5(a) shows the transmitted power when the mirror is moved to increase the cavity length, and the line width becomes narrower than in the absence of the photothermal effect. Fig. 5.5(b) shows the transmitted power when the mirror is moved to decrease the cavity length, and a unique spectrum is observed that takes a lot of time to reach the resonance state. We found $\alpha > 0$ because the cavity length increases as the intracavity power increases. These tendencies are consistent with the simulation results described in Fig. 5.2. We attempted to estimate photothermal parameters from the measured spectra. However, there was a significant difference between the theoretical model and measured results. The discrepancy may be because of the poor linearity of the PZT. Another possibility is that the photothermal relaxation rate was not constant because the intracavity power slowly changed, as discussed later.

5.3.3 Slow photothermal effect

There is one approach to estimate the parameters of the photothermal effect, i.e., to measure the temperature of the crystal. Our experimental system is equipped with a crystal heater and thermometer for phase matching. We measured the time variation of the crystal temperature and attempted to estimate the parameters.

Let us consider heating the crystal to temperature T_1 using a heater and then switching off the heater and cooling it down to temperature T_0 . From Eq. (5.7), we obtain the differential equation for the crystal temperature T as

$$\frac{\partial T}{\partial t} = -\frac{T - T_0}{Ck}. \quad (5.22)$$

The initial condition is $T(0) = T_1$. The time variation of T can be written as

$$T(t) = (T_1 - T_0)e^{-t/(Ck)} + T_0. \quad (5.23)$$

Next, let us consider heating a crystal with an initial temperature of T_0 at a constant heat rate of w_0 . The differential equation of this case is

$$\frac{\partial T}{\partial t} = \frac{w_0}{C} - \frac{T - T_0}{Ck}, \quad (5.24)$$

and the initial condition is $T(0) = T_0$. The time variation of T can be written as

$$T(t) = kw_0 \left(1 - e^{-t/kC}\right) + T_0. \quad (5.25)$$

First, we measured the temperature change during the cooling of the PPLN from approximately 50 °C to room temperature. The temperature change is shown in Fig. 5.6. We initially attempted fitting using the whole time data indicated with a red line; however, the measured data significantly deviated from Eq. (5.23). We concluded that thermal radiation was not negligible because of the significant temperature difference between the crystal and its surroundings. By fitting only data below 23 °C, we can estimate that $1/Ck = 1.1 \times 10^{-3} \text{ s}^{-1}$ and $T_0 = 22 \text{ °C}$. The theoretical curve derived from these parameters is indicated with a green line. The time rate of heat outflow by thermal radiation q' can be written as

$$q' = l(T^4 - T_0^4), \quad (5.26)$$

with l as the proportionality constant. The blue line indicates the simulation results with $l/C = 1.6 \times 10^{-8} \text{ s}^{-1} \text{ K}^{-3}$. The measurement results well agree with the results of the theoretical model, including thermal radiation.

Next, we measured the temperature change when the cavity was locked at approximately $\delta_0 = 1.0$, and the crystal absorbed a constant amount of heat. We injected approximately 600 mW. The temperature change is shown in Fig. 5.7. The blue line indicates the simulation results with $w_0/C = 2.1 \times 10^{-3} \text{ K/s}$.

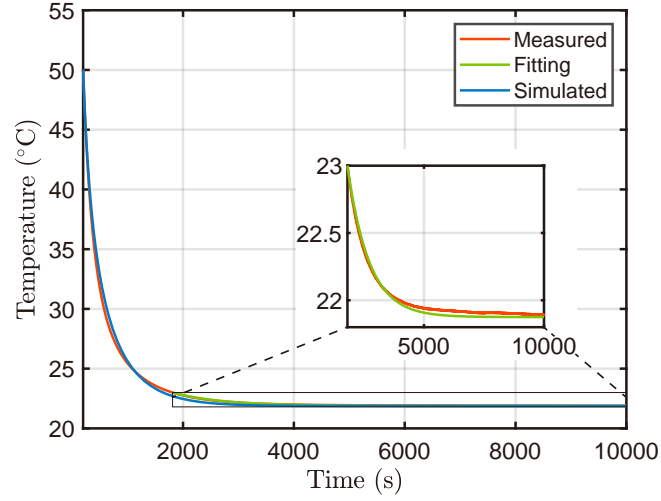


Fig. 5.6: Measurement results of slow thermal relaxation. The red line indicates the measurement results, the green line indicates the fitting results using the data below 23 °C ignoring the thermal radiation, and the blue line indicates the simulation results using the whole time data, including thermal radiation.

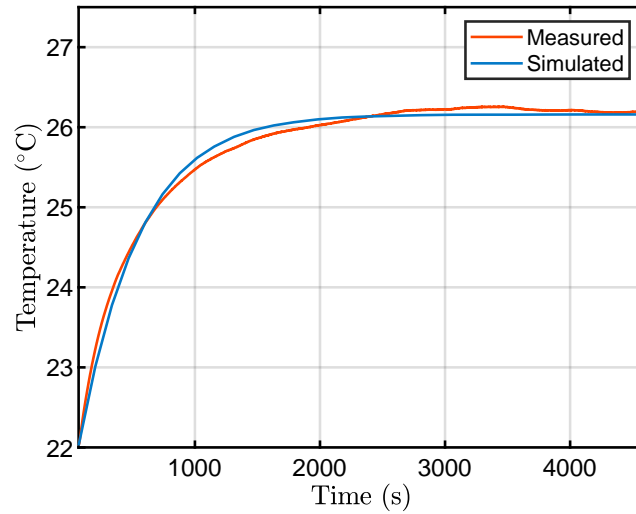


Fig. 5.7: Measurement results of slow photothermal absorption. The red line indicates the measurement results, and the blue line indicates the simulation results, including thermal radiation.

In summary, thermal absorption and relaxation occur at a very slow timescale. However, photothermal parameters that can be estimated based on these measurements were quite different from those estimated based on transfer function measurements. The experimental results reflect that we can only measure the temperature of the crystal surface if the measurement takes so long time that the temperature of the entire crystal becomes uniform. The temperature inside the crystal cannot be measured using this technique to estimate the photothermal parameters related to the modification of the optical spring.

5.3.4 Self-locking of the cavity based on the photothermal effect

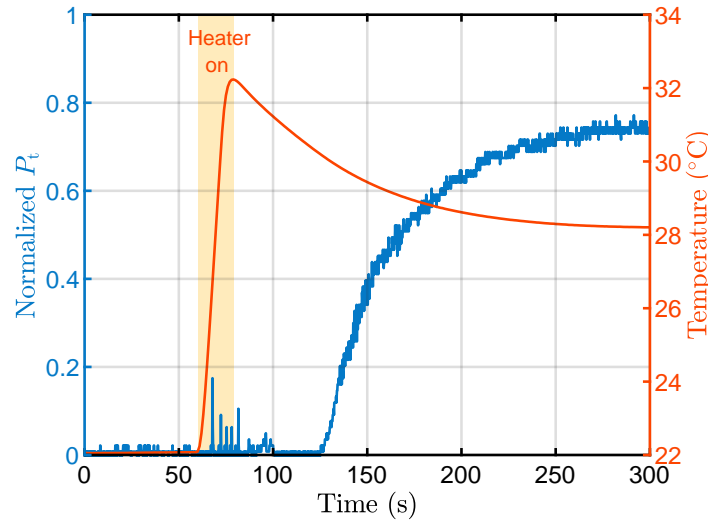


Fig. 5.8: Temperature and transmitted power during the self-locking of the cavity based on the photothermal effect. The crystal is heated for 60 ~ 79 s, filled in yellow.

The cavity can be locked without a feedback control mechanism by using the photothermal effect that cancels out the change in the cavity length [139, 168]. In particular, our experimental system was equipped with a heater of the nonlinear optical crystal, which allows the locking of the cavity using the temperature controller. Fig. 5.8 shows the self-locking of the cavity based on the photothermal effect. The crystal is around room temperature, and the cavity is out of the resonant state for 0 ~ 60 s. The heater was switched on for 60 ~ 79 s, and the crystal was heated at a constant amount of heat. At this time, some resonance peaks are observed because the cavity length is extended by a few μm owing to thermal expansion. After the heater is switched off, a slow thermal relaxation occurs, and the cavity length decreases as the crystal temperature decreases. However, after 130 s, the cavity is close to the resonance state, the intracavity power becomes robust, and the heat inflow caused by the thermal absorption of the laser light starts.

The self-locking of the cavity is achieved when thermal equilibrium is established, where thermal relaxation and absorption are balanced.

5.3.5 Transfer function measurement with a PZT

If the photothermal absorption rate ω_{th} is sufficiently larger than the photothermal relaxation rate γ_{th} , the photothermal effect modifies the frequency response of the cavity. The PPLN crystal possesses a relatively large thermal absorption coefficient, and the condition $\omega_{th} \gtrsim \gamma_{th}$ can be easily achieved. We measured H_{th} with the setup illustrated in Fig. 5.3. However, when we injected an intense laser light with a power of approximately 600 mW, the mode mismatch caused by the thermal lensing effect could not be neglected; thus, the PPLN crystal was re-installed at the beam waist of 300 μm . Then, the crystal clipped the beam, and the finesse was reduced to approximately $\mathcal{F} = 70 \pm 10$. Even under these conditions, ω_{th} was sufficiently large to measure the phase change caused by the photothermal effect.

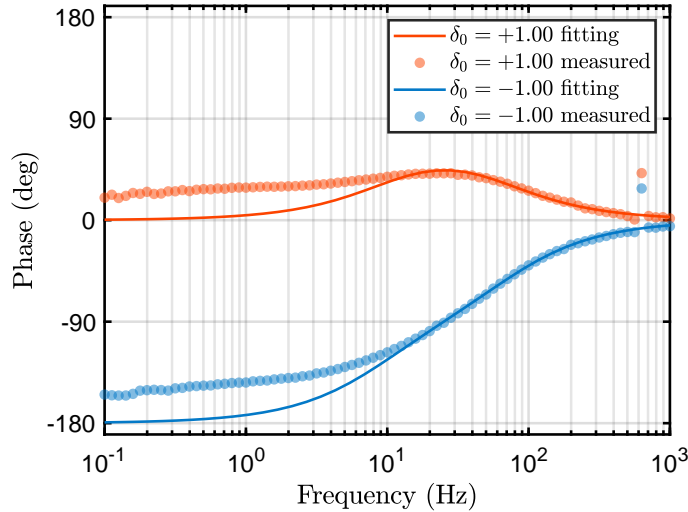


Fig. 5.9: Phase measurement results of the frequency response of the cavity H_{th} using a PPLN crystal. Only data above 15 Hz were used for fitting.

The measurement results of H_{th} with $P_0 = 600$ mW and $|\delta_0| = 1.00 \pm 0.02$ is shown in Fig. 5.9. The red and blue circles show the measured data, corresponding to positive and negative cavity detuning, respectively. As discussed in Sec. 5.2.3, the phase leads when cavity detuning is positive. In contrast, when cavity detuning is negative, the sign of the poles is reversed, and the phase in the low-frequency band becomes -180 degrees. However, it does not agree with theoretical predictions below approximately 15 Hz. We concluded that the effective specific heat capacity might be increased when the signal slowly varied because the region contributing to the photothermal relaxation was expanded. As discussed in Sec. 5.3.3, γ_{th} has a frequency dependence that decreases in the low-frequency band. The red

and blue solid lines indicate the results of fitting the respective data above 15 Hz. The theoretical model and measured data are in high precision agreement above 15 Hz.

The estimated parameters are $\omega_{\text{th}}/2\pi = 51.7 \pm 4.4 \text{ Hz}$ and $\gamma_{\text{th}}/2\pi = 12.0 \pm 1.5 \text{ Hz}$ for $\delta_0 = 1.00$, and $\omega_{\text{th}}/2\pi = -79.3 \pm 20.5 \text{ Hz}$ and $\gamma_{\text{th}}/2\pi = 8.95 \pm 5.4 \text{ Hz}$ for $\delta_0 = -1.00$. Note that the parameter estimation accuracy is low for $\delta_0 < 0$ because the transfer function does not change significantly as these parameters change. We can simultaneously estimate ω_{th} and γ_{th} at high accuracy by measuring H_{th} with $\delta_0 > 0$. However, it is necessary to achieve the condition $\omega_{\text{th}} \gtrsim \gamma_{\text{th}}$.

In addition, as described in the following subsection, we used a PPKTP crystal to measure the optical spring and needed to measure γ_{th} in advance. γ_{th} does not depend on δ_0 . We measured H_{th} using the PPKTP crystal with multiple values of δ_0 and estimated γ_{th} at high accuracy. The crystal was installed at the beam waist of $40 \mu\text{m}$ because the PPKTP crystal possessed a relatively small thermo-optic coefficient, and the thermal lensing effect was negligible. The estimation results

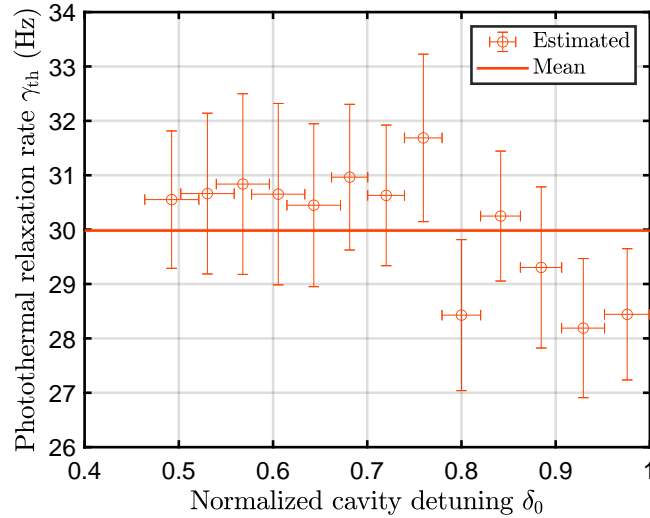


Fig. 5.10: Estimation of the photothermal relaxation rate γ_{th} for a PPKTP crystal. The input power is 600 mW, and we use only the data with around $\delta_0 \sim 1/\sqrt{3}$. The red circles indicate the estimated value from the phase measurements of H_{th} , and the red line indicates their weighted average. The error bars on the vertical and horizontal axes indicate the standard error estimated from fitting and the setting error of δ_0 estimated from the fluctuations in the transmitted light, respectively.

of γ_{th} for the PPKTP crystal are shown in Fig. 5.10. PPKTP possesses a larger γ_{th} and smaller ω_{th} than PPLN, so that $\omega_{\text{th}} \sim \gamma_{\text{th}}$ with $P_0 = 600 \text{ mW}$ and $\delta_0 \sim 1$. We estimated γ_{th} using measurements where ω_{th} is reasonably large. By taking a weighted average with the inverse of the variance as the weight, we obtained $\gamma_{\text{th}} = 30.0 \pm 0.3 \text{ Hz}$.

5.3.6 Transfer function measurement with a suspended mirror

Before measuring the optical spring with photothermal effect, the resonant frequency and damping constant of the mechanical spring were re-evaluated because the way of mirror attachment slightly alters the characteristics of the suspension. The resonant frequency of the mechanical spring was estimated by applying a signal to the coil magnet actuator and measuring the amplitude using an interferometer; we obtained $\Omega_m/2\pi = 14.2 \pm 0.1$ Hz. The damping constant was estimated based on the ring-down measurements of the mechanical suspension. The Q factor of the mechanical suspension $Q_m = m\Omega_m/\Gamma_m$ was measured using the shadow sensing method. We attached a cutter knife blade to a magnet glued to the back of the mirror and measured its oscillation as the laser beam was blocked by it. The mirror was given an initial velocity by bringing a large magnet close to it and then vigorously moving it away.

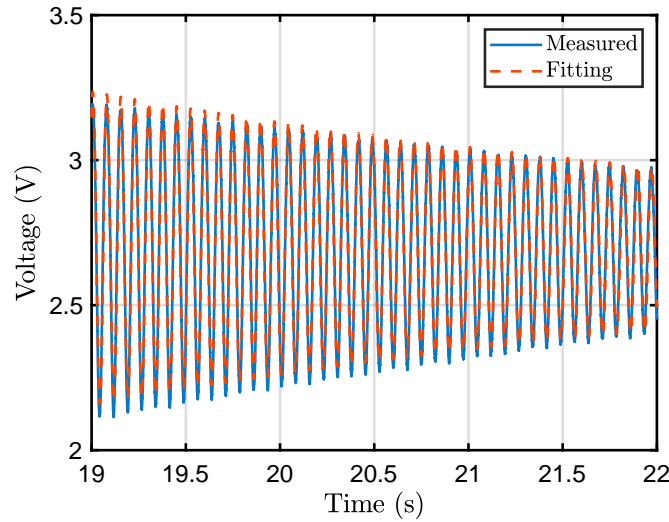


Fig. 5.11: Measurements of the ring down of the mirror using the shadow sensing method.

The measurement results of the shadow sensing method are shown in Fig. 5.11. The vertical axis shows the voltage $V(t)$, and the fitting was conducted using the following equation:

$$V(t) = A \operatorname{erf} \left[B \exp \left(-\frac{\Omega_m}{2Q_m} \right) \sin(\Omega_m t + \phi_0) \right] + V_{\text{off}}, \quad (5.27)$$

where A and B denote coefficients representing the magnitude of the signal, ϕ_0 denotes the initial phase, V_{off} denotes the offset of the voltage, and $\operatorname{erf}[z]$ denotes

the error function:

$$\text{erf}[z] = \frac{2}{\sqrt{\pi}} \int_0^z e^{-y^2} dy. \quad (5.28)$$

We used six parameters, A , B , ω_m , Q_m , ϕ_0 , and V_{off} , in the fitting to estimate Q_m . The multiple estimation results are shown in Fig. 5.12. As shown in Fig. 5.11,

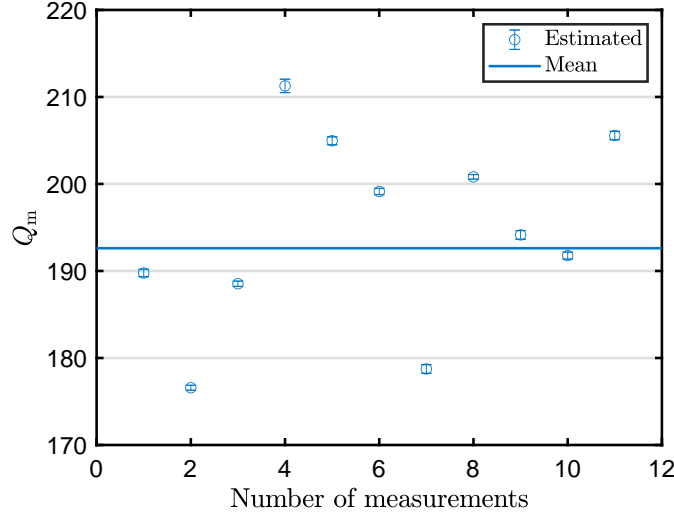


Fig. 5.12: Estimation results of the Q factor of the mechanical suspension Q_m . The blue circles indicate the estimation results from fitting and the error bars indicate the standard errors. The solid blue line shows the weighted average of the estimated results. Note that systematic errors mainly cause measurement errors.

each measurement well agreed with the fitting function, with minor standard errors but relatively large systematic errors. As the direction of mirror oscillation was different for each measurement, there is a possibility that a slightly different mode of vibration was excited. We estimated $Q_m = 193 \pm 3$ by taking a weighted average with the inverse of the variance as a weight. In contrast, the Q factor of the optical spring without the photothermal effect can be calculated as $m\Omega_{\text{opt}}/\Gamma_{\text{opt}} \simeq -\Omega_{\text{opt}}/\gamma \sim -10^{-5}$. Mechanical damping is dominant in the absence of the photothermal effect, and optical damping can be negligible.

Next, we selected the crystal to be used for the measurement. As described in Sec. 5.2.4, when $\omega_{\text{th}} \sim \gamma_{\text{th}}$, the conversion of the optical spring constant owing to the photothermal effect was maximum, and the maximum optical damping was induced. The photothermal parameters of each crystal with $P_0 = 600 \text{ mW}$ and $\delta_0 \sim 1$ were estimated in the previous subsection. The ω_{th} value of the PPLN was approximately 4 times larger than γ_{th} , and the thermal lensing effect was not negligible. In contrast, ω_{th} of the PPKTP was comparable to γ_{th} , and the thermal lensing effect was negligible; thus, the measurements of the optical spring were conducted using this crystal.

We measured the transfer function of the optical system with a suspended mirror in the setup illustrated in Fig. 5.4. In this case, the transfer function from the force applied to the mirror F_{ext} to the cavity length x was measured. The optomechanical response function can be denoted as $H_{\text{th}}\chi_{\text{eff}}$ using the susceptibility of optomechanical oscillator $\chi_{\text{eff}}(\Omega)$ defined in Eq. (5.20). The input power P_0 was set to three patterns of 600, 300, and 150 mW, and the normalized cavity detuning δ_0 was finely varied in the range of approximately $0 \sim 3$.

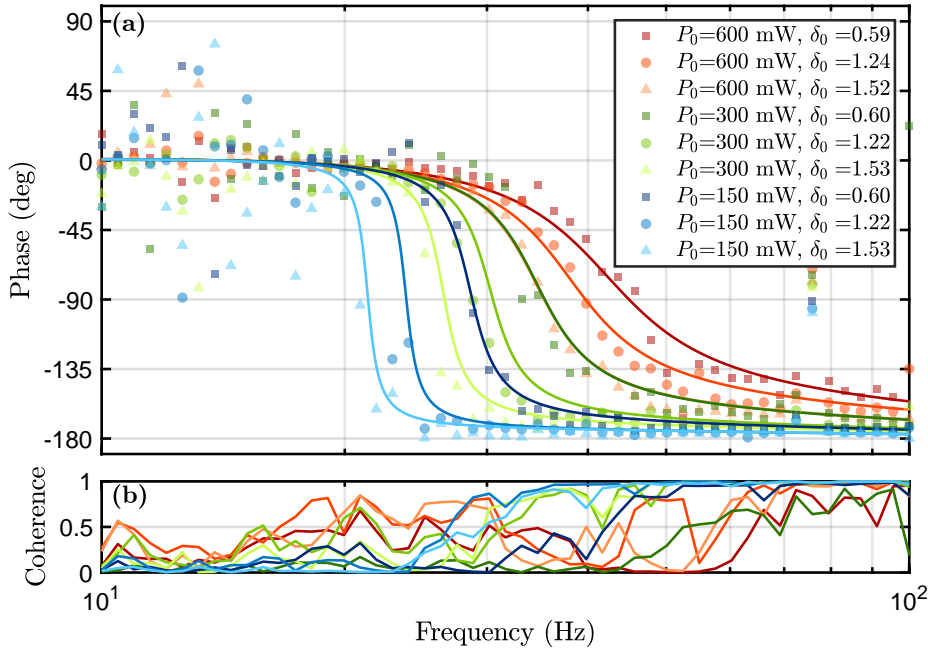


Fig. 5.13: (a) Measurement results of the transfer function. The red dots indicate the data for $P_0 = 600$ mW, green dots for $P_0 = 300$ mW, and blue dots for $P_0 = 150$ mW, and the square for $\delta_0 \sim 0.6$, circle for $\delta_0 \sim 1.2$, and triangle for $\delta_0 \sim 1.5$. The solid lines show the results of fitting the respective measurements with k_{opt} and ω_{th} as parameters. (b) Coherence between the input and measured signals. The average numbers are 200 for all the measurements.

The representative measurement results of the transfer function are shown in Fig. 5.13(a). k_{opt} and ω_{th} exhibit maximum values with $\delta_0 = 1/\sqrt{3} \sim 0.58$. Therefore, with regard to the data of this figure, k_{opt} and ω_{th} increase with a decrease in δ_0 and an increase in P_0 . The effect of k_{opt} on the optomechanical response function appears at the resonant frequency, at which the phase is approximately -90 degrees. A larger value of P_0 and smaller value of δ_0 result in a higher resonant frequency. The effect of ω_{th} is evident in the optical damping and phase leading. Optical damping is caused by converting the real component of the complex optical spring constant into an imaginary component through the photothermal effect. Even if optical damping in the absence of the photothermal effect is

negligible, this conversion process can significantly change the damping constant of the entire optomechanical system. The measurement results show that the phase inversion of the optomechanical response function was more gradual than it would be in the absence of the photothermal effect. In addition, the phase lead is caused because H_{th} is multiplied by the transfer function. The measured phase is led by more than -180 degrees in a band higher than the resonant frequency.

If P_0 and δ_0 are selected to provide the same value of k_{opt} , the value of ω_{th} would be equal. For example, the bright red ($P_0 = 600$ mW, $\delta_0 = 1.52$) and dark green lines ($P_0 = 300$ mW, $\delta_0 = 0.60$) in Fig. 5.13(a) are overlapped, indicating that the estimated k_{opt} and ω_{th} are almost identical. The estimation results show that k_{opt} and ω_{th} exhibit identical functional dependence on the parameters related to the cavity.

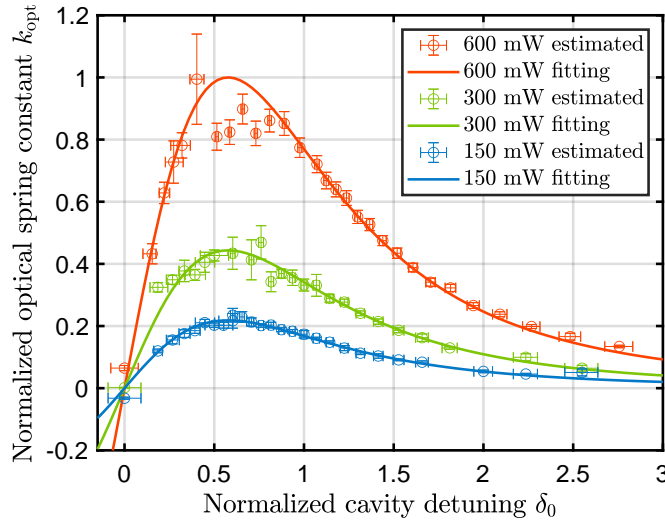


Fig. 5.14: Estimation results of the optical spring constant. The solid line indicates the fitting result using the inverse of the variance as weights, with the maximum value of k_{opt} as a parameter. The vertical axis is normalized by the maximum value of k_{opt} estimated for $P_0 = 600$ mW.

The estimation results of k_{opt} and ω_{th} are shown in Figs. 5.14 and 5.15, respectively. The circles with error bars represent the estimated values obtained using the same fitting method as illustrated in Fig. 5.13(a). In these measurements, we varied δ_0 such that the ranges of P_0 variations were approximately equal. However, there were some measurement data for which the parameters could not be estimated using the fitting program, and the variance was estimated to be zero. Such data were excluded in Figs. 5.14 and 5.15. The solid lines indicate the results of the weighted fitting. The estimated maximum k_{opt} for $P_0 = 600$ mW corresponds to 56.1 ± 0.5 Hz in terms of the resonant frequency of the optical spring.

We have neglected the influence of intracavity optical losses owing to second harmonic generation and other factors in those estimations. Optical loss caused

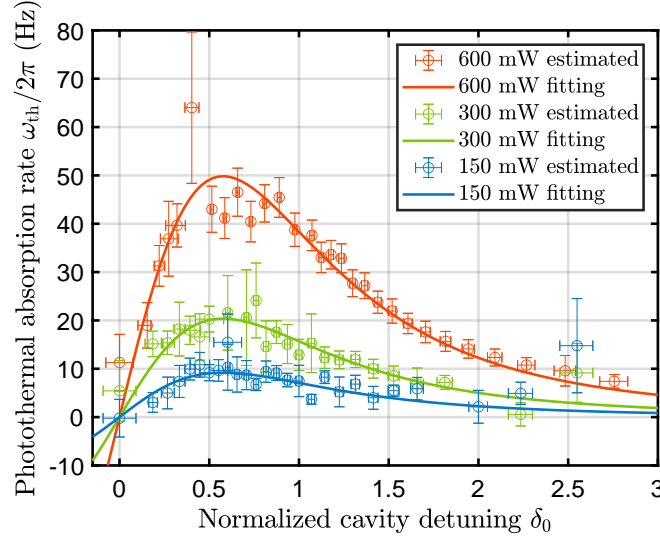


Fig. 5.15: Estimation results of the photothermal absorption rate. The solid line indicates the fitting result using the inverse of the variance as weights, with the maximum value of ω_{th} as a parameter.

by second harmonic generation was maximum at $P_0 = 600$ mW and $\delta_0 = 0$. The maximum intracavity loss was estimated to be approximately 0.074 times that of the input coupler based on the measurement of reflected light power at resonance; thus, the condition of over-coupling was sufficiently achieved. When k_{opt} and ω_{th} are maximum, the influence of the optical loss proportional to the intracavity power is most pronounced. In Figs. 5.14 and 5.15, both estimation results of $P_0 = 600$ mW and $\delta_0 \sim 1/\sqrt{3}$ deviate slightly from the fitting function, possibly owing to the optical loss caused by nonlinear optical effects. Although we have successfully estimated the parameters with reasonable accuracy, the effect of optical loss, which depends on the intracavity power, should be considered while using optical systems that are more susceptible to nonlinear optical effects.

Fig. 5.16 shows the estimated maximum values of k_{opt} and ω_{th} . The circles with error bars indicate the maximum values estimated from the fittings shown in Figs. 5.14 and 5.15. The error bars on the vertical axis indicate the standard errors, and the error bars on the horizontal axis indicate the measurement errors of P_0 determined based on the measurement accuracy of a power meter ($\pm 7\%$). In addition, weighted fitting exhibits a linear function with an intercept of zero for both parameters.

5.3.7 Comparison of methods for estimating the photothermal absorption rate

The photothermal absorption rate ω_{th} can be estimated based on both measurements using the fixed mirror, as shown in Fig. 5.3, and suspended mirror, as shown

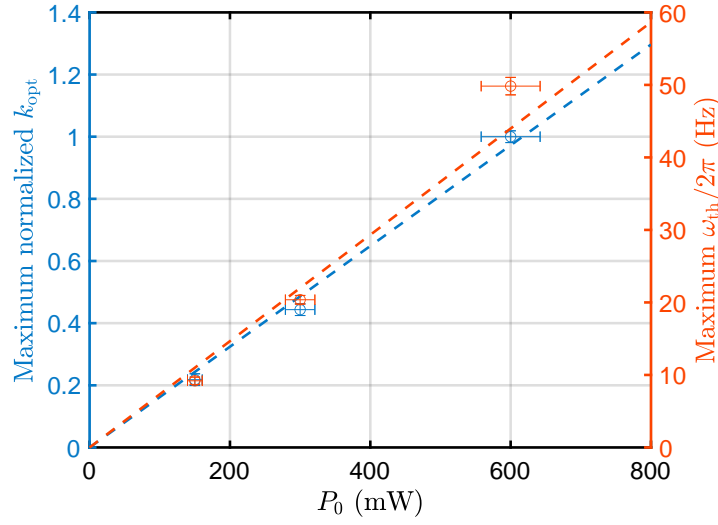


Fig. 5.16: Estimated maximum value of the optical spring constant k_{opt} and photothermal absorption rate ω_{th} . The dotted lines indicate the weighted fitting of each result using a linear function with an intercept of zero.

in Fig. 5.4. The frequency response of the cavity H_{th} can be measured using a fixed mirror. However, unless ω_{th} is sufficiently larger than the photothermal relaxation rate γ_{th} , sufficient phase lead cannot be caused, and parameter estimation cannot be achieved. In contrast, when a suspended mirror is used, $H_{\text{th}}\chi_{\text{eff}}$ can be measured, where χ_{eff} denotes the susceptibility of the optomechanical oscillator. Even when ω_{th} is smaller than γ_{th} , photothermal effects can produce non-negligible optical damping. The measurement using a suspended mirror is a promising parameter estimation method for minor photothermal effects.

The estimation of ω_{th} using suspended mirrors is shown in Fig. 5.15. A similar estimation was conducted using a fixed mirror, and the results are shown in Fig. 5.17. The value of γ_{th} is estimated when ω_{th} is sufficiently large, as shown in Fig. 5.10. The circles with error bars indicate the estimated results of fitting the measured transfer function with only ω_{th} as a parameter. Error bars and solid lines are defined similarly to Fig. 5.15. To compare the two parameter estimation methods, we calculated the root mean square error (RMSE) for the estimation of the maximum value of ω_{th} . The RMSE means the deviation between the data and fitting function. We compare the RMSEs normalized by the estimated value because the RMSE depends on it. The normalized RMSEs of the estimate with a suspended mirror were 0.0074 for $P_0 = 600$ mW, 0.011 for $P_0 = 300$ mW, and 0.035 for $P_0 = 150$ mW. In contrast, the normalized RMSE of the estimate with the fixed mirror was 0.052 for $P_0 = 600$ mW, 0.16 for $P_0 = 300$ mW, and 0.41 for $P_0 = 150$ mW. In both cases, systematic errors increase with lower P_0 and smaller ω_{th} . In particular, the normalized RMSEs with the fixed mirror are approximately 10 times worse than those with the suspended mirror. This result indicates that the

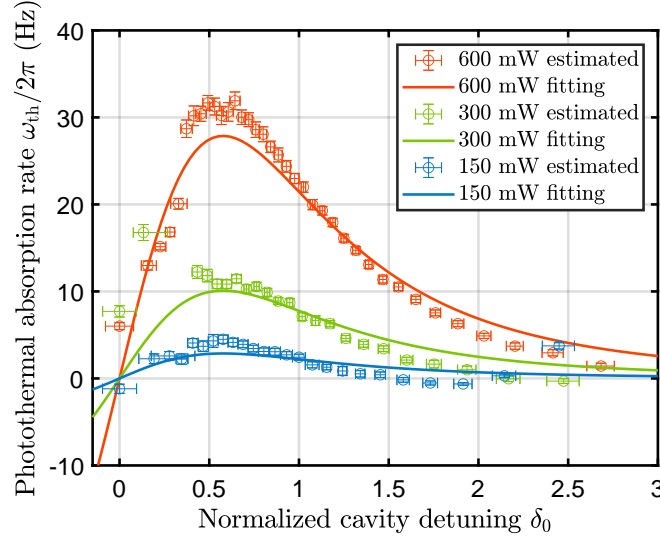


Fig. 5.17: Estimation of the photothermal absorption rate using a fixed mirror. The solid lines indicate the weighted fitting results with the inverse of the variance as the weight and maximum value of ω_{th} as the parameter.

systematic error in the measurement of H_{th} is non-negligible when $\omega_{th} \lesssim \gamma_{th}$. We note that there is also a lower limit of ω_{th} that can be estimated with a suspended mirror, which is determined by the minimum value of optical damping that can be measured.

5.4 Summary of this chapter

Photothermal effects can affect optical interferometers in various ways. In our experimental system, we found that photothermal effects modified the effective cavity length, causing the cavity to exhibit a frequency dependence even on a frequency band sufficiently lower than the cavity decay rate. Moreover, the photothermal effect modifies the characteristics of the optical spring. We can virtually eliminate the photothermal effect by measuring the susceptibility of the optomechanical oscillator and simultaneously estimating the optical spring constant k_{opt} and photothermal absorption rate ω_{th} . This method is still effective when ω_{th} is smaller than the photothermal relaxation rate γ_{th} . We succeeded in estimating the photothermal parameters with approximately one order better accuracy than the method of measuring the frequency response of the cavity.

In our experiment, γ_{th} was estimated based on the measurement of the frequency response of the cavity H_{th} . If the beam radius r_0 is constant in the region contributing to thermal absorption, γ_{th} can be calculated using the physical property values of the crystal [172]:

$$\gamma_{th} = \frac{\kappa_{th}}{\rho C_0 r_0^2}, \quad (5.29)$$

where κ_{th} denotes the thermal conductivity, ρ denotes the density, and C_0 denotes the specific heat capacity. For the experiment using PPKTP, the beam radius of the waist is $40\ \mu\text{m}$, the crystal length is $10\ \text{mm}$, the refractive index is 1.7 , the thermal conductivity of KTP is $\kappa_{\text{th}} \sim 2.2\ \text{W}/(\text{m} \cdot \text{K})$ [173], the specific heat capacity is $C_0 = 6.9 \times 10^2\ \text{J} \cdot \text{kg} \cdot \text{K}$, and the density is $\rho = 3.0 \times 10^3\ \text{kg}/\text{m}^3$; considering these values, the average value of $\gamma_{\text{th}}/2\pi$ is approximately $95\ \text{Hz}$. This value is approximately 3.2 times larger than the measured value. This difference may be because of the extra thermal resistance at the junction of the periodic polarization inversion. In addition, the value of the beam radius used in the calculation may be inaccurate because the beam radius is sensitive to the position of the curvature mirror and crystal. If the beam radius is accurately measured, this method is sufficiently accurate to be applied to the high-precision estimation of thermal conductivity [159].

As shown in Fig. 5.17, even when ω_{th} can be accurately estimated based on the measurements using a fixed mirror ($P_0 = 600\ \text{mW}$, $\delta_0 \sim 1/\sqrt{3}$), the estimated values are significantly smaller than those estimated using a suspension mirror. This difference may be caused by a slight shift in the position of the beam as it passes through the crystal, which occurs when the suspended mirror is replaced by a fixed mirror, resulting in a change in the photothermal parameters. The estimated γ_{th} obtained from the measurements with a fixed mirror may also differ from γ_{th} with a suspended mirror. In other words, γ_{th} cannot be accurately estimated from measurements using a focused beam whose Rayleigh length is comparable to the crystal length.

The optical spring constant is the proportionality factor of the relationship between the fluctuation of radiation pressure force and cavity length. Moreover, a proportional relationship exists between the fluctuation of thermal absorption and cavity length, and the photothermal absorption rate is obtained by multiplying this proportionality coefficient by the thermal expansion coefficient per heat capacity. As the radiation pressure force and thermal absorption are proportional to the intracavity power, the optical spring constant and photothermal absorption rate are identical except for the proportionality constant determined by the physical property value of the crystal. In other words, the optical spring constant and photothermal absorption rate change by the same factor for cavity parameters such as input power, finesse, and cavity detuning. A detailed discussion in the next chapter shows that intracavity squeezing enhances the optical spring constant and photothermal absorption rate by the same factor. It is impossible to avoid the photothermal effect in the intracavity signal amplification system comprising macroscopic and massive test masses. Such a system should be designed to utilize the stabilization of the optical spring based on the photothermal effect. The combination of the photothermal effect and intracavity squeezing allows us to generate a stable and stiff optical spring.

Chapter 6

Signal amplification experiment based on Kerr scheme

In Chapter 4, we implemented intracavity squeezing using optical parametric amplification (OPA) and conducted signal amplification experiments. However, we found that the OPA process could not be maintained because of the strong intracavity power required to generate the optical spring. In this chapter, we implement intracavity squeezing using the optical Kerr effect. The Kerr scheme can achieve strong intracavity power and large signal amplification gain because the stronger Kerr effect can be induced as the intracavity power increases.

The general Kerr effect requires extremely high intensity because it is a third-order nonlinear optical effect. However, it is known that a chain of second-order nonlinear optical effects can induce phenomena equivalent to the Kerr effect by setting the phase-mismatched condition. This phenomenon is known as the cascaded nonlinear optical effect^{*1} [174,175]. Even in experiments using continuous-wave lasers, it is possible to produce a sufficient Kerr effect using the aforementioned phenomenon. Nevertheless, the required intracavity power is approximately an order of magnitude stronger than that in the experiment with the OPA scheme; thus, the photothermal effect cannot be neglected. In the previous chapter, we discussed a method to model and virtually eliminated the photothermal effect. However, it should be noted that the Kerr effect also modifies photothermal parameters.

6.1 Theory of intracavity signal amplification based on the Kerr effect

This section discusses the Kerr signal amplification effect and impact of the Kerr effect on photothermal parameters.

^{*1} See App. B.3.4.

6.1.1 Enhancement of the optical spring based on the Kerr effect

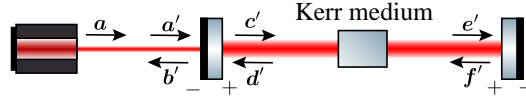


Fig. 6.1: Schematic of Fabry-Perot cavity containing a Kerr medium. The end mirror is supposed to work as a test mass, and the initial phase is modified so that the carrier light on the test mass is in the amplitude quadrature.

First, we obtain a formula of the optical spring enhanced by the Kerr effect using the two-photon formalism. Let us consider a Fabry-Perot cavity containing a Kerr medium, as shown in Fig. 6.1. Let r^2 and $t^2 = T$ be the power reflectivity and transmissivity of the input mirror, respectively; ϕ and α be the phase change and delay during a half cycle in the cavity, respectively; L be the half cycle length of the cavity. Similar to the intracavity OPA discussed in the previous chapter, we assume that the intracavity carrier E is in the amplitude quadrature.

As expressed in Eq. (3.57), the Kerr effect changes a phase of $\Phi := \Phi_{F'} = \Phi_{E'} = d_K P_{E'}$ for the carrier light, considering d_K as a constant depending on the gain of the Kerr effect. By defining the normalized cavity detuning δ in addition to the phase change caused by the Kerr effect, the intracavity power in the presence of the Kerr effect can be denoted by Lorentzian:

$$P_{E'} = \frac{4}{T} \frac{1}{1 + \delta^2} P_A, \quad (6.1)$$

where we defined $\delta_C = \Delta_C/\gamma$, $\delta_K = \Delta_K/\gamma$, and $\delta = \delta_C + \delta_K$. Here, $\Delta_C = \phi c/L$ and $\Delta_K = \Phi c/(2L)$ denote the cavity detuning associated with the cavity length and Kerr effect, and $\gamma = Tc/(4L)$ denotes the cavity decay rate. Moreover, we define ζ , a dimensionless quantity that characterizes the gain of the Kerr effect and is independent of cavity detuning, as

$$\zeta = \delta_K(1 + \delta^2) = \frac{8d_K}{T^2} P_A. \quad (6.2)$$

The normalized intracavity power $p = 1/(1 + \delta^2)$ can be written as

$$p = \frac{1}{1 + (\delta_C + p\zeta)^2}. \quad (6.3)$$

Fig. 6.2 shows the relationship between δ_C and p when $\zeta = -1$ and $\zeta = 0$.

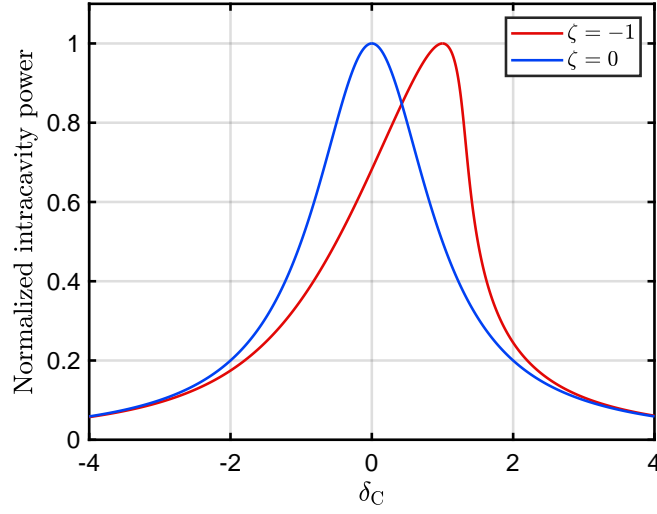


Fig. 6.2: Normalized intracavity power p as a function of δ_C .

When δ_C is varied by moving a mirror at a constant speed, we can observe that the spectrum is wholly tilted owing to the Kerr effect. The gain of the Kerr effect can be estimated by measuring the value of δ_C at resonance because $\delta_C \rightarrow -\zeta$ when $\delta = 0$.

Let us calculate light field fluctuations and derive the optical spring constant. From Eq. (3.58), the intracavity light field fluctuation can be written as

$$e = 2k_0 E'_0 r e^{2i\alpha} [I - r e^{2i\alpha} R(2\phi + \Phi)P(-2\Phi)]^{-1} R(2\phi + \Phi)P(-2\Phi) \begin{pmatrix} 0 \\ 1 \end{pmatrix} \delta x. \quad (6.4)$$

Here, we neglected input light field fluctuation α . Considering Eq. (4.1), the complex optical spring constant $K_{\text{opt}}(\Omega)$ can be obtained as

$$\begin{aligned} K_{\text{opt}}(\Omega) &= 4\hbar k_0^2 (E'_0)^2 \frac{\sin(2\phi + \Phi)}{r e^{2i\alpha} + r^{-1} e^{-2i\alpha} - 2\cos(2\phi + \Phi) + 2\Phi \sin(2\phi + \Phi)} \\ &\simeq \frac{4k_0 P_{E'}}{L} \frac{\Delta}{(\gamma + i\Omega)^2 + \Delta^2 + 2\Delta\Delta_K} \\ &= \frac{4k_0 P_{E'}}{L\gamma} \frac{\delta}{(1 + i\Omega/\gamma)^2 + \delta^2 + 2\delta\delta_K}. \end{aligned} \quad (6.5)$$

The signal amplification effect induced by the Kerr effect corresponds to a squeezing angle of $\theta = 0$, and the effective squeezing factor is a function of the intracavity power and cavity detuning.

The experimentally measurable cavity detuning dependence of the optical

spring can be written as

$$K_{\text{opt}}(\Omega) \simeq \frac{16k_0 P_A}{L\gamma T} \frac{1}{1 + \delta^2} \frac{\delta}{1 + \delta^2 + 2\delta\delta_K} \left[1 - i \frac{2}{\gamma(1 + \delta^2 + 2\delta\delta_K)} \Omega \right] \\ := k_{\text{opt}} + i\Gamma_{\text{opt}}\Omega, \quad (6.6)$$

where k_{opt} denotes the optical spring constant, and Γ_{opt} denotes the optical damping constant. Fig. 6.3 shows the cavity detuning dependence of the optical spring

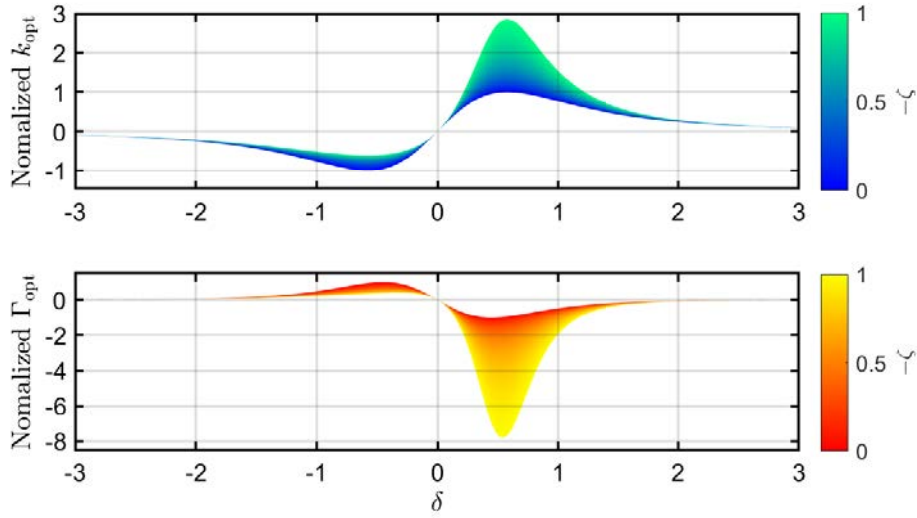


Fig. 6.3: Optical spring constant k_{opt} and optical damping constant Γ_{opt} with intracavity Kerr squeezing. Each vertical axis is normalized so that the maximum value at $\zeta = 0$ is 1.

and damping constant. When the parameters are $\zeta < 0$ and $\delta > 0$, the optical spring constant is enhanced by the signal amplification effect owing to the Kerr effect. Normalized cavity detuning that generates the maximum optical spring constant is $\delta = 1/\sqrt{3}$, even in the presence of the Kerr effect. However, k_{opt} rapidly decreases as δ increases because the effective squeezing decay rate depends on the cavity detuning.

6.1.2 Optomechanical system with photothermal and Kerr effects

The last subsection discusses that the Kerr effect can enhance the optical spring. Our experimental system is also affected by the photothermal effect. As the photothermal absorption rate and optical spring constant are equivalent except for the proportionality factor, we can expect that the photothermal absorption rate is also enhanced by the same factor. To analyze optomechanical systems with photothermal and Kerr effects, we derive the optical spring constant and photothermal ab-

sorption rate based on the Hamiltonian notation [61, 176]. We note that the same derivation can be obtained from the two-photon formalism.

In discussion with the Hamiltonian notation, we calculate the stochastic differential equation for the complex light-field amplitude $a(t)$. In our system, we must consider the Kerr Hamiltonian \hat{H}_{Kerr} , which can be written as [177]

$$\hat{H}_{\text{Kerr}} = \frac{\hbar}{2} \chi (\hat{a}^\dagger)^2 \hat{a}^2, \quad (6.7)$$

where χ denotes a constant that refers to the gain of the Kerr effect and \hat{a}^\dagger and \hat{a} denote the creation and annihilation operator, respectively. Thus, the term added to the stochastic differential equation can be calculated as

$$-\frac{i}{\hbar} [\hat{a}, \hat{H}_{\text{Kerr}}] = -i\chi \hat{a}^\dagger \hat{a}^2. \quad (6.8)$$

Considering the aforementioned calculation, the stochastic differential equation for the complex light-field amplitude $a(t)$ can be written as [61, 178]

$$\dot{a} = [i\Delta' + iG_0x - i\chi n - \gamma] a + \gamma a_{\text{max}}, \quad (6.9)$$

where Δ' denotes the angular frequency of cavity detuning, $x = x_{\text{act}} + x_{\text{th}}$ denotes the effective cavity length, x_{act} denotes the displacement of the test mass, x_{th} denotes the photothermal displacement, G_0 denotes the optomechanical frequency shift per displacement, γ denotes the cavity decay rate, and a_{max} denotes the maximum value of $a(t)$ at resonance. Herein, we define the quantity corresponding to the number operator as $n = |a|^2$. The differential equation for x_{th} can be obtained from Eq (5.3) as follows:

$$\dot{x}_{\text{th}} = -\gamma_{\text{th}} x_{\text{th}} + d\hbar G_0 n, \quad (6.10)$$

where γ_{th} denotes the photothermal relaxation rate, $d = \alpha\alpha' L'^2 c / (2C)$ denotes the proportionality coefficient for heat absorption, α denotes the coefficient of linear thermal expansion, α' denotes the thermal absorption coefficient, L' denotes the crystal length, and C denotes the heat capacity. The equation of motion for x_{act} can be written as

$$m\ddot{x}_{\text{act}} = -m\Omega_{\text{m}}^2 x_{\text{act}} - m\Gamma_{\text{m}} \dot{x}_{\text{act}} + \hbar G_0 n + F_{\text{ext}}, \quad (6.11)$$

where m denotes the mass of the mirror, Ω_{m} denotes the mechanical resonance angular frequency, Γ_{m} denotes the mechanical damping constant, and F_{ext} denotes the external force applied to the test mass. The third term on the right side corresponds to the radiation pressure force F_{rad} .

Suppose that a stable point is found where $\dot{x}_{\text{act}} = 0$, $\dot{x}_{\text{th}} = 0$, and $\dot{a} = 0$, and we make a linear approximation as $x_{\text{act}}(t) = \bar{x}_{\text{act}} + \delta x_{\text{act}}(t)$, $x_{\text{th}}(t) = \bar{x}_{\text{th}} + \delta x_{\text{th}}(t)$, and $a(t) = \bar{a} + \delta a(t)$. Moreover, we define $\bar{x} = \bar{x}_{\text{act}} + \bar{x}_{\text{th}}$, $\delta x = \delta x_{\text{act}} + \delta x_{\text{th}}$, $\bar{n} = |\bar{a}|^2$, and $\delta n = \bar{a}^* \delta a + \bar{a} \delta a^*$. Herein, δ represents small fluctuating terms,

not normalized cavity detuning. The simultaneous differential equations for the first-order small fluctuating terms are written as

$$\delta \dot{a} = [i\Delta - \gamma]\delta a + i\bar{a}(G_0\delta x - \chi\delta n), \quad (6.12)$$

$$\delta \dot{x}_{\text{th}} = -\gamma_{\text{th}}\delta x_{\text{th}} + d\hbar G_0\delta n, \quad (6.13)$$

$$\delta \ddot{x}_{\text{act}} = -\Omega_{\text{m}}^2\delta x_{\text{act}} - \Gamma_{\text{m}}\delta \dot{x}_{\text{act}} + \hbar G_0\delta n/m + \delta F_{\text{ext}}/m, \quad (6.14)$$

where $\Delta = \Delta' + G_0\bar{x} - \chi\bar{n}$ denotes effective cavity detuning. Each equation is Fourier transformed to derive the frequency response. From Eq. (6.12), we obtain

$$\delta a(\Omega) = \chi_{\text{c}}(\Omega)i\bar{a}(G_0\delta x(\Omega) - \chi\delta n(\Omega)), \quad (6.15)$$

where $\chi_{\text{c}} = 1/(i\Omega - i\Delta + \gamma)$ denotes the susceptibility of the cavity. Moreover, we obtain

$$(\delta a^*)(\Omega) = \chi_{\text{c}}^*(-\Omega)(-i\bar{a}^*)(G_0\delta x(\Omega) - \chi\delta n(\Omega)) \quad (6.16)$$

because $(\delta a^*)(\Omega) = (\delta a(-\Omega))^*$. We have used $(\delta x(-\Omega))^* = \delta x(\Omega)$ and $(\delta n(-\Omega))^* = \delta n(\Omega)$ because $\delta x(t)$ and $\delta n(t)$ are real numbers. The photon number fluctuation $\delta n(\Omega)$ can be calculated as

$$\begin{aligned} \delta n(\Omega) &= i\bar{n} [\chi_{\text{c}}(\Omega) - \chi_{\text{c}}^*(-\Omega)] (G_0\delta x(\Omega) - \chi\delta n(\Omega)) \\ &= i\bar{n}G_0 \frac{[\chi_{\text{c}}(\Omega) - \chi_{\text{c}}^*(-\Omega)]}{1 + i\chi\bar{n} [\chi_{\text{c}}(\Omega) - \chi_{\text{c}}^*(-\Omega)]} \delta x(\Omega) \\ &= -2\bar{n}G_0 \frac{\Delta}{(\gamma + i\Omega)^2 + \Delta^2 - 2\Delta\chi\bar{n}} \delta x(\Omega). \end{aligned} \quad (6.17)$$

Here,

$$\chi_{\text{c}}(\Omega) - \chi_{\text{c}}^*(-\Omega) = \frac{2i\Delta}{(\gamma + i\Omega)^2 + \Delta^2} \quad (6.18)$$

is used for the variation of the equation. Based on Eq. (6.13), the influence of the Kerr effect on the photothermal effect can be calculated as

$$(i\Omega + \gamma_{\text{th}})\delta x_{\text{th}} = -\omega_{\text{th}}(\Omega)\delta x(\Omega), \quad (6.19)$$

where

$$\omega_{\text{th}}(\Omega) = 2d\hbar G_0^2\bar{n} \frac{\Delta}{(\gamma + i\Omega)^2 + \Delta^2 - 2\Delta\chi\bar{n}} \quad (6.20)$$

is the photothermal absorption rate. Based on Eq. (6.14), the susceptibility of the optomechanical oscillator can be calculated as

$$\frac{\delta x_{\text{act}}(\Omega)}{\delta F_{\text{ext}}(\Omega)} = \frac{1}{m(-\Omega^2 + \Omega_{\text{m}}^2 + i\Omega\Gamma_{\text{m}}) + \Sigma_{\text{th}}(\Omega)}, \quad (6.21)$$

where $\Sigma_{\text{th}}(\Omega)$ denotes optomechanical self-energy, which is defined as

$$\Sigma_{\text{th}}(\Omega) = \frac{\gamma_{\text{th}} + i\Omega}{(\omega_{\text{th}}(\Omega) + \gamma_{\text{th}}) + i\Omega} K_{\text{opt}}(\Omega). \quad (6.22)$$

$K_{\text{opt}}(\Omega)$ is the complex optical spring constant and can be calculated as

$$K_{\text{opt}}(\Omega) = 2\hbar G_0^2 \bar{n} \frac{\Delta}{(\gamma + i\Omega)^2 + \Delta^2 - 2\Delta\chi\bar{n}}. \quad (6.23)$$

Here, \bar{n} denotes the intracavity photon number and the correspondence with the intracavity power $P_{E'}$ is $P_{E'} = (\hbar\omega_0/2)(c/L)\bar{n}$. In addition, using $G_0 \simeq \omega_0/L$ and $\Delta_K = -\chi\bar{n}$, Eqs. (6.5) and (6.23) are consistent. The complex optical spring constant and photothermal absorption rate are identical except for the proportionality factor, even in the presence of intracavity squeezing induced by the Kerr effect. The intracavity squeezing enhances the optical spring constant and photothermal absorption rate by the same factor.

6.2 Kerr experiments

6.2.1 Experimental setup

The experiment in this section aims to observe the optical spring enhanced by the Kerr effect. The Kerr effect, in this experiment, is produced by cascaded non-linear optical effects. The experimental setup for measuring the optical spring is the same as illustrated in Fig. 5.4. Moreover, we have measured the frequency response of the cavity with the setup shown in Fig. 5.3 to investigate the influence of the Kerr effect on the photothermal effect.

In this experiment, phase-mismatched conditions are realized at several crystal temperatures. Fig. 6.4 shows the relationship between the crystal temperature and transmitted light power at resonance. The transmitted light power is the lowest at approximately 33.6 °C, corresponding to the phase-matched condition. The transmitted light power is increased at several temperatures, corresponding to a phase-mismatched condition. With this crystal, signal amplification for the positive optical spring can be achieved when the temperature is higher than under the phase-matched condition; 39.2, 44.8, and 49.2 °C correspond to the first, second, and third phase-mismatched conditions, respectively. The strongest Kerr effect is induced when we set the temperature to the first phase-mismatched condition^{*2}.

The Kerr effect is reduced under the second or third phase-mismatched condition, and the increase or decrease in the signal amplification effect can be confirmed. However, the first phase-mismatched condition incurs higher intracavity losses than the other conditions. We have compared the optical spring constants by measuring under the first phase-mismatched condition and conditions whose temperature slightly shifted from the second and third phase-mismatched conditions to equalize the intracavity power to the first phase-mismatched condition. In addition, as shown in Fig. 6.4(b), the transmitted light power at resonance finely

^{*2} In practice, there is a state in which the Kerr effect is the strongest between the phase-matched and first phase-mismatched conditions. However, the optical spring was measured under the phase-mismatched condition owing to the large optical loss resulting from the SHG in this state.

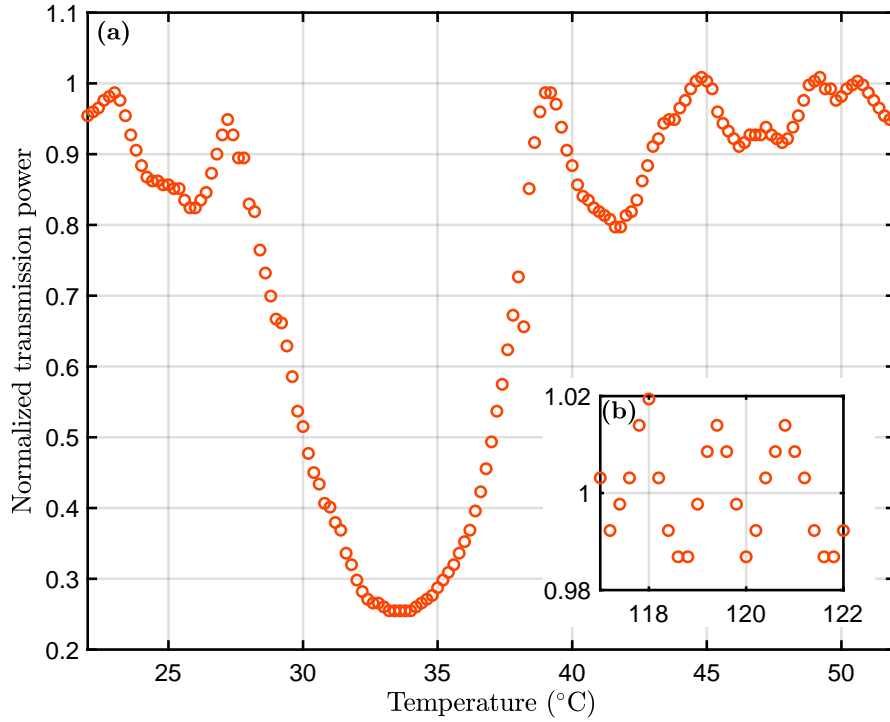


Fig. 6.4: Crystal temperature and transmitted light power at resonance. We measured (a) in the range of 22 °C~ 52 °C and (b) in the range of 117 °C~ 122 °C with steps of 0.2 °C. The vertical axis is normalized by the mean value measured in (b).

fluctuates when the temperature is approximately 120 °C. The vertical axes of the graphs shown in Fig. 6.4 are normalized by the transmitted light power at resonance measured in the range of 117 °C~ 122 °C.

6.2.2 Confirmation of Kerr effect

The Kerr effect via cascaded nonlinear optical effects can be confirmed by measuring the transmitted light power. The measured spectra when the crystal temperature was set to the first phase-mismatch state are shown in Fig. 6.5. Carrier light and counterpropagating light are incident on the cavity. As the pump light is not incident, there is no intrinsic difference in the direction of the laser light into the cavity. In this case, the Kerr effect only affects the carrier light because the carrier light is sufficiently more intense than the counterpropagating light. The temperature of the crystal providing the first phase-mismatched condition is slightly different from that shown in Fig. 6.4 because the crystal was installed at an inclination to the optical axis to reduce coupling between the carrier light and counterpropagating light. We incident the counterpropagating light of sufficient intensity to avoid coupling in the transmitted light power measurement. The cavity length was var-

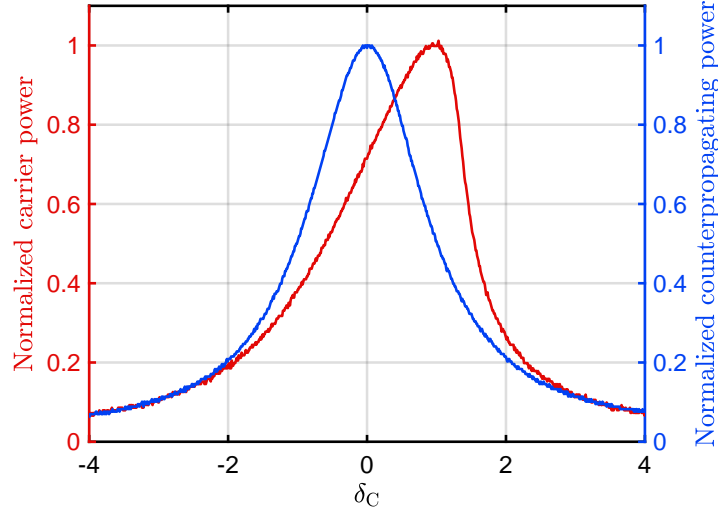


Fig. 6.5: Transmitted carrier and counterpropagating light power from the cavity under the first phase-mismatched condition. The crystal temperature was set to 37.3°C. The input carrier power and counterpropagating light power are 530 mW and 50 mW, respectively.

ied as fast as the photothermal effect can be neglected, and the counterpropagating transmission power exhibited a Lorentz curve. As the carrier transmission power reached a resonance state at approximately $\delta_C \sim 1$, the gain of the Kerr effect can be estimated to be approximately $\zeta \sim -1$.

6.2.3 Enhancement of optical spring by Kerr effect

The impact of the Kerr effect on the optical spring can be estimated by measuring the transfer function of the optical system with a suspended mirror. We can expect to confirm the change in the signal amplification effect depending on the gain of the Kerr effect by comparing measurements under several phase-mismatched conditions. If we set the intracavity loss that does not change with the gain of the Kerr effect and observe a change in the optical spring constant, we can confirm that the signal amplification effect enhances the optical spring. As shown in Fig. 6.4, the gain of the Kerr effect can be varied without changing the intracavity loss by selecting a specific crystal temperature. Herein, the transfer function was measured at three different crystal temperatures at 39.5°C, 45.5°C, and 50.0°C, considered as measurements with the strong, moderate, and weak Kerr effects.

Fig. 6.6 shows the phase measurement results with a suspended mirror. As shown in Fig. 6.3, the optical spring constant reaches its maximum at $\delta = 1/\sqrt{3} \sim 0.58$, even with the Kerr effect. In these measurements, the optical spring constant and photothermal absorption rate increase as δ decreases. Comparing measurements shown in (a)-(c) with $\delta = 0.58$, the resonance frequency of the optome-

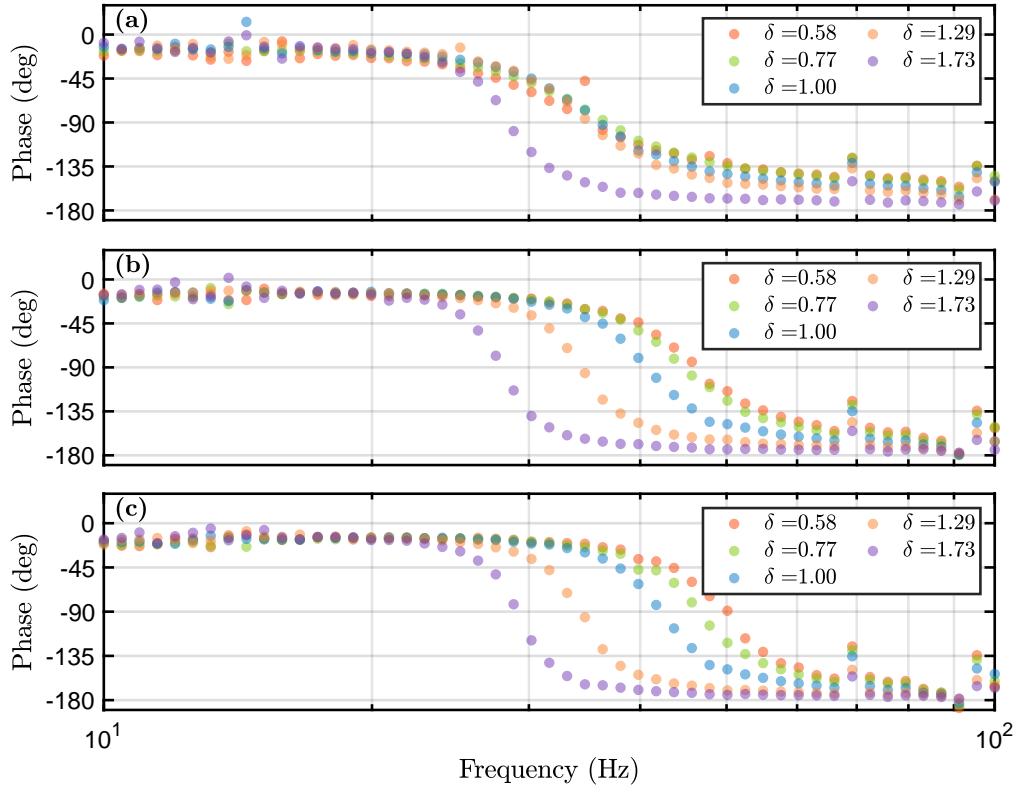


Fig. 6.6: Measured transfer function of the optical system for several cavity detuning δ with a suspended mirror. (a), (b), and (c) correspond to the measurements with the strong, moderate, and weak Kerr effects, respectively.

chanical oscillator decreases as the Kerr effect strengthens. We can conclude that the conversion of the optical spring constant to an imaginary component owing to the enhanced photothermal effect may be more dominant than the enhancement of the optical spring owing to the Kerr effect. The measurement results indicate that the optical damping increases as the Kerr effect strengthens.

Moreover, we measured the transfer function of the optical system with a PZT to examine the frequency response of the cavity. The gain and phase measurement results are shown in Figs. 6.7, 6.8, and 6.9. The original data exhibited a low-pass characteristic owing to the capacitance of the PZT in the high-frequency band above 1 kHz. The frequency response of PZT is removed by measuring the transfer function without the nonlinear optical crystal and subtracting the gain and phase, respectively. Even with the Kerr effect, the photothermal effect is expected to be negligible in the high-frequency band. Owing to the mechanical resonance of the PZT in the band above 7 kHz, the gain is normalized by the average value of 6 ~ 7 kHz. The measurement results with a strong Kerr effect indicate that the gain is reduced up to approximately -12 dB, thus reducing the optical spring constant.

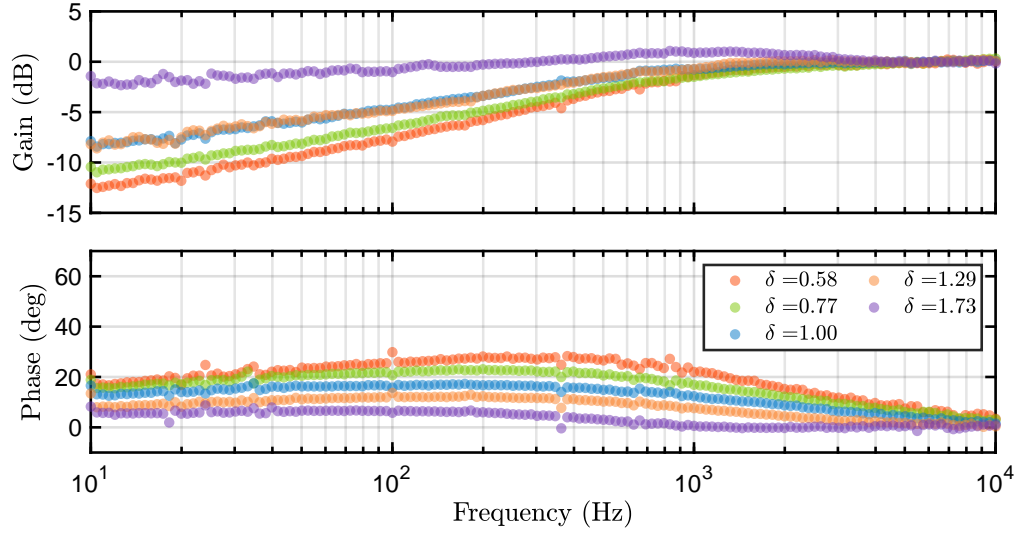


Fig. 6.7: Measured transfer function of the optical system for several cavity detuning δ with a PZT. These results correspond to the measurement with a strong Kerr effect. The measured gain is normalized by the mean value in 6 ~ 7 kHz.

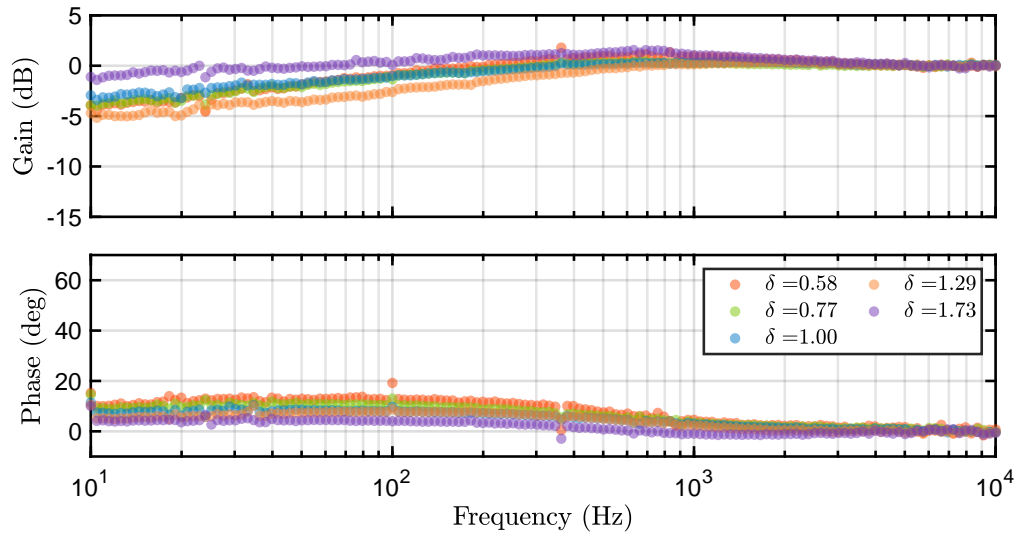


Fig. 6.8: Measured transfer function with a moderate Kerr effect. The gain is normalized in the same manner as in Fig. 6.7.

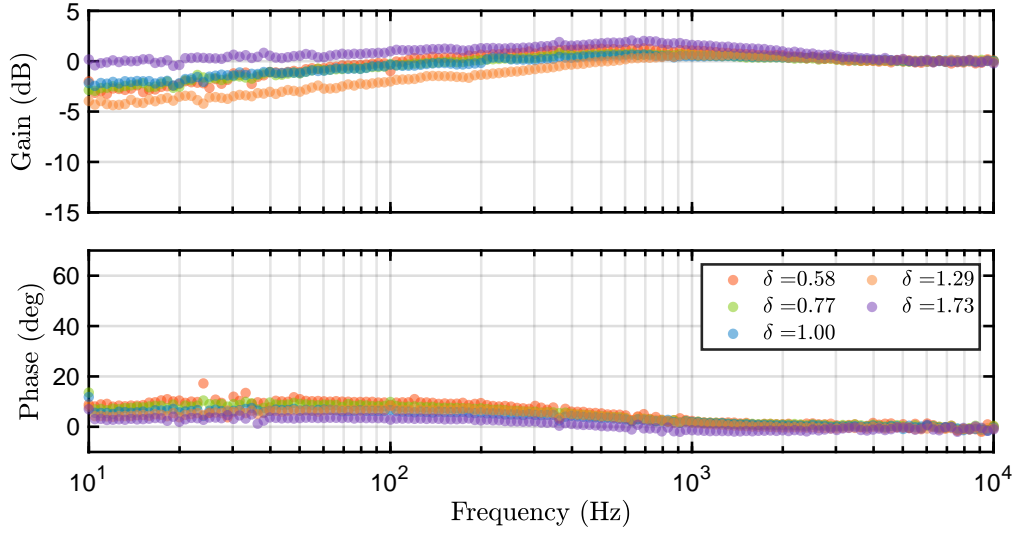


Fig. 6.9: Measured transfer function with a weak Kerr effect. The gain is normalized in the same manner as in Fig. 6.7.

The measurements also indicate that the phase does not follow a one-pole, one-zero transfer function over a wide frequency bandwidth. We can expect the Kerr effect to enhance the photothermal absorption rate because the measurement bandwidth is sufficiently lower than the cavity decay rate. However, the measured phase is roughly constant in the band lower than approximately 100 Hz, indicating that the photothermal relaxation rate increases. The frequency response does not follow the theoretical prediction in the frequency range below the photothermal relaxation rate, as shown in Fig. 5.9. We estimate that self-focusing induced by the Kerr effect reduces the effective beam radius. The impact of the Kerr lens is discussed in the next section^{*3}.

In summary, it is difficult to analytically estimate the photothermal effect when we perform the intracavity Kerr effect. However, as the measurement results with the PZT can be regarded as the frequency response of the cavity, we can eliminate the photothermal effect using these results. Therefore, we removed the photothermal effect from the measurements with a suspended mirror and estimated the optical spring constant as the only parameter. The parameters of the photothermal effect strongly depend on the beam position in the nonlinear optical crystal. When replacing a suspended mirror with a mirror equipped with PZT, only the position and angle of the replaced mirror are adjusted to restore alignment.

The optical spring constant k_{opt} is predicted to follow a function of

$$k_{\text{opt}} = \frac{16}{3\sqrt{3}} k_{\text{opt-0}} \frac{1}{1 + \delta^2} \frac{\delta}{1 + \delta^2 + 2\zeta\delta/(1 + \delta^2)}, \quad (6.24)$$

^{*3} See also App. E.2.4.

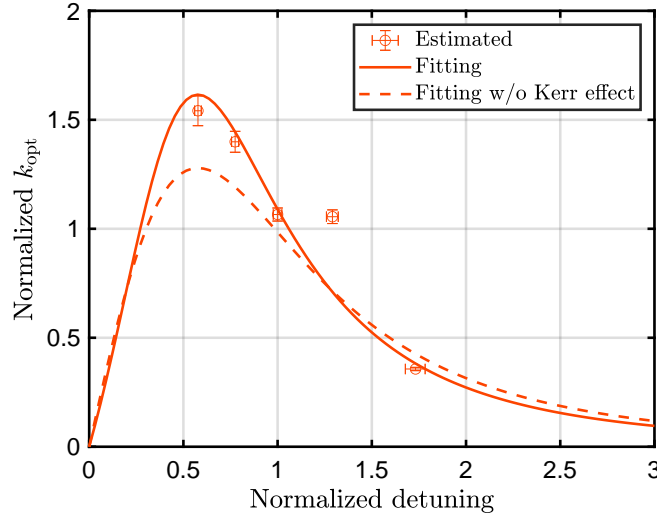


Fig. 6.10: Enhancement of the optical spring based on the Kerr effect. The error bars on the vertical and horizontal axes denote the standard error and the setting error of δ_0 estimated based on the fluctuations in the transmitted light, respectively.

where $k_{\text{opt-0}}$ denotes the maximum value of the optical spring constant without the Kerr effect. The estimated optical spring constants in measurement with a strong Kerr effect are shown in Fig. 6.10. The solid line represents the fitting results with $k_{\text{opt-0}}$ and ζ as parameters, and the gain of the Kerr effect is estimated to be $\zeta = -0.59 \pm 0.29$. The vertical axis is normalized by the estimated $k_{\text{opt-0}}$. The optical spring constant is estimated to be enhanced by a factor of up to 1.6 via the signal amplification effect. The dotted line indicates the fitting results with $\zeta = 0$ and only $k_{\text{opt-0}}$ as a parameter. These fitting results indicate that the measurement results do not agree with the fitting function unless the signal amplification effect is assumed. In other words, the change in the shape of the optical spring constant function is caused by the signal amplification effect. Note that these fittings are strongly dependent on data of $\delta_0 \sim 1.7$; thus, we need to increase the number of measurements.

Fig. 6.11 shows the optical spring constants for different gains of the Kerr effect. The vertical axis is normalized with the same value described in Fig. 6.10. The measurements with the moderate and weak Kerr effects demonstrate a decrease in the optical spring constant compared with the measurement with the strong Kerr effect. In addition, the transfer function measurements indicate that there is no significant difference in the magnitude of the optical spring constants in the measurements with the moderate and weak Kerr effects. The gains of the Kerr effect estimated for the measurement with the moderate and weak Kerr effects are $\zeta = -0.55 \pm 0.19$ and $\zeta = -0.49 \pm 0.19$, respectively, and we have not observed a significant difference in the measurements with the strong Kerr effect. By measuring the transfer function with finely varying cavity detuning, the

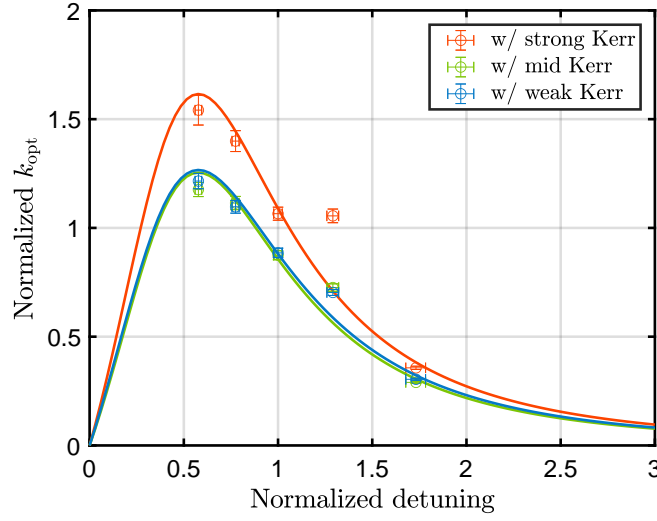


Fig. 6.11: Comparison of the optical spring constants for different gains of the Kerr effect. The error bars are defined in the same manner as in Fig. 6.10.

difference in the signal amplification effect can be clearly identified.

In summary, we can conclude that we succeeded in observing an optical spring enhanced by the signal amplification effect because the magnitude of the optical spring constant differed depending on the gain of the Kerr effect, and the change in the shape of the optical spring constant function induced by the Kerr effect was confirmed. However, the estimation error of the gain of the Kerr effect is significant, and the estimation method of the optical spring constant needs to be further improved.

6.2.4 Estimation of Kerr lensing effect

In this experiment, the photothermal relaxation rate may have increased with the Kerr effect. The nonlinear optical crystal may have behaved as a lens owing to self-focusing induced by the Kerr effect. The focal length of the Kerr lens f_K can be written as [179]

$$\begin{aligned} \frac{1}{f_K} &= \frac{8n_{\text{NL}}P_EL'}{\pi r_0^4} \\ &\simeq \frac{\lambda_0 T \zeta}{\pi r_0^2(1 + \delta^2)}, \end{aligned} \quad (6.25)$$

where r_0 denotes the beam radius, and we used that the nonlinear refractive index n_{NL} can be calculated as

$$n_{\text{NL}} = \frac{T^2 \zeta c \pi r_0^2}{16 P_A \omega_0 L'}. \quad (6.26)$$

Calculating the parameters as $T = 0.06$, $\zeta = -0.59$, $r_0 = 40 \mu\text{m}$, and $\delta = 1$, the Kerr lens possess a concave focal length of approximately 27 cm. If a concave lens is placed between the curved mirrors, the beam radius that satisfies the self-consistent equation reduces. In the case of this experiment, the effective beam radius may have decreased to approximately $30 \mu\text{m}$ ^{*4}. The photothermal relaxation rate is inversely proportional to the square of the beam radius, and we can estimate that the photothermal relaxation rate increased by approximately 1.8.

6.3 Summary of this chapter

In addition to the OPA, the Kerr effect can be applied to implement the intracavity signal amplification effect. This chapter derives the optical spring constant with the Kerr effect and confirms that the Kerr effect is a squeezer that depends on the intracavity power. Moreover, we found that the photothermal absorption rate is enhanced by the same factor that enhances the optical spring constant. Experimentally, we succeeded in observing an optical spring enhanced by the signal amplification effect by eliminating the photothermal effect from the transfer function measurements.

Cascaded nonlinear optical effects can produce a relatively significant nonlinear refractive effect. The nonlinear refractive index from the third-order nonlinear polarization of the KTP is approximately $3 \times 10^{-19} \text{ m}^2/\text{W}$ [180]. In contrast, as expressed in Eq. (6.26), the nonlinear refractive index from the cascaded nonlinear optical effects observed in this experiment is approximately $2 \times 10^{-17} \text{ m}^2/\text{W}$. Compared with the estimated accuracy of the gain of the Kerr effect, the third-order nonlinear optical effect is negligible. By improving the measurement accuracy, it may be possible to measure the Kerr effect produced by the third-order nonlinear optical effect as a signal amplification effect independent of phase mismatch.

In this experiment, the effective beam diameter may have been modified by the Kerr lens. If the beam radius changed from the designed value, the conversion efficiency of the nonlinear optical effect might have decreased. Therefore, the gain of the Kerr effect ζ might have depended on the intracavity power. The focal length of the Kerr lens might have also varied with the conversion efficiency. In addition, the optical loss caused by the SHG effect was relatively significant under the first phase-mismatched condition. We can estimate from the reflected light measurements that the intracavity loss at resonance was approximately 0.23 times that of the input coupler, which may have impacted the measurement of the optical spring. Thus, optical springs should be modeled considering more factors. The combined effect of these factors may be responsible for the non-negligible difference in the ζ estimated from the spectra and optical spring measurements.

On the transfer function, the resonance frequency of the optical spring decreased as the Kerr effect strengthened. In the experiment, the conversion of the optical

^{*4} See App. E.2.4.

spring constant based on the photothermal effect was predominant. When a signal amplification system is introduced in an actual gravitational wave detector, a mechanism is required to radically cancel the photothermal effect.

Note added on April 4, 2024

1. We later found that the reference on the Kerr lensing effect [179] assumes the beam radius is sufficiently larger than the crystal length. The parameters in our experiment did not satisfy this condition. Even in such a case, the equations in the following references are available:

V. Magni, G. Cerullo, S. De Silvestri, “ABCD matrix analysis of propagation of gaussian beams through Kerr media”, *Optics Communications*, Vol. 96, pp. 348–355, (1993).

The Kerr lensing effect may have been negligible in our experiments. Although the cause of the change in photothermal relaxation rate has not been determined, it could simply be the observed temperature dependence of the physical property values of the crystal.

2. We later increased the measurement points and improved the analysis method to ensure the “Kerr-enhanced optical spring.” The results of this study were summarized in the following letter:

S. Otabe *et al.*, “Kerr-Enhanced Optical Spring”, *Phys. Rev. Lett.*, Vol. 132, p. 143602, (2024).

Chapter 7

Conclusion

7.1 Theoretical overview

To observe gravitational waves emitted from binary neutron star post-merger remnants or supernovae, research and development are required to improve the sensitivity of gravitational wave detectors in the high-frequency band. The signal amplification system using nonlinear optical effects is a promising scheme for observing high-frequency gravitational waves. The essence of the gravitational wave signal amplification system is that the nonlinear optical effect enhances the optical spring generated in the cavity. This study considered conducting experiments using a Fabry-Perot cavity, which is an experimentally tractable interferometer compared to the actual interferometric configuration of the gravitational wave detector. Based on the established appropriate analogy, the Fabry-Perot cavity and dual recycling Michelson interferometer (DRMI) are equivalent in terms of sensitivity. To consider the optical spring generated in the Fabry-Perot cavity equivalent to it generated in the DRMI, we need to normalize the optical spring constant by the intracavity power and appropriately define the squeezing angle.

The signal amplification effect can be induced using nonlinear optical effects. In this study, we investigated two types of nonlinear optical effects, i.e., optical parametric amplification (OPA) and the optical Kerr effect, to configure a signal amplification system. Experiments using the OPA scheme indicated that the carrier light power required to generate an observable optical spring is considerably strong that the OPA process cannot be maintained. The conditions for signal amplification effects should be determined based on simulations because it is impossible to analytically formulate three-wave mixing with non-negligible attenuation of the pump light. In the experiments using the Kerr scheme, we found that the photothermal effect prevented the measurement of the optical spring because it requires relatively high laser light power. The photothermal effect converts the real and imaginary components of the complex optical spring constant into each other, allowing us to simultaneously generate a positive optical spring and damping. In addition, the photothermal effect and optical spring are phenomena that result from the intracavity power proportional to the cavity length, and the photothermal absorption rate and optical spring constant are identical except for the

proportionality factor. Furthermore, the signal amplification effect enhances the optical spring constant and photothermal absorption rate by the same factor. We can conclude that the photothermal effect is one of the essential factors that determine the characteristics of the signal amplification system.

7.2 Summary of experiments

We experimentally attempted to observe an optical spring enhanced by nonlinear optical effects. In the OPA experiment, we constructed a second harmonic generation (SHG) cavity and optical parametric oscillator (OPO) cavity with excellent conversion efficiency. This experiment required acquiring a squeezing angle error signal for a detuned cavity. We showed that the squeezing angle of the detuned OPO cavity could be controlled using the coherent control method and succeeded in controlling it to maximize power amplification. Theoretical predictions indicated that we achieved sufficient signal amplification to observe an enhancement of the optical spring; however, we could not confirm the signal amplification effect because the OPA process was suppressed.

In the experiments on photothermal effects, we have developed a method for estimating photothermal parameters by measuring the susceptibility of the optomechanical oscillator. This method can estimate even a slight photothermal effect that cannot be estimated from the measurement of the frequency response of the cavity. By simultaneously estimating the optical spring constant and the photothermal absorption rate, we succeeded in estimating the optical spring constant without the photothermal effect with a high precision of less than 1% standard error. Moreover, we succeeded in estimating the photothermal absorption rate with an accuracy of approximately one order of magnitude better than the method of measuring the frequency response of the cavity.

In the Kerr experiments, we found that the Kerr effect also modified the photothermal parameters. The signal amplification effect enhanced the photothermal absorption rate. Moreover, the Kerr effect increased the photothermal relaxation rate because the Kerr lens reduced the effective beam radius. In this case, it is difficult to analytically model the photothermal effect. We measured the frequency response of the cavity using a PZT to remove the photothermal effect from the optical spring measurements. Consequently, we successfully observed an optical spring enhanced by the signal amplification effect.

7.3 Prospects

The Kerr effect reduced the optical spring constant on the transfer function measured in this experiment. The conversion of the optical spring constant owing to the photothermal effect may have predominated compared with the enhancement of the optical spring owing to the Kerr effect. A compensation crystal with a negative thermo-optic coefficient should be used to radically eliminate the photothermal effect. The condition for canceling the photothermal effect over the

entire frequency band is that the compensation crystal possesses a photothermal absorption rate of -1 times that of the nonlinear optical crystal and the same photothermal relaxation rate as that of the nonlinear optical crystal. These can be adjusted by changing the crystal length of the compensation crystal; however, it is not easy to tune them separately. It would be sufficient to set them so that the impact of the photothermal effect is eliminated near the resonance frequency of the optical spring.

This experiment confirmed a signal amplification effect of up to approximately 1.6. An actual gravitational wave detector requires a signal amplification effect of roughly 10. The gain of the Kerr effect increases as the finesse of the cavity increases. If the gain can be increased several times, we can expect the critical Kerr effect to be realized. In this case, developing a new control method may be necessary because the signal amplification effect becomes significant, making stable control difficult.

The experiment was performed using a Fabry-Perot cavity; however, it is also essential to experiment using a signal-recycling Michelson interferometer (SRMI), which is a similar configuration to an actual gravitational wave detector. The OPA scheme can be used in the SRMI because the carrier light intensity on the nonlinear optical crystal can be weak. The OPA scheme can vary the squeezing angle; thus, we expect to obtain further insight into signal amplification systems from the SRMI experiments.

In experiments with macroscopic oscillators, it is challenging to directly measure quantum noise reduction by the optical spring. In contrast, it is possible to demonstrate quasi-back action evasion by injecting classical noise. We can expect the signal amplification system to allow the frequency of the dip in spectral density to shift with the gain of the nonlinear optical effect.

High gain signal amplification effects and large cavity detuning are required to improve the sensitivity of gravitational wave detectors; however, this characteristic is difficult to achieve with the signal amplification system configured in this study. Further theoretical consideration of the near-threshold behavior of the OPA and Kerr effects and further experiments with high-gain signal amplification effects are required.

This study has conducted a proof-of-principle verification of the signal amplification system for a gravitational wave detector. Based on further validation experiments, we expect to implement the signal amplification system in actual gravitational wave detectors and observe high-frequency gravitational waves with high sensitivity, thereby contributing to cosmology and astronomy.

Appendix A

Derivation of gravitational waves

Gravitational waves are derived from a linear approximation of the Einstein equation, which links spacetime and the distribution of matter [1,2]. This appendix provides derivations of gravitational wave propagation and emission and describes the principles of interferometric gravitational wave detectors.

A.1 Propagation of gravitational waves

In a flat spacetime with no gravitational field, Minkowski spacetime, the small distance between two spacetime points ds can be written as

$$ds^2 = \sum_{\mu=0}^3 \sum_{\nu=0}^3 \eta_{\mu\nu} dx^\mu dx^\nu := \eta_{\mu\nu} dx^\mu dx^\nu, \quad (\text{A.1})$$

where $\eta_{\mu\nu} = \text{diag}(-1, 1, 1, 1)$ represents the metric tensor in Minkowski spacetime. Here, Greek letters such as μ and ν are defined to take the values 0, 1, 2, 3 and take summation for the same index. Because ds^2 is invariant even in a distorted spacetime with a gravitational field, we can define the metric tensor in a distorted spacetime $g_{\mu\nu}$ from the Lorentz transformation $x^\mu \rightarrow x'^\mu$:

$$\begin{aligned} ds^2 &= \eta_{\mu\nu} dx'^\mu dx'^\nu \\ &= \eta_{\mu\nu} \frac{\partial x'^\mu}{\partial x^\alpha} \frac{\partial x'^\nu}{\partial x^\beta} dx^\alpha dx^\beta \\ &:= g_{\alpha\beta} dx^\alpha dx^\beta. \end{aligned} \quad (\text{A.2})$$

The metric tensor is a physical quantity that determines the distance between spacetime points in the original coordinate or the geometry of spacetime and follows the Einstein equation:

$$G_{\mu\nu} = \frac{8\pi G}{c^4} T_{\mu\nu}, \quad (\text{A.3})$$

where $G_{\mu\nu}$ is the Einstein tensor and $T_{\mu\nu}$ is the energy-momentum tensor. The Einstein tensor is defined using the Ricci tensor $R_{\mu\nu}$, Ricci scalar R , Riemann tensor $R^\mu{}_{\nu\lambda\kappa}$, and Christoffel symbol $\Gamma^\mu_{\nu\lambda}$:

$$G_{\mu\nu} := R_{\mu\nu} - \frac{1}{2}g_{\mu\nu}R, \quad R = R^\mu{}_\mu, \quad R_{\mu\nu} = R^\alpha{}_{\mu\alpha\nu}, \quad (\text{A.4})$$

$$R^\mu{}_{\nu\lambda\kappa} := \Gamma^\mu_{\nu\kappa,\lambda} - \Gamma^\mu_{\nu\lambda,\kappa} + \Gamma^\mu_{\sigma\lambda}\Gamma^\sigma_{\nu\kappa} - \Gamma^\mu_{\sigma\kappa}\Gamma^\sigma_{\nu\lambda}, \quad (\text{A.5})$$

$$\Gamma^\mu_{\nu\lambda} := \frac{1}{2}g^{\mu\sigma}(g_{\sigma\nu,\lambda} + g_{\sigma\lambda,\nu} - g_{\nu\lambda,\sigma}). \quad (\text{A.6})$$

Let us assume that the gravity field is sufficiently small, and the metric tensor can be denoted as

$$g_{\mu\nu} = \eta_{\mu\nu} + h_{\mu\nu}, \quad (\text{A.7})$$

where $h_{\mu\nu}$ is the perturbation term. The Einstein tensor can be calculated as

$$G_{\nu\lambda} = \frac{1}{2}[h^\delta{}_{\lambda,\nu\delta} + h^\delta{}_{\nu,\lambda\delta} - \square h_{\nu\lambda} - h_{,\nu\lambda} - \eta_{\nu\lambda}(h^{\delta\sigma}{}_{,\delta\sigma} - \square h)], \quad (\text{A.8})$$

with

$$h = h^\mu{}_\mu, \quad \square = \partial^\mu \partial_\mu. \quad (\text{A.9})$$

Eq. (A.8) can be organized by using a trace-reverse tensor of $h_{\mu\nu}$ as

$$G_{\nu\lambda} = \frac{1}{2}(\tilde{h}^\delta{}_{\lambda,\nu\delta} + \tilde{h}^\delta{}_{\nu,\lambda\delta} - \square \tilde{h}_{\nu\lambda} - \eta_{\nu\lambda} \tilde{h}^{\delta\sigma}{}_{,\delta\sigma}), \quad (\text{A.10})$$

with

$$\tilde{h}_{\mu\nu} = h_{\mu\nu} - \frac{1}{2}\eta_{\mu\nu}h, \quad \tilde{h} = \tilde{h}^\mu{}_\mu = -h. \quad (\text{A.11})$$

Lorentz gauge and transverse-traceless (TT) gauge can be imposed simultaneously as gauge conditions [181]. Lorentz gauge can be expressed as

$$\tilde{h}^{\delta\sigma}{}_{,\delta} = 0. \quad (\text{A.12})$$

TT gauge can be expressed as

$$\begin{cases} \tilde{h}_{\mu 0} = 0, \\ \tilde{h}^\mu{}_\mu = 0. \end{cases} \quad (\text{A.13})$$

$$(\text{A.14})$$

Accordingly, we obtain the linearized Einstein equation:

$$\square h_{\mu\nu} = -\frac{16\pi G}{c^4}T_{\mu\nu}. \quad (\text{A.15})$$

The perturbation term follows the wave equation in a vacuum as $T_{\mu\nu} = 0$. Because the perturbation term is a symmetric tensor, the monochromatic plane wave

solution propagating along the x^3 axis can be denoted in matrix form as

$$h_{\mu\nu} = \begin{pmatrix} 0 & 0 & 0 & 0 \\ 0 & h_+ & h_\times & 0 \\ 0 & h_\times & -h_+ & 0 \\ 0 & 0 & 0 & 0 \end{pmatrix} \exp[-ik(ct - z)], \quad (\text{A.16})$$

where k denotes the wave number of the gravitational wave and h_+ and h_\times represent the amplitude of the $+$ mode \times modes, respectively. Gravitational waves are transverse waves propagating at the speed of light with two modes.

A.2 Impact of gravitational waves on free masses

The trajectory of a free mass in distorted spacetime with a gravitational field follows a geodesic equation:

$$\frac{d^2 x^\alpha}{d\tau^2} + \Gamma_{\nu\lambda}^\alpha \frac{dx^\nu}{d\tau} \frac{dx^\lambda}{d\tau} = 0, \quad (\text{A.17})$$

where τ denotes the proper time. If one free mass is stationary in the initial state, we obtain

$$\frac{d^2 x^\alpha}{d\tau^2} \propto -\Gamma_{00}^\alpha = 0 \quad (\because h_{\mu 0} = 0), \quad (\text{A.18})$$

indicating that acceleration does not act on the test mass, and the influence of gravitational waves cannot be observed.

Now, we examine the effect of gravitational waves on the distance between the origin $x_{(1)}^\mu = (-ct, 0, 0, 0)$ and point $x_{(2)}^\mu = (-ct, R \cos \theta, R \sin \theta, 0)$ which is located at a distance R from the origin in Minkowski spacetime. When a $+$ mode gravitational wave $h_{\mu\nu} = \text{diag}(0, 1, 1, 0)h_+ \cos \Omega t$ with wavelength sufficiently larger than R is incident from the direction of the z -axis, the distance between two points d_+ can be expressed as

$$\begin{aligned} d_+ &= \int_{x_{(1)}^\mu}^{x_{(2)}^\mu} |g_{\mu\nu} dx^\mu dx^\nu|^{1/2} \\ &\simeq \sqrt{(1 + h_+ \cos \Omega t)(R \cos \theta)^2 + (1 - h_+ \cos \Omega t)(R \sin \theta)^2} \\ &\simeq R \left(1 + \frac{1}{2} h_+ \cos 2\theta \cos \Omega t \right), \end{aligned} \quad (\text{A.19})$$

thus indicating that the distance between two points changes owing to the gravitational waves. When a \times mode gravitational wave is incident, the distance between two points d_\times can be expressed as

$$d_\times = R \left(1 + \frac{1}{2} h_\times \sin 2\theta \cos \Omega t \right). \quad (\text{A.20})$$

A.3 Radiation of gravitational waves

We consider the case where a gravitational wave source exists ($T_{\mu\nu} \neq 0$).

A.3.1 Generation of gravitational waves

The requirements that gravitational waves in the TT gauge must satisfy are

$$h_{ij}\delta^{ij} = 0, \quad (\text{A.21})$$

$$h_{ij}k^j = 0, \quad (\text{A.22})$$

where k^i is the wave number vector, and Latin characters such as i and j are defined to take values 1, 2, 3. The TT component of the plane wave can be written as

$$h_{\text{TT}}^{ij} = P_k^i h^{kl} P_l^j - \frac{1}{2} P^{ij} P_{kl} h^{kl}, \quad (\text{A.23})$$

where $P_j^i = \delta_j^i - n^i n_j$ is the projection operator and $n^i = x^i/|\mathbf{x}|$ is the unit vector in the direction of the observation point.

Let us calculate the equation that h_{TT}^{ij} obeys when the gravitational wave source exists. By solving Eq. (A.15) using Green's function of the wave equation, we obtain

$$h^{\mu\nu}(t, \mathbf{x}) = \frac{4G}{c^4} \int \frac{T^{\mu\nu}(t - |\mathbf{x} - \mathbf{x}'|/c, |\mathbf{x}'|)}{|\mathbf{x} - \mathbf{x}'|} d^3\mathbf{x}'. \quad (\text{A.24})$$

Assume that the distance to the observation point $|\mathbf{x}|$ is sufficiently larger than the wavelength of the gravitational wave. Note that the distance to the point significantly contributes to the integration $|\mathbf{x}'|$, which is comparable to the wavelength. Furthermore, assuming that the time variability of the wave source is sufficiently slow compared to the speed of light, Eq. (A.24) can be approximated as follows [182]:

$$h^{ij}(t, \mathbf{x}) = \frac{4G}{|\mathbf{x}|c^4} \int \sum_{m=0}^{\infty} \frac{\partial^m}{\partial t^m} T^{ij}(t - |\mathbf{x}|/c, \mathbf{x}') \frac{(\mathbf{n} \cdot \mathbf{x}')^m}{m!} d^3\mathbf{x}'. \quad (\text{A.25})$$

The lowest term of this equation can be calculated using $T^{\mu\nu}_{;\nu} = 0$ as

$$\begin{aligned} h^{ij}(t, \mathbf{x}) &= \frac{4G}{|\mathbf{x}|c^4} \int T^{ij}(t - |\mathbf{x}|/c, \mathbf{x}') d^3\mathbf{x}' \\ &= \frac{2G}{|\mathbf{x}|c^2} \int T^{00}_{,00}(t - |\mathbf{x}|/c, \mathbf{x}') x^i x^j d^3\mathbf{x}'. \end{aligned} \quad (\text{A.26})$$

Note that the Bianchi identities yield $T_{\mu}{}^{\nu}_{;\nu} = 0$; hence, we need to redefine the effective energy-momentum tensor that follows the conservation laws more rigorously [183]. When the wave source is a perfect fluid of density $\rho \simeq T^{00}$, we

obtain

$$h_{ij}^{TT}(t, \mathbf{x}) = \frac{2G}{|\mathbf{x}|c^4} \left(\ddot{\mathcal{I}}_{lm} P_i^l P_j^m - \frac{1}{2} P_{ij} P^{jm} \ddot{\mathcal{I}}_{lm} \right), \quad (\text{A.27})$$

where

$$\mathcal{I}_{ij} = \int \rho \left(x'_i x'_j - \frac{1}{3} \delta_{ij} |\mathbf{x}'|^2 \right) d^3 \mathbf{x}' \quad (\text{A.28})$$

is the quadrupole moment for mass distribution. Gravitational waves are generated from the asymmetric acceleration motion of objects, whose lowest order is quadrupole radiation. Let M be the mass of the wave source and v be the velocity. Then, we obtain roughly $\ddot{\mathcal{I}}_{ij} \sim Mv^2$.

A.3.2 Quadrupole formula

We have calculated $h_{\mu\nu}$ as a first-order small fluctuating term. Within this approximation, the energy flux T^{i0} is zero. By calculating the effective energy-momentum tensor, including second-order small fluctuating terms for $h_{\mu\nu}$, the time variation of the energy \mathcal{E} can be written as [184]

$$W = \frac{d\mathcal{E}}{dt} = \frac{G}{5c^5} \ddot{\mathcal{I}}_{ij} \ddot{\mathcal{I}}^{ij}. \quad (\text{A.29})$$

This equation is called the quadrupole formula.

Let us roughly derive the effect of gravitational waves on a binary system of two stars of mass M with semi-major axis a . From Kepler's law, the angular velocity of the orbit Ω_{orb} can be written as

$$\Omega_{\text{orb}} = \sqrt{\frac{2GM}{a^3}}. \quad (\text{A.30})$$

Therefore, the power of gravitational waves W emitted from this binary system is roughly

$$W \sim \frac{G^4 M^5}{c^5 a^5}. \quad (\text{A.31})$$

Because the energy of the binary system is roughly $\mathcal{E} \sim -GM^2/a$, the time variation of the semi-major axis can be written as

$$\frac{da}{dt} \sim -\frac{G^3 M^3}{c^5 a^3}. \quad (\text{A.32})$$

By solving this differential equation, we obtain the time for binary mergers to occur as

$$t_M \sim \frac{c^5 a^4}{G^3 M^3}. \quad (\text{A.33})$$

Note that the coefficients can be obtained from a more rigorous calculation [185] and that the time required for coalescence is approximately two orders of magnitude less than this estimate.

A.4 Principle of interferometric gravitational wave detectors

Let us derive the response of the Michelson interferometer, as shown in Fig. 2.3(a). Let L_x and L_y denote the lengths of the x-arm and y-arm, respectively. Assume that a + mode gravitational wave ($h_{\times} = 0$) denoted by Eq. (A.16) is incident on the Michelson interferometer. Because the speed of light is invariant to any inertial system, the micro distance traveled by the photon ds is constantly zero. For light traveling in the x-axis, from Eq. (A.2), we obtain

$$\left(1 - \frac{1}{2}h(t)\right) c dt = dx, \quad (\text{A.34})$$

where we defined $h(t) = h_+ \exp(-\Omega t)$ with Ω as the angular frequency of the gravitational wave. Let Δt_x be the round-trip time required for a photon to travel the x-arm and integrate both sides of Eq. (A.34), obtaining

$$\int_{t-\Delta t_x}^t \left\{1 - \frac{1}{2}h(t')\right\} dt' = \frac{2L_x}{c}, \quad (\text{A.35})$$

which yields

$$\Delta t_x \simeq \frac{2L_x}{c} + \frac{1}{2} \int_{t-\frac{2L_x}{c}}^t h(t') dt'. \quad (\text{A.36})$$

For the y-arm, we obtain

$$\Delta t_y \simeq \frac{2L_y}{c} - \frac{1}{2} \int_{t-\frac{2L_y}{c}}^t h(t') dt'. \quad (\text{A.37})$$

Michelson interferometers can measure the phase difference between the x- and y-arms $\phi'_- = \omega_0(\Delta t_x - \Delta t_y)$, modified by gravitational waves. By assuming $L \simeq L_x \simeq L_y$, we obtain

$$\phi'_- \simeq \frac{2(L_x - L_y)\omega_0}{c} + \omega_0 \int_{t-\frac{2L}{c}}^t h(t') dt' = \phi_- + \delta\phi_{\text{GW}}, \quad (\text{A.38})$$

where $\phi_- = 2(L_x - L_y)\omega_0/c$ is the phase difference without gravitational waves and $\delta\phi_{\text{GW}}$ is the phase variation induced by gravitational waves. Denoting the inverse Fourier transform of $h(t)$ as

$$h(t) = \frac{1}{2\pi} \int_{-\infty}^{\infty} h(\Omega) e^{i\Omega t} d\Omega, \quad (\text{A.39})$$

the frequency response of the gravitational wave can be written as

$$\delta\phi_{\text{GW}} = \int_{-\infty}^{\infty} H_{\text{MI}}(\Omega) h(\Omega) e^{i\Omega t} d\Omega, \quad (\text{A.40})$$

$$H_{\text{MI}}(\Omega) = \frac{2\omega_0}{\Omega} \sin\left(\frac{L\Omega}{c}\right) e^{-iL\Omega/c}, \quad (\text{A.41})$$

which corresponds to the second term on the right-hand side of Eq. (3.63). For the range of baseline lengths that can realistically be constructed, the response for gravitational waves of ~ 100 Hz becomes better with longer arms.

A.5 Amplitude spectral density

When a physical quantity $x(t)$ is measured for a sufficiently long time, the integrated amount of this deviation from the average is zero. The effective amplitude magnitude of $x(t)$ can be evaluated by the root-mean-square, which is the amount obtained by integrating the square of the deviation from the average. Let $\sqrt{\langle x^2 \rangle}$ be the root-mean-square for $x(t)$. Thus, we obtain

$$\begin{aligned} \langle x^2 \rangle &= \frac{1}{T} \int_{-T/2}^{T/2} [x(t)]^2 dt \\ &= \frac{1}{2\pi} \int_{-\infty}^{\infty} \frac{|X(\Omega)|^2}{T} d\Omega, \end{aligned} \quad (\text{A.42})$$

where T is the measurement time and $X(\Omega)$ is the Fourier-transformed physical quantity of $x(t)$. The integrated function excluding the coefficients in Eq. (A.42), $P(\Omega) = |X(\Omega)|^2/T$, is called the power spectral density, and $A(\Omega) = \sqrt{P(\Omega)}$ is called the amplitude spectral density. The amplitude spectral density represents the frequency component contained in the physical quantity, which can be used to discuss noise.

Appendix B

Nonlinear optical effects

This appendix describes the classical theory of nonlinear optical effects used in the experiments.

B.1 Overview of nonlinear optical effects

In ordinary optics, light and matter interact because of the induced electric polarization proportional to the light field. However, when light becomes sufficiently intense, the nonlinearity of crystal polarization becomes non-negligible. In this section, the second- and third-order nonlinear optical effects are overviewed. The polarization $P(t)$ is represented with the electric susceptibility $\chi^{(1)}$, the second-order nonlinear susceptibility $\chi^{(2)}$, and the third-order nonlinear susceptibility $\chi^{(3)}$ as follows:

$$P(t) = \varepsilon_0 \chi^{(1)} E(t) + \varepsilon_0 \chi^{(2)} [E(t)]^2 + \varepsilon_0 \chi^{(3)} [E(t)]^3 + \dots \quad (\text{B.1})$$

Let us consider that a light field $E(t) = E_0 \cos \omega_0 t$ with angular frequency ω_0 is incident on a nonlinear optical crystal. The second- and third-order nonlinear polarization $P^{(2)}(t)$ and $P^{(3)}(t)$, respectively, are induced, resulting in nonlinear optical effects corresponding to the respective orders.

The second-order nonlinear polarization can be written as

$$P^{(2)}(t) = \varepsilon_0 \chi^{(2)} E_0^2 \cos^2 \omega_0 t = \frac{1}{2} \varepsilon_0 \chi^{(2)} E_0^2 \cos(2\omega_0 t) + \frac{1}{2} \varepsilon_0 \chi^{(2)} E_0^2. \quad (\text{B.2})$$

Light with angular frequency $\omega_3 = 2\omega_0$ is emitted, indicating the occurrence of wavelength conversion of light. This phenomenon is called the second harmonic generation (SHG) and corresponds to the generation of one photon with energy $\hbar\omega_3$ from two photons with energy $\hbar\omega_0$. On the other hand, the reverse process occurs if light with angular frequency ω_3 is sufficiently strong. It corresponds to the generation of two photons with energy $\hbar\omega_1$ and $\hbar\omega_2$ from one photon with energy $\hbar\omega_3$. This phenomenon is called the optical parametric process and satisfies $\omega_3 = \omega_1 + \omega_2$, corresponding to the energy conservation law.

The third-order nonlinear polarization can be written as

$$P^{(3)}(t) = \varepsilon_0 \chi^{(3)} E_0^3 \cos^3 \omega_0 t = \frac{3}{4} \varepsilon_0 \chi^{(3)} E_0^3 \cos \omega_0 t + \frac{1}{4} \varepsilon_0 \chi^{(3)} E_0^3 \cos(3\omega_0 t). \quad (\text{B.3})$$

The polarization corresponding to the second term of the right-hand side of Eq. (B.3) results in the light emission with angular frequency $3\omega_0$. This conversion process is called the third harmonic generation. In addition, the polarization corresponding to the first term of the right-hand side emits a fundamental wave with angular frequency ω_0 . The total polarization corresponding to the fundamental wave can be written as

$$P_{\text{tot}}^{(1)}(t) = \varepsilon_0 \left(\chi^{(1)} + \frac{3}{4} \chi^{(3)} E_0^2 \right) E_0 \cos \omega_0 t, \quad (\text{B.4})$$

which implies that the relationship between the susceptibility and refractive index n is modified as follows:

$$n^2 = 1 + \chi^{(1)} + \frac{3}{4} \chi^{(3)} E_0^2. \quad (\text{B.5})$$

Therefore, the refractive index varies in proportion to the light intensity I_0 :

$$n = n_0 + n_{\text{NL}} I_0, \quad (\text{B.6})$$

where n_0 and n_{NL} are the linear and nonlinear refractive indexes, respectively. The phenomenon that provides the nonlinear refractive index is called the optical Kerr effect.

Third-order nonlinear optical effects can be generally neglected in experiments using continuous-wave lasers because the third-order nonlinear polarization is extremely small. However, a chain of second-order nonlinear optical effects can produce phenomena equivalent to higher-order nonlinear optical effects [174, 175]. This phenomenon is called the cascaded nonlinear optical effect. Our experiment used the Kerr effect owing to the cascaded nonlinear optical effect.

B.2 Principle of three-wave mixing

Second-order nonlinear optical effects are caused by the interaction of three light waves propagating through a nonlinear optical crystal. In this section, we derive the coupled-wave equations, which are the fundamental equations for three-wave mixing, and discuss the phase matching necessary to induce significant nonlinear optical effects.

B.2.1 Coupled-wave equations

The Maxwell equations in a nonlinear optical crystal, similar to those in ordinary crystals, can be written as

$$\nabla \cdot \mathbf{D}(\mathbf{r}, t) = 0, \quad (\text{B.7})$$

$$\nabla \cdot \mathbf{B}(\mathbf{r}, t) = 0, \quad (\text{B.8})$$

$$\nabla \times \mathbf{E}(\mathbf{r}, t) = -\frac{\partial \mathbf{B}(\mathbf{r}, t)}{\partial t}, \quad (\text{B.9})$$

$$\nabla \times \mathbf{H}(\mathbf{r}, t) = \frac{\partial \mathbf{D}(\mathbf{r}, t)}{\partial t}. \quad (\text{B.10})$$

Here, we assume that there is no current or free charge in the nonlinear optical crystal and that absorption of the electromagnetic field is negligible. The relationship between the electric flux density $\mathbf{D}(\mathbf{r}, t)$ and electric field $\mathbf{E}(\mathbf{r}, t)$ can be written as

$$\mathbf{D}(\mathbf{r}, t) = \varepsilon_0 \varepsilon \mathbf{E}(\mathbf{r}, t) + \mathbf{P}^{(2)}(\mathbf{r}, t), \quad (\text{B.11})$$

with the second-order nonlinear polarization $\mathbf{P}^{(2)}(\mathbf{r}, t)$. ε is the relative permittivity, which is related to the refractive index of the crystal n by $\varepsilon = n^2$. In contrast, because the nonlinearity of magnetization can be neglected in a frequency band of light, the relationship between the magnetic flux density $\mathbf{B}(\mathbf{r}, t)$ and magnetic field $\mathbf{H}(\mathbf{r}, t)$ can be written as

$$\mathbf{B}(\mathbf{r}, t) = \mu_0 \mathbf{H}(\mathbf{r}, t). \quad (\text{B.12})$$

The wave equation for the electric field $\mathbf{E}(\mathbf{r}, t) = \mathbf{E}(\mathbf{r}) \cos \omega t$ with angular frequency ω is obtained from Eqs. (B.7) to (B.12):

$$-\nabla^2 \mathbf{E}(\mathbf{r}) + \nabla(\nabla \cdot \mathbf{E}(\mathbf{r})) - \frac{\omega^2}{c^2} \varepsilon \mathbf{E}(\mathbf{r}) = \frac{\omega^2}{\varepsilon_0 c^2} \mathbf{P}^{(2)}(\mathbf{r}). \quad (\text{B.13})$$

Let the amplitude of the electric field $\mathbf{E}(\mathbf{r})$ be represented as

$$\mathbf{E}(\mathbf{r}) = \mathbf{u} F(z) e^{ikz}, \quad (\text{B.14})$$

where $k = \omega n/c$ is the wavenumber, $F(z)$ is the complex amplitude, and the electric field is assumed to propagate along the z -axis. \mathbf{u} is a unit vector in the direction of polarization and is orthogonal to the z -axis such that $\nabla \cdot \mathbf{E}(\mathbf{r}) = 0$. We further assume that $F(z)$ is a slowly varying function with z such that $d^2 F/dz^2$ is sufficiently small. Eq. (B.13) can be written as

$$\frac{d}{dz} F(z) = \frac{i\omega}{2\varepsilon_0 c n} \mathbf{u}^* \cdot \mathbf{P}^{(2)}(z). \quad (\text{B.15})$$

Let us consider three light waves with angular frequencies ω_1 , ω_2 , and $\omega_3 = \omega_1 + \omega_2$ in a nonlinear optical crystal. Similar to Eq. (B.2), the nonlinear polarization $\mathbf{P}_3^{(2)}(z)$ for an electric field with angular frequency ω_3 is induced by electric fields with angular frequencies ω_1 and ω_2 as follows:

$$\mathbf{P}_3^{(2)}(z) = \varepsilon_0 \chi_3^{(2)} F_1 F_2 e^{i(k_1 + k_2)z}, \quad (\text{B.16})$$

where F_1 , F_2 , k_1 , and k_2 are complex amplitudes and wavenumbers of electric fields with angular frequencies ω_1 and ω_2 , respectively. Further, $\chi_3^{(2)}$ denotes the nonlinear susceptibility vector. Nonlinear polarization for electric fields with other angular frequencies can be considered similarly. By substituting these into Eq. (B.15), the following equations are derived because of the intrinsic permutation symmetry of the nonlinear susceptibility [186]:

$$\begin{cases} \frac{dF_1}{dz} = \frac{i\omega_1 \chi^{(2)}}{2cn_1} F_2^* F_3 e^{i\Delta k z}, \\ \frac{dF_2}{dz} = \frac{i\omega_2 \chi^{(2)}}{2cn_2} F_1^* F_3 e^{i\Delta k z}, \\ \frac{dF_3}{dz} = \frac{i\omega_3 \chi^{(2)}}{2cn_3} F_1 F_2 e^{-i\Delta k z}, \end{cases} \quad (\text{B.17})$$

with the identical effective nonlinear susceptibility $\chi^{(2)}$ in all equations. Here, $\chi^{(2)}$ is a real number, and $\Delta k = k_3 - k_2 - k_1$ denotes phase mismatch. The simultaneous differential equations for complex amplitudes are called coupled-wave equations.

B.2.2 Phase matching and quasi-phase matching

When the phase $\Delta k L'$ (where L' is the length of the nonlinear optical crystal) is reached approximately π , the nonlinear optical effects are suppressed because the generated electric fields weaken each other. Therefore, the phase-matching condition $\Delta k = 0$ must be satisfied to maximize the nonlinear optical effect. This condition, for the second harmonic generation or degenerate optical parametric amplification, is satisfied when the refractive index of the fundamental and second harmonic are equivalent. However, generally, it is not achievable because of material dispersion. There are several methods for satisfying the phase-matching condition, such as birefringence and waveguides. In our experiment, we used quasi-phase matching by periodic poling.

The length $l_c = \pi/\Delta k$ at which nonlinear optical effects become suppressed is called the coherence length. Periodic poling is a method of inverting the sign of nonlinear susceptibility with a period Λ that is an integer multiple of $2l_c$, as shown in Fig. B.1. Because the phase of the light generated by nonlinear optical effects is reversed as it propagates for a length l_c , the phase-matching condition is quasi-satisfied by periodically inverting the sign of the nonlinear susceptibility. The quasi-phase-matching condition can be written as follows:

$$\Delta k = \pm mK \quad (m = 0, \pm 1, \pm 2, \dots), \quad (\text{B.18})$$

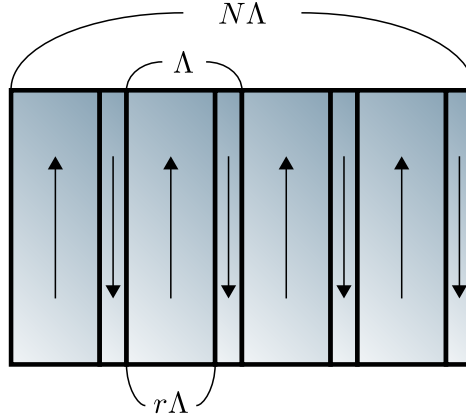


Fig. B.1: Schematic of periodic poling. r denotes the duty cycle, and $N = L'/\Lambda$ is the number of periodic poling. Arrows indicate the direction of the crystal axis, and the sign of the nonlinear susceptibility is opposite for upward and downward directions.

where $K = 2\pi/\Lambda$ denotes the wavenumber of periodic poling.

Quasi-phase matching allows the use of materials and polarizations that standard phase matching cannot satisfy. For example, the nonlinear susceptibility of lithium niobate (LiNbO_3) to the second harmonic generation has its maximum when both the polarization of the fundamental and second harmonics are parallel to the c -axis (extraordinary rays). However, this combination of polarizations cannot achieve phase matching using birefringence. In our experiment, we used periodically poled lithium niobate (PPLN) for second harmonic generation, where both the fundamental and second harmonic waves were extraordinary rays. A comparison of the conversion efficiencies of standard and quasi-phase matching is discussed in the following section.

B.3 Second harmonic generation

Second harmonic generation (SHG) is the process of generating the harmonic wave with angular frequency $\omega_3 = 2\omega_0$ from the fundamental wave with angular frequency ω_0 . The complex amplitudes of each light are denoted as F_0 and F_3 .

B.3.1 SHG with low conversion efficiency

Let us consider the case of standard phase matching. If the absorption of the light field by the nonlinear optical crystal is negligible, the coupled-wave equations can be written as

$$\begin{cases} \frac{dF_0}{dz} = \frac{i\omega_0\chi^{(2)}}{2cn_0} F_0^* F_3 e^{i\Delta kz}, \\ \frac{dF_3}{dz} = \frac{i\omega_0\chi^{(2)}}{cn_3} F_0^2 e^{-i\Delta kz}, \end{cases} \quad (\text{B.19})$$

where $\Delta k = k_3 - 2k_0$. If the conversion efficiency is low and F_0 can be assumed to be constant, the complex amplitude of the second harmonic wave from the crystal can be calculated as

$$F_3(L') = \frac{\omega_0 \chi^{(2)} F_0^2}{c n_3 \Delta k} \left(1 - e^{-i \Delta k L'} \right). \quad (\text{B.20})$$

Here, we assume $F_3(0) = 0$ because the second harmonic wave is not injected into the crystal. The light intensity I_j ($j = 0, 3$) can be denoted as $I_j = n_j |F_j|^2 / (2\mu_0 c)$. The intensity of the generated second harmonic wave I_3 can be written as

$$I_3 = 8\pi^2 \mu_0 c \left(\frac{(\chi^{(2)})^2 L'^2}{n_0^2 n_3 \lambda_0} \right) \text{sinc}^2 \left(\frac{\Delta k L'}{2} \right) I_0^2, \quad (\text{B.21})$$

where $\text{sinc}(x) = \sin(x)/x$ is the sinc function. The normalized efficiency of SHG is presented in Fig. B.2. The intensity of the second harmonic wave generated by the SHG is proportional to the square of the intensity of the incident fundamental wave and varies periodically with the phase mismatch.

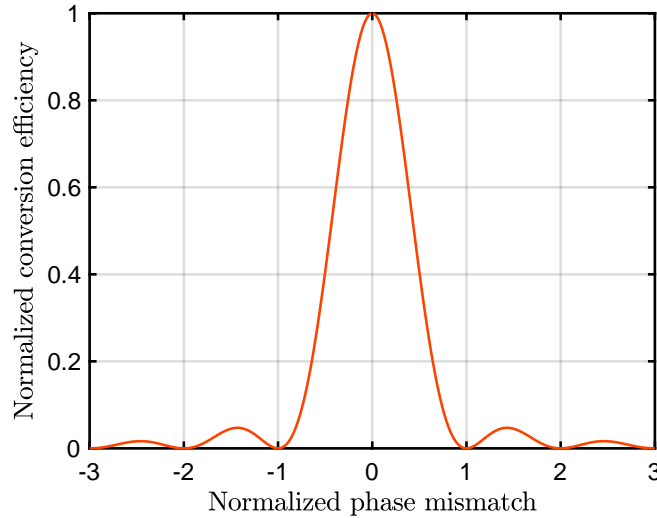


Fig. B.2: Relationship between phase mismatch and SHG efficiency.

B.3.2 SHG with a periodically polled crystal

Let us consider the SHG with a periodically polled crystal of period Λ and duty cycle r . The effective nonlinear susceptibility is $\chi^{(2)}$ in the range $(n-1)\Lambda \leq z < (n+r-1)\Lambda$ and $-\chi^{(2)}$ in the range $(n+r-1)\Lambda \leq z < n\Lambda$, with $n = 1, 2, \dots, N$. From the coupled-wave equation (B.19), the complex amplitude of the second

harmonic wave transmitted from the crystal can be calculated as

$$F'_3(L') = \frac{\omega_0 \chi^{(2)} F_0^2}{c n_3} \frac{(1 + e^{-i\Delta k \Lambda} - 2e^{-i\Delta k r \Lambda})(1 - e^{-iN\Delta k \Lambda})}{\Delta k (1 - e^{-i\Delta k \Lambda})}. \quad (\text{B.22})$$

The normalized efficiency of SHG is presented in Fig. B.3. We denote the intensity

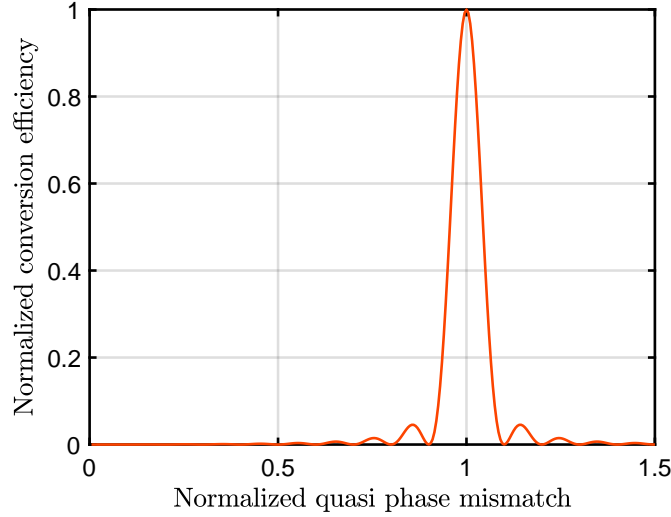


Fig. B.3: Relationship between quasi-phase mismatch and SHG efficiency with $r = 0.5$ and $N = 10$.

of the second harmonic wave with quasi-phase matching as I'_3 . A comparison of the intensity with the quasi-phase matching condition $\Delta k \Lambda = 2m\pi$ and standard phase-matching condition is as follows:

$$\frac{I'_3}{I_3} = \frac{4N^2 \sin^2(mr\pi)}{m^2\pi^2}, \quad (\text{B.23})$$

which is maximized when the duty cycle is set to $r = (2j+1)/(2m)$ ($j = 1, 2, \dots$).

B.3.3 SHG with high conversion efficiency

If the conversion efficiency is high, the coupled-wave equations can be solved using the energy conservation law, which is denoted as follows:

$$n_0 |F_0(z)|^2 + n_3 |F_3(z)|^2 = n_0 |F_0(0)|^2. \quad (\text{B.24})$$

Let us consider the case when the phase-matching condition is satisfied. Based on the differential of the second equation of Eqs. (B.19) with z , we obtain

$$\frac{d^2 F_3}{dz^2} + \frac{\omega_0^2 (\chi^{(2)})^2}{c^2 n_0^2 n_3} (n_0 |F_0(0)|^2 - n_3 |F_3|^2) F_3 = 0. \quad (\text{B.25})$$

By assuming F_3 as a real number and non-dimensionalizing it with

$$\eta^2 = \frac{\omega_0^2 (\chi^{(2)})^2 |F_0(0)|^2}{2c^2 n_0 n_3}, \quad (\text{B.26})$$

$$x = \eta z, \quad (\text{B.27})$$

$$y = \sqrt{\frac{n_3}{n_0}} \frac{F_3}{|F_0(0)|}, \quad (\text{B.28})$$

we obtain

$$\frac{d^2 y}{dx^2} + 2(1 - y^2)y = 0. \quad (\text{B.29})$$

The solution of this differential equation is $y = \tanh x$. Therefore, the intensity of the second harmonic wave transmitted from the crystal can be written as

$$I_3(L') = I_0(0) \tanh^2(\eta L'). \quad (\text{B.30})$$

B.3.4 Cascaded nonlinear optical effect

Let us investigate the behavior of the fundamental wave in the phase-mismatched condition. Based on the differential of the first equation of Eqs. (B.19) with z , we obtain

$$\frac{d^2 F_0}{dz^2} - i\Delta k \frac{dF_0}{dz} + \frac{\omega_0^2 (\chi^{(2)})^2}{2c^2 n_0 n_3} \left(|F_0|^2 - \frac{n_3}{2n_0} |F_3|^2 \right) F_0 = 0. \quad (\text{B.31})$$

When the phase mismatch is sufficiently large, we can assume that the intensity of the fundamental wave does not change and that of the second harmonic wave is zero. By approximating Eq. (B.31), we obtain

$$\frac{d^2 F_0}{dz^2} - i\Delta k \frac{dF_0}{dz} + \eta^2 F_0 = 0, \quad (\text{B.32})$$

where η is the parameter defined in Eq. (B.26). Under the condition $\Delta k \gg \eta$, the complex amplitude of the fundamental wave transmitted from the crystal can be written as

$$F_0(L') = F_0(0) \exp(i\Phi), \quad (\text{B.33})$$

with

$$\Phi = -\frac{\omega_0^2 (\chi^{(2)})^2 \mu_0 L'}{\Delta k c n_0^2 n_3} I_0(0). \quad (\text{B.34})$$

While the intensity of the fundamental wave does not change, the phase changes in proportion to the intensity. In this case, a phenomenon equivalent to the optical Kerr effect occurs, and the nonlinear refractive index n_{NL} can be written as

$$n_{\text{NL}} = \frac{c\Phi}{\omega_0 L' I_0(0)} = -\frac{\omega_0 (\chi^{(2)})^2 \mu_0}{\Delta k n_0^2 n_3}. \quad (\text{B.35})$$

This phenomenon can be explained as follows. Even in the phase-mismatched condition, a slight second harmonic wave is generated while the fundamental wave propagates a distance of approximately the coherence length l_c . However, when the fundamental wave propagates a distance exceeding l_c , the phase of the generated second harmonic wave becomes inverted. The canceled second harmonic wave is reconverted to the fundamental wave. It should be noted that the fundamental and second harmonic waves propagate at different speeds through the crystal in the phase-mismatched condition. That is, the phase of the reconverted fundamental wave is different from the original. Because the overall phase of the fundamental wave depends on the amplitude of the intermediate-generated second harmonic wave, the phase changes in proportion to the intensity of the incident fundamental wave. This phenomenon is called cascaded nonlinear optical effects [174, 175] because it occurs in a chain of second-order nonlinear optical effects. We can achieve a sufficiently large nonlinear refractive index using this phenomenon even with a continuous wave laser. It is also worth noting that the magnitude and sign of the nonlinear refractive index can be adjusted by varying the phase mismatch.

B.4 Optical parametric process

In the optical parametric process, the lights with angular frequency ω_1 and ω_2 are generated from the light with angular frequency ω_3 , which satisfies $\omega_1 + \omega_2 = \omega_3$. Optical parametric amplification (OPA) is a phenomenon in which a seed light of angular frequency ω_1 incident on a nonlinear optical crystal is amplified. An optical parametric oscillator (OPO) is a system that generates signal light with an angular frequency of ω_1 and idler light with an angular frequency of ω_2 by oscillating a cavity that contains a nonlinear optical crystal. The light with angular frequency ω_3 used in these applications is called pump light.

B.4.1 Optical parametric amplification

The coupled-wave equations for the optical parametric process can be written as

$$\begin{cases} \frac{dF_1}{dz} = \frac{i\omega_1\chi^{(2)}}{2cn_1} F_2^* F_3 e^{i\Delta kz}, \\ \frac{dF_2}{dz} = \frac{i\omega_2\chi^{(2)}}{2cn_2} F_1^* F_3 e^{i\Delta kz}, \\ \frac{dF_3}{dz} = \frac{i\omega_3\chi^{(2)}}{2cn_3} F_1 F_2 e^{-i\Delta kz}, \end{cases} \quad (\text{B.36})$$

where $\Delta k = k_3 - k_1 - k_2$. Let us assume that the conversion efficiency is sufficiently low such that the attenuation of the pump light is negligible^{*1}. The follow-

^{*1} The coupled wave equations for pump and seed light of comparable intensity are not easily solved. The general solution of the coupled-wave equations is denoted with Jacobi's elliptic function [146, 187].

ing differential equation for the seed light is derived:

$$\frac{d^2 F_1}{dz^2} - i\Delta k \frac{dF_1}{dz} - g_0^2 F_1 = 0, \quad (\text{B.37})$$

$$g_0^2 = \frac{\omega_1 \omega_2 (\chi^{(2)})^2}{4c^2 n_1 n_2} |F_3|^2. \quad (\text{B.38})$$

The seed light exponentially increases when $|\Delta k| < 2g_0$. When the phase-matching condition $\Delta k = 0$ is satisfied, the light transmitted from the crystal can be written as

$$F_1(L') = F_1(0) \cosh u + ie^{i\phi_3} \left(\frac{n_2 \omega_1}{n_1 \omega_2} \right)^{1/2} F_2^*(0) \sinh u, \quad (\text{B.39})$$

$$F_2^*(L') = -ie^{-i\phi_3} \left(\frac{n_1 \omega_2}{n_2 \omega_1} \right)^{1/2} F_1(0) \sinh u + F_2^*(0) \cosh u, \quad (\text{B.40})$$

where ϕ_3 is the initial phase of the pump light. We defined $u = g_0 L'$. The case where the angular frequencies of signal and idler light are equal ($\omega_1 = \omega_2 = \omega_0$) corresponds to a degenerate OPA. The amplification factor of the degenerate OPA can be written as

$$\frac{I_0(L')}{I_0(0)} = \cosh 2u + \sinh 2u \cos 2\theta, \quad (\text{B.41})$$

with $2\theta = \phi_3 - 2\phi_1 + \pi/2$.

OPA can also be used as a squeezer for the vacuum field. Then $s = \exp(u)$ and θ correspond to the squeezing factor and squeezing angle, respectively.

B.4.2 Optical parametric oscillator

OPO can be achieved by using the intracavity OPA. When the rate of light generation by the OPA, which corresponds to the squeezing decay rate, exceeds the cavity decay rate, the cavity results in lasing. In this case, signal and idler light satisfying the phase-matching condition is transmitted from the cavity even without seed light.

Let us calculate the threshold of oscillation. Here, we assume an over-coupled optical cavity in which the input mirror has the same power reflectivity $R = e^{-\mu L'}$ for both signal and idler light. When the gain of the OPA reaches the oscillation threshold, the light field that circles the cavity is consistent with the initial light field:

$$F_1(0) = \left[F_1(0) \cosh u_t + ie^{i\phi_3} \left(\frac{n_2 \omega_1}{n_1 \omega_2} \right)^{1/2} F_2^*(0) \sinh u_t \right] e^{-\mu L'/2}, \quad (\text{B.42})$$

$$F_2^*(0) = \left[-ie^{-i\phi_3} \left(\frac{n_1 \omega_2}{n_2 \omega_1} \right)^{1/2} F_1(0) \sinh u_t + F_2^*(0) \cosh u_t \right] e^{-\mu L'/2}, \quad (\text{B.43})$$

where u_t denotes the value of u at the threshold. The determinant of the matrix formed by the coefficients of the homogeneous equations must be zero because the complex amplitude is finite. When the finesse of the cavity is sufficiently high, we can calculate $u_t = \mu/2$.

Now let us consider the conversion efficiency at a steady state. Here, we assume that the pump light does not resonate in the optical cavity. Hence, the OPA process does not follow Eqs. (B.39) and (B.40) because the attenuation of the pump light cannot be neglected. Nevertheless, the amplification of the light field is saturated because the intensity of signal and idler light transmitted from the cavity are sufficiently lower than the intracavity intensity. That is, the complex amplitudes F_1 and F_2 in the cavity can be assumed constant. From the coupled-wave equations (B.36), the change in the complex amplitude of the pump light can be calculated as

$$F_3(L') - F_3(0) = \frac{i\omega_3\chi^{(2)}}{2cn_3} F_1 F_2 L'. \quad (\text{B.44})$$

Because the number of photons of the signal and idler light transmitted from the cavity is equal to the change in those of the pump light, we also obtain

$$\frac{I_3(L') - I_3(0)}{\hbar\omega_3} = \mu L' \frac{I_1}{\hbar\omega_1} = \mu L' \frac{I_2}{\hbar\omega_2}, \quad (\text{B.45})$$

where I_1 and I_2 are the intracavity intensities of the signal and idler light, respectively. From these equations and the requirement for the threshold, we obtain the following equation:

$$\sqrt{I_3(0)} - \sqrt{I_3(L')} = \frac{I_3(0) - I_3(L')}{2\sqrt{I_{3t}}}, \quad (\text{B.46})$$

where I_{3t} denotes the intensity of the pump light at the threshold. Therefore, we can calculate the conversion efficiency:

$$\frac{I_3(0) - I_3(L')}{I_3(0)} = 4 \frac{\sqrt{\rho} - 1}{\rho}, \quad (\text{B.47})$$

with

$$\rho = \frac{I_3(0)}{I_{3t}}. \quad (\text{B.48})$$

The conversion efficiency is shown in Fig. B.4, which takes 1 when $\rho = 4$.

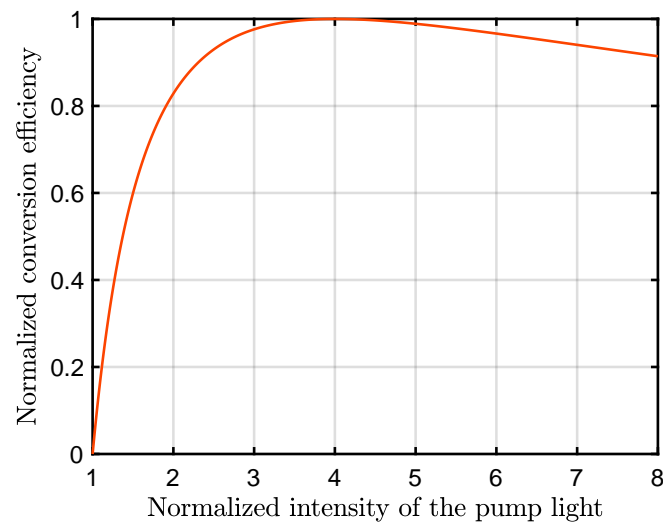


Fig. B.4: Relationship between the intensity of the pump light and conversion efficiency of OPO.

Appendix C

Quantum noise in advanced interferometers

This appendix discusses the methods of improving the sensitivity of gravitational wave detectors that were not covered in the main article. Resonant sideband extraction (RSE) improves the detector bandwidth and is the interferometer configuration used in all second-generation gravitational wave detectors. The filter cavity, used with the input squeezing, improves sensitivity in all frequency bands and is beginning to be implemented in actual gravitational wave detectors.

C.1 Resonant sideband extraction and its applications

This section discusses the RSE interferometer and its applications. First, we briefly describe the properties of the Fabry-Perot Michelson interferometer (FPMI), which is an interferometer configured by assembling a Fabry-Perot cavity into the arms of a Michelson interferometer. The RSE interferometer is an interferometric configuration that combines FPMI with a signal recycling cavity. We obtain the conditions for the bandwidth expansion of the cavity. Next, we derive the signal resonance phenomena in the RSE interferometer with a long signal recycling cavity length. We finally discuss the quantum expander idea, a method to achieve further bandwidth expansion and long SRC effect by intracavity squeezing. The plots in this section assume that the arm length is $L = 3$ km and the mass of the mirror is $m = 23$ kg.

C.1.1 Fabry-Perot Michelson interferometer

Let us consider an FPMI with perfect over-coupling cavities of length L on both arms with an input test mass (ITM) of power transmissivity $T_1 = t_1^2$, as shown in Fig. C.1. Assume that the Michelson interferometer, comprising the beam splitter (BS) and ITM, operates at the dark fringe and performs measure-

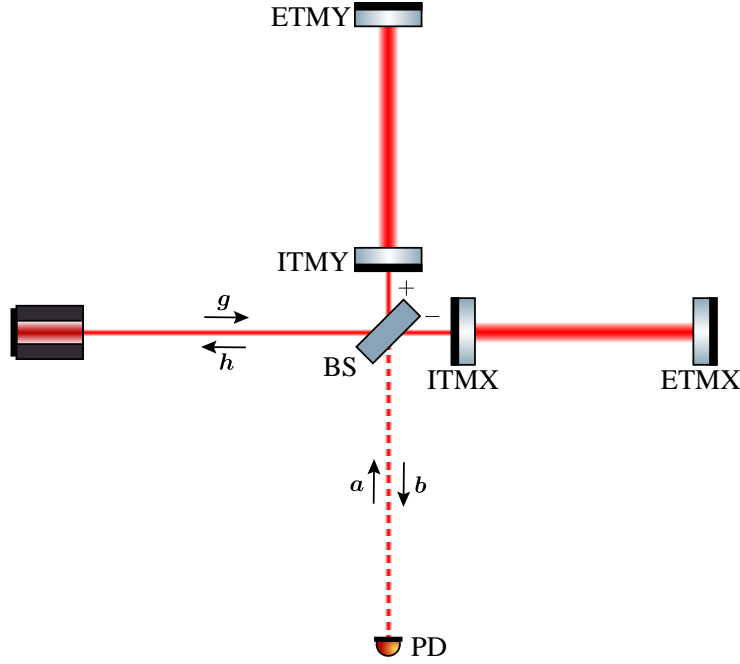


Fig. C.1: Schematic of the Fabry-Perot Michelson interferometer. The mirrors that constitute the Fabry-Perot cavity are supposed to work as a test mass.

ments at appropriate positions. The Fabry-Perot cavities in both arms are in a resonance condition, and the effective phase delay in the arms is equal in both arms as $\beta = \arctan(-\Omega/\gamma)$, where $\gamma = T_c/(4L)$ is the cavity decay rate of the arm cavities. Note that the parameters are multiplied by a factor compared to the Fabry-Perot cavity considered in Sec. 3.3.2 because we consider the case where the ITM is a free mass with an equal mass to the end test mass (ETM). Considering the equations of motion for the relative motion of ITM and ETM, we can calculate parameters in terms of the reduced mass of the test masses, and the effective mass is multiplied by 1/2. In addition, the effective coupling constant is multiplied by 2 because ponderomotive squeezing also occurs at ITM. From Eq. (3.90), the input-output relation can be calculated as

$$\mathbf{b} = e^{2i\beta} \begin{pmatrix} 1 & 0 \\ -\mathcal{K} & 1 \end{pmatrix} \mathbf{a} + e^{i\beta} \frac{\sqrt{2\mathcal{K}}}{h_{\text{SQL}}} \begin{pmatrix} 1 \\ 0 \end{pmatrix} h(\Omega), \quad (\text{C.1})$$

where $\mathcal{K} = 2\gamma\iota/(\Omega^2(\gamma^2 + \Omega^2))$ is the optomechanical coupling constant, $h_{\text{SQL}} = \sqrt{8\hbar/(mL^2\Omega^2)}$ is the standard quantum limit, and we defined $\iota = 16\mathcal{F}_{\text{arm}}P_G\omega_0/(\pi m L c)$ and $\mathcal{F}_{\text{arm}} = 2\pi/T_1$. The sensitivity of FPMI can be written as

$$S_h(\Omega) = \frac{h_{\text{SQL}}^2}{2} \left(\mathcal{K} + \frac{1}{\mathcal{K}} \right). \quad (\text{C.2})$$

This sensitivity is consistent with that for the dual-recycling Michelson interferometer (DRMI), except for the factor where the finesse of the signal recycling cavity (SRC) and power recycling cavity (PRC) is \mathcal{F}_{arm} .

C.1.2 Resonant sideband extraction interferometer

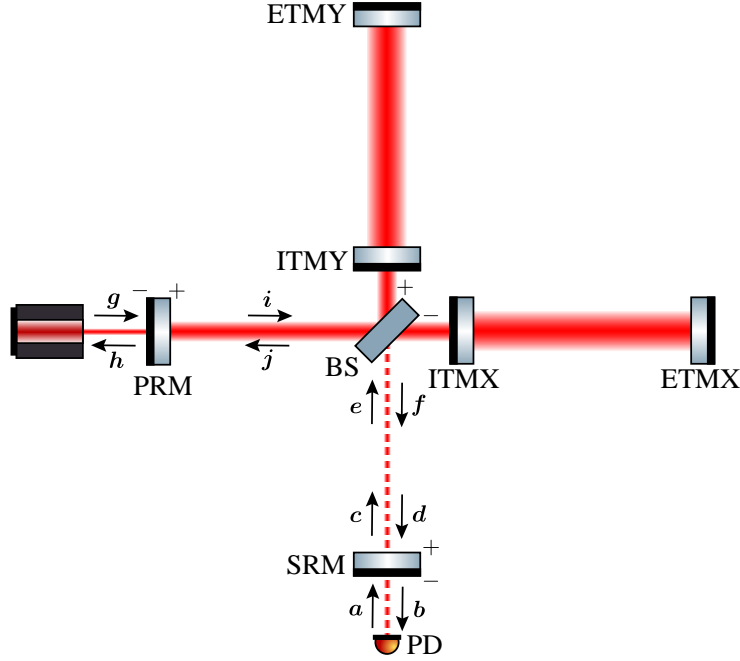


Fig. C.2: Schematic of dual-recycling Fabry-Perot Michelson interferometer. The mirrors that constitute the Fabry-Perot cavity are supposed to work as a test mass.

Let us consider a Fabry-Perot Michelson interferometer with two recycling cavities, as shown in Fig. C.2. This configuration is the dual-recycling Fabry-Perot Michelson interferometer (DRFPMI). However, as described below, this optical configuration is usually called the RSE interferometer because signal recycling is not performed for a km-scale FPMI.

Let L be the arm length, r_I^2 and $t_I^2 = T_I$ be the power reflectivity and transmissivity of ITM, and r_S^2 and $t_S^2 = T_S$ be the power reflectivity and transmissivity of the signal recycling mirror (SRM). From Eq. (C.1), we obtain

$$\mathbf{f} = e^{2i\beta} \begin{pmatrix} 1 & 0 \\ -\mathcal{K} & 1 \end{pmatrix} \mathbf{e} + e^{i\beta} \frac{\sqrt{2\mathcal{K}}}{h_{\text{SQL}}} \begin{pmatrix} 0 \\ 1 \end{pmatrix} h(\Omega), \quad (\text{C.3})$$

where we defined $\gamma = T_I c / (4L)$, $\beta = \arctan(-\Omega/\gamma)$, $\mathcal{K} = 2\gamma\iota / (\Omega^2(\gamma^2 + \Omega^2))$, $h_{\text{SQL}} = \sqrt{8\hbar/(mL^2\Omega^2)}$, and $\iota = 16\mathcal{F}_{\text{arm}}P_I\omega_0/(\pi mLc) = 32\mathcal{F}_{\text{arm}}\mathcal{F}_P P_G\omega_0/(\pi^2 mLc)$. $\mathcal{F}_{\text{arm}} = 2\pi/T_I$ is the finesse of the arm cavities, $\mathcal{F}_P = 2\pi/T_P$ is the finesse of the PRC, and T_P is the power transmissivity of the power recycling mirror (PRM).

First, let us consider the case where the SRC is resonant and in the broadband signal recycling (BSR) condition. Here, we assume that the distance between BS and SRM is sufficiently shorter than the arm length, and the finesse of SRC is sufficiently lower than that of the arm cavity. The phase delay between BS and SRM can, therefore, be neglected. The input-output relation is the same as for the Fabry-Perot cavity with the phase delay per half cycle being β and the coupling constant being \mathcal{K} , which can be calculated as

$$\mathbf{b} = \frac{e^{2i\beta}}{(1 - r_S e^{2i\beta})^2} \left[\begin{pmatrix} 1 + r_S^2 - 2r_S \cos 2\beta & 0 \\ -t_S^2 \mathcal{K} & 1 + r_S^2 - 2r_S \cos 2\beta \end{pmatrix} \mathbf{a} + t_S e^{-i\beta} \frac{\sqrt{2\mathcal{K}}}{h_{\text{SQL}}} \begin{pmatrix} 0 \\ 1 - r_S e^{2i\beta} \end{pmatrix} h(\Omega) \right]. \quad (\text{C.4})$$

The operator for signal-to-noise ratio $h_n(\Omega)$ can be written as

$$h_n(\Omega) = \frac{h_{\text{SQL}}}{\sqrt{2\mathcal{K}}} \frac{e^{i\beta}}{t_S(1 - r_S e^{2i\beta})} (-t_S^2 \mathcal{K} a_1 + [1 + r_S^2 - 2r_S \cos 2\beta] a_2). \quad (\text{C.5})$$

Thus, we obtain the sensitivity of DRFPMI:

$$S_h(\Omega) = \frac{h_{\text{SQL}}^2}{2} \left(\mathcal{K}_{\text{BSR}} + \frac{1}{\mathcal{K}_{\text{BSR}}} \right), \quad (\text{C.6})$$

where we defined

$$\mathcal{K}_{\text{BSR}} = \frac{t_S^2}{1 + r_S^2 - 2r_S \cos 2\beta} \mathcal{K} \simeq \frac{2\gamma_{\text{BSR}}\iota}{\Omega^2(\gamma_{\text{BSR}}^2 + \Omega^2)}, \quad (\text{C.7})$$

and $\gamma_{\text{BSR}} = \gamma \times \pi / (2\mathcal{F}_S)$ is the effective cavity decay rate, and $\mathcal{F}_S = 2\pi/T_S$ is the finesse of SRC. BSR for FPMI reduces the effective cavity decay rate by roughly the inverse of the finesse of SRC.

Fig. C.3 shows the sensitivity curve. Power recycling has the same effect as increasing the input laser light power so that the sensitive band can be moved to higher frequencies. In contrast, BSR reduces the effective cavity decay rate without changing the intra-arm power, thus narrowing the interferometer's bandwidth and deteriorating the high-frequency band's sensitivity. In addition, the response to the signal is further enhanced, increasing radiation pressure noise. Therefore, BSR is not used for FPMI with km-scale arms.

The effective laser light power can be increased by increasing the power recycling gain $2\mathcal{F}_p/\pi$. Nevertheless, as the laser light power in the BS becomes robust, it causes technical problems such as thermal lensing effects. The finesse of the arm cavity needs to be increased to increase the intra-arm power further. However, the cavity decay rate decreases, resulting in a narrower detector bandwidth. To solve the trade-off problem, actual gravitational wave detectors adopt a method called resonant sideband extraction (RSE) [102], in which the SRC is operated around the anti-resonance condition.

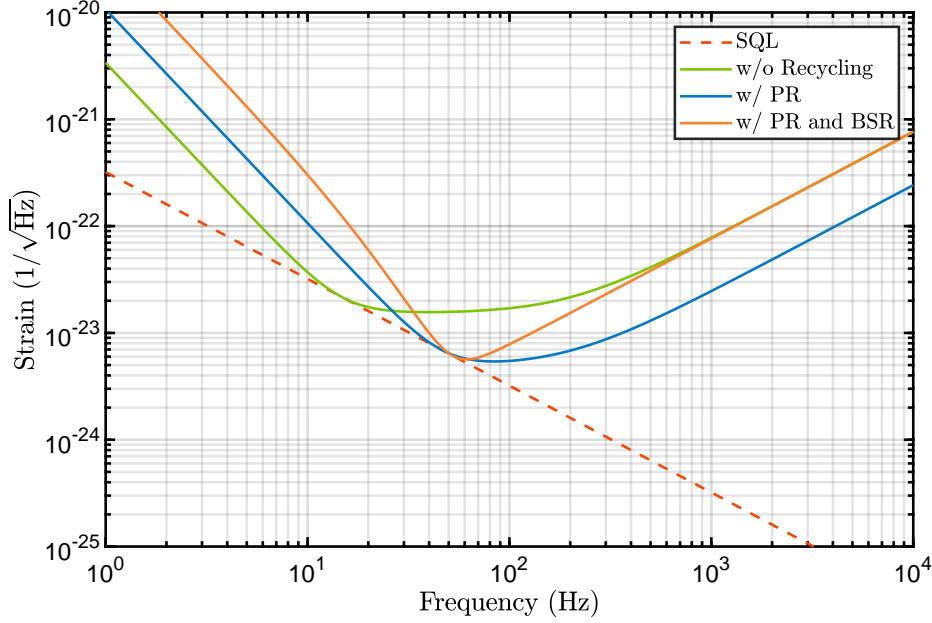


Fig. C.3: Sensitivity of DRFPMI. The parameters are set to $P_G = 1 \times 10^2$ W and $T_I = 0.05$. The green line corresponds to the case without recycling ($2\mathcal{F}_P/\pi \rightarrow 1$, $2\mathcal{F}_S/\pi \rightarrow 1$), the blue line corresponds to the case with only PR ($2\mathcal{F}_P/\pi = 10$, $2\mathcal{F}_S/\pi \rightarrow 1$), the orange line corresponds to the case with PR and BSR ($2\mathcal{F}_P/\pi = 10$, $2\mathcal{F}_S/\pi = 10$).

Let us consider the case where the SRC is in the anti-resonance condition, and the phase change in the SRC can be written as $\phi \equiv l\omega_0/c \pmod{2\pi} = \pi/2$, where l is the distance between the BS and SRM. Such a condition is called broadband RSE (BRSE)^{*1}. The interferometer is given an effect that multiplies the amplitude reflectivity of the SRM by -1 in the BSR calculation. That is, the sensitivity of the BRSE condition can be written as

$$S'_h(\Omega) = \frac{h_{\text{SQL}}^2}{2} \left(\mathcal{K}_{\text{BRSE}} + \frac{1}{\mathcal{K}_{\text{BRSE}}} \right), \quad (\text{C.8})$$

where the coupling constant is

$$\mathcal{K}_{\text{BRSE}} = \frac{t_S^2}{1 + r_S^2 + 2r_S \cos 2\beta} \mathcal{K} \simeq \frac{2\gamma_{\text{BRSE}} l}{\Omega^2 (\gamma_{\text{BRSE}}^2 + \Omega^2)}, \quad (\text{C.9})$$

and $\gamma_{\text{BRSE}} = \gamma \times 2\mathcal{F}_S/\pi$ is the effective cavity decay rate. BRSE for FPMI increases the effective cavity decay rate by roughly the finesse of SRC.

^{*1} The SRC in the BRSE condition is actually in a resonance condition because the cavity inverts the phase of the light field. In such a depiction, the PRC in the DRFPMI is in an anti-resonance condition.

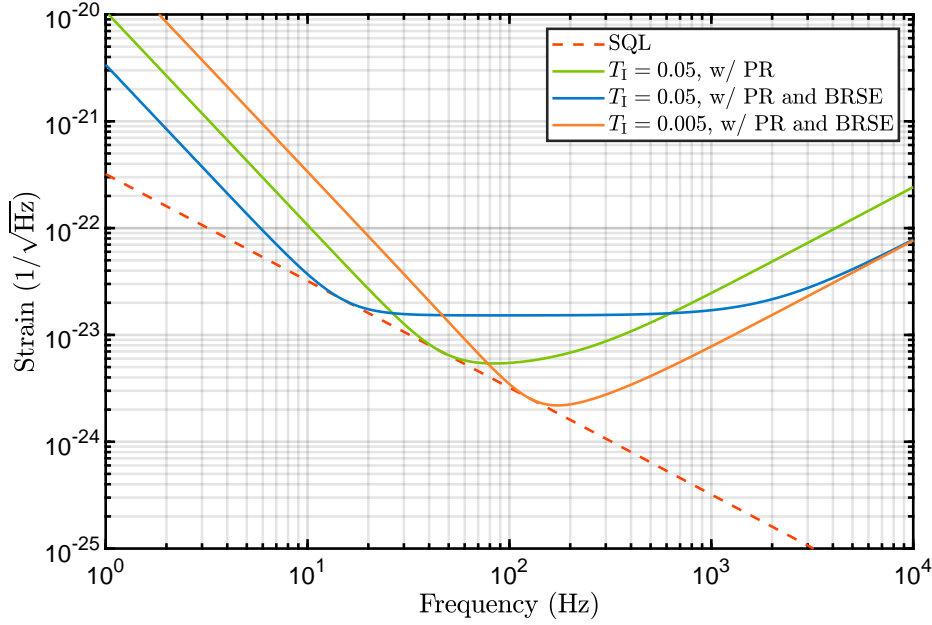


Fig. C.4: Sensitivity of DRFPMI. The parameters are set to $P_G = 1 \times 10^2$ W and $2\mathcal{F}_P/\pi = 10$. The green line corresponds to the case of a low-finesse arm cavity without BRSE ($T_I = 0.05$, $2\mathcal{F}_S/\pi \rightarrow 1$), the blue line corresponds to the case of a low-finesse arm cavity with BRSE ($T_I = 0.05$, $2\mathcal{F}_S/\pi = 10$), and the orange line corresponds to the case of a high-finesse arm cavity with BRSE ($T_I = 0.005$, $2\mathcal{F}_S/\pi = 10$).

Fig. C.4 shows the sensitivity curve. BRSE increases the cavity decay rate and detector's bandwidth, but it also increases the shot noise. Combining a high finesse arm cavity with BRSE, as shown by the orange line, the sensitivity is equivalent to a low finesse and increased PR gain without RSE ($T_I = 0.05$, $2\mathcal{F}_S/\pi \rightarrow 1$, $2\mathcal{F}_P/\pi = 100$). BRSE allows interferometers with high intra-arm power and wide bandwidth without changing the laser light power at the BS.

Fig. C.5 shows the comparison of the shot noise of DRFPMI. When T_I and $2\mathcal{F}_P/\pi$ have the same value, meaning that the intra-arm power is equal, the product of shot noise and bandwidth is constant:

$$\lim_{\Omega \rightarrow 0} \frac{2\mathcal{K}}{h_{\text{SQL}}^2} \times \gamma = \lim_{\Omega \rightarrow 0} \frac{2\mathcal{K}_{\text{BSR}}}{h_{\text{SQL}}^2} \times \gamma_{\text{BSR}} = \lim_{\Omega \rightarrow 0} \frac{2\mathcal{K}_{\text{BRSE}}}{h_{\text{SQL}}^2} \times \gamma_{\text{BRSE}} = \frac{mL^2\iota}{2\hbar}. \quad (\text{C.10})$$

Generally, this trade-off relationship is called the Mizuno limit [99].

C.1.3 Long signal recycling cavity

In the last section, the phase delay between the BS and SRM was assumed to be negligible. When this phase delay becomes comparable to that of the arms,

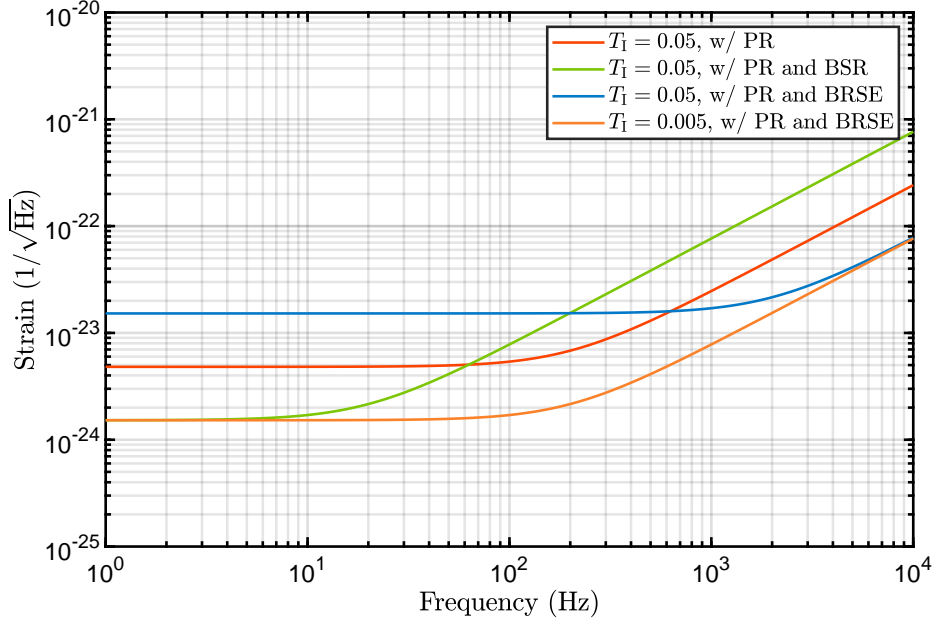


Fig. C.5: Sensitivity of DRFPMI determined by shot noise. The parameters are set as in Figs. C.3 and C.4.

the effect resulting from the finite SRC length becomes negligible, and the sensitivity curve is modified. Let $\alpha_S = -l\Omega/c$ be the phase delay between BS and SRM, where l is the distance between BS and SRM. The BRSE coupling constant, denoted by Eq. (C.9), is modified as

$$\mathcal{K}'_{\text{BRSE}} = \frac{t_S^2}{1 + r_S^2 + 2r_S \cos(2\beta + 2\alpha_S)} \mathcal{K}. \quad (\text{C.11})$$

By approximating that α_S are much smaller than unity, we obtain

$$\mathcal{K}'_{\text{BRSE}} \simeq \frac{2\gamma_{\text{BRSE}}\ell}{\Omega^2[\gamma_{\text{BRSE}}^2 + (1 - 2\gamma_{\text{BRSE}}/\gamma_S + (\Omega/\gamma_S)^2)\Omega^2]}, \quad (\text{C.12})$$

where we defined $\gamma_S = T_S c/(4l)$.

Even without detuning the SRC, a dip appears in the sensitivity curve. Fig. C.6 shows the sensitivity curve. This dip is derived from the phase quadrature of the vacuum field, implying that the signal satisfies the resonance condition at this frequency, similar to the optical resonance of the detuned signal recycling (DSR). The SRC, which was in an anti-resonance condition, switches to a quasi-resonance condition near this frequency owing to the phase delay between the BS and SRM. The sensitivity determined by the shot noise, $h_{\text{SQL}}^2/2 \times 1/\mathcal{K}'_{\text{BRSE}}$, minimizes at $\Omega_{\text{LSRC}} = \gamma_S \sqrt{\rho - 1/2}$, indicating that this is the angular frequency of the dip. Here, we defined $\rho = \gamma_{\text{BRSE}}/\gamma_S$. At this frequency, the term derived from the

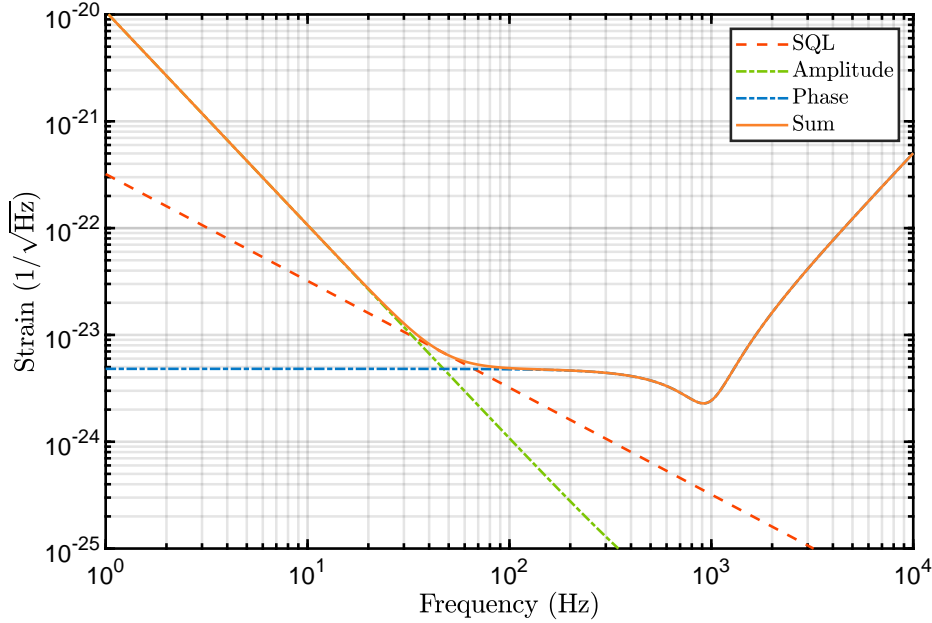


Fig. C.6: Sensitivity of the RSE interferometer with a long SRC. The parameters are set to $P_G = 1 \times 10^2$ W, $2\mathcal{F}_P/\pi = 10$, $2\mathcal{F}_S/\pi = 100$, $l = 1000$ m, and $T_I = 0.005$.

amplitude quadrature temporarily deteriorates; hence, the depth of the dip does not beat the SQL. If the sensitivity at the dip is sufficiently larger than SQL, the relative depth of the dip can be written as

$$\frac{1/\Omega^2 \mathcal{K}'_{\text{BRSE}}|_{\Omega=\Omega_{\text{LSRC}}}}{1/\Omega^2 \mathcal{K}'_{\text{BRSE}}|_{\Omega \rightarrow 0}} = \frac{4\rho - 1}{4\rho^2}. \quad (\text{C.13})$$

In the frequency band higher than the dip, the sensitivity worsens in proportion to the frequency square because the two composite cavities attenuate the signal.

The long SRC effect is valuable as a method of improving sensitivity in the high-frequency band because it can produce a dip in the bandwidth of a few kHz, similar to the system considered in Sec. 3.5.2. The SRC length of the second-generation gravitational wave detectors is not quite long that it is challenging to produce a dip. The proposed design of NEMO incorporates the long SRC effect in the optical configuration [19].

C.1.4 Quantum expander

The long SRC effect is a promising method for improving sensitivity in a high-frequency band. However, it is not easy to achieve as an upgrade idea for current gravitational wave detectors because it requires both a relatively high-finesse SRC and a long SRC length. Hence, let us consider applying intracavity squeezing to the RSE interferometer to increase the SRC's effective finesse. Intracavity squeez-

ing can significantly reduce the requirements for producing a dip resulting from the long SRC effect while increasing the effective bandwidth of the interferometer. This interferometer configuration is called a quantum expander [188].

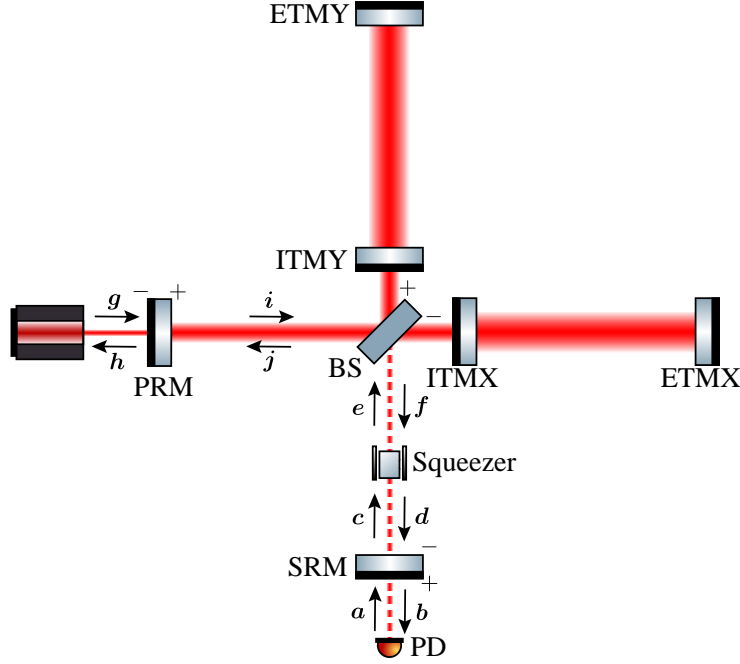


Fig. C.7: Schematic of intracavity squeezing for the RSE interferometer.

We consider intracavity squeezing in the SRC of the RSE interferometer, as shown in Fig. C.7. The SRC is in resonance condition, and the squeezing angle is set to 0. The sign of the amplitude reflectivity of the SRM is inverted for the calculation because the BRSE condition is considered. The input-output relation can be written as

$$\begin{aligned} \mathbf{b} &= r_S \mathbf{a} + t_S \mathbf{d}, \quad \mathbf{c} = t_S \mathbf{a} - r_S \mathbf{d}, \quad \mathbf{d} = e^{i\alpha_S} S(u, 0) \mathbf{f}, \\ \mathbf{e} &= e^{i\alpha_S} \mathbf{c}, \quad \mathbf{f} = e^{2i\beta} P(\mathcal{K}, 0) \mathbf{e} + e^{i\beta} \frac{\sqrt{2\mathcal{K}}}{h_{\text{SQL}}} \begin{pmatrix} 0 \\ 1 \end{pmatrix} h(\Omega). \end{aligned} \quad (\text{C.14})$$

Thus, the measured light field fluctuation \mathbf{b} can be calculated as

$$\begin{aligned} \mathbf{b} &= \left(r_S + t_S^2 e^{2i(\beta+\alpha_S)} S(u, 0) P(\mathcal{K}, 0) \left[I + r_S e^{2i(\beta+\alpha_S)} S(u, 0) P(\mathcal{K}, 0) \right]^{-1} \right) \mathbf{a} \\ &\quad + t_S e^{i(\beta+\alpha_S)} \frac{\sqrt{2\mathcal{K}}}{h_{\text{SQL}}} \left[I + r_S e^{2i(\beta+\alpha_S)} S(u, 0) P(\mathcal{K}, 0) \right]^{-1} S(u, 0) \begin{pmatrix} 0 \\ 1 \end{pmatrix} h(\Omega) \\ &= \frac{1}{C} [\mathbb{A} \mathbf{a} + \mathcal{H} h(\Omega)], \end{aligned} \quad (\text{C.15})$$

with

$$C = - \left(r_S e^{2i(\beta+\alpha_S)} + \frac{1}{r_S} e^{-2i(\beta+\alpha_S)} + 2 \cosh u \right), \quad (C.16)$$

$$A_{11} = (r_S + \frac{1}{r_S}) \cosh u + 2 \cos(2\beta + 2\alpha_S) - (\frac{1}{r_S} - r_S) \sinh u, \quad (C.17)$$

$$A_{12} = 0, \quad (C.18)$$

$$A_{21} = -\frac{1}{r_S} e^{-u} t_S^2 \mathcal{K}, \quad (C.19)$$

$$A_{22} = (r_S + \frac{1}{r_S}) \cosh u + 2 \cos(2\beta + 2\alpha_S) + (\frac{1}{r_S} - r_S) \sinh u, \quad (C.20)$$

$$\mathcal{H} = -t_S \frac{\sqrt{2\mathcal{K}}}{h_{\text{SQL}}} \left(e^{i(\beta+\alpha_S)} + \frac{0}{r_S} e^{-u} e^{-i(\beta+\alpha_S)} \right). \quad (C.21)$$

By approximating that t and u are much smaller than unity, the sensitivity can be denoted in a simple formula:

$$S_h(\Omega) = \frac{h_{\text{SQL}}^2}{2} \left(\mathcal{K}_{\text{QE}} + \frac{1}{\mathcal{K}_{\text{QE}}} \right), \quad (C.22)$$

where

$$\mathcal{K}_{\text{QE}} = \frac{T_S \mathcal{K}}{2 + \frac{1}{4} T_S^2 - T_S u + u^2 + 2 \cos(\beta + \alpha_S)}$$

is the effective coupling constant. As in the last section, by approximating that α_S are much smaller than unity, we obtain

$$\mathcal{K}_{\text{QE}} \simeq \frac{2\gamma_{\text{BRSE}} \ell}{\Omega^2 [\gamma_{\text{BRSE}}^2 + ((1 - \Sigma_S/\gamma_S)^2 - 2\gamma_{\text{BRSE}}/\gamma_S + (\Omega/\gamma_S)^2) \Omega^2]}, \quad (C.23)$$

where we defined $\Sigma_S = uc/(2l)$.

Fig. C.8 shows the sensitivity curve. The angular frequency of a dip is modified as $\Omega_{\text{LSRC-QE}} = \gamma_S \sqrt{\rho - (1 - \sigma_S)^2/2}$, where we defined $\sigma_S = \Sigma_S/\gamma_S$. The relative depth of the dip can be written as

$$\frac{1/\Omega^2 \mathcal{K}_{\text{QE}}|_{\Omega=\Omega_{\text{LSRC-QE}}}}{1/\Omega^2 \mathcal{K}_{\text{QE}}|_{\Omega \rightarrow 0}} = \frac{4\rho - (1 - \sigma_S^2)}{4\rho^2} (1 - \sigma_S)^2, \quad (C.24)$$

indicating that the requirement for the generation of the dip can be significantly relaxed by setting σ_S as close to 1. This technique hardly changes the radiation pressure noise and can improve the interferometer's sensitivity over a whole bandwidth. Realistic optical losses do not detract from this advantage [188]. Intracavity squeezing is a promising method for upgrading current gravitational wave detectors.

C.2 Frequency-dependent squeezing

Sec. 3.4.2 discussed a method to improve the sensitivity of gravitational wave detectors via input squeezing. The sensitivity depends on the squeezing angle, and

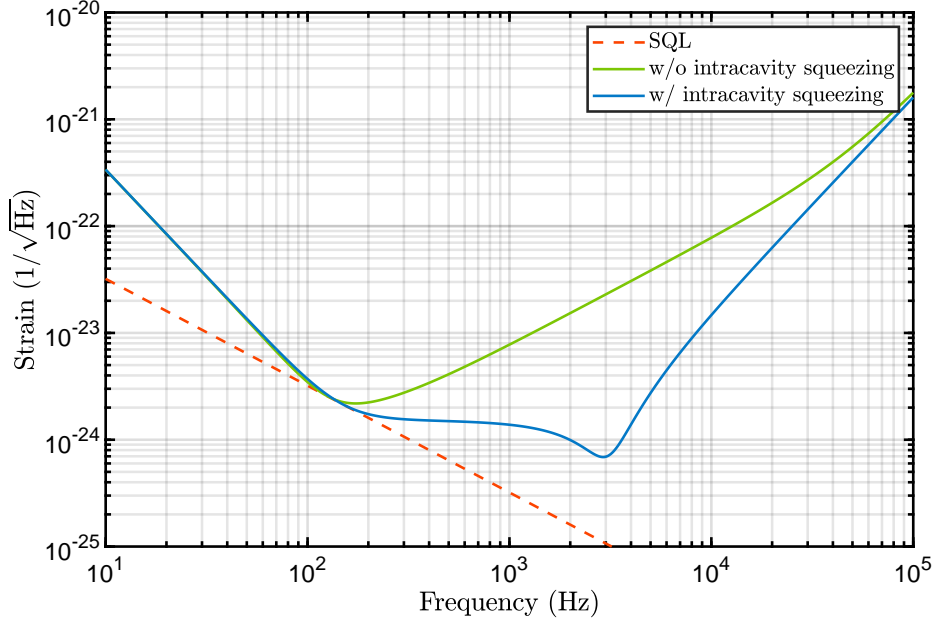


Fig. C.8: Sensitivity of the RSE interferometer with intracavity squeezing. The parameters are set to $P_G = 1 \times 10^2$ W, $2\mathcal{F}_P/\pi = 10$, $2\mathcal{F}_S/\pi = 10$, $l = 100$ m, and $T_l = 0.005$. The green and blue lines correspond to the case with $\sigma_S = 0$ and $\sigma_S = 0.97$, respectively. The plot range of the horizontal axis is changed to $10 \sim 10^5$ Hz.

achieving a frequency-dependent squeezing angle is necessary to improve sensitivity over the whole bandwidth. This section discusses methods for achieving frequency-dependent squeezing.

C.2.1 Input squeezing with a filter cavity

Frequency-dependent squeezing can be achieved using a detuned Fabry-Perot cavity called a filter cavity [95]. Let us consider frequency-dependent input squeezing for a dual-recycling Michelson interferometer, as shown in Fig. C.9. We consider the case where the optical loss is absent in the filter cavity for simplicity. This filter cavity is triangular over coupled ring cavity. Let r_F^2 and t_F^2 be the power reflectivity and transmissivity of the input mirror, respectively; $\phi_F \equiv L_F \omega_0 / c \pmod{2\pi}$ and $\alpha_F = -L_F \Omega / c$ be the phase change and delay per half cycle, respectively; and L_F be the cavity half cycle length. We now solve the same equation as in Eq. (3.83), assuming that no carrier light is present in the

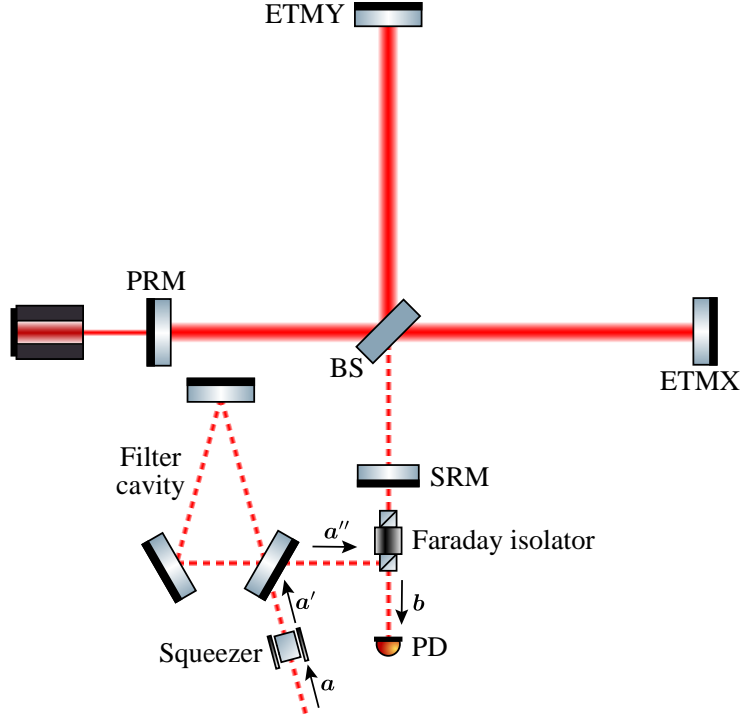


Fig. C.9: Schematic of frequency-dependent input squeezing with filter cavity.

filter cavity. The input-output relation can be calculated similarly to Eq. (4.20):

$$\begin{aligned} \mathbf{a}'' &= \left[-r_F I + t_F^2 e^{2i\alpha_F} [I - r_F e^{2i\alpha_F} R(2\phi_F)]^{-1} R(2\phi_F) \right] \mathbf{a}' \\ &\simeq \frac{1}{(\gamma_F - i\Omega)^2 + \Delta_F^2} \begin{pmatrix} \gamma_F^2 - \Delta_F^2 + \Omega^2 & -2\gamma_F \Delta_F \\ 2\gamma_F \Delta_F & \gamma_F^2 - \Delta_F^2 + \Omega^2 \end{pmatrix} \mathbf{a}', \quad (\text{C.25}) \end{aligned}$$

where $\gamma_F = T_F c / 4L_F$ and $\Delta_F = \phi_F c / L_F$ are the cavity decay rate and cavity detuning of the filter cavity, respectively.

Even with a fixed squeezing angle of OPA, an optimal sensitivity can be achieved if the filter cavity has an effect the same as a rotation matrix that gives a phase change of 0 in a high-frequency band ($\Omega > \gamma$), $\pi/2$ in a low-frequency band ($\Omega < \gamma$), and $\pi/4$ at $\Omega = \gamma$. By setting $\Delta_F = \gamma_F$, the transformation matrix of Eq. (C.25) corresponds to the rotation matrix \times (phase term) of angle 0 in the high-frequency band ($\Omega \gg \gamma_F$) and the rotation matrix of angle $\pi/2$ in the low-frequency band ($\Omega \ll \gamma_F$). In addition, by setting $\gamma_F = \gamma/\sqrt{2}$, it corresponds to the rotation matrix \times (phase term) of angle $\pi/4$ at $\Omega = \gamma$. The sensitivity, in this case, can be written as

$$S_h(\Omega) = \frac{h_{\text{SQL}}^2}{2\mathcal{K}} \frac{1}{\gamma^4 + \Omega^4} \left[s^2 (-\mathcal{K}\Omega^2 + \gamma^2)^2 + \frac{1}{s^2} (\mathcal{K}\gamma^2 + \Omega^2)^2 \right]. \quad (\text{C.26})$$

Fig. C.10 shows the sensitivity curve. The filter cavity achieves almost optimal sensitivity. Several experiments have demonstrated the rotation of the squeezing

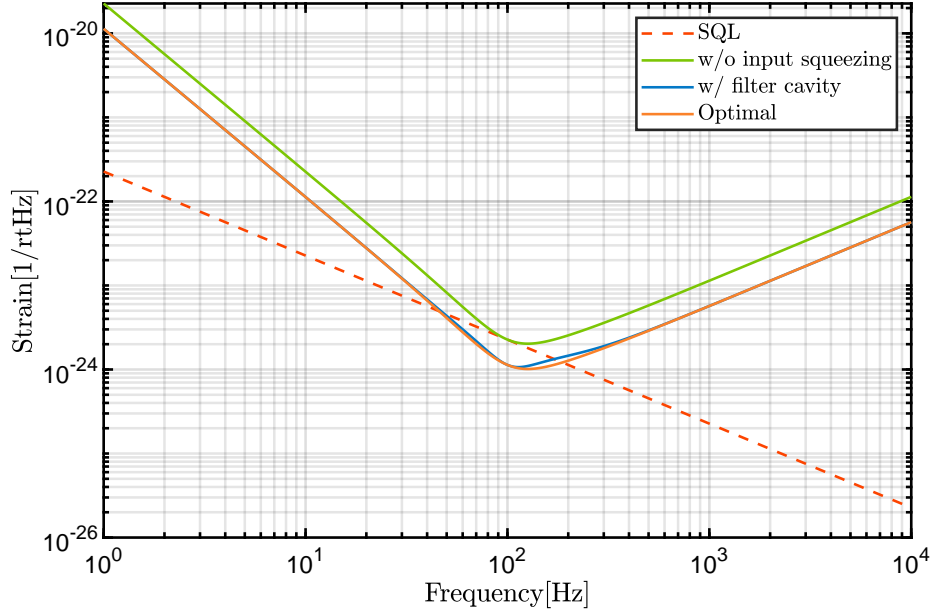


Fig. C.10: Sensitivity with frequency-dependent input squeezing by the filter cavity. The parameters are set to $\iota = 2\gamma^3$, $\gamma = 2\pi \times 100$ Hz, and $u = \log(2)$.

angle using a filter cavity [106–109], and it has been and will be implemented in actual gravitational wave detectors [110, 111]. Note that the transmissivity of the input mirror of the filter cavity must be extremely low to achieve a low cavity decay rate of $\sim 2\pi \times 100$ Hz with a short filter cavity that is not costly to construct. Optical loss is an essential factor in determining the performance of a filter cavity because a slight optical loss in such cavities can limit the effective squeezing factor. For example, calculations including optical losses are detailed in [189].

Appendix D

Sideband cooling with intracavity squeezing

One possible application of intracavity squeezing is ground-state cooling of optomechanical oscillators in an unresolved sideband regime [22–24]. Recently, it has been experimentally demonstrated that intracavity squeezing relaxes the conditions required for ground-state cooling [190]. This appendix briefly reviews the fundamental theory of sideband cooling and the impact of intracavity squeezing.

D.1 Thermal phonon number

Quantum mechanics is a well-established theory for describing the dynamics of microscopic objects. However, whether quantum mechanics can be applied to macroscopic objects remains uncertain. To investigate the quantum nature of macroscopic objects, we need to reach the quantum ground state of the macroscopic oscillator. The closeness to the quantum ground state of an oscillator with resonance frequency Ω_{eff} is evaluated by the phonon occupation number n :

$$n = \frac{m\Omega_{\text{eff}}}{\hbar} \langle x^2 \rangle - \frac{1}{2}, \quad (\text{D.1})$$

where m is the mass of the oscillator. The mean square displacement $\langle x^2 \rangle$ can be calculated from the two-sided power spectral density of displacement of the oscillator $S_x^{(2)}(\Omega)$:

$$\langle x^2 \rangle = \int_{-\infty}^{\infty} S_x^{(2)}(\Omega) \frac{d\Omega}{2\pi} = \int_{-\infty}^{\infty} \frac{S_f^{(2)}(\Omega)}{|m(\Omega_{\text{eff}}^2 + i\gamma_{\text{eff}}\Omega - \Omega^2)|^2} \frac{d\Omega}{2\pi}, \quad (\text{D.2})$$

where $S_f^{(2)}(\Omega)$ is the two-sided power spectral density of the force applied to the oscillator and $\Gamma_{\text{eff}} = m\gamma_{\text{eff}}$ is the effective damping constant of the oscillator. If the Q factor of the oscillator $Q = \Omega_{\text{eff}}/\gamma_{\text{eff}}$ is sufficiently large, the susceptibility of the oscillator is significant only near the resonant frequency. Hence, $\langle x^2 \rangle$ can

be calculated as

$$\begin{aligned}\langle x^2 \rangle &\simeq S_f^{(2)}(\Omega_{\text{eff}}) \int_{-\infty}^{\infty} \frac{1}{|m(\Omega_{\text{eff}}^2 + i\gamma_{\text{eff}}\Omega - \Omega^2)|^2} \frac{d\Omega}{2\pi} \\ &\simeq \frac{S_f^{(2)}(\Omega_{\text{eff}})}{2m^2\Omega_{\text{eff}}^2\gamma_{\text{eff}}}.\end{aligned}\quad (\text{D.3})$$

Let us calculate the thermal phonon number resulting from interacting with a heat bath with ambient temperature T . The effective resonant frequency and damping constant correspond to the mechanical resonant frequency Ω_m and damping constant $\Gamma_m = m\gamma_m$. From the fluctuation-dissipation theorem [83], the power spectral density of the force applied to the oscillator is

$$S_{f,\text{th}}^{(2)}(\Omega) = 2k_B T \gamma_m m, \quad (\text{D.4})$$

and the thermal phonon number n_{th} can be calculated as

$$n_{\text{th}} \simeq \frac{k_B T}{\hbar \Omega_m}. \quad (\text{D.5})$$

For example, $n_{\text{th}} \sim 10^6$ for $T = 300$ K and $\Omega_m = 10^6$ Hz, which is quite far from the ground state. Then, we consider binding the oscillator with an optical spring with resonant frequency Ω_{opt} and damping constant $\Gamma_{\text{opt}} = m\gamma_{\text{opt}}$. Optical damping does not cause thermal fluctuations to the oscillator because the stabilized laser is at thermal equilibrium with a very low-temperature bath. When the mechanical oscillator and optical damping are adequately stiff and large, respectively ($\Omega_m \gg \Omega_{\text{opt}}$, $\gamma_m \ll \gamma_{\text{opt}}$), the effective thermal phonon number can be calculated as

$$n'_{\text{th}} = \frac{k_B T \gamma_m}{\hbar \omega_m \gamma_{\text{opt}}}. \quad (\text{D.6})$$

Therefore, it is possible to significantly decrease the effective ambient temperature of the optomechanical oscillator by generating a low noise-damping source with light. This technique is called sideband cooling or radiation pressure cooling [155, 191, 192], and some experiments have reached the ground state [193–198], which refers to $n < 1$ in optomechanics. However, optical damping generates radiation pressure phonons because of quantum fluctuations in the radiation pressure force, which determine the cooling limit of sideband cooling. Here, we investigated a sideband cooling system with intracavity squeezing and the impact of intracavity squeezing on the radiation pressure phonon number.

D.2 Radiation pressure phonon number

Let us calculate the radiation pressure phonon number of the Fabry-Perot cavity with intracavity squeezing, as shown in Fig. D.1. The derivation using Hamiltonian notation is detailed in the supporting information in [24]. Here, we attempted

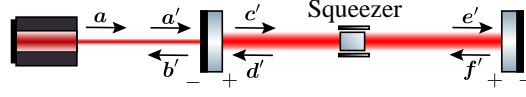


Fig. D.1: Schematic of sideband cooling with intracavity squeezing. This system is the same as Fig. 4.6. The initial phase of the incident carrier is $\varphi = -\arctan((\delta + \sigma \sin 2\theta)/(1 - \sigma \cos 2\theta))$. The end mirror is supposed to work as a test mass and be cooled by the intracavity light field.

a derivation using two-photon formalism. To calculate the quantum radiation pressure fluctuation, we neglected a small fluctuation of the test mass $\delta x(\Omega)$ and solved the input-output relation (4.14) for e' , obtaining

$$\begin{aligned}
 e' &= te^{i\alpha} [I - re^{2i\alpha} R(2\phi)S(u, \theta)]^{-1} R(\varphi)a \\
 &= \frac{2\gamma}{t} \frac{1}{(\gamma + i\Omega)^2 + \Delta^2 - \Sigma^2} \begin{pmatrix} \gamma + i\Omega + \Sigma \cos 2\theta & -\Delta + \Sigma \sin 2\theta \\ \Delta + \Sigma \sin 2\theta & \gamma + i\Omega - \Sigma \cos 2\theta \end{pmatrix} R(\varphi)a \\
 &= \frac{2}{t} \frac{1}{(1 + i\Omega/\gamma)^2 + \delta^2 - \sigma^2} \\
 &\quad \times \begin{pmatrix} 1 + i\Omega/\gamma + \sigma \cos 2\theta & -\delta + \sigma \sin 2\theta \\ \delta + \sigma \sin 2\theta & 1 + i\Omega/\gamma - \sigma \cos 2\theta \end{pmatrix} R(\varphi)a, \tag{D.7}
 \end{aligned}$$

where r^2 and $t^2 = T$ are the input mirror's reflectivity and transmissivity, respectively; ϕ and α are the phase change and delay during a half cycle in the cavity, $s = e^u$ and θ are the squeezing factor and angle, respectively; $\gamma = Tc/(4L)$ is the cavity decay rate; L is the cavity half cycle length; $\Delta = \phi c/L$ is the cavity detuning; $\Sigma = uc/(2L)$ is the squeezing decay rate. Further, $\delta = \Delta/\gamma$ is the normalized cavity detuning, and $\sigma = \Sigma/\gamma$ is the normalized squeezing decay rate. Here, the rotation matrix for the input carrier $R(\varphi)$ is defined as Eq. (4.11). From Eq. (4.1), quantum radiation pressure fluctuation $\delta F_{\text{qrp}}(\Omega)$ can be written as

$$\delta F_{\text{qrp}}(\Omega) = 2\hbar k_0 E'_0 e'_1(\Omega) = \eta_1 a_1 + \eta_2 a_2. \tag{D.8}$$

The one-sided power spectral density of the quantum radiation pressure fluctuation $S_{\text{f,qrp}}(\Omega)$ is defined as

$$\frac{1}{2} 2\pi \delta(\Omega - \Omega') S_{\text{f,qrp}}(\Omega) = \frac{1}{2} \langle 0 | [\delta F_{\text{qrp}}(\Omega) \delta F_{\text{qrp}}^\dagger(\Omega') + \delta F_{\text{qrp}}^\dagger(\Omega') \delta F_{\text{qrp}}(\Omega)] | 0 \rangle. \tag{D.9}$$

Similarly to the power spectral density to signal-to-noise ratio, $S_{f,\text{qrp}}(\Omega)$ can be calculated as

$$\begin{aligned} S_{f,\text{qrp}} &= |\eta_1|^2 + |\eta_2|^2 \\ &= \frac{8\hbar k_0 P_{E'}}{\gamma L} \frac{1 + \delta^2 + \sigma^2 + (\Omega/\gamma)^2 + 2\sigma(\cos 2\theta - \delta \sin 2\theta)}{(1 + \delta^2 - \sigma^2 - (\Omega/\gamma)^2)^2 + (2\Omega/\gamma)^2}. \end{aligned} \quad (\text{D.10})$$

From Eq. (D.1), the radiation pressure phonon number n_{rp} can be written as

$$n_{\text{rp}} = \frac{m\Omega_{\text{eff}}}{\hbar} \langle x^2 \rangle_{\text{rp}} - \frac{1}{2}, \quad (\text{D.11})$$

where the mean square displacement resulting from the quantum radiation pressure fluctuation can be calculated as

$$\langle x^2 \rangle_{\text{rp}} = \int_0^\infty \frac{S_{f,\text{qrp}}(\Omega)}{|m(\Omega_{\text{eff}}^2 + i\gamma_{\text{opt}}\Omega - \Omega^2)|^2} \frac{d\Omega}{2\pi}, \quad (\text{D.12})$$

and γ_{opt} can be written as

$$\begin{aligned} \gamma_{\text{opt}} &= \frac{1}{m} \Im \left[\frac{K_{\text{opt}}}{\Omega} \right]_{\Omega=\Omega_{\text{eff}}} \\ &= -\frac{8k_0 P_{E'}}{mL\gamma^2} \frac{\delta - \sigma \sin 2\theta}{(1 + \delta^2 - \sigma^2 - (\Omega_{\text{eff}}/\gamma)^2)^2 + (2\Omega_{\text{eff}}/\gamma)^2}. \end{aligned} \quad (\text{D.13})$$

Here, intracavity power $P_{E'}$ and complex optical spring constant K_{opt} are calculated as expressed Eq. (4.13) and Eq. (4.16), and mechanical damping is negligible because of sufficient sideband cooling. If the Q factor is sufficiently high, we can calculate Eq. (D.12) the same as in Eq. (D.3):

$$\begin{aligned} \langle x^2 \rangle_{\text{rp}} &= S_{f,\text{qrp}}^{(2)}(\Omega_{\text{eff}}) \int_{-\infty}^\infty \frac{1}{|m(\Omega_{\text{eff}}^2 + i\gamma_{\text{opt}}\Omega - \Omega^2)|^2} \frac{d\Omega}{2\pi} \\ &= \frac{S_{f,\text{qrp}}^{(2)}(\Omega_{\text{eff}})}{2m^2\Omega_{\text{eff}}^2\gamma_{\text{opt}}}, \end{aligned} \quad (\text{D.14})$$

where $S_{f,\text{qrp}}^{(2)}(\Omega) = S_{f,\text{qrp}}(\Omega)/2$ is the two-sided power spectral density of the quantum radiation pressure fluctuation^{*1}. Therefore, the radiation pressure phonon number is calculated as

$$n_{\text{rp}} = -\frac{(1 + \sigma \cos 2\theta)^2 + (\Omega_{\text{eff}}/\gamma + \delta - \sigma \sin 2\theta)^2}{4(\delta + \sigma \sin 2\theta)\Omega_{\text{eff}}/\gamma}, \quad (\text{D.15})$$

and this result is consistent with [24] by denoting the squeezing parameter as $\varepsilon_r = -\Sigma \sin 2\theta/2$ and $\varepsilon_i = \Sigma \cos 2\theta/2$.

^{*1} Rigorously, the two-sided power spectral density of the radiation pressure fluctuation is asymmetric around $\Omega = 0$ and needs to be defined from the susceptibility of the cavity [61].

First, let us consider the case without intracavity squeezing ($\sigma = 0$). n_{rp} takes the minimum value when $\delta = -\sqrt{1 + (\omega_{\text{eff}}/\gamma)^2}$:

$$n_{\text{rp}} \geq \left(\frac{\gamma}{2\Omega_{\text{eff}}} \right)^2 \frac{2}{1 + \sqrt{1 + (\gamma/\Omega_{\text{eff}})^2}}. \quad (\text{D.16})$$

An optomechanical system with $\gamma \lesssim \Omega_{\text{eff}}$ is called a good cavity, and that with $\gamma \gtrsim \Omega_{\text{eff}}$ is called a bad cavity. If the mechanical resonance frequency is high enough ($\Omega_{\text{eff}} \simeq \omega_{\text{m}}$), the bad cavity results in $n_{\text{rp}} \gg 1$, indicating that the oscillator cannot reach the ground state owing to quantum fluctuations in the radiation pressure force. Intuitively, a bad cavity amplifies the upper and lower sidebands simultaneously. Hence, the optical damping with negative cavity detuning cannot efficiently remove energy from the oscillator. Therefore, it is necessary to use oscillators with high mechanical resonance frequency and high finesse cavity to cool oscillators to the ground state when using sideband cooling. However, macroscopic objects may have difficulty achieving good cavity conditions because of their low resonant frequency and the limited finesse values that can be achieved.

Now let us consider the impact of intracavity squeezing ($\sigma \neq 0$). In this case, n_{rp} takes the minimum value when $\delta = \sigma \sin 2\theta - \sqrt{(1 + \sigma \cos 2\theta)^2 + (\omega_{\text{eff}}/\gamma)^2}$:

$$n_{\text{rp}} \geq \left(\frac{\gamma}{2\Omega_{\text{eff}}} \right)^2 \frac{2(1 + \sigma \cos 2\theta)^2}{1 + \sqrt{1 + (1 + \sigma \cos 2\theta)^2 (\gamma/\Omega_{\text{eff}})^2}}. \quad (\text{D.17})$$

By setting $\theta = \pi/2$ and $\sigma \rightarrow 1$, we can obtain $n_{\text{rp}} \rightarrow 0$ independent of the sideband resolution. It should be noted that the cavity becomes close to the oscillation state with an extremely bad cavity condition because those parameters correspond to $\delta \rightarrow -\Omega_{\text{eff}}/\gamma$. Fig. D.2 shows the radiation pressure phonon number with intracavity squeezing. Without intracavity squeezing, the radiation pressure phonon number cannot be lower than 1 because this parameter is in a bad cavity condition. In contrast, the intracavity squeezing with somewhat gain can reduce the radiation pressure phonon number to less than 1. It should also be noted that the calculation method in this thesis can only be applied in the weak coupling regime ($G_0 \bar{a} \ll \gamma$, where G_0 and \bar{a} are defined in Sec. 6.1.2). The cooling limit in the strong coupling regime ($G_0 \bar{a} \gg \gamma$) is derived from the master equation [24].

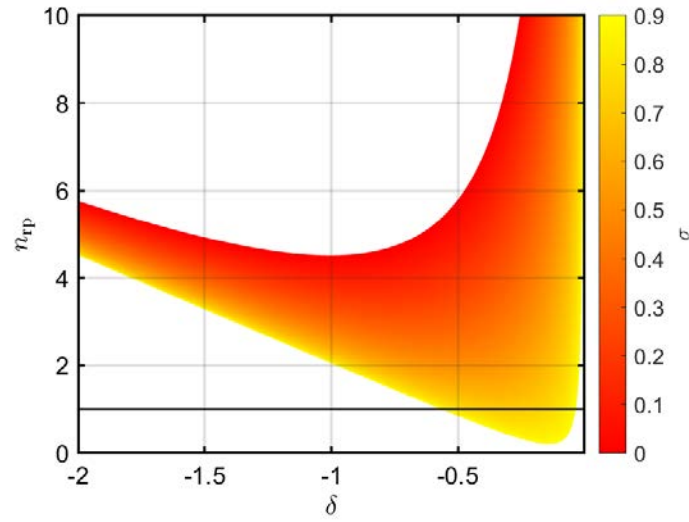


Fig. D.2: Modification of the radiation pressure phonon number by the intracavity squeezing. The parameters are set to $\Omega_{\text{eff}}/\gamma = 0.1$ and $\theta = \pi/2$. The black line shows the precondition for reaching the ground state, $n_{rp} = 1$.

Appendix E

Supplementary materials for the experiments

This appendix provides supplemental material to the experiments.

E.1 Feedback control

In this experiment, it is necessary to investigate the system's response while keeping the cavity detuning and squeezing angle within a narrow range. We used a feedback control to achieve a pull to the control point and a stable operation.

E.1.1 Stability of the feedback control

Transfer functions representing the system's frequency response are used to discuss a feedback control system. The transfer function for an element $T(\Omega)$ is the ratio of the input signal to the element $U(\Omega)$ and the output signal from the element $V(\Omega)$ in the frequency domain:

$$T(\Omega) := \frac{V(\Omega)}{U(\Omega)}. \quad (\text{E.1})$$

The block diagram is a schematic of the elements that constitute the system un-

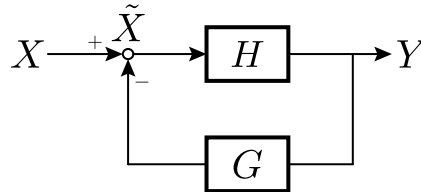


Fig. E.1: Block diagram of the optical system.

der control, represented as a concise diagram using transfer functions. Fig. E.1 presents a block diagram of the feedback control for the optical system, where

$H(\Omega)$ and $G(\Omega)$ denote the transfer function of the optical system and filter, $X(\Omega)$ denotes noises that fluctuate a mirror, $\tilde{X}(\Omega)$ denotes the effective displacement of a mirror, and $Y(\Omega)$ denotes the error signal from the optical system. The error signal is passed through a filter and multiplied by -1 before giving feedback to the mirror. The effective displacement of the mirror \tilde{X} can be written as

$$\begin{aligned}\tilde{X} &= X - HG\tilde{X} \\ &= \frac{1}{1 + HG}X.\end{aligned}\tag{E.2}$$

The product of the transfer functions HG is called the open loop transfer function (OLTF), and its magnitude $|HG|$ is called the open loop gain (OLG). The effective transfer function formed by the feedback component $1/(1 + HG)$ is called the closed loop transfer function (CLTF).

Let us compare $\tilde{X}(\Omega)$ with the displacement in the absence of feedback control $X(\Omega)$. If OLG is sufficiently larger than 1, CLTF equals approximately the inverse of OLG, indicating that the disturbance can be suppressed. It also implies that the same factor suppresses gravitational wave signals entering the system from the same path. In general, the feedback control does not change the interferometer's sensitivity. In contrast, if the OLG is sufficiently smaller than 1, the CLTF equals ~ 1 , which implies that the system is not under control. The frequency that satisfies $|H(\Omega)G(\Omega)| = 1$, which is the split-off point that determines whether the control is applied or not, is called the unity gain frequency (UGF).

If there is a frequency at which $H(\Omega)G(\Omega) = -1$, meaning that the phase of OLTF at UGF is -180 degrees, this system amplifies the noise of UGF. The transfer function of the optical system $H(\omega)$ cannot be easily changed; hence, we avoided this instability by implementing the filter with an analog circuit using op-amps. The phase margin is the sum of the phase at UGF plus 180 degrees, and the gain margin is the gain (dB) at the frequency where the phase is -180 degrees times -1 . These are used as a reference to consider the stability of the control system.

E.1.2 Phase compensation

The suspended mirror significantly oscillates near the resonant frequency of the mechanical suspension. The UGF must be sufficiently higher than the resonant frequency to control the optical system containing the suspended mirror. However, the transfer function of the mechanical suspension has a phase of -180 degrees in a band sufficiently higher than the resonant frequency, as shown in Eq. (4.40). In other words, when the error signal is fed back directly to the suspended mirror, the control system becomes unstable at the UGF. In this experiment, we avoided this instability by leading the phase near the UGF with a filter. The transfer function of the filter circuit can be written as

$$G_{\text{PLF}}(\Omega) = A_{\text{PLF}} \frac{1 + i\Omega\tau_1}{1 + i\Omega\tau_2} \quad (\tau_1 > \tau_2),\tag{E.3}$$

where A_{LPF} is the filter gain, and $1/\tau_1$ and $1/\tau_2$ are the zero and pole of the filter, respectively. This filter can lead the phase in the angular frequencies $1/\tau_1$ to $1/\tau_2$. By adjusting the gain such that UGF is within this range, the stability of the control system can be ensured while controlling with high gain in the frequency band below $1/\tau_1$. The compensation method that ensures a phase margin by leading the phase is called phase-lead compensation.

When an actuator with a wide linear operating range is used, such as a piezoelectric element, the UGF should be set in a band lower than the mechanical resonance frequency of the PZT. The OLG must be sufficiently lower than 1 at the mechanical resonance frequency to ensure stability. This experiment used a low-pass filter in a control system with a PZT. The transfer function of the filter circuit can be written as

$$G_{\text{LPF}}(\Omega) = A_{\text{LPF}} \frac{1}{1 + i\Omega\tau_0}, \quad (\text{E.4})$$

where A_{LPF} is the filter gain, and $1/\tau_0$ is the pole of the filter. This filter can reduce the gain in the frequency band above $1/\tau_0$. The compensation method that ensures a gain margin by delaying the phase is called phase-delay compensation.

E.2 Design of cavities

The laser source used in the experiment has a Gaussian beam profile with a specific beam size and intensity distribution. Therefore, it cannot be regarded as a plane wave resonating in a cavity. This section discusses the design method of optical cavities for Gaussian modes by tracking the trajectory of the Gaussian beam using the ABCD matrix.

E.2.1 ABCD matrix

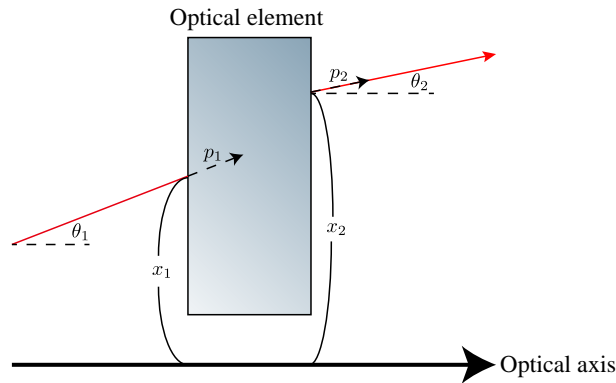


Fig. E.2: Schematic of an optical element modifies the trajectory of the ray.

As shown in Fig. E.2, the impact of the optical element on the ray can be quantitatively calculated if the distance from the optical axis x and the angle for the

optical axis^{*1} $p = \tan \theta$ of the ray before and after it enters the optical element are known. The properties of this optical element can be denoted by a 2×2 matrix as follows:

$$\begin{pmatrix} x_1 \\ q_1 \end{pmatrix} = \begin{pmatrix} A & B \\ C & D \end{pmatrix} \begin{pmatrix} x_2 \\ q_2 \end{pmatrix}. \quad (\text{E.5})$$

This matrix is called ray or ABCD matrix.

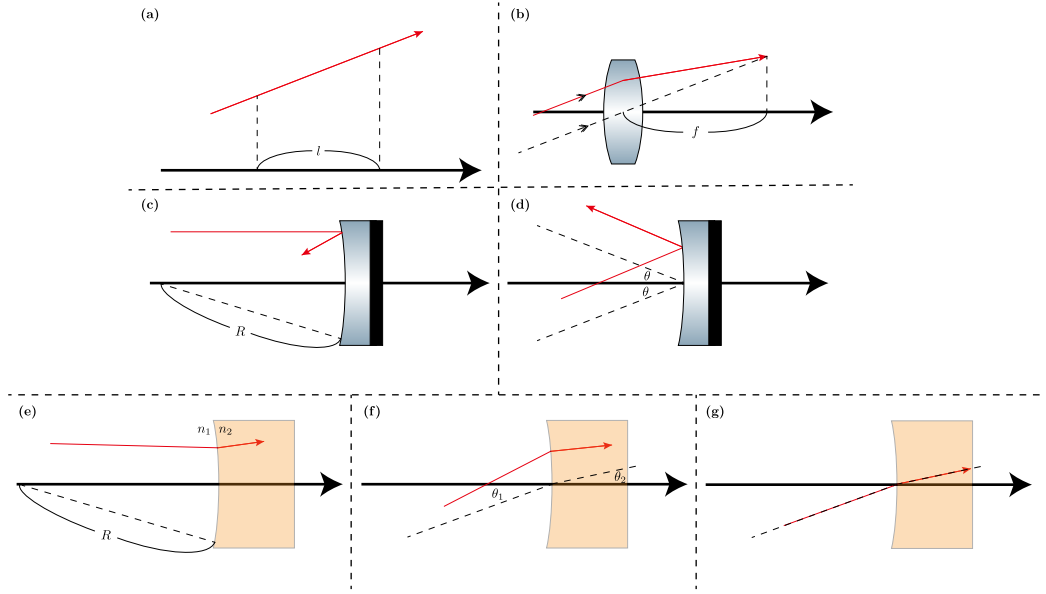


Fig. E.3: Ray tracing by the ABCD matrix.

The ABCD matrix for the optical elements shown in Fig. E.3 is summarized as follows [199].

(a) For propagation at distance l in free space,

$$\begin{pmatrix} 1 & l \\ 0 & 1 \end{pmatrix}. \quad (\text{E.6})$$

(b) For a thin lens with a focal length of f ,

$$\begin{pmatrix} 1 & 0 \\ -1/f & 1 \end{pmatrix}, \quad (\text{E.7})$$

where $f > 0$ for a convex lens.

(c) For the reflection by a mirror with curvature R ,

$$\begin{pmatrix} 1 & 0 \\ -2/R & 1 \end{pmatrix}, \quad (\text{E.8})$$

^{*1} When considering the trajectory of a paraxial ray, the angle can be regarded as sufficiently small, $p \approx \theta$. In addition, p is sometimes defined by multiplying the refractive index of the optical element n .

where $R > 0$ for a concave mirror.

(d) For the reflection at angle θ with curvature mirror,

$$\begin{pmatrix} 1 & 0 \\ -2/R_e & 1 \end{pmatrix}, \quad (\text{E.9})$$

where

$$R_e = \begin{cases} R \cos \theta & (\text{tangential plane}), \\ R / \cos \theta & (\text{sagittal plane}). \end{cases} \quad (\text{E.10})$$

(e) For the incident to the dielectric interface of refractive index n_1 to n_2 with curvature R ,

$$\begin{pmatrix} 1 & 0 \\ (n_2 - n_1)/R & 1 \end{pmatrix}, \quad (\text{E.11})$$

where $R > 0$ for the concave incident side.

(f) For the incidence to curved dielectric interface in the tangential plane at an angle of incidence θ_1 and angle of refraction θ_2 ,

$$\begin{pmatrix} \frac{\cos \theta_2}{\cos \theta_1} & 0 \\ \Delta n_e / R & \frac{\cos \theta_1}{\cos \theta_2} \end{pmatrix}, \quad (\text{E.12})$$

where

$$n_1 \sin \theta_1 = n_2 \sin \theta_2, \quad (\text{E.13})$$

$$\Delta n_e = (n_2 \cos \theta_2 - n_1 \cos \theta_1) / \cos \theta_1 \cos \theta_2. \quad (\text{E.14})$$

(g) For the incidence to curved dielectric interface in the sagittal plane at an angle of incidence θ_1 and angle of refraction θ_2 ,

$$\begin{pmatrix} 1 & 0 \\ \Delta n_e / R & 1 \end{pmatrix}, \quad (\text{E.15})$$

where

$$n_1 \sin \theta_1 = n_2 \sin \theta_2, \quad (\text{E.16})$$

$$\Delta n_e = n_2 \cos \theta_2 - n_1 \cos \theta_1. \quad (\text{E.17})$$

E.2.2 Gaussian beam

The wave equation for the electric field $\mathbf{E}(\mathbf{x}, t)$ can be written as

$$\left(\nabla^2 - \frac{1}{c^2} \frac{\partial^2}{\partial t^2} \right) \mathbf{E}(\mathbf{x}, t) = 0. \quad (\text{E.18})$$

By solving this equation under the paraxial approximation, we can obtain a Hermite-Gaussian mode propagating in the z -axis $U_{lm}(\mathbf{x}, t)$ as one of the solutions [199]. In correspondence with Eq. (3.2), the solution can be denoted as

$$\mathbf{E}(\mathbf{x}, t) = U_{lm}^*(\mathbf{x}, t)E_0^*e^{-i(\omega_0 t - k_0 z)} + U_{lm}(\mathbf{x}, t)E_0e^{i(\omega_0 t - k_0 z)}, \quad (\text{E.19})$$

with

$$U_{lm}(\mathbf{x}, t) = \sqrt{\frac{2}{\pi w^2(z)}} \frac{1}{\sqrt{2^{l+m} l! m!}} H_l \left(\frac{\sqrt{2}x}{w(z)} \right) H_m \left(\frac{\sqrt{2}y}{w(z)} \right) \\ \times \exp \left[\left(-\frac{1}{w^2(z)} - i \frac{k}{2R(z)} \right) (x^2 + y^2) + i(l + m + 1)\zeta(z) \right], \quad (\text{E.20})$$

$$w(z) = w_0 \sqrt{1 + \left(\frac{z}{z_R} \right)^2}, \quad (\text{E.21})$$

$$z_R = \frac{\pi w_0^2}{\lambda_0}, \quad (\text{E.22})$$

$$R(z) = z \left[1 + \left(\frac{z_R}{z} \right)^2 \right], \quad (\text{E.23})$$

$$\zeta(z) = \arctan \left(\frac{z}{z_R} \right). \quad (\text{E.24})$$

Here, H_l denotes the Hermite polynomial. The mode with $l = m = 0$ is called the fundamental mode or 00 modes and other modes are called higher-order modes. $w(z)$ denotes the size of the Gaussian beam (spot size), and an intensity of $1 - e^{-2} \sim 86.5\%$ of the whole is contained within the radius of the fundamental mode $w(z)$. w_0 denotes the spot size at the point where the spot size is minimum (beam waist). z_R denotes the Rayleigh length, the range where the beam behaves as a plane wave. A beam far from the beam waist, where z is sufficiently larger than the Rayleigh length, can be considered a spherical wave. $R(z)$ denotes the radius of curvature of the equiphase surface of the light field. $\zeta(z)$ denotes the Gouy phase, the phase difference between higher-order modes that differ by one order.

E.2.3 Self-consistent equation

All parameters of the Gaussian beam can be written only by the distance from the waist z and Rayleigh range z_R . We define the q -parameters of the Gaussian beam as

$$\frac{1}{q} := \frac{1}{z + iz_R} = \frac{1}{R(z)} - i \frac{2}{k_0 w^2(z)}. \quad (\text{E.25})$$

The modification of the Gaussian beam trajectory by the optical elements can be described only by the q -parameter. The transformation of the q -parameter $q_1 \rightarrow q_2$

by an optical element with a specific ABCD matrix follows the ABCD law [200]:

$$q_2 = \frac{Aq_1 + B}{Cq_1 + D}. \quad (\text{E.26})$$

This relationship can be used to discuss the cavity's stability. The laser injected into the cavity can be regarded as a Gaussian beam with 00 modes. The cavity should satisfy the condition that the q-parameter does not change during one cycle of the cavity to treat a superposition of wavefronts equivalent to a plane wave. That is, using the ABCD matrix during one cavity round, the q-parameter satisfies

$$q = \frac{Aq + B}{Cq + D}. \quad (\text{E.27})$$

This equation is called the self-consistent equation. From the condition that the q-parameter becomes a pure imaginary value, we obtain the spot size at the beam waist w_0 as

$$w_0 = \sqrt{\frac{\lambda_0}{\pi} \frac{|B|}{\sqrt{1 - \left(\frac{A+D}{2}\right)^2}}}. \quad (\text{E.28})$$

Here, we used the fact that the determinant of the ABCD matrix is 1 ($AD = BC$) when the optical elements that constitute the cavity do not absorb or scatter.

E.2.4 Design of bow-tie cavities

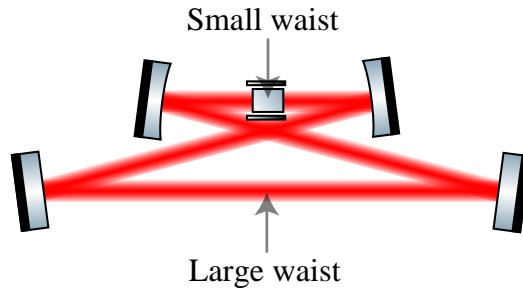


Fig. E.4: Schematic of a bow-tie cavity.

The SHG and OPO cavities used in this experiment were bow-tie cavities containing two curvature mirrors. As shown in Fig. E.4, this type of cavity has two beam waists: one in the midpoint of the curvature mirror and one in the midpoint of the flat mirror. The former was called a small waist, and the latter a large waist. The small waist size was set to be approximately $40 \mu\text{m}$ to maximize the efficiency of the nonlinear optical effect. The mirror positions were calculated using the ABCD matrix, the large waist was then determined, and the incident beam mode matching was performed. Let d be the distance between the curvature mirrors, and $2L$ be the one-round length of the cavity, and $l = 2L - d$.

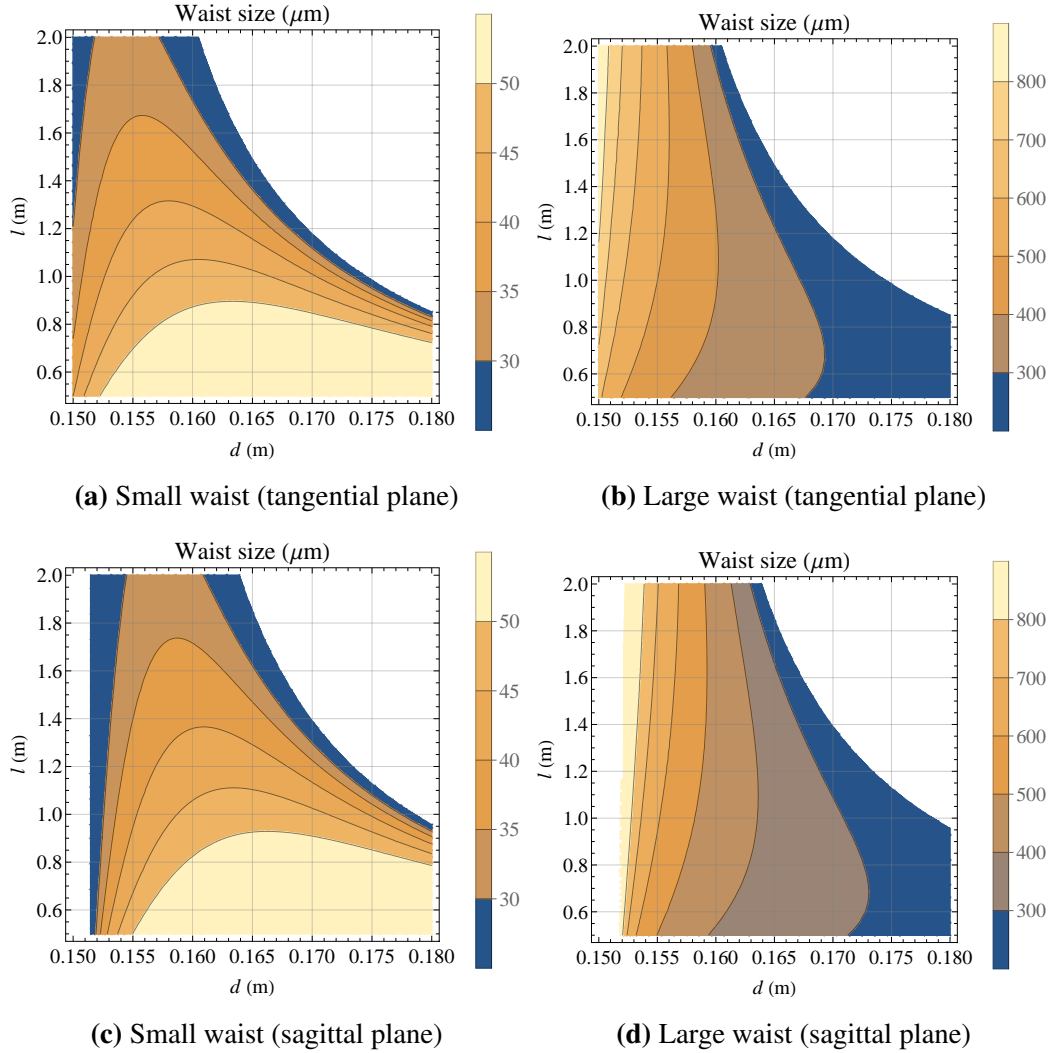


Fig. E.5: Waist sizes of the SHG cavity.

Curved mirrors with a curvature of 150 mm were used for the SHG cavity. As denoted in Eq. (E.9), the effective radius of curvature for tangential and sagittal planes is different when a curved mirror reflects the beam at an angle of incidence. The angle of incidence should be set as small as possible to reduce the effect of astigmatism, and it was set to 8 degrees because a margin must be made to insert a nonlinear optical crystal. Simulations for the tangential and sagittal planes with these parameters are shown in Fig. E.5. Based on these results, we set $d = 0.16$ m and $l = 1.2$ m.

Curved mirrors with a curvature of 68.5 mm were used for the OPO cavity. It is more compact than the SHG cavity, considering the possibility of constructing a cavity for the pump light. The angle of incidence was set to 17 degrees. Simulations for the tangential and sagittal planes with these parameters are shown in Fig. E.6. Based on these results, we set $d = 0.078$ m and $l = 0.35$ m.

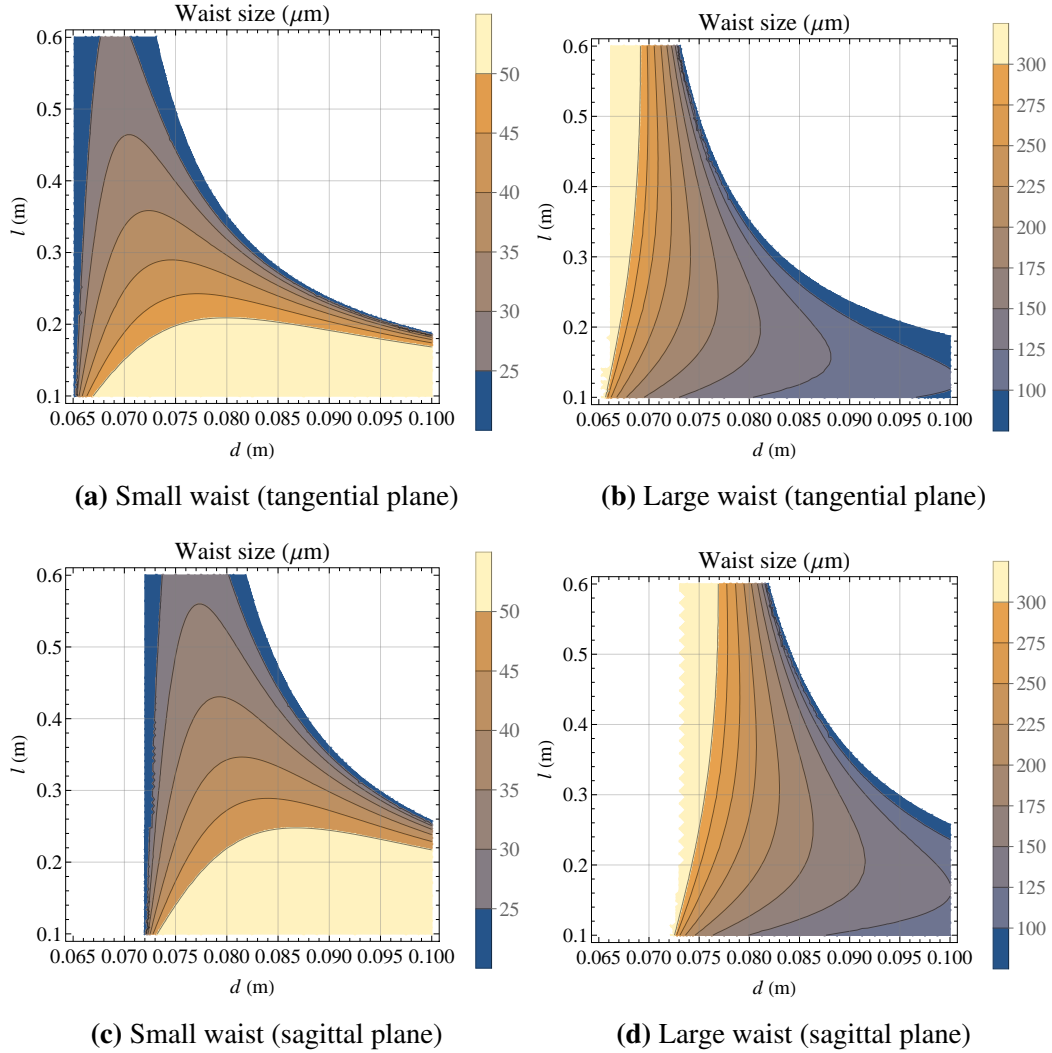


Fig. E.6: Waist sizes of the OPO cavity.

Moreover, in Sec. 6.2.3, the nonlinear optical crystal behaves as a lens owing to the Kerr effect. From Eq. (6.25), the focal length of the Kerr lens is approximately -27 cm. Simulations are shown in Fig. E.7, assuming that a thin concave lens is placed in the midpoint of the curved mirror of the OPO cavity. For $d = 0.078$ m and $l = 0.35$ m, the small waist size was reduced to roughly $30 \mu\text{m}$. In contrast, the large waist size hardly changes, meaning that the beam diameter that should enter the cavity does not change. That is, the Kerr lens does not affect the stability requirements of the intracavity beam.

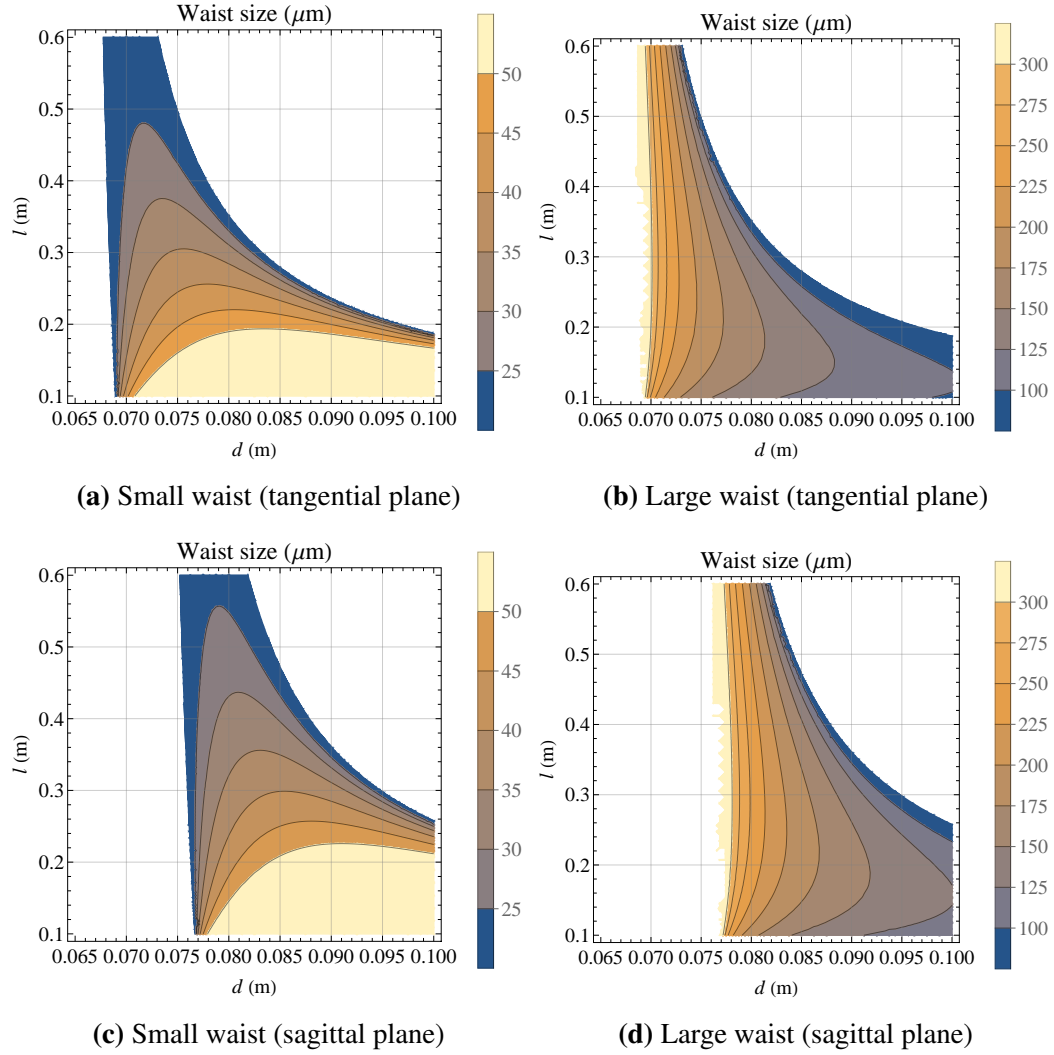
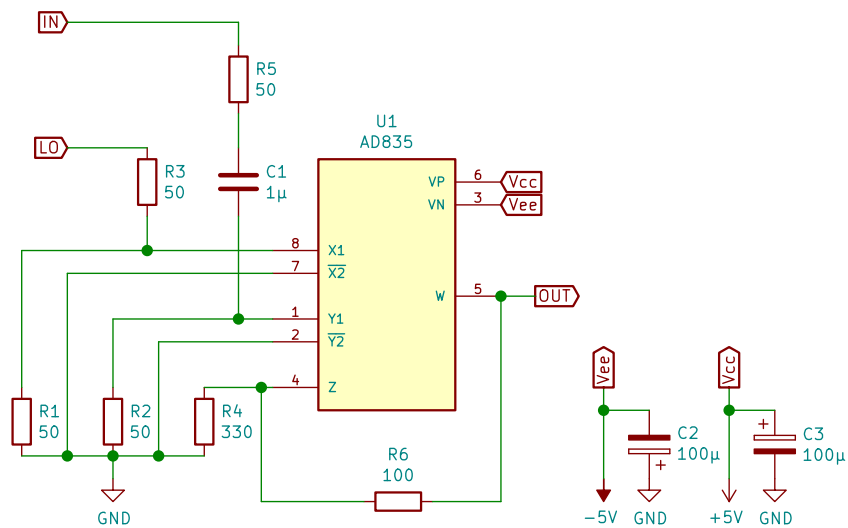


Fig. E.7: Waist sizes of the OPO cavity with Kerr lens.

E.3 Circuit used in the experiment

Fig. E.8 shows the circuit of the mixer used in the PLL demodulation. The same circuit was used for the PDH technique to demodulate and obtain the error signal.

**Fig. E.8:** Circuit of the mixer.

Acknowledgments

This work has been supported by many people. I would like to express my gratitude to them.

First of all, I would like to thank my supervisor Kentaro Somiya. He gave me a very interesting research topic and continued to support my research. This study was made possible by his extensive knowledge and precise advice. Undoubtedly the most fortunate thing in my life has been the opportunity to work on gravitational wave detectors in the Somiya laboratory for six years.

I would like to thank Ken-ichi Harada for his kind support in the experiment. Thanks to his extensive experience, the experimental system has been significantly improved. In addition, his approach to research has been a great source of mental support for me.

I would like to thank Masakatsu Fujimoto for his valuable insight. He has been working on gravitational wave detectors for a very long time and has been an essential adviser of our laboratory. His comments in the lab seminar were helpful in furthering my understanding.

Yuta Michimura provided precise comments on the results of the experiment. I would not have been able to conclude this thesis without his incisive feedback. He also frequently introduced us to interesting research, which helped broaden my horizons.

Kentaro Komori has greatly assisted me in key points of my research. He gave serious consideration to even my naive questions. The discussions with him are reflected in every part of this study, whether theoretical or experimental.

Yusuke Tominaga joined our discussion on research. His unique research was enormously inspiring to me. He provided me with an opportunity to consider the applications of our research.

Jerome Degallaix and his colleagues provided us with a mirror with an extremely high-quality coating. Their world's best technology has expanded the possibilities for our research.

Teruya Sugihara and his colleagues produced a beryllium copper suspension for us. The measurement accuracy in our experiments have improved dramatically thanks to their technical skills.

I would also like to thank the members of our laboratory, especially the ones who are conducting experiments in the clean room with me.

Kaido Suzuki has helped me many times with my unreasonable requests. His research has greatly facilitated our experiments.

Wataru Usukura has helped to upgrade the experiment. He also accompanied me in theoretical discussions, which helped me greatly.

Daiki Haba has launched a new experiment. His genuine commitment to his experiment was motivating to me.

Junko Kasuya, Takuya Yaginuma, Kohei Kusayanagi, and Masahiro Hisatomi, who were my seniors in Somiya laboratory, helped me a great deal in the early stages of my research. Hiraku Sasaki, Ryosuke Nakashima, Mélodie Ribes, Shaun Ren, Yuting Liu, Takashi Inoue, Jun Ogawa, Homare Abe, Makoto Kuribayashi, Koki Tachihara, Takanori Suzuki, Yilun Hou, Seiya Sasaoka, Sakino Takeda, Kotaro Takeguchi, Diego Dominguez, and Hayato Tanaka, who are or were my colleagues in Somiya laboratory, have discussed with me on seminars and various other occasions. Naomi Maekawa and Fumiko Miyama, who were the lab office staff, assisted me with the clerical procedures.

This thesis was reviewed by Mikio Kozuma, Takuya Satoh, Osamu Jinnouchi, and Kiyotaka Aikawa. Their comments helped me to improve this paper considerably. I would like to thank them for their invaluable support and insightful advice.

I have been financially supported by Japan Society for the Promotion of Science (JSPS) Research Fellowships for Young Scientists (DC1). This work was supported by JSPS KAKENHI Grant No. 20J22778.

Finally, I would like to thank my family. My brother gave me the technical advice that was essential for the experiment. My parents have been supportive and understanding to my thinking, and have given me sound advices. Thank you.

Bibliography

- [1] A. Einstein, “Näherungsweise Integration der Feldgleichungen der Gravitation”, *Sitzungsberichte der Königlich Preussischen Akademie der Wissenschaften*, pp. 688–696, (1916).
- [2] A. Einstein, “Über Gravitationswellen”, *Sitzungsberichte der Königlich Preussischen Akademie der Wissenschaften*, pp. 154–167, (1918).
- [3] B. P. Abbott *et al.*, “Observation of Gravitational Waves from a Binary Black Hole Merger”, *Phys. Rev. Lett.*, Vol. 116, p. 061102, (2016).
- [4] The LIGO Scientific Collaboration *et al.*, “GWTC-3: Compact Binary Coalescences Observed by LIGO and Virgo During the Second Part of the Third Observing Run”, (2021).
- [5] B. P. Abbott *et al.*, “GW170817: Observation of Gravitational Waves from a Binary Neutron Star Inspiral”, *Phys. Rev. Lett.*, Vol. 119, p. 161101, (2017).
- [6] B. P. Abbott *et al.*, “Multi-messenger Observations of a Binary Neutron Star Merger*”, *The Astrophysical Journal Letters*, Vol. 848, No. 2, p. L12, (2017).
- [7] B. P. Abbott *et al.*, “Gravitational Waves and Gamma-Rays from a Binary Neutron Star Merger: GW170817 and GRB 170817A”, *The Astrophysical Journal Letters*, Vol. 848, No. 2, p. L13, (2017).
- [8] E. Pian *et al.*, “Spectroscopic identification of r-process nucleosynthesis in a double neutron-star merger”, *Nature*, Vol. 551, No. 7678, pp. 67–70, (2017).
- [9] B. P. Abbott *et al.*, “A gravitational-wave standard siren measurement of the Hubble constant”, *Nature*, Vol. 551, No. 7678, pp. 85–88, (2017).
- [10] G. M. H. and, “Advanced LIGO: the next generation of gravitational wave detectors”, *Classical and Quantum Gravity*, Vol. 27, No. 8, p. 084006, (2010).
- [11] F. Acernese *et al.*, “Advanced Virgo: a second-generation interferometric gravitational wave detector”, *Classical and Quantum Gravity*, Vol. 32, No. 2, p. 024001, (2014).
- [12] K. Somiya, “Detector configuration of KAGRA - the Japanese cryogenic gravitational-wave detector”, *Classical and Quantum Gravity*, Vol. 29, No. 12, p. 124007, (2012).
- [13] K. Kotake, K. Sato, K. Takahashi, “Explosion mechanism, neutrino burst and gravitational wave in core-collapse supernovae”, *Reports on Progress in Physics*, Vol. 69, No. 4, p. 971, (2006).
- [14] R. Prix, “*Gravitational Waves from Spinning Neutron Stars*”, Springer

- Berlin Heidelberg, Berlin, Heidelberg, (2009), pp. 651–685.
- [15] L. Baiotti, L. Rezzolla, “Binary neutron star mergers: a review of Einstein’s richest laboratory”, *Reports on Progress in Physics*, Vol. 80, No. 9, p. 096901, (2017).
 - [16] N. Sarin, P. D. Lasky, “The evolution of binary neutron star post-merger remnants: a review”, *General Relativity and Gravitation*, Vol. 53, No. 6, p. 59, (2021).
 - [17] M. Oertel *et al.*, “Equations of state for supernovae and compact stars”, *Rev. Mod. Phys.*, Vol. 89, p. 015007, (2017).
 - [18] C. M. Caves, “Quantum-Mechanical Radiation-Pressure Fluctuations in an Interferometer”, *Phys. Rev. Lett.*, Vol. 45, pp. 75–79, (1980).
 - [19] K. Ackley *et al.*, “Neutron Star Extreme Matter Observatory: A kilohertz-band gravitational-wave detector in the global network”, *Publications of the Astronomical Society of Australia*, Vol. 37, p. e047, (2020).
 - [20] A. Buonanno, Y. Chen, “Signal recycled laser-interferometer gravitational-wave detectors as optical springs”, *Phys. Rev. D*, Vol. 65, p. 042001, (2002).
 - [21] K. Somiya *et al.*, “Parametric signal amplification to create a stiff optical bar”, *Physics Letters A*, Vol. 380, No. 4, pp. 521–524, (2016).
 - [22] S. Huang, G. S. Agarwal, “Enhancement of cavity cooling of a micromechanical mirror using parametric interactions”, *Phys. Rev. A*, Vol. 79, p. 013821, (2009).
 - [23] M. Asjad *et al.*, “Optomechanical cooling with intracavity squeezed light”, *Opt. Express*, Vol. 27, No. 22, pp. 32427–32444, (2019).
 - [24] J.-H. Gan *et al.*, “Intracavity-Squeezed Optomechanical Cooling”, *Laser & Photonics Reviews*, Vol. 13, No. 11, p. 1900120, (2019).
 - [25] R. A. Hulse, J. H. Taylor, “Discovery of a pulsar in a binary system.”, *Astrophys. J.*, Vol. 195, pp. L51–L53, (1975).
 - [26] T. Damour, J. H. Taylor, “On the orbital period change of the binary pulsar PSR-1913+16”, *Astrophys. J.*, Vol. 366, pp. 501–511, (1991).
 - [27] Corral-Santana, J. M. *et al.*, “BlackCAT: A catalogue of stellar-mass black holes in X-ray transients”, *A&A*, Vol. 587, p. A61, (2016).
 - [28] T. Kinugawa *et al.*, “Possible indirect confirmation of the existence of Pop III massive stars by gravitational wave”, *Monthly Notices of the Royal Astronomical Society*, Vol. 442, No. 4, pp. 2963–2992, (2014).
 - [29] M. Sasaki *et al.*, “Primordial black holes—perspectives in gravitational wave astronomy”, *Classical and Quantum Gravity*, Vol. 35, No. 6, p. 063001, (2018).
 - [30] R. Abbott *et al.*, “Observation of Gravitational Waves from Two Neutron Star-Black Hole Coalescences”, *The Astrophysical Journal Letters*, Vol. 915, No. 1, p. L5, (2021).
 - [31] K. Liu *et al.*, “Pulsar-black hole binaries: prospects for new gravity tests with future radio telescopes”, *Monthly Notices of the Royal Astronomical Society*, Vol. 445, No. 3, pp. 3115–3132, (2014).
 - [32] R. Abbott *et al.*, “GW190814: Gravitational Waves from the Coalescence

- of a 23 Solar Mass Black Hole with a 2.6 Solar Mass Compact Object”, *The Astrophysical Journal Letters*, Vol. 896, No. 2, p. L44, (2020).
- [33] K. Riles, “Gravitational waves: Sources, detectors and searches”, *Progress in Particle and Nuclear Physics*, Vol. 68, pp. 1–54, (2013).
 - [34] C. J. Moore, R. H. Cole, C. P. L. Berry, “Gravitational-wave sensitivity curves”, *Classical and Quantum Gravity*, Vol. 32, No. 1, p. 015014, (2014).
 - [35] N. Aggarwal *et al.*, “Challenges and opportunities of gravitational-wave searches at MHz to GHz frequencies”, *Living Reviews in Relativity*, Vol. 24, No. 1, p. 4, (2021).
 - [36] M. Volonteri, “Formation of supermassive black holes”, *The Astronomy and Astrophysics Review*, Vol. 18, No. 3, pp. 279–315, (2010).
 - [37] B. P. Abbott *et al.*, “Searches for Gravitational Waves from Known Pulsars at Two Harmonics in 2015-2017 LIGO Data”, *The Astrophysical Journal*, Vol. 879, No. 1, p. 10, (2019).
 - [38] B. P. Abbott *et al.*, “GW190425: Observation of a Compact Binary Coalescence with Total Mass $\sim 3.4M_{\odot}$ ”, *The Astrophysical Journal Letters*, Vol. 892, No. 1, p. L3, (2020).
 - [39] B. Giacomazzo, L. Rezzolla, L. Baiotti, “Accurate evolutions of inspiralling and magnetized neutron stars: Equal-mass binaries”, *Phys. Rev. D*, Vol. 83, p. 044014, (2011).
 - [40] K. Hotokezaka *et al.*, “Binary neutron star mergers: Dependence on the nuclear equation of state”, *Phys. Rev. D*, Vol. 83, p. 124008, (2011).
 - [41] K. Takami, L. Rezzolla, L. Baiotti, “Constraining the Equation of State of Neutron Stars from Binary Mergers”, *Phys. Rev. Lett.*, Vol. 113, p. 091104, (2014).
 - [42] K. Takami, L. Rezzolla, L. Baiotti, “Spectral properties of the post-merger gravitational-wave signal from binary neutron stars”, *Phys. Rev. D*, Vol. 91, p. 064001, (2015).
 - [43] R. De Pietri *et al.*, “Modeling equal and unequal mass binary neutron star mergers using public codes”, *Phys. Rev. D*, Vol. 93, p. 064047, (2016).
 - [44] A. Bauswein, N. Stergioulas, H.-T. Janka, “Exploring properties of high-density matter through remnants of neutron-star mergers”, *The European Physical Journal A*, Vol. 52, No. 3, p. 56, (2016).
 - [45] A. Endrizzi *et al.*, “General relativistic magnetohydrodynamic simulations of binary neutron star mergers with the APR4 equation of state”, *Classical and Quantum Gravity*, Vol. 33, No. 16, p. 164001, (2016).
 - [46] W. Kastaun, R. Ciolfi, B. Giacomazzo, “Structure of stable binary neutron star merger remnants: A case study”, *Phys. Rev. D*, Vol. 94, p. 044060, (2016).
 - [47] T. Kawamura *et al.*, “Binary neutron star mergers and short gamma-ray bursts: Effects of magnetic field orientation, equation of state, and mass ratio”, *Phys. Rev. D*, Vol. 94, p. 064012, (2016).
 - [48] R. Ciolfi *et al.*, “General relativistic magnetohydrodynamic simulations of binary neutron star mergers forming a long-lived neutron star”, *Phys. Rev.*

- D*, Vol. 95, p. 063016, (2017).
- [49] M. Shibata, K. Kiuchi, “Gravitational waves from remnant massive neutron stars of binary neutron star merger: Viscous hydrodynamics effects”, *Phys. Rev. D*, Vol. 95, p. 123003, (2017).
 - [50] D. Radice *et al.*, “Probing Extreme-density Matter with Gravitational-wave Observations of Binary Neutron Star Merger Remnants”, *The Astrophysical Journal Letters*, Vol. 842, No. 2, p. L10, (2017).
 - [51] M. Hanauske *et al.*, “Rotational properties of hypermassive neutron stars from binary mergers”, *Phys. Rev. D*, Vol. 96, p. 043004, (2017).
 - [52] M. Breschi *et al.*, “Kilohertz gravitational waves from binary neutron star remnants: Time-domain model and constraints on extreme matter”, *Phys. Rev. D*, Vol. 100, p. 104029, (2019).
 - [53] R. De Pietri *et al.*, “Numerical-relativity simulations of long-lived remnants of binary neutron star mergers”, *Phys. Rev. D*, Vol. 101, p. 064052, (2020).
 - [54] A. Figura *et al.*, “Binary neutron star merger simulations with hot microscopic equations of state”, *Phys. Rev. D*, Vol. 103, p. 083012, (2021).
 - [55] S. L. Liebling, C. Palenzuela, L. Lehner, “Effects of high density phase transitions on neutron star dynamics”, *Classical and Quantum Gravity*, Vol. 38, No. 11, p. 115007, (2021).
 - [56] N. Christensen, “Stochastic gravitational wave backgrounds”, *Reports on Progress in Physics*, Vol. 82, No. 1, p. 016903, (2018).
 - [57] L. P. Grishchuk, “Relic gravitational waves and limits on inflation”, *Phys. Rev. D*, Vol. 48, pp. 3513–3516, (1993).
 - [58] J. Weber, “Evidence for Discovery of Gravitational Radiation”, *Phys. Rev. Lett.*, Vol. 22, pp. 1320–1324, (1969).
 - [59] O. D. Aguiar, “Past, present and future of the Resonant-Mass gravitational wave detectors”, *Research in Astronomy and Astrophysics*, Vol. 11, No. 1, p. 1, (2011).
 - [60] G. E. Moss, L. R. Miller, R. L. Forward, “Photon-Noise-Limited Laser Transducer for Gravitational Antenna”, *Appl. Opt.*, Vol. 10, No. 11, pp. 2495–2498, (1971).
 - [61] M. Aspelmeyer, T. J. Kippenberg, F. Marquardt, “Cavity optomechanics”, *Rev. Mod. Phys.*, Vol. 86, pp. 1391–1452, (2014).
 - [62] C.-M. Chen, J. M. Nester, W.-T. Ni, “A brief history of gravitational wave research”, *Chinese Journal of Physics*, Vol. 55, No. 1, pp. 142–169, (2017).
 - [63] B. P. Abbott *et al.*, “LIGO: the Laser Interferometer Gravitational-Wave Observatory”, *Reports on Progress in Physics*, Vol. 72, No. 7, p. 076901, (2009).
 - [64] C. Bradaschia *et al.*, “The VIRGO Project: A wide band antenna for gravitational wave detection”, *Nuclear Instruments and Methods in Physics Research Section A: Accelerators, Spectrometers, Detectors and Associated Equipment*, Vol. 289, No. 3, pp. 518 – 525, (1990).
 - [65] K. Tsubono, “300-m laser interferometer gravitational wave detector (TAMA300) in Japan.”, *First Edoardo Amaldi Conference on Gravitational*

- Wave Experiments* (eds. E. Coccia, G. Pizzella, F. Ronga), (1995), p. 112.
- [66] K. Danzmann *et al.*, “GEO 600 - a 600 m laser interferometric gravitational wave antenna.”, *First Edoardo Amaldi Conference on Gravitational Wave Experiments* (eds. E. Coccia, G. Pizzella, F. Ronga), (1995), p. 100.
 - [67] B. Willke *et al.*, “The GEO-HF project”, *Classical and Quantum Gravity*, Vol. 23, No. 8, p. S207, (2006).
 - [68] H. Grote (for the LIGO Scientific Collaboration), “The GEO 600 status”, *Classical and Quantum Gravity*, Vol. 27, No. 8, p. 084003, (2010).
 - [69] R. Narayan, T. Piran, A. Shemi, “Neutron Star and Black Hole Binaries in the Galaxy”, *Astrophysical Journal Letters*, Vol. 379, p. L17, (1991).
 - [70] A. Buikema *et al.*, “Sensitivity and performance of the Advanced LIGO detectors in the third observing run”, *Phys. Rev. D*, Vol. 102, p. 062003, (2020).
 - [71] C. S. UNNIKRISHNAN, “IndIGO AND LIGO-INDIA: SCOPE AND PLANS FOR GRAVITATIONAL WAVE RESEARCH AND PRECISION METROLOGY IN INDIA”, *International Journal of Modern Physics D*, Vol. 22, No. 01, p. 1341010, (2013).
 - [72] T. L. S. Collaboration *et al.*, “First joint observation by the underground gravitational-wave detector KAGRA with GEO 600”, *Progress of Theoretical and Experimental Physics*, Vol. 2022, No. 6, (2022), 063F01.
 - [73] B. P. Abbott *et al.*, “Prospects for observing and localizing gravitational-wave transients with Advanced LIGO, Advanced Virgo and KAGRA”, *Living Reviews in Relativity*, Vol. 23, No. 1, p. 3, (2020).
 - [74] Y. Aso *et al.*, “Interferometer design of the KAGRA gravitational wave detector”, *Phys. Rev. D*, Vol. 88, p. 043007, (2013).
 - [75] M. Punturo *et al.*, “The Einstein Telescope: a third-generation gravitational wave observatory”, *Classical and Quantum Gravity*, Vol. 27, No. 19, p. 194002, (2010).
 - [76] B. P. Abbott *et al.*, “Exploring the sensitivity of next generation gravitational wave detectors”, *Classical and Quantum Gravity*, Vol. 34, No. 4, p. 044001, (2017).
 - [77] D. Reitze *et al.*, “Cosmic Explorer: The U.S. Contribution to Gravitational-Wave Astronomy beyond LIGO”, (2019).
 - [78] K. Danzmann, A. R. LIGO, “LISA technology concept, status, prospects”, *Classical and Quantum Gravity*, Vol. 20, No. 10, pp. S1–S9, (2003).
 - [79] S. Kawamura *et al.*, “The Japanese space gravitational wave antenna: DECIGO”, *Classical and Quantum Gravity*, Vol. 28, No. 9, p. 094011, (2011).
 - [80] T. Akutsu *et al.*, “Construction of KAGRA: an underground gravitational-wave observatory”, *Progress of Theoretical and Experimental Physics*, Vol. 2018, No. 1, (2018), 013F01.
 - [81] M. G. Beker *et al.*, “Newtonian noise and ambient ground motion for gravitational wave detectors”, *J. Phys. Conf. Ser.*, Vol. 363, p. 012004, (2012).
 - [82] H. Abe *et al.*, “The Current Status and Future Prospects of KAGRA, the Large-Scale Cryogenic Gravitational Wave Telescope Built in the Kamioka

- Underground”, *Galaxies*, Vol. 10, No. 3, (2022).
- [83] H. B. Callen, T. A. Welton, “Irreversibility and Generalized Noise”, *Phys. Rev.*, Vol. 83, pp. 34–40, (1951).
 - [84] V. Braginsky, M. Gorodetsky, S. Vyatchanin, “Thermodynamical fluctuations and photo-thermal shot noise in gravitational wave antennae”, *Physics Letters A*, Vol. 264, No. 1, pp. 1–10, (1999).
 - [85] L. Landau, E. Lifshitz, “*Statistical Physics*”, No. Volume 5, Elsevier Science, (2013).
 - [86] M. Evans *et al.*, “Thermo-optic noise in coated mirrors for high-precision optical measurements”, *Phys. Rev. D*, Vol. 78, p. 102003, (2008).
 - [87] V. Braginsky, M. Gorodetsky, S. Vyatchanin, “Thermo-refractive noise in gravitational wave antennae”, *Physics Letters A*, Vol. 271, No. 5, pp. 303 – 307, (2000).
 - [88] J. Cripe *et al.*, “Measurement of quantum back action in the audio band at room temperature”, *Nature*, Vol. 568, No. 7752, pp. 364–367, (2019).
 - [89] V. B. Braginskii, Y. I. Vorontsov, “Quantum-mechanical limitations in macroscopic experiments and modern experimental technique”, *Soviet Physics Uspekhi*, Vol. 17, No. 5, pp. 644–650, (1975).
 - [90] C. M. Caves, B. L. Schumaker, “New formalism for two-photon quantum optics. I. Quadrature phases and squeezed states”, *Phys. Rev. A*, Vol. 31, pp. 3068–3092, (1985).
 - [91] B. L. Schumaker, C. M. Caves, “New formalism for two-photon quantum optics. II. Mathematical foundation and compact notation”, *Phys. Rev. A*, Vol. 31, pp. 3093–3111, (1985).
 - [92] M. Xiao, L.-A. Wu, H. J. Kimble, “Precision measurement beyond the shot-noise limit”, *Phys. Rev. Lett.*, Vol. 59, pp. 278–281, (1987).
 - [93] P. Grangier *et al.*, “Squeezed-light-enhanced polarization interferometer”, *Phys. Rev. Lett.*, Vol. 59, pp. 2153–2156, (1987).
 - [94] R. Schnabel, “Squeezed states of light and their applications in laser interferometers”, *Physics Reports*, Vol. 684, pp. 1–51, (2017).
 - [95] H. J. Kimble *et al.*, “Conversion of conventional gravitational-wave interferometers into quantum nondemolition interferometers by modifying their input and/or output optics”, *Phys. Rev. D*, Vol. 65, p. 022002, (2001).
 - [96] K. Kasai, G. Jiangrui, C. Fabre, “Observation of squeezing using cascaded nonlinearity”, *Europhysics Letters*, Vol. 40, No. 1, p. 25, (1997).
 - [97] K. S. Zhang *et al.*, “Generation of bright squeezed light at 1.06 μm using cascaded nonlinearities in a triply resonant cw periodically-poled lithium niobate optical parametric oscillator”, *Phys. Rev. A*, Vol. 64, p. 033815, (2001).
 - [98] H. Rehbein *et al.*, “Optical Transfer Functions of Kerr Nonlinear Cavities and Interferometers”, *Phys. Rev. Lett.*, Vol. 95, p. 193001, (2005).
 - [99] J. Mizuno, “*Comparison of optical configurations for laser-interferometric gravitational-wave detectors*”, PhD thesis, Hannover U., (1995).
 - [100] H. Miao *et al.*, “Towards the Fundamental Quantum Limit of Linear Mea-

- surements of Classical Signals”, *Phys. Rev. Lett.*, Vol. 119, p. 050801, (2017).
- [101] H. Wittel, “*Compensation of the thermal lens in the GEO600 beam splitter*”, PhD thesis, Hannover, Max Planck Inst. Grav., (2009).
 - [102] J. Mizuno *et al.*, “Resonant sideband extraction: a new configuration for interferometric gravitational wave detectors”, *Physics Letters A*, Vol. 175, No. 5, pp. 273–276, (1993).
 - [103] Y. Chen, “Macroscopic quantum mechanics: theory and experimental concepts of optomechanics”, *Journal of Physics B: Atomic, Molecular and Optical Physics*, Vol. 46, No. 10, p. 104001, (2013).
 - [104] S. Vyatchanin, E. Zubova, “Quantum variation measurement of a force”, *Physics Letters A*, Vol. 201, No. 4, pp. 269–274, (1995).
 - [105] C. M. Caves, “Quantum-mechanical noise in an interferometer”, *Phys. Rev. D*, Vol. 23, pp. 1693–1708, (1981).
 - [106] S. Chelkowski *et al.*, “Experimental characterization of frequency-dependent squeezed light”, *Phys. Rev. A*, Vol. 71, p. 013806, (2005).
 - [107] E. Oelker *et al.*, “Audio-Band Frequency-Dependent Squeezing for Gravitational-Wave Detectors”, *Phys. Rev. Lett.*, Vol. 116, p. 041102, (2016).
 - [108] Y. Zhao *et al.*, “Frequency-Dependent Squeezed Vacuum Source for Broadband Quantum Noise Reduction in Advanced Gravitational-Wave Detectors”, *Phys. Rev. Lett.*, Vol. 124, p. 171101, (2020).
 - [109] L. McCuller *et al.*, “Frequency-Dependent Squeezing for Advanced LIGO”, *Phys. Rev. Lett.*, Vol. 124, p. 171102, (2020).
 - [110] M. Evans *et al.*, “Realistic filter cavities for advanced gravitational wave detectors”, *Phys. Rev. D*, Vol. 88, p. 022002, (2013).
 - [111] C. Cahillane, G. Mansell, “Review of the Advanced LIGO Gravitational Wave Observatories Leading to Observing Run Four”, *Galaxies*, Vol. 10, No. 1, (2022).
 - [112] K. Somiya, “Quantum noise reduction techniques in KAGRA”, *The European Physical Journal D*, Vol. 74, No. 1, p. 10, (2020).
 - [113] H. Miao, “*Exploring macroscopic quantum mechanics in optomechanical devices*”, PhD thesis, (2010).
 - [114] A. Buonanno, Y. Chen, “Optical noise correlations and beating the standard quantum limit in advanced gravitational-wave detectors”, *Classical and Quantum Gravity*, Vol. 18, No. 15, pp. L95–L101, (2001).
 - [115] N. Matsumoto *et al.*, “Direct measurement of optical-trap-induced decoherence”, *Phys. Rev. A*, Vol. 94, p. 033822, (2016).
 - [116] K. Komori *et al.*, “Improving force sensitivity by amplitude measurements of light reflected from a detuned optomechanical cavity”, *Phys. Rev. A*, Vol. 104, p. L031501, (2021).
 - [117] M. Korobko *et al.*, “Beating the Standard Sensitivity-Bandwidth Limit of Cavity-Enhanced Interferometers with Internal Squeezed-Light Generation”, *Phys. Rev. Lett.*, Vol. 118, p. 143601, (2017).

-
- [118] M. Korobko, F. Khalili, R. Schnabel, “Engineering the optical spring via intra-cavity optical-parametric amplification”, *Physics Letters A*, Vol. 382, No. 33, pp. 2238–2244, (2018), Special Issue in memory of Professor V.B. Braginsky.
 - [119] S. Huang, G. S. Agarwal, “Normal-mode splitting in a coupled system of a nanomechanical oscillator and a parametric amplifier cavity”, *Phys. Rev. A*, Vol. 80, p. 033807, (2009).
 - [120] T. Kumar, A. B. Bhattacharjee, ManMohan, “Dynamics of a movable micromirror in a nonlinear optical cavity”, *Phys. Rev. A*, Vol. 81, p. 013835, (2010).
 - [121] V. Peano *et al.*, “Intracavity Squeezing Can Enhance Quantum-Limited Optomechanical Position Detection through Deamplification”, *Phys. Rev. Lett.*, Vol. 115, p. 243603, (2015).
 - [122] G. S. Agarwal, S. Huang, “Strong mechanical squeezing and its detection”, *Phys. Rev. A*, Vol. 93, p. 043844, (2016).
 - [123] S. Huang, A. Chen, “Improving the cooling of a mechanical oscillator in a dissipative optomechanical system with an optical parametric amplifier”, *Phys. Rev. A*, Vol. 98, p. 063818, (2018).
 - [124] S. Liu *et al.*, “Realization of a highly sensitive mass sensor in a quadratically coupled optomechanical system”, *Phys. Rev. A*, Vol. 99, p. 033822, (2019).
 - [125] W.-A. Li, G.-Y. Huang, “Enhancement of optomechanically induced sum sidebands using parametric interactions”, *Phys. Rev. A*, Vol. 100, p. 023838, (2019).
 - [126] W. Qin *et al.*, “Emission of photon pairs by mechanical stimulation of the squeezed vacuum”, *Phys. Rev. A*, Vol. 100, p. 062501, (2019).
 - [127] B. Xiong *et al.*, “Strong Squeezing of Duffing Oscillator in a Highly Dissipative Optomechanical Cavity System”, *Annalen der Physik*, Vol. 532, No. 4, p. 1900596, (2020).
 - [128] D.-Y. Wang *et al.*, “Enhanced photon blockade in an optomechanical system with parametric amplification”, *Opt. Lett.*, Vol. 45, No. 9, pp. 2604–2607, (2020).
 - [129] J.-S. Zhang, A.-X. Chen, “Large and robust mechanical squeezing of optomechanical systems in a highly unresolved sideband regime via Duffing nonlinearity and intracavity squeezed light”, *Opt. Express*, Vol. 28, No. 24, pp. 36620–36631, (2020).
 - [130] Y.-M. Liu *et al.*, “Simultaneous Cooling of Two Mechanical Resonators with Intracavity Squeezed Light”, *Annalen der Physik*, Vol. 533, No. 8, p. 2100074, (2021).
 - [131] X. Ye *et al.*, “Improving the Stochastic Feedback Cooling of a Mechanical Oscillator Using a Degenerate Parametric Amplifier”, *Photonics*, Vol. 9, No. 4, (2022).
 - [132] Q. Liao *et al.*, “Cooling of mechanical resonator in a hybrid intracavity squeezing optomechanical system”, *Opt. Express*, Vol. 30, No. 21, pp. 38776–38788, (2022).

- [133] T. J. Kippenberg *et al.*, “Analysis of Radiation-Pressure Induced Mechanical Oscillation of an Optical Microcavity”, *Phys. Rev. Lett.*, Vol. 95, p. 033901, (2005).
- [134] O. Miyakawa *et al.*, “Measurement of optical response of a detuned resonant sideband extraction gravitational wave detector”, *Phys. Rev. D*, Vol. 74, p. 022001, (2006).
- [135] T. Corbitt *et al.*, “Measurement of radiation-pressure-induced optomechanical dynamics in a suspended Fabry-Perot cavity”, *Phys. Rev. A*, Vol. 74, p. 021802, (2006).
- [136] T. Corbitt *et al.*, “An All-Optical Trap for a Gram-Scale Mirror”, *Phys. Rev. Lett.*, Vol. 98, p. 150802, (2007).
- [137] J. Cripe *et al.*, “Observation of an optical spring with a beam splitter”, *Opt. Lett.*, Vol. 43, No. 9, pp. 2193–2196, (2018).
- [138] D. Kelley *et al.*, “Observation of photothermal feedback in a stable dual-carrier optical spring”, *Phys. Rev. D*, Vol. 92, p. 062003, (2015).
- [139] P. A. Altin *et al.*, “A robust single-beam optical trap for a gram-scale mechanical oscillator”, *Sci. Rep.*, Vol. 7, No. 1, p. 14546, (2017).
- [140] R. W. P. Drever *et al.*, “Laser phase and frequency stabilization using an optical resonator”, *Applied Physics B*, Vol. 31, No. 2, pp. 97–105, (1983).
- [141] S. Chelkowski *et al.*, “Coherent control of broadband vacuum squeezing”, *Phys. Rev. A*, Vol. 75, p. 043814, (2007).
- [142] H. Vahlbruch *et al.*, “Coherent Control of Vacuum Squeezing in the Gravitational-Wave Detection Band”, *Phys. Rev. Lett.*, Vol. 97, p. 011101, (2006).
- [143] N. Aritomi *et al.*, “Control of a filter cavity with coherent control sidebands”, *Phys. Rev. D*, Vol. 102, p. 042003, (2020).
- [144] N. Aritomi *et al.*, “Demonstration of length control for a filter cavity with coherent control sidebands”, *Phys. Rev. D*, Vol. 106, p. 102003, (2022).
- [145] B. S. Sheard *et al.*, “Observation and characterization of an optical spring”, *Phys. Rev. A*, Vol. 69, p. 051801, (2004).
- [146] J. A. Armstrong *et al.*, “Interactions between Light Waves in a Nonlinear Dielectric”, *Phys. Rev.*, Vol. 127, pp. 1918–1939, (1962).
- [147] K. Inoue, “Suppression of signal fluctuation induced by crosstalk light in a gain saturated laser diode amplifier”, *IEEE Photonics Technology Letters*, Vol. 8, No. 3, pp. 458–460, (1996).
- [148] H. Pakarzadeh, A. Zakery, “Modelling of noise suppression in gain-saturated fiber optical parametric amplifiers”, *Optics Communications*, Vol. 309, pp. 30–36, (2013).
- [149] N. Othman *et al.*, “Saturation Behavior of Fiber Optical Parametric Amplifier in Presence of Dispersion Fluctuations”, *2018 IEEE 7th International Conference on Photonics (ICP)*, (2018), pp. 1–3.
- [150] S. Otabe *et al.*, “Photothermal effect in macroscopic optomechanical systems with an intracavity nonlinear optical crystal”, *Opt. Express*, Vol. 30, No. 23, pp. 42579–42593, (2022).

-
- [151] M. Pinard, A. Dantan, “Quantum limits of photothermal and radiation pressure cooling of a movable mirror”, *New Journal of Physics*, Vol. 10, No. 9, p. 095012, (2008).
 - [152] S. De Liberato, N. Lambert, F. Nori, “Quantum noise in photothermal cooling”, *Phys. Rev. A*, Vol. 83, p. 033809, (2011).
 - [153] J. Restrepo *et al.*, “Classical and quantum theory of photothermal cavity cooling of a mechanical oscillator”, *Comptes Rendus Physique*, Vol. 12, No. 9, pp. 860–870, (2011).
 - [154] M. Abdi, A. R. Bahrapour, D. Vitali, “Quantum optomechanics of a multimode system coupled via a photothermal and a radiation pressure force”, *Phys. Rev. A*, Vol. 86, p. 043803, (2012).
 - [155] S. Gigan *et al.*, “Self-cooling of a micromirror by radiation pressure”, *Nature*, Vol. 444, No. 7115, pp. 67–70, (2006).
 - [156] C. H. Metzger, K. Karrai, “Cavity cooling of a microlever”, *Nature*, Vol. 432, No. 7020, pp. 1002–1005, (2004).
 - [157] C. Metzger *et al.*, “Optical self cooling of a deformable Fabry-Perot cavity in the classical limit”, *Phys. Rev. B*, Vol. 78, p. 035309, (2008).
 - [158] G. Jourdan, F. Comin, J. Chevrier, “Mechanical Mode Dependence of Bolometric Backaction in an Atomic Force Microscopy Microlever”, *Phys. Rev. Lett.*, Vol. 101, p. 133904, (2008).
 - [159] J. Ma *et al.*, “Optical back-action on the photothermal relaxation rate”, *Optica*, Vol. 8, No. 2, pp. 177–183, (2021).
 - [160] J. Ma *et al.*, “Photothermally induced transparency”, *Science Advances*, Vol. 6, No. 8, p. eaax8256, (2020).
 - [161] M. Clementi *et al.*, “Thermo-optically induced transparency on a photonic chip”, *Light: Science & Applications*, Vol. 10, No. 1, p. 240, (2021).
 - [162] K.-J. Boller, A. Imamoglu, S. E. Harris, “Observation of electromagnetically induced transparency”, *Phys. Rev. Lett.*, Vol. 66, pp. 2593–2596, (1991).
 - [163] M. Fleischhauer, A. Imamoglu, J. P. Marangos, “Electromagnetically induced transparency: Optics in coherent media”, *Rev. Mod. Phys.*, Vol. 77, pp. 633–673, (2005).
 - [164] G. S. Agarwal, S. Huang, “Electromagnetically induced transparency in mechanical effects of light”, *Phys. Rev. A*, Vol. 81, p. 041803, (2010).
 - [165] S. Weis *et al.*, “Optomechanically Induced Transparency”, *Science*, Vol. 330, No. 6010, pp. 1520–1523, (2010).
 - [166] A. H. Safavi-Naeini *et al.*, “Electromagnetically induced transparency and slow light with optomechanics”, *Nature*, Vol. 472, No. 7341, pp. 69–73, (2011).
 - [167] J. Steinlechner *et al.*, “Optical absorption measurements on crystalline silicon test masses at 1550 nm”, *Classical and Quantum Gravity*, Vol. 30, No. 9, p. 095007, (2013).
 - [168] T. Carmon, L. Yang, K. J. Vahala, “Dynamical thermal behavior and thermal self-stability of microcavities”, *Opt. Express*, Vol. 12, No. 20, pp. 4742–

- 4750, (2004).
- [169] K. Konthasinghe *et al.*, “Self-sustained photothermal oscillations in high-finesse Fabry-Perot microcavities”, *Phys. Rev. A*, Vol. 95, p. 013826, (2017).
 - [170] J. Qin *et al.*, “Cancellation of photothermally induced instability in an optical resonator”, *Optica*, Vol. 9, No. 8, pp. 924–932, (2022).
 - [171] J. Ma *et al.*, “Observation of nonlinear dynamics in an optical levitation system”, *Commun. Phys.*, Vol. 3, No. 1, p. 197, (2020).
 - [172] M. Cerdonio *et al.*, “Thermoelastic effects at low temperatures and quantum limits in displacement measurements”, *Phys. Rev. D*, Vol. 63, p. 082003, (2001).
 - [173] C. A. Ebbers, S. P. Velsko, “Optical and thermo-optical characterization of KTP and its isomorphs for 1.06- μ m-pumped OPOs”, *Nonlinear Frequency Generation and Conversion* (eds. M. C. Gupta, W. J. Kozlovsky, D. C. MacPherson), Vol. 2700, International Society for Optics and Photonics, SPIE, (1996), pp. 227 – 239.
 - [174] C. Bosshard *et al.*, “Kerr Nonlinearity via Cascaded Optical Rectification and the Linear Electro-optic Effect”, *Phys. Rev. Lett.*, Vol. 74, pp. 2816–2819, (1995).
 - [175] G. I. Stegeman, “cascading: nonlinear phase shifts”, *Quantum and Semi-classical Optics: Journal of the European Optical Society Part B*, Vol. 9, No. 2, p. 139, (1997).
 - [176] C. K. Law, “Interaction between a moving mirror and radiation pressure: A Hamiltonian formulation”, *Phys. Rev. A*, Vol. 51, pp. 2537–2541, (1995).
 - [177] P. D. Drummond, D. F. Walls, “Quantum theory of optical bistability. I. Nonlinear polarisability model”, *Journal of Physics A: Mathematical and General*, Vol. 13, No. 2, p. 725, (1980).
 - [178] X. Lu *et al.*, “Optical Kerr nonlinearity in a high-Q silicon carbide microresonator”, *Opt. Express*, Vol. 22, No. 25, pp. 30826–30832, (2014).
 - [179] A. Hasnaoui, M. Fromager, K. Ait-Ameur, “About the validity of the parabolic approximation in Kerr lensing effect”, *Optik*, Vol. 193, p. 162986, (2019).
 - [180] H. Li *et al.*, “Bound electronic Kerr effect and self-focusing induced damage in second-harmonic-generation crystals”, *Optics Communications*, Vol. 144, No. 1, pp. 75–81, (1997).
 - [181] M. Maggiore, “*Gravitational waves: Volume 1: Theory and experiments*”, Vol. 1, Oxford university press, (2008).
 - [182] R. Epstein, R. V. Wagoner, “Post-Newtonian generation of gravitational waves”, *Astrophys. J.*, Vol. 197, pp. 717–723, (1975).
 - [183] C. W. Misner, K. S. Thorne, J. A. Wheeler, “*Gravitation*”, Princeton University Press, (2017).
 - [184] L. D. Landau, “*The classical theory of fields*”, Vol. 2, Elsevier, (2013).
 - [185] P. C. Peters, “Gravitational Radiation and the Motion of Two Point Masses”, *Phys. Rev.*, Vol. 136, pp. B1224–B1232, (1964).
 - [186] R. W. Boyd, “Chapter 1 - The Nonlinear Optical Susceptibility”, *Nonlinear*

-
- Optics (Third Edition)* (ed. R. W. Boyd), Academic Press, Burlington, third edition edition, (2008), pp. 1–67.
- [187] M. Milton, “General expression for the efficiency of phase-matched and nonphase-matched second-order nonlinear interactions between plane waves”, *IEEE Journal of Quantum Electronics*, Vol. 28, No. 3, pp. 739–749, (1992).
 - [188] M. Korobko *et al.*, “Quantum expander for gravitational-wave observatories”, *Light: Science & Applications*, Vol. 8, No. 1, p. 118, (2019).
 - [189] F. Y. Khalili, “Optimal configurations of filter cavity in future gravitational-wave detectors”, *Phys. Rev. D*, Vol. 81, p. 122002, (2010).
 - [190] D. Zoepfl *et al.*, “Kerr Enhanced Backaction Cooling in Magnetomechanics”, *Phys. Rev. Lett.*, Vol. 130, p. 033601, (2023).
 - [191] O. Arcizet *et al.*, “Radiation-pressure cooling and optomechanical instability of a micromirror”, *Nature*, Vol. 444, No. 7115, pp. 71–74, (2006).
 - [192] A. Schliesser *et al.*, “Radiation Pressure Cooling of a Micromechanical Oscillator Using Dynamical Backaction”, *Phys. Rev. Lett.*, Vol. 97, p. 243905, (2006).
 - [193] J. D. Teufel *et al.*, “Sideband cooling of micromechanical motion to the quantum ground state”, *Nature*, Vol. 475, No. 7356, pp. 359–363, (2011).
 - [194] J. Chan *et al.*, “Laser cooling of a nanomechanical oscillator into its quantum ground state”, *Nature*, Vol. 478, No. 7367, pp. 89–92, (2011).
 - [195] E. Verhagen *et al.*, “Quantum-coherent coupling of a mechanical oscillator to an optical cavity mode”, *Nature*, Vol. 482, No. 7383, pp. 63–67, (2012).
 - [196] M. Underwood *et al.*, “Measurement of the motional sidebands of a nanogram-scale oscillator in the quantum regime”, *Phys. Rev. A*, Vol. 92, p. 061801, (2015).
 - [197] R. W. Peterson *et al.*, “Laser Cooling of a Micromechanical Membrane to the Quantum Backaction Limit”, *Phys. Rev. Lett.*, Vol. 116, p. 063601, (2016).
 - [198] L. Qiu *et al.*, “Laser Cooling of a Nanomechanical Oscillator to Its Zero-Point Energy”, *Phys. Rev. Lett.*, Vol. 124, p. 173601, (2020).
 - [199] A. Siegman, “*Lasers*”, University Science Books, (1986).
 - [200] H. Kogelnik, “On the Propagation of Gaussian Beams of Light Through Lenslike Media Including those with a Loss or Gain Variation”, *Appl. Opt.*, Vol. 4, No. 12, pp. 1562–1569, (1965).